THE FRONTIERS OF BATTERY DEVELOPMENT

Selected research from ***Advanced Energy Materials*** and ***Batteries & Supercaps***

Sponsored by

Imprint

Boschstr. 12, 69469 Weinheim, Germany

Email: info@wiley-vch.de
Editors: Dr Tianyu Liu and Dr Till von Graberg
Ad Sales: Jan Käppler

Cover image © Merck KGaA

Contents

Introduction

To reflect the current progress of the battery research field, we organized this collection of articles published by leading scientists in *Advanced Energy Materials* and *Batteries & Supercaps*. The articles are definitive references on the state-of-the-art in electrodes, electrolytes and mechanisms related to various battery systems.

Fast charging is a critical performance metric for battery implementation. Jürgen Janek and colleagues from Justus Liebig University Giessen reviewed the design strategies for fast-charging lithium-ion batteries (DOI: 10.1002/aenm.202101126). Furthermore, monitoring the variability in cell capacity and resistance is critical to ensuring consistent performance in applications. Dirk Uwe Sauer and colleagues from RWTH Aachen University reported the minimum sample sizes required to estimate cell-to-cell manufacturing variability (DOI: 10.1002/batt.202100148).

Alongside fast charging, increasing the energy density is another popular research topic in the battery community. Gerbrand Ceder of the University of California, Berkeley, and Samsung Research America collaborated to develop a NASICON-type compound, $Na_4MnCr(PO_4)_3$, for high-energy-density Na-ion batteries. The high-voltage redox reactions associated with $Mn^{2+/3+}$ (3.5 V), $Mn^{3+/4+}$ (4.0 V), and $Cr^{3+/4+}$ (4.0 V) gave this electrode material a specific capacity of 130 mAh/g (4.35 V). In another thread, Ceder's team demonstrated that increasing the size ratio of cathode to electrolyte particles improves the energy density of all-solid-state batteries (DOI: 10.1002/aenm.201902881).

Lithium–sulfur batteries have a high energy density, but their capacity diminishes quickly. Chunsheng Wang of the University of Maryland and colleagues created a high-fluorinated electrolyte to improve the stability of lithium–sulfur batteries (DOI: 10.1002/aenm.201803774). 1 M lithium bis(fluorosulfonyl) imide/dimethoxyether is blended with 1H,1H,5H-octafluoropentyl-1,1,2,2-tetrafluoroethyl ether (OFE) to form the electrolyte. OFE decreased the solubility of high-order lithium polysulfides from the sulfur cathode and smoothed out lithium deposition and stripping on the anode. This electrolyte enabled a cathode capacity of 775 mAh/g for 150 cycles (electrolyte: 4.56 g/Ah).

Dr Tianyu Liu
Associate Editor - Materials Science & Physics
Wiley

ADVANCED ENERGY MATERIALS
www.advenergymat.de

Fast Charging of Lithium-Ion Batteries: A Review of Materials Aspects

Manuel Weiss, Raffael Ruess, Johannes Kasnatscheew, Yehonatan Levartovsky, Natasha Ronith Levy, Philip Minnmann, Lukas Stolz, Thomas Waldmann, Margret Wohlfahrt-Mehrens, Doron Aurbach, Martin Winter, Yair Ein-Eli, and Jürgen Janek**

Fast charging is considered to be a key requirement for widespread economic success of electric vehicles. Current lithium-ion batteries (LIBs) offer high energy density enabling sufficient driving range, but take considerably longer to recharge than traditional vehicles. Multiple properties of the applied anode, cathode, and electrolyte materials influence the fast-charging ability of a battery cell. In this review, the physicochemical basics of different material combinations are considered in detail, identifying the transport of lithium inside the electrodes as the crucial rate-limiting steps for fast-charging. Lithium diffusion within the active materials inherently slows down the charging process and causes high overpotentials. In addition, concentration polarization by slow lithium-ion transport within the electrolyte phase in the porous electrodes also limits the charging rate. Both kinetic effects are responsible for lithium plating observed on graphite anodes. Conclusions drawn from potential and concentration profiles within LIB cells are complemented by extensive literature surveys on anode, cathode, and electrolyte materials—including solid-state batteries. The advantages and disadvantages of typical LIB materials are analyzed, resulting in suggestions for optimum properties on the material and electrode level for fast-charging applications. Finally, limitations on the cell level are discussed briefly as well.

1. Introduction

1.1. Aims, Scope, and Framework

A dozen senior battery and supercapacitor expert scientists, and approximately 30 Ph.D. students and postdoctoral fellows from both Israel and Germany gathered in 2019, in the frame of the 4th German-Israeli Battery School (GIBS 4) in Berlin, Germany. The Berlin workshop was focused on in-depth discussions on four "hot subjects," including the following topics: 1) How will the far future of electrochemical power sources be after the lithium era, if ever? 2) Will the future of portable power sources be based on liquid or solid electrolytes? 3) Fuel cells versus battery technologies—complementary or competitors? And lastly, the 4th topic of fast charging—a reality or just a dream?

Here, we bring to the readers the outcome of Group 4 discussions that continued over the last two years on fast charging and materials aspects from a physicochemical point of view.

Dr. M. Weiss, Dr. R. Ruess, P. Minnmann, Prof. J. Janek
Institute of Physical Chemistry
Justus Liebig University Giessen
Heinrich-Buff-Ring 17, 35392 Giessen, Germany
E-mail: juergen.janek@phys.chemie.uni-giessen.de

Dr. M. Weiss, Dr. R. Ruess, P. Minnmann, Prof. J. Janek
Center for Materials Research (LaMa)
Justus Liebig University Giessen
Heinrich-Buff-Ring 16, 35392 Giessen, Germany

Dr. J. Kasnatscheew, L. Stolz, Prof. M. Winter
Helmholtz-Institute Münster
IEK-12
Forschungszentrum Jülich GmbH
Corrensstraße 46, 48149 Münster, Germany

The ORCID identification number(s) for the author(s) of this article can be found under https://doi.org/10.1002/aenm.202101126.

DOI: 10.1002/aenm.202101126

Y. Levartovsky, Prof. D. Aurbach
Department of Chemistry and BINA
BIU Institute of Nanotechnology and Advanced Materials
Bar-Ilan University
Ramat-Gan 5290002, Israel

N. R. Levy, Prof. Y. Ein-Eli
Department of Materials Science and Engineering
Technion – Israel Institute of Technology
Haifa 3200003, Israel
E-mail: eineli@technion.ac.il

Dr. T. Waldmann, Dr. M. Wohlfahrt-Mehrens
ZSW – Zentrum für Sonnenenergie- und Wasserstoff-Forschung
Baden-Württemberg
Helmholtzstrasse 8, 89081 Ulm, Germany

Prof. M. Winter
MEET Battery Research Center
Institute of Physical Chemistry
University of Münster
Corrensstraße 46, 48149 Münster, Germany

Prof. Y. Ein-Eli
Grand Technion Energy Program (GTEP)
Technion – Israel Institute of Technology
Haifa 3200003, Israel

1.2. An Overview

More energy in shorter time at lower cost and increased safety—battery research has always been striving for improvement. Significant progress has been made in the field of lithium-ion batteries (LIBs) since their commercialization in 1991.[1,2] LIBs store more energy, meaning their specific energy could be significantly increased by alternative cathode materials, reaching, for example, 421 W h kg^{-1} using $LiNi_xCo_yMn_{1-x-y}O_2$ (NCM) compared to 279 W h kg^{-1} of the original $LiCoO_2$ (LCO).[3] Additionally, the use of solid-state batteries (SSBs) exclusively consisting of solid components may enable the application of lithium metal anodes (LMAs), which can offer higher energy density compared to batteries with graphite anodes.[4] Furthermore, SSBs may also improve the mechanical stability of the cell,[5] making it safer—especially when using flexible polymer electrolytes (PEs). However, a major challenge for widespread adoption of electric vehicles is the charging speed of the batteries used, that is, LIBs take too long to refill compared to traditional combustion engine powered vehicles. Based on that experience of refueling (500–800) km of range at a gas station in just five minutes, customers expect similar practice from electric vehicles.[6] Therefore, charging to 80% state of charge (SOC) within 15 min is targeted by the US Advanced Battery Consortium (USABC).[7] In this review, we analyze how this target transforms into requirements for materials and components on the cell level.

To achieve fast-charging capabilities, the power density P_V of utilized battery cells has to be increased, which comes at the cost of reduced energy density W_V. Therefore, there are always trade-offs between wide range and fast charging. Kinetic models of battery cells show that overpotentials exist in every part of the battery cell. From transport of lithium ions and electrons in the electrodes, charge transfer across phase boundaries to transport through the electrolyte, polarization effects limiting the charging rate lead to Li metal plating, limited utilization of active material, and temperature increase.[8] Current-state high-voltage DC chargers can deliver peak powers of up to 350 kW.[9,10] The Porsche Taycan with 93.4 kW h battery allows a maximum charging power of 270 kW, while the average during charging is 187 kW.[9–11] Thus, recharging from 5% to 80% SOC takes 23 min. For comparison, the Tesla Model 3 with 75 kW h battery is recharged to 80% SOC in 27 min using Tesla's own Supercharger delivering a peak power of 250 kW in its third generation. Thus, the average charging power is about 130 kW, with the maximum value only reached for five minutes during the initial 20%.[12] Of course, bigger battery packs will charge longer at given charging power. Thus, the charger has to be improved as well for long-range vehicles with big battery packs.[13]

These state-of-the-art parameters are still significantly below what is required to reach the USABC goal for extreme fast charging (XFC): recharging within 15 min.[7] In the following, we take a closer look at the materials applied to reach these values in order to identify the rate-limiting steps. Considering the example of Tesla, $LiNi_xCo_yAl_{1-x-y}O_2$ (NCA) cathodes are used[14] in combination with graphite anodes. We assume a 100 kW h battery pack providing 500 km of driving range. With a volume of 400 L at system level and 200 L at cell level, this pack reaches an energy density W_V of 500 W h L^{-1} at cell level. Using the average voltage of 3.7 V, the charge density Q_V is thus 135 A h L^{-1}. If we assume an electrode thickness of 200 µm (neglecting current collectors and separator), the resulting Q_A arises as 2.7 mA h cm^{-2}, thus approximately 3 mA h cm^{-2}. The required current density for charging is therefore 3 mA cm^{-2} at 1C or 12 mA cm^{-2} (4C), which would be needed to reach the XFC goal of 15 min charging time.

In view of research on fast charging, a few key steps have been identified as rate-limiting: a) diffusion of lithium ions within the anode active material, b) diffusion of lithium ions in the cathode active material (CAM), c) lithium-ion transport in the electrolyte phase (liquid or solid), and d) charge-transfer kinetics at the phase boundaries. In this case, we define charge transfer as the whole process of transport between electrolyte and electrode, thus it includes desolvation in the case of liquid electrolytes, the actual charge transfer across the electrolyte–electrode interface, and—for the presence of an interphase—also the ion transport through this interphase, which goes along with two charge-transfer processes across the electrolyte–interphase and the interphase–electrode boundary, respectively. The influence of lithium-ion transport in the electrolyte is rather small within the separator, but inside the porous electrodes it plays a major role in the fast-charging ability of a given battery cell.

From the materials perspective, lithium plating at the graphite anode and lithium diffusion in the CAM are primarily rate-limiting. Essentially, slow diffusion of lithium in the liquid electrolyte and the active materials causes the true rate-limiting steps. Morphology, shape, and orientation of active material particles can improve the limiting influence of lithium diffusion in the solid-state, which explains, for example, the recent trend to single crystalline CAM.[15] On the electrode level, the active particle size distribution, tortuosity, and porosity are relevant, since diffusion-based lithium transport on the electrode scale is strongly influenced by those parameters in anodes and—to less extent—in cathodes.[16–22] For the latter, lithium-ion mobility greatly depends on the SOC,[22–26] since the crystal structure and the sequence of diffusion jumps typically change with the lithium content. Though, a high ionic conductivity on the material level does not necessarily translate to a fast-chargeable electrode if the tortuosity is high, for example. Going further on the size scale to the cell level, the relevance of engineering aspects—thermal management and the applied charging protocol, for example—takes precedence over physicochemical properties of the materials involved. Thus, this will only be discussed briefly in this review.

The physicochemical basics of LIBs with focus on kinetics will be summarized in Section 2. The origin of different overpotentials is discussed by means of electrochemical potential profiles. Thereby, the role of a small active particle size is noted, which allows for full utilization of the active material. Furthermore, differences between non-phase-transformation and phase-transformation electrodes (along with conversion-type ones as a special case thereof) will be highlighted, concluding that the evaluation of diffusion phenomena is challenging in the latter type and that conversion electrodes are much less suitable for fast-charging applications.[27–29]

In addition to these electrode-related overpotentials, charge transfer at interfaces and interface degradation leading to interphase formation also have to be considered at both anode and cathode.[30–34] For liquid electrolytes (LEs), concentration polarization is responsible as the decisive factor for electrolyte overpotentials, showing that the limiting current can be a major problem for thick electrodes in particular. Solid electrolytes (SEs) offer increased charge-carrier concentrations and a lithium-ion transference number near unity, thus concentration polarization does not occur.[35] Hence, the rate is not affected by current limitation due to depletion of lithium ions in the electrodes, but rather by the generally limited (effective) ionic conductivity of SEs. Furthermore, SEs are suggested to enable the use of a lithium metal anode. As a consequence, lithium plating would not be fatal anymore but rather desired, in the case that dendrite growth can effectively be suppressed.

Subsequently, these concepts will be translated to recent materials' applications in the following sections. For the anode (Section 3), studies showing the superior fast-charging performance of materials with low diffusion barriers are presented. The benefits of small particles are highlighted as well, but also the pitfalls of increased degradation because of higher surface area. We present an overview of different anode materials and discuss their advantages and disadvantages. Following with the cathode in Section 4, the SOC dependence of the cathode overpotential is established using experimental data of state-of-the-art NCM material. In addition, the dependence of rate performance on lithium diffusivity is highlighted, that is, faster charging is possible with increasing lithium diffusion coefficient, by comparing to other CAMs. Section 5 focuses on electrolytes, both on liquid and solid electrolytes. Experimental studies are presented, which show that ionic conductivity in the separator liquid electrolyte is not rate-determining. At the anode side, transport within the liquid electrolyte (in the porous electrode) becomes rate-limiting, however. At high current densities, reactions are confined at the anode parts close to the separator, leading to a severe local potential drop and lithium plating eventually. It will also be elaborated in Section 5 that charge transfer at the electrode interfaces may become critical. The mechanical properties of solid electrolytes are particularly critical, as contact loss and significant increase in charge-transfer resistance may result from missing plasticity. In any case, the electrode microstructure—together with the active particle morphology and microstructure—is crucial and needs to be tailored to allow for high current densities and fast charging. High temperatures can be applied to overcome this shortcoming, as shown using experimental studies. In fact, preheating the EV battery in cold climate either internally or by external means to allow for faster charging is common practice.[7] However, an increased temperature for better kinetics is always accompanied by accelerated degradation and thus shorter lifetime. Therefore, we briefly discuss thermal management systems along with optimized charging protocols and other measures utilized on the cell level to enable fast-charging applications in Section 6.

By highlighting the rate-limiting aspects of different battery components on the material level and suggesting optimal properties required for fast-charging applications, we hope to stimulate further research on this crucial topic, which thus might lead to better market adaptation of electric vehicles in the future. While certain aspects of anode and cathode materials are comparable, they are specific enough to justify the separation of their discussion.

2. Physicochemical Basics of Fast Charging

Fast charging of batteries requires high current densities that cause high overpotentials, which occur at the different components in the battery. If these overpotentials exceed certain limits, a physicochemical reaction takes place and the battery is likely to fail. The most prominent mechanism that leads to cell failure is lithium plating at the negative electrode,[36,37,38] typically graphite. Degradation processes can also occur at the cathode, namely oxygen evolution at oxide cathode active materials such as NCM and other layered oxides.[39]

The voltage of a battery cell V is given by the difference between the electrochemical potentials of electrons (Fermi levels) at the anode $\tilde{\mu}^{\mathrm{a}}_{\mathrm{e}^-}$ and cathode $\tilde{\mu}^{\mathrm{c}}_{\mathrm{e}^-}$, respectively, according to

$$V = -\frac{1}{F}\left(\tilde{\mu}^{\mathrm{c}}_{\mathrm{e}^-} - \tilde{\mu}^{\mathrm{a}}_{\mathrm{e}^-}\right) = V_{\mathrm{oc}} + \Delta\varphi^{\mathrm{c}} + \Delta\varphi^{\mathrm{a}} \tag{1}$$

Hereby, F is Faraday's constant, $\tilde{\mu}_i$ is the electrochemical potential of species i (in this case either electrons or Li^+ ions), which in turn is the sum of the chemical potential of this species μ_i and its electrical potential $z_iF\phi$ with the charge number z_i, given by

$$\tilde{\mu}_i = \mu_i + z_iF\varphi \tag{2}$$

During battery operation, lithium ions are transported within the cell and, therefore, $\tilde{\mu}_{\mathrm{Li}^+}$ is lifted from its equilibrium value as schematically shown in **Figure 1**.[40] Such transport needs to be driven by an overpotential, which is induced in the cell via a lifted $\tilde{\mu}^{\mathrm{c}}_{\mathrm{e}^-}$ or $\tilde{\mu}^{\mathrm{a}}_{\mathrm{e}^-}$ at the cathode or anode contacts, respectively. The total overpotential at each electrode in the battery $\Delta\varphi^{\mathrm{c}}$ or $\Delta\varphi^{\mathrm{a}}$ can be considered as the sum of the overpotentials needed to drive the solid-state diffusion inside the respective active cathode or anode material ($\Delta\varphi^{\mathrm{c}}_{\mathrm{AM}}$ or $\Delta\varphi^{\mathrm{a}}_{\mathrm{AM}}$), the overpotential to drive the charge transfer between electrode and electrolyte ($\Delta\varphi^{\mathrm{c}}_{\mathrm{CT}}$ or $\Delta\varphi^{\mathrm{a}}_{\mathrm{CT}}$), and the overpotential to drive ionic transport in the electrolyte phase ($\Delta\varphi^{\mathrm{c}}_{\mathrm{EL}}$ or $\Delta\varphi^{\mathrm{a}}_{\mathrm{EL}}$) within a porous electrode:

$$\Delta\varphi^{\mathrm{c}} = \Delta\varphi^{\mathrm{c}}_{\mathrm{AM}} + \Delta\varphi^{\mathrm{c}}_{\mathrm{CT}} + \Delta\varphi^{\mathrm{c}}_{\mathrm{EL}} \tag{3}$$

$$\Delta\varphi^{\mathrm{a}} = \Delta\varphi^{\mathrm{a}}_{\mathrm{AM}} + \Delta\varphi^{\mathrm{a}}_{\mathrm{CT}} + \Delta\varphi^{\mathrm{a}}_{\mathrm{EL}} \tag{4}$$

In the active materials, the electronic conductivities are mostly significantly higher than the ionic conductivities.[41] Therefore, any overpotentials $\Delta\varphi^{\mathrm{c}}_{\mathrm{AM}}$ or $\Delta\varphi^{\mathrm{a}}_{\mathrm{AM}}$ are caused primarily by ionic transport. This leads to a gradient of μ_{Li^+} inside the active material because of the solid-state diffusion that is driven by an applied voltage during charging or by the cell voltage during discharging. Solid-state diffusion is further elaborated in Section 2.1.1.

At the interfaces between the electrodes and the electrolyte, charge transfer takes place, which also requires some driving

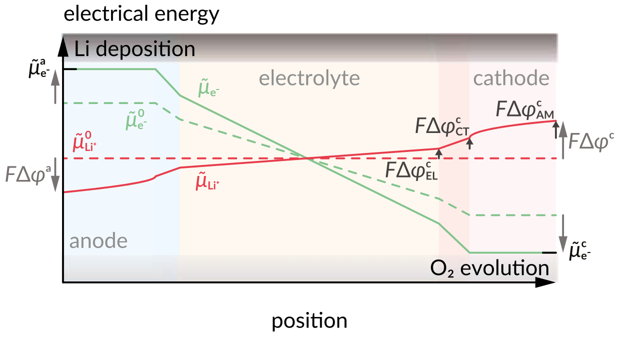

Figure 1. Schematic representation of the electrochemical potential profiles of electrons $\tilde{\mu}_{e^-}$ and lithium ions $\tilde{\mu}_{Li^+}$ in a battery cell during charging (solid lines) and in equilibrium (dashed lines). A higher electrochemical potential of electrons at the anode $\tilde{\mu}^a_{e^-}$ or lower at the cathode $\tilde{\mu}^c_{e^-}$ (relative to the OCV case) needs to be applied to drive the transport of lithium ions through the cell with the corresponding overpotentials $\Delta\phi^a$ and $\Delta\phi^c$, respectively. The overpotentials themselves drop at the different components in the battery, namely the electrolyte ($\Delta\varphi^c_{EL}$ and $\Delta\varphi^a_{EL}$), the interface between electrolyte and electrode ($\Delta\varphi^c_{CT}$ and $\Delta\varphi^a_{CT}$), and inside the electrode active material ($\Delta\varphi^c_{AM}$ and $\Delta\varphi^a_{AM}$).

force $\Delta\varphi_{CT}$ that further alleviates $\tilde{\mu}_{e^-}$.[40] As most CAMs in LIBs are high-voltage materials that exceed the stability window of typical electrolytes, side-reactions at the interface will occur that lead to the formation of a solid electrolyte interphase (SEI, or CEI for "cathode–electrolyte interphase").[30–33] Therefore, the charge transfer between active materials and electrolyte can involve several intermediate steps and may lead to significant overpotentials.[30–33,40] The charge transfer is discussed in Section 2.1.2.

Also the transport of ions in the electrolyte needs to be driven by an overpotential $\Delta\varphi_{EL}$ and adds up to the total overvoltage.[40] Here, we have to distinguish typical liquid electrolytes with comparably low ion concentrations and transference number ($t_{Li^+} < 1$) and solid electrolytes with high ion concentrations and $t_{Li^+} \cong 1$.[40] Transport in the electrolyte occurs via both diffusion (driven by $\nabla\mu_{Li^+}$) and migration (driven by $\nabla\varphi$). Thereby, migration in liquid electrolytes is typically neglected whereas transport in the solid electrolyte is exclusively caused by migration.[40,42] These mechanisms are further discussed in Sections 2.2.1 and 2.2.2, respectively.

2.1. Electrode Overpotentials

2.1.1. Solid-State Diffusion

Single-Phase Intercalation Electrodes: The overpotential that is required to drive the solid-state diffusion in an intercalation-type electrode is determined by the gradient of the chemical potential of the ions ($z_{Li^+} = 1$)

$$\Delta\varphi^c_{AM} = -\frac{1}{F}\left[\mu_{Li^+}(x = L) - \mu_{Li^+}(x = 0)\right] \tag{5}$$

under the assumption that electronic conductivity is significantly higher than ionic conductivity inside the electrode. Under this condition, the chemical diffusion coefficient $\tilde{D}_{Li}$ of the neutral component lithium (Li^0) is only controlled by the mobility of the lithium ions, and we use the symbol $\tilde{D}_{Li^+}$ to denote this. Formally, however, in every electrochemical experiment $\tilde{D}_{Li}$ is evaluated. The effect of mixed electronic and ionic conduction on the electrode polarization is discussed in detail by Usiskin and Meier.[43] For simplicity, we consider here the overpotential at the cathode, and the analogue anode case is added below. In Equation (5), $\Delta\varphi_{AM}$ is described by the difference between μ_{Li^+} at the surface of the active material ($x = L$) and at the center of the active material particle ($x = 0$) in the case of spherical particle type (radius L) electrode materials.

Nernst's equation connects the chemical potentials with the respective activities of Li^+ ions (a_{Li^+}) according to

$$\Delta\varphi^c_{AM} = -\frac{RT}{F}\left[\ln\left(a_{Li^+}(L)\right) - \ln\left(a_{Li^+}(0)\right)\right] = -\frac{RT}{F}\Delta\ln\left(a_{Li^+}\right) \tag{6}$$

Hereby, R is the gas constant, T the temperature, and F Faraday's constant. If now only a small concentration gradient Δc_{Li^+} as compared to the total concentration of Li^+ ions in the electrode c_{Li^+} is established, Equation (6) can be written as[44]

$$\Delta\varphi^c_{AM} = -\frac{RT}{F}\left(\frac{\partial\ln\left(a_{Li^+}\right)}{\partial\ln\left(c_{Li^+}\right)}\right)\Delta\ln\left(c_{Li^+}\right) = -\frac{RT}{F}W\frac{\Delta c_{Li^+}}{c_{Li^+}} \tag{7}$$

Equation (7) links the overpotential with the gradient of Li^+ ions inside the electrode via the thermodynamic enhancement factor $W = \frac{\partial\ln(a_{Li^+})}{\partial\ln(c_{Li^+})}$.[44] W can be determined from coulometric titration of an electrode under the assumption that the electrode is not undergoing any phase transformation during lithium intercalation.[44] The anode overpotential results similarly as

$$\Delta\varphi^a_{AM} = \frac{RT}{F}\left(\frac{\partial\ln\left(a_{Li^+}\right)}{\partial\ln\left(c_{Li^+}\right)}\right)\Delta\ln\left(c_{Li^+}\right) = \frac{RT}{F}W\frac{\Delta c_{Li^+}}{c_{Li^+}} \tag{8}$$

The concentration profile of Li^+ can be calculated via Fick's second law

$$\frac{\partial c_{Li^+}}{\partial t} = \tilde{D}_{Li^+}\frac{\partial^2 c_{Li^+}}{\partial x^2} \tag{9}$$

with the solid-state chemical diffusion coefficient of Li^+ ions in the intercalation electrode $\tilde{D}_{Li^+}$. We note that Equation (9) can only be applied for small concentration gradients, that is, under the assumption of constant $\tilde{D}_{Li^+}$ inside the active material. To solve the differential Equation (9), the following boundary conditions (Equations (10)–(12)) can be assumed, which represent the galvanostatic charging with current I from $t = 0$ onward.[45] The current induces a higher concentration of Li^+ ions at the electrode's surface (initial concentration $c^0_{Li^+}$), which then leads to an expansion of the Nernstian diffusion layer over time throughout the volume of the electrode.

$$c_{Li^+} = c^0_{Li^+} \quad 0 \le x \le L; \quad t = 0 \tag{10}$$

$$-\tilde{D}_{Li^+}\frac{\partial c_{Li^+}}{\partial x} = \frac{I}{AF} \quad x = L; \quad t > 0 \tag{11}$$

$$\frac{\partial c_{\mathrm{Li}^+}}{\partial x} = 0 \quad x = 0; \quad t \geq 0 \tag{12}$$

With A being the surface area of the electrode, this leads to the solution[45]

$$c_{\mathrm{Li}^+} = c^0_{\mathrm{Li}^+} + \frac{It}{FAL} + \frac{IL}{FA\tilde{D}_{\mathrm{Li}^+}} \left[\frac{3x^2 - L^2}{6L^2} - \frac{2}{\pi^2}\sum_{n=1}^{\infty}\frac{(-1)^2}{n^2}\exp\left(-\frac{n^2\pi^2\tilde{D}_{\mathrm{Li}^+}}{L^2}t\right)\cos\left(\frac{n\pi x}{L}\right)\right] \tag{13}$$

We note that Equation (12) generally only applies for a flat plate; for other geometries, such as cylinders or spheres, geometry-related constants have to be included,[43] but the differences in the equations are only minor, which implies that the flat plate geometry describes the system sufficiently well. The concentration polarization can now be calculated as the difference in concentrations between the surface ($x = L$) and the center of the spherical particle ($x = 0$) as

$$\Delta c_{\mathrm{Li}^+} = c_{\mathrm{Li}^+}(x = L) - c_{\mathrm{Li}^+}(x = 0) = \frac{IL}{FA\tilde{D}_{\mathrm{Li}^+}}\left[\frac{1}{2} - \frac{4}{\pi^2}\sum_{n=1}^{\infty}\frac{1}{(2n-1)^2}\exp\left(-\frac{(2n-1)^2\pi^2\tilde{D}_{\mathrm{Li}^+}}{L^2}t\right)\right] \tag{14}$$

We note that although the concentration polarization would describe the solid-state diffusion overpotential as defined in Equation (13), the practical overpotential can be considered as the difference of electrode potential from the equilibrium open-circuit potential. Therefore, from an application point-of-view, the overpotential is given by the difference in concentration at the surface of the electrode and the equilibrated concentration

$$\Delta c^{\mathrm{eq}}_{\mathrm{Li}^+} = c_{\mathrm{Li}^+}(x = L) - \frac{It}{FAL} = \frac{IL}{FA\tilde{D}_{\mathrm{Li}^+}}\left[\frac{1}{3} - \frac{2}{\pi^2}\sum_{n=1}^{\infty}\frac{1}{n^2}\exp\left(-\frac{n^2\pi^2\tilde{D}_{\mathrm{Li}^+}}{L^2}t\right)\right] \tag{15}$$

Equation (15) can now be inserted into Equation (7) to obtain the overpotential. Under the assumption of either short $\left(t_{\mathrm{charge}} \ll \frac{L^2}{\tilde{D}_{\mathrm{Li}^+}}\right)$ or long $\left(t_{\mathrm{charge}} \gg \frac{L^2}{\tilde{D}_{\mathrm{Li}^+}}\right)$ charging times t_{charge}, Equations (16) and (17) are obtained.[46]

$$\Delta\varphi_{\mathrm{AM}} = \frac{2}{\sqrt{\pi}}\frac{IWRT}{F^2Ac_{\mathrm{Li}^+}\sqrt{\tilde{D}_{\mathrm{Li}^+}}}\sqrt{t} \tag{16}$$

$$\Delta\varphi_{\mathrm{AM}} = \frac{1}{3}\frac{IWRTL}{F^2Ac_{\mathrm{Li}^+}\tilde{D}_{\mathrm{Li}^+}} \tag{17}$$

In **Figure 2**a,b it is schematically shown how the concentration profiles in the material develop during delithiation. We use a nickel-rich NCM as example since it is a typical single-phase material at high concentration of intercalated Li$^+$ ions (steps I–III). In step I, the concentration gradient did not yet fully progress throughout the material (semi-infinite diffusion) and the overpotential follows Equation (16). After charging for longer time, the concentration gradient will eventually reach the center of the active material particles (step II) and diffusion will be finite from this point on (step III). The overpotential is given by Equation (17) in this case. Upon relaxation, the concentration and the chemical potential equilibrate again (Figure 2c,d). The practical overpotential can then be visualized as in Figure 2d.

We emphasize that, even if fast charging of electrodes is desired, the electrodes should be designed to fully utilize the volume of active materials. Namely, the particle size should fulfil the relation[47]

$$L < \sqrt{t_{\mathrm{charge}}\tilde{D}_{\mathrm{Li}^+}} \tag{18}$$

Therefore, Equation (17) would give a good measure of the overpotential from solid-state diffusion for realistic electrodes. To achieve this condition (Equation (18)), sufficiently small active materials should be employed whereas the maximum reasonable size should be correlated with $\tilde{D}_{\mathrm{Li}^+}$. We note that it needs to be considered that $\tilde{D}_{\mathrm{Li}^+}$ is not a constant value for every material but is a function of temperature, lithium concentration, and lithium vacancy concentration.[41,48,49]

To understand these dependencies, we have to take a look at the mechanism of ion transport in solids. The crystal structure creates a periodic potential profile with its minima being crystallographic sites for the transported species.[50] Ion transport occurs when an ion moves from an occupied lattice site to a neighboring empty lattice site. The free energy barrier of migration ΔG_{m} that has to be overcome depends on the difference between initial state and the transition state of the jump. Thereby, the probability of a forward, that is, successful, jump is increased in the case of crystallographically equivalent initial and final states, which result in a symmetrical activation profile.[51]

Here, the number of vacant sites n_{V} and that of normal sites N per unit volume gives the defect concentration per unit volume $[d]$ as[52]

$$[d] = \frac{n_{\mathrm{V}}}{N} \tag{19}$$

The self-diffusion coefficient of lithium ions D_{Li^+} can then be obtained from the jump frequency ν, the reciprocal number of jump directions α, and the jump distance a_0 by[52,53]

$$D_{\mathrm{Li}^+} = \alpha[d]a_0{}^2\nu \tag{20}$$

If each jump were successful, ν would simply be equal to the vibrational frequency of the atoms ν_0. Since this is not the case, ν is given as the product of ν_0 and the probability of a successful jump as

$$\nu = \nu_0 \exp\left(-\frac{\Delta G_{\mathrm{m}}}{k_{\mathrm{B}}T}\right) \tag{21}$$

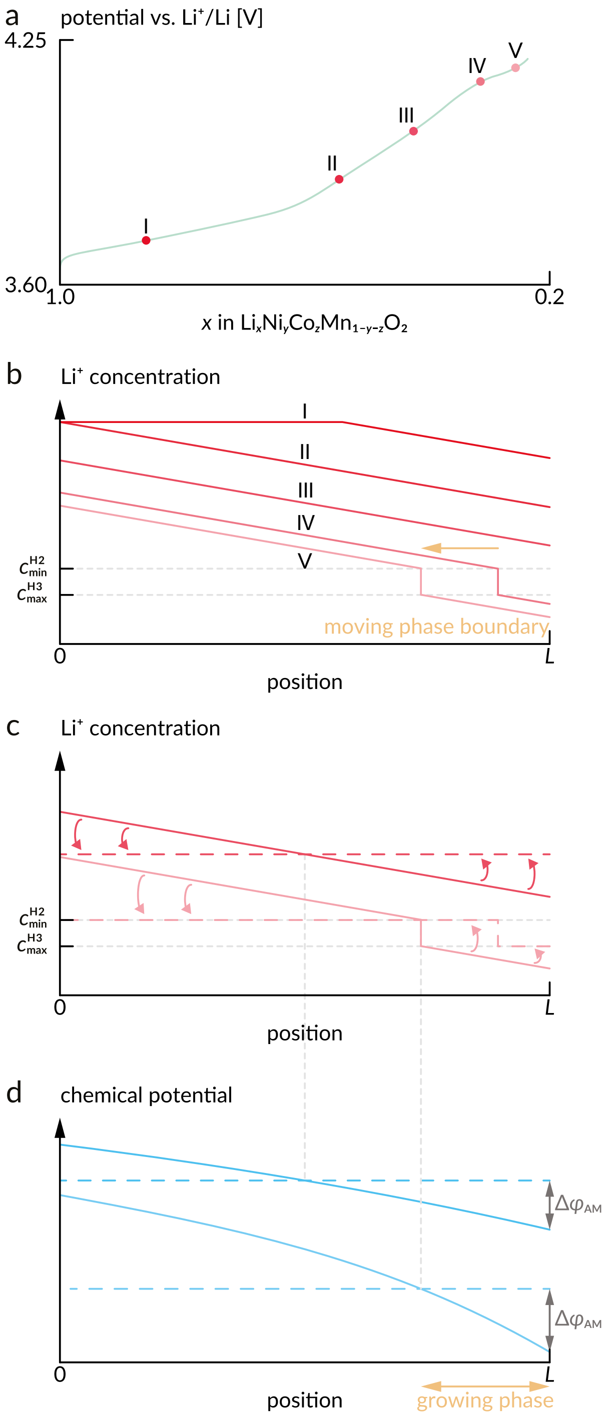

Figure 2. a) Exemplary charging profile of a nickel-rich NCM cathode. b) Simplified representation of the concentration gradients at the points I–V during charging of the NCM cathode in (a). For steps I–III, nickel-rich NCM behaves like a single-phase material, while for steps IV–V the H2 and H3 phases coexist with limited solubility of lithium ions $c_{\mathrm{min}}^{\mathrm{H2}}$ and $c_{\mathrm{max}}^{\mathrm{H3}}$, respectively. c) Concentration profiles for steps III and V during charging (solid lines) and if the cell was in equilibrium (dashed line). A phase boundary in step V still exists in equilibrium. d) Chemical potential profiles for the cases shown in (c). The practical overpotential $\Delta\varphi_{\mathrm{AM}}$ is given by the difference of the chemical potential during charging and the chemical potential in equilibrium. In the case of a two-phase coexistence, the overpotential is only determined by the phase, which is growing during charging.

using Boltzmann's constant k_{B}.[52] Now, α can be replaced by a geometrical factor γ, which also accounts for different diffusion anisotropies.[51,52] This leads to

$$D_{\mathrm{Li^+}} = \gamma [d] a_0^2 \nu_0 \exp\left(-\frac{\Delta G_{\mathrm{m}}}{k_{\mathrm{B}} T}\right) \tag{22}$$

as general expression for $D_{\mathrm{Li^+}}$.[52] The free energy can be separated into the enthalpy of migration ΔH_{m} and the entropy of migration ΔS_{m}, which gives

$$D_{\mathrm{Li^+}} = \gamma [d] a_0^2 \nu_0 \exp\left(\frac{\Delta S_{\mathrm{m}}}{k_{\mathrm{B}}}\right) \exp\left(-\frac{\Delta H_{\mathrm{m}}}{k_{\mathrm{B}} T}\right) \tag{23}$$

Now, the constants can be combined into a pre-exponential factor D_0, which also contains the migration entropy, resulting in an Arrhenius-type form

$$D_{\mathrm{Li^+}} = [d]\, D_0 \exp\left(-\frac{\Delta H_{\mathrm{m}}}{k_{\mathrm{B}} T}\right) \tag{24}$$

for the self-diffusion coefficient, where ΔH_{m} is the activation energy of the transport process.[51] We note that $D_{\mathrm{Li^+}}$ is linked to $\tilde{D}_{\mathrm{Li^+}}$ via the Li$^+$ concentration dependent enhancement factor W (as defined above) by[44]

$$\tilde{D}_{\mathrm{Li^+}} = W D_{\mathrm{Li^+}} \tag{25}$$

However, for an assessment of the fast-charging capability of electrodes, the concentration dependence only plays a minor role. Therefore, the overpotential needed to drive the solid-state diffusion in the active materials (Equation (17)) and its dependence on key parameters (active electrode area A and particle radius L) can be simplified as

$$\Delta\varphi_{\mathrm{AM}} \sim I \cdot \frac{L}{A \cdot \tilde{D}_{\mathrm{Li^+}}} \tag{26}$$

We find that the overpotential is proportional to the particle size, the reciprocal surface area, and the reciprocal (chemical) lithium-ion diffusion coefficient of the electrode material at a given temperature of cell operation.

Phase-Transformation and Conversion-Type Electrodes: Other than in the previous section, phase-transformation electrodes do not necessarily exhibit a uniform concentration gradient throughout the full active material volume, but rather show distinctly separated phase boundaries within the material (moving boundary model). Upon lithiation or delithiation, the phase boundaries are considered to move.[54,55] Therefore, as the activities of Li$^+$ ions $a_{\mathrm{Li^+}}$ within each phase stay constant during the phase-transformation reaction, the equilibrium potentials also remain constant and a plateau in the charge/discharge curves is observed for phase-transformation electrodes. As a result, a unique relation between $c_{\mathrm{Li^+}}$ and $\Delta\varphi_{\mathrm{AM}}$ does not exist in this case. However, within each phase a concentration gradient of lithium may be present that obeys the same equations as for non-phase-transformation materials (Equations (16) and (17)).[54–56]

The concentration and potential in phase-transformation materials can again be visualized in the example in Figure 2, because nickel-rich NCM also has two coexisting phases at low concentrations of intercalated Li^+ ions (steps IV and V). As depicted in Figure 2a, the electrode potential reaches a plateau at these steps, where the H2 and H3 phases coexist in parallel.[57] The concentration of intercalated Li^+ ions is different in both phases and further delithiation leads to a progression of the phase boundary. If the potential is relaxed, the concentration and chemical potential will equilibrate according to Figure 2c,d. As can be seen, only the phase that grows upon delithiation determines the overpotential. Therefore, it is hardly quantitatively accessible as the position of the phase boundary needs to be known.[56] However, Equation (17) can still be used for estimation as it represents an upper limit for the overpotential also in the case of phase-transformation electrodes.

It is important to note that the overpotential as defined in Equation (1) requires knowledge of the open-circuit potential, which is well defined by the lithium concentration in the material for non-phase-transformation electrodes. For phase-transformation electrodes, however, there is a well-known hysteresis between the open-circuit potentials at charge and discharge.[28,58] As a result, determination of W from coulometric titration can be intricate for phase-transformation electrodes. Therefore, the assessment and quantification of diffusion-related processes in such materials is challenging. The hysteresis is discussed to originate from residual strain from the phase transformation within the material that needs to be accommodated, leading to an offset of the open-circuit potential by the strain-accommodation energy.[59] Another explanation is given by the coexistence of different phase fractions in individual particles in the electrode and, thus, the coexistence of various equilibria in the electrode.[58]

Conversion-type electrodes can be considered as a special case of phase-transformation electrodes. However, the structural difference between lithiated and delithiated phases is much more substantial. Thus, besides a mostly very sluggish lithium transport within the material, the strain that has to be accommodated and the resulting hysteresis in open-circuit potential is huge.[27–29] Both of these effects make this kind of electrodes still quite unattractive for fast-charging batteries, however, interesting approaches employing nanomaterials have early been reported, including impressively fast cycling kinetics.[60]

2.1.2. Charge Transfer at Interfaces

The overpotential $\Delta\varphi_{\mathrm{CT}}$ to drive the charge transfer of lithium at the interface between electrode and electrolyte is governed by many factors. Again, we use $\Delta\varphi_{\mathrm{CT}}$ as a simplified expression for the overpotential at an electrode and it has to be noted that both the anode and cathode contribute individual overpotentials $\Delta\varphi_{\mathrm{CT}}^{\mathrm{a}}$ and $\Delta\varphi_{\mathrm{CT}}^{\mathrm{c}}$, respectively. In the simplest case, the electrode material is in direct contact with the electrolyte and no additional interfacial layers impede the charge transfer. Further, it is assumed that the lithium-ion transfer determines the overpotential and that electrons are readily available. In this case, the overpotential is related to the interfacial current I via the Butler–Volmer equation[61,62]

$$I = j_0\, A\left[\exp\left(\frac{\alpha F}{RT}\Delta\varphi_{\mathrm{CT}}\right) - \exp\left(-\frac{(1-\alpha)F}{RT}\Delta\varphi_{\mathrm{CT}}\right)\right] \tag{27}$$

Hereby, j_0 is the exchange current density and α is the charge-transfer coefficient that describes the potential landscape at the interface. j_0 is a function of the lithium-ion concentration in the electrolyte $c_{\mathrm{Li^+}}^{\mathrm{EL}}$ and the concentrations of lithium ions, lithium vacancies, and electrons in the electrode $c_{\mathrm{Li^+}}$, $c_{\mathrm{V'_{Li}}}$, $c_{\mathrm{e^-}}$, as well as the rate constants and activation energies for lithium insertion and extraction k_{in}, k_{ex}, E_{in}, E_{ex}, respectively, and can be expressed as[61]

$$j_0 = F\exp\left(-\frac{\alpha E_{\mathrm{ex}}}{RT}\right)\exp\left(-\frac{(1-\alpha)E_{\mathrm{in}}}{RT}\right)\left[k_{\mathrm{ex}}c_{\mathrm{Li^+}}\right]^{\alpha}\left[k_{\mathrm{in}}c_{\mathrm{Li^+}}^{\mathrm{EL}}c_{\mathrm{V'_{Li}}}c_{\mathrm{e^-}}\right]^{1-\alpha} \tag{28}$$

Under the assumption that the energy barrier for lithium insertion and extraction is equivalent ($E_{\mathrm{in}} = E_{\mathrm{ex}} = E_{\mathrm{A}}$),

$$j_0 = j_0'\exp\left(-\frac{E_{\mathrm{A}}}{RT}\right) \tag{29}$$

can be obtained as simplified expression for the exchange current density. Here, j_0' is a prefactor that contains the rate constants and is dependent on the concentrations of lithium ions, vacancies, and electrons in the active material and the electrolyte. The charge-transfer resistance R_{CT} is given by[63]

$$R_{\mathrm{CT}} = \frac{RT}{zFAj_0} \tag{30}$$

and can thus be rewritten using Equation (29) as

$$\frac{1}{R_{\mathrm{CT}}} = \frac{zFAj_0'}{RT}\exp\left(-\frac{E_{\mathrm{A}}}{RT}\right) \tag{31}$$

revealing its temperature dependence. Linearization of Equation (27) under the assumption of small $\Delta\varphi_{\mathrm{CT}}$ yields

$$\Delta\varphi_{\mathrm{CT}} \sim I\cdot\frac{1}{Aj_0} \tag{32}$$

which presents the overpotential as a function of the electrode surface area and the exchange current density of the interface between electrode and electrolyte at a given temperature. However, as most electrode materials operate at potentials, where the electrolyte components are unstable, often an SEI layer forms at the interface between electrode and electrolyte that impedes the charge transfer between them. Additionally, artificial interfacial layers, that is, coatings, are commonly used on certain electrode materials to gain better control of such interfacial processes.[64] These interfacial layers can manipulate the charge-transfer kinetics drastically and determine the energy landscape as well as the charge-transfer coefficients,[65] as will be shown in Section SEI and Artificial SEI.

In the case of phase-transformation or conversion-type electrodes, charge transfer followed by insertion or removal of Li^+ ions from the electrode host structure initiates a phase transformation of the material. To initiate this phase transformation, a certain driving force is required, which can take very substantial values.[28] The required overpotential to drive the phase-transformation or conversion reaction depends on the individual reaction pathway of the electrode material.[28] It is possible to catalyze the phase transformation, for example, by using certain electrolyte additives that take part in the reaction.[66]

2.2. Electrolyte Overpotentials

2.2.1. Concentration Polarization in Liquid Electrolytes

Application of a potential difference between the electrodes initiates an ionic current in the electrolyte. Despite ionic currents in electrolytes are caused by migration (field-driven) and diffusion (concentration gradient driven), diffusion is considered as eventually limiting cell performance at high rates.[42] Therefore, we will focus on diffusion in the liquid electrolyte in the following.

Inside a porous electrode, the ionic flux is progressively consumed by the active materials, which can even lead to the depletion of ions deeper inside the electrode (close to the current collector). When using a 1D-description of Fick's law, the differential equation needs to be modified by a term that accounts for the consumption of ionic flux[47]

$$\frac{\partial c_{\mathrm{Li}^+}^{\mathrm{EL}}}{\partial t} = \widetilde{D}_{\mathrm{Li}^+}^{\mathrm{EL}} \frac{\partial^2 c_{\mathrm{Li}^+}^{\mathrm{EL}}}{\partial x^2} + \frac{I}{FAd}\left(1 - t_{\mathrm{Li}^+}\right) \tag{33}$$

with $c_{\mathrm{Li}^+}^{\mathrm{EL}}$ being the concentration of Li^+ ions in the electrolyte phase, d the thickness of the electrode, and $\widetilde{D}_{\mathrm{Li}^+}^{\mathrm{EL}}$ the chemical diffusion coefficient of Li^+ ions in the electrolyte. x is the spatial coordinate in the electrolyte with $x = 0$ being the tip of the electrode (at the separator) and $x = d$ being the bottom of the electrode (at the current collecting foil). Equation (33) can be solved using the boundary conditions in Equations (34)–(36) with $c_{\mathrm{Li}^+,0}^{\mathrm{EL}}$ being the concentration of lithium ions in equilibrium.

$$\frac{\partial c_{\mathrm{Li}^+}^{\mathrm{EL}}}{\partial x} = -\frac{I}{FA}\left(1 - t_{\mathrm{Li}^+}\right) \quad x = 0; \quad t \geq 0 \tag{34}$$

$$\frac{\partial c_{\mathrm{Li}^+}^{\mathrm{EL}}}{\partial x} = 0 \quad x = d; \quad t \geq 0 \tag{35}$$

$$c_{\mathrm{Li}^+}^{\mathrm{EL}} = c_{\mathrm{Li}^+,0}^{\mathrm{EL}} \quad t = 0 \tag{36}$$

Solution of Equation (33) under the given boundary conditions yields the concentration profile of lithium ions in the electrolyte phase inside the composite electrode as[47]

$$c_{\mathrm{Li}^+}^{\mathrm{EL}} = c_{\mathrm{Li}^+,0}^{\mathrm{EL}}\left(1 - \alpha \frac{I}{FA}\right) - \frac{I}{FAd}\frac{1 - t_{\mathrm{Li}^+}}{2\widetilde{D}_{\mathrm{Li}^+}^{\mathrm{EL}}}\left(x^2 - 2L_{\mathrm{EL}}x - 2dx\right) \tag{37}$$

Hereby, α is a parameter (unit m^{-1}) that depends on the electrode geometry as detailed by Newman et al.[47] When the concentration is fully depleted at one of the battery electrodes, the limiting current density is reached, which is derived based on Equation (37) as follows.[47] The limiting current is likely to differ between anode and cathode, $j_{\mathrm{lim}}^{\mathrm{a}}$ and $j_{\mathrm{lim}}^{\mathrm{c}}$ respectively, but for simplicity the limiting current density is only expressed as

$$j_{\mathrm{lim}} = \frac{F\widetilde{D}_{\mathrm{Li}^+}^{\mathrm{EL}} c_{\mathrm{Li}^+,0}^{\mathrm{EL}}}{\left(1 - t_{\mathrm{Li}^+}\right)L_{\mathrm{EL}}\beta} \tag{38}$$

in the following. Thereby, L_{EL} is the thickness of the separator and β is a parameter that describes the electrode geometry.[47] β accounts for the porosity and thickness of the electrode and will effectively lead to a reduced j_{lim} in the case that lithium transport pathways are tortuous. The most ideal electrode is a flat plate, for which β equals 0.5.[47] Far higher values of β are reached in practical battery electrodes. For the assessment of the overpotential needed to drive the diffusion of lithium in the electrolyte phase, an alternate form of Nernst's equation can be used[63]

$$\mu_{\mathrm{Li}^+} = \mu_{\mathrm{Li}^+}^{0} + \frac{RT}{F}\ln\left(1 - \frac{j}{j_{\mathrm{lim}}}\right) \tag{39}$$

The total overpotential to drive the diffusion of Li^+ ions in the electrolyte would be the difference in the chemical potentials in the electrolyte between the anode and cathode surfaces. The individual overpotential at each electrode takes the following form. Again, for simplicity we avoid using anode- and cathode-specific indices ($\Delta\varphi_{\mathrm{EL}}^{\mathrm{a}}$ and $\Delta\varphi_{\mathrm{EL}}^{\mathrm{c}}$) and use

$$\Delta\varphi_{\mathrm{EL}} = \mu_{\mathrm{Li}^+} - \mu_{\mathrm{Li}^+}^{0} = \frac{RT}{F}\ln\left(1 - \frac{I}{j_{\mathrm{lim}}A_{\varnothing}}\right) \tag{40}$$

as generalized expression instead. Hereby, $A_{\varnothing}$ describes the cross-sectional cell area. Different limiting currents j_{lim} at each electrode can be expected because the transport in the electrolyte phase of porous electrodes strongly depends on the microstructure resulting in different ionic tortuosities.[19] As can be seen in Equation (40), the overpotential increases drastically once the current approaches the limiting current. In the case $\frac{I}{A_{\varnothing}} \ll j_{\mathrm{lim}}$, Equation (40) can be linearized resulting in

$$\Delta\varphi_{\mathrm{EL}} \sim I\frac{T}{A_{\varnothing} \cdot j_{\mathrm{lim}}} \tag{41}$$

thus showing an ohmic relation between current and overpotential for comparably small currents. We note that according to Equation (39), j_{lim} determines the temperature dependence of $\Delta\varphi_{\mathrm{EL}}$ as $\widetilde{D}_{\mathrm{Li}^+}^{\mathrm{EL}}$ typically shows an Arrhenius-type behavior.[67] The limiting current caused by concentration polarization can become an issue especially in thick electrodes with high mass loading.[19,42,68] Although the overpotentials to drive charge transfer and solid-state diffusion may be sufficiently low in such a case due to high interfacial areas A between electrode and electrolyte, the overpotential to drive diffusion in the electrolyte does depend on the cross-sectional area $A_{\varnothing}$ of the cell and may actually limit the cell performance in some cases.[19,42] The limiting current densities can be lifted by optimizing ionic diffusion pathways in the porous electrodes, by increasing temperature, or using solvents with low viscosity and high Li$^+$ ion diffusion coefficients.[19,69]

2.2.2. Migration in Solid Electrolytes

Other than in liquid electrolytes, in (inorganic) solid electrolytes the transference number of Li$^+$ ions can be considered as 1 and the concentration of Li$^+$ is substantially higher, thus, the electric field between the electrodes alone drives the ionic current.[35] Therefore, the relation between ionic current and overpotential is simply ohmic according to

$$\Delta\varphi_{\mathrm{EL}} = I\frac{L_{\mathrm{EL}}}{A_{\varnothing}}\frac{1}{\sigma_{\mathrm{SE}}} \tag{42}$$

with the ionic conductivity σ_{SE}, and there is no concentration polarization that will eventually lead to current limitations.[35] However, the (effective) conductivities of typical solid electrolytes are comparably low[70] and the associated overpotentials to the ionic transport can still be substantial, especially because of the tortuous conduction pathways inside composite electrodes.[71] If the overpotential to drive ionic conduction through a composite electrode is higher than the overpotential to drive the charge transfer and solid-state diffusion, the lithiation or delithiation of the electrode will occur inhomogeneously.[47] The ionically easily accessible parts of the electrode, that is, close to the solid electrolyte separator, are lithiated or delithiated first and the parts that are more distant from the separator, that is, close to the current collector, remain inactive until the reaction in the easily accessed parts is completed.[47] Thus, a reaction zone progresses through the composite electrode during lithiation or delithiation.[47,72] In the case of low conductivities, Equation (42) would be replaced by

$$\Delta\varphi_{\mathrm{EL}} = I\frac{L_{\mathrm{sep}}}{A_{\varnothing}}\frac{1}{\sigma_{\mathrm{SE}}} + I^2 t_{\mathrm{charge}}\frac{1}{q\sigma_{\mathrm{SE}}} \tag{43}$$

where the pathway length for ionic transport L_{EL} is split up into one part covering the transport in the separator L_{sep} and another part describing the transport in the composite electrode and the expansion of the reaction zone.[47,72] Hereby, t_{charge} is the charging time of the cell and q is the capacity density of the respective composite electrode. This would mean that when the cutoff potential for charging is reached some parts of the electrode have not been accessed by the reaction zone and remain inactive. This is especially important in thick electrodes.[72] Therefore, high ionic conductivity is an important factor to achieve full active material utilization at high charging rates.[71,73] High temperatures can significantly accelerate the ionic transport and improve the conductivity, which is a benefit of solid electrolytes compared to liquid electrolytes, as they can be operated at comparably high temperatures.[68]

3. Anode

3.1. Limiting Processes/Parameters on the Anode Side

Regarding anodes, fast charging is limited by processes on the material, electrode, and cell level (see **Figure 3**). The limitations on these three levels are discussed in the following sections. We focus mainly on graphite and carbon materials, $Li_4Ti_5O_{12}$ (LTO), and silicon as most important anode materials yet and briefly consider the lithium metal anode.

3.1.1. Limitation of Fast Charging on the Material Level

An important limiting factor for fast charging is the transfer of Li$^+$ ions into the anode active material in the form of intercalation, insertion, alloying, or deposition as metal. The most relevant processes in the case of intercalation, insertion, and alloying include the transfer of Li$^+$ ions into the active material and their solid-state diffusion inside the active material, driven by the local electric field and by concentration gradients, respectively. These processes are hindered by energetic barriers as discussed in the following sections, whereas lower barriers and higher probabilities of overcoming them increase the fast-charging capability. The formed SEI also plays an important role as it modifies the charge-transfer steps.

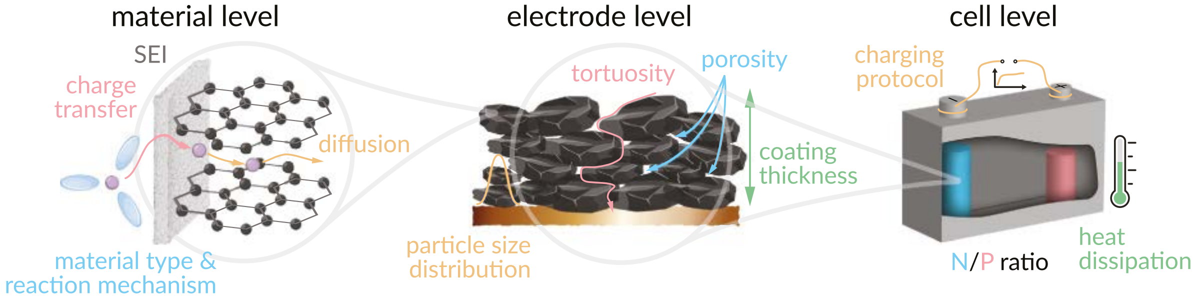

Figure 3. Overview of parameters relevant for fast-charging capability from material to cell level. On the material level, charge transfer from electrolyte to anode material, which depends on the type of material and the corresponding reaction mechanism, is relevant in addition to diffusivity within the material. The particle morphology, particle size distribution, tortuosity, porosity, and coating thickness all influence the fast-charging ability on the electrode level. Lastly, the ratio between the areal capacities of anode and cathode (N/P ratio), the charging protocol, and heat dissipation become relevant on the cell level.

Barriers for Migration of Li$^+$ Ions from Electrolyte into Anode Active Materials: During fast charging, a high amount of Li$^+$ ions per electrochemically active surface area and per time unit has to be transferred from the electrolyte into the active material particles. As detailed in Section 2.1.2, a charge-transfer barrier E_A is present, limiting this migration process. The charge-transfer barrier is related to an Li$^+$ ion crossing the electrolyte|electrode interface including stripping-off the Li$^+$ ion's solvation shell, transfer through the SEI layer, and acceptance of an electron provided by an external circuit from the cathode.[34] This barrier is connected to the charge-transfer resistance[34,74] and causes the charge-transfer overpotential $\Delta\varphi_{CT}^{a}$, as shown in Equation (32). Due to its temperature dependence, the charge-transfer resistance is lower at higher temperatures (see Equation (31)).

For graphite, the activation barrier from the electrolyte into the active material is in the order of ≈0.6 eV as determined in most cases using $LiClO_4$ as conductive salt dissolved in dimethyl sulfoxide (DMSO), 1,2-dimethoxyethane (DME), ethylene carbonate (EC), dimethyl carbonate (DMC), EC:DMC, or EC:DEC (diethyl carbonate).[75–77] Xu et al. obtained a quite close value of (0.54 ± 0.03) eV for intercalation into graphite for the more common $LiPF_6$ in EC:DMC.[78] On the other hand, the energy barrier for the Li$^+$ ion transfer into LTO was found to be only 0.33 eV (while using a similar calculation method). The difference was attributed to the absence of an SEI layer on the LTO surface.[78] This lower barrier for LTO explains part of its improved fast-charging capability compared to graphite.

Yao et al. investigated the insertion barriers of Li$^+$ ions through the graphene planes by density functional theory (DFT) calculations.[79] The energy barrier for Li$^+$ passing a C_6 ring of 10.2 eV is very high and therefore unlikely to be overcome.[79] However, the barrier is decreased by different atomic defects, for example, the Stone–Wales defect, mono-vacancies, or di-vacancies reduce the energy barrier to 6.35, 8.86, and 2.36 eV, respectively.[79] For LiC_6, dispersion-corrected DFT calculations also yielded high values in the order of 8 eV for Li$^+$ moving through a C_6 ring.[80] Therefore, intercalation proceeds for graphite mainly through the edge planes and not through the basal planes as shown in **Figure 4**a. However, irreversible capacity loss also happens mainly via these edge sites.[81] Therefore, graphite materials with more edge sites and thus larger BET surface area usually show both a better fast-charging behavior and increased initial capacity losses.

A similar trend was observed for Li$^+$ insertion into carbon nanotubes. The barrier for insertion into the nanotube through a wall (24.0 to 2.0 eV) is unfavorable compared to insertion through an open-end (≈0.3 eV) as shown in Figure 4a.[82] This barrier decreases by one order of magnitude when the nanotube wall's ring size increases from a pentagon to an octagon.[82] However, this barrier of 2.0 eV is still comparably high. Therefore, the pathway through the open end is favored.

Kaghazchi studied the intercalation barrier of Li$^+$ via Si(100) and Si(111) surfaces by DFT calculations as a function of the surface density of adsorbed Li adatoms.[83] The author obtained barriers in the range of (0.63–1.26) eV.[83] The lowest barrier of 0.63 eV was found for intercalation of Li$^+$ via the Si(100) surface, which was fully covered with Li adatoms.[83] This value is similar to the range of diffusion barriers reported for Li atoms in Si.[84–88] For comparison, a significantly higher barrier of 0.97 eV was obtained for the Si(111) surface fully covered with Li adatoms; therefore it was concluded that the Li$^+$ transfer proceeds most likely via the Si(100) surface, as depicted in Figure 4a.[83]

The energetic barriers for Li$^+$ transfer into Si nanowires were studied by DFT calculations as well. The diffusion barrier for Li$^+$ on the surface of Si nanowires was reported to be in the range of (0.12–0.20) eV, which is low compared to the transfer from the surface to the inner of the wire (≈0.9 eV) (see Figure 4b,c).[89]

By and large, charge transfer is often favored at specific crystallographic surfaces which—along with potential diffusion anisotropy within the bulk phase—is the basis for optimizing materials for fast charging by morphology control.

Solid-State Li$^+$ Diffusion inside Active Materials: Once the Li$^+$ ion is located inside an active material, the dominating limiting factor for fast charging is its solid-state diffusion inside the bulk phase, which highly influences the overpotential $\Delta\varphi_{AM}^{a}$, as shown in Equations (16), (17).[74–76] Next to lithium diffusion, electron transport mostly plays a less limiting, but not insignificant role for fast-charging applications. While it is not an issue for lithium metal and graphite with electronic conductivities of over 10^7 S cm^{-1} and 10^4 S cm^{-1},[90,91] respectively, silicon (<10^{-3} S cm^{-1})[92] and LTO (<10^{-7} S cm^{-1})[93] suffer from low electronic conductivity, adversely affecting their fast-charging capability. Therefore, methods to increase the electronic conductivity by means of heat treatment or introduction of conductive agents, for instance, are actively investigated.[92,94]

Li Diffusion in Lithium Metal: Diffusion within LMAs takes place via a monovacancy mechanism.[95] With a self-diffusion coefficient of (6–9) × 10^{-11} cm^2 s^{-1} and a diffusion barrier of ≈0.55 eV, this transport is slower than Li$^+$ diffusion in SEs commonly paired with LMAs.[90,96] During fast charging, high current densities at Li/SE anodes lead to accumulation of Li at the interface causing local mechanical stress,[97] ultimately resulting in dendrite growth and short circuits. Therefore, the critical current density, which leads to cell failure, is reported to be below 1 mA cm^{-2} for most SEs, far from the target of 12 mA cm^{-2} defined previously.[90] Recent reports from industry suggest much higher critical current densities for protected LMAs and Li/SE anodes, however, due to a lack of details we cannot comment on these results.

Li$^+$ Diffusion in Graphite: First-principles calculations show that the Li$^+$ diffusion barriers (ΔH_m in Equation (24)) between the graphene sheets of graphite are in the range of (0.2–0.5) eV.[80,98,99] This range obtained from first-principles calculations is in accordance with experiments conducted in the range of (−40 to +40) °C, where an Arrhenius analysis yields a value of 0.363 eV.[100] In contrast, the barrier for Li$^+$ moving through graphene layers in graphite is in the order of (2–10) eV,[79,80] close to the results for charge transfer, and therefore very unlikely compared to in-plane diffusion.

The Li$^+$ diffusion barriers[98] and chemical diffusion coefficients[101] vary with the lithiation degree of graphite. For example, the diffusion barriers are 0.308 eV and 0.4 eV for $Li_{0.2}C_6$ and LiC_6, respectively.[98] The increase of the diffusion barrier of Li$^+$ in graphite with SOC is unfavorable for the fast-charging capability since it leads to a higher probability of Li metal deposition for high SOCs.[102–105]

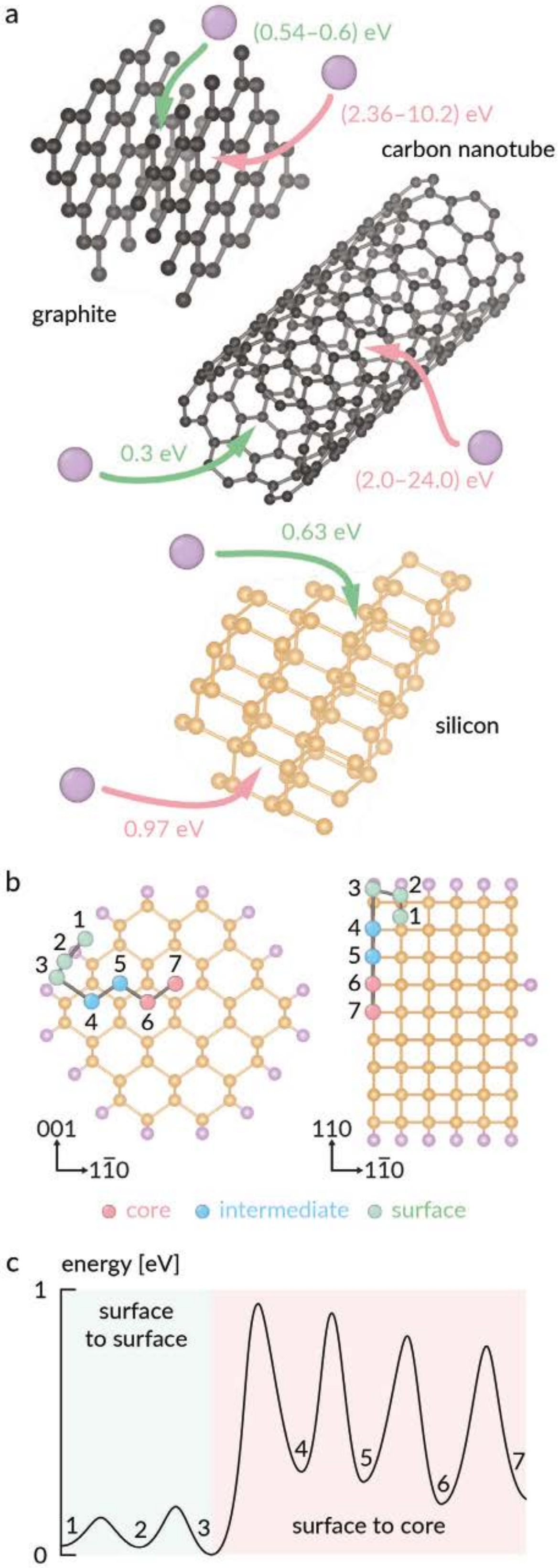

Figure 4. a) Preferred (green) and unfavored (red) diffusion pathways of lithium into graphite, carbon nanotubes, and silicon, as reported in literature.[75–78,82,83] For graphite, the activation barrier for intercalation through an edge plane is lower than through a basal plane. Intercalation into carbon nanotubes preferentially occurs through the open end compared to the walls. For silicon, the activation barrier is lower via the Si(100) surface than via the Si(111) surface. b) Diffusion pathway and c) corresponding barriers for Li$^+$ in Si[110] nanowires. Data in (b, c) (redrawn) from ref. [89].

Cai et al. coated graphite particles with a 6.5 nm thick turbostratic carbon layer, which improves the initial Coulombic efficiency, the specific capacity, and the rate performance by creating additional active sites and improving the diffusion coefficient. At 3C, the capacity of the coated graphite particles is nearly doubled compared to the uncoated graphite particles and the cycle life is also improved.[106]

Li$^+$ Diffusion on Graphene: When graphene is the material of choice, Li$^+$ is not intercalating, however, the diffusion barrier of Li$^+$ on graphene ((0.247–0.376) eV) is still substantial and depends on the graphene sheet's curvature.[107,108] For example, the diffusion barrier is lower on the concave side by ≈0.1 eV and higher on the convex side of a graphene sheet.[108] The differences for adsorbed Li on both sides can therefore be in the order of 0.2 eV. Consequently, differences of one to two orders of magnitude can be expected for the diffusion coefficient.[108]

Li Diffusion in Bulk Silicon: The energy barriers for the diffusion of a single Li atom in Si were obtained from first-principles calculations by different groups and are in the range of (0.47–0.6) eV.[84–88] Chou et al. found that the diffusion barrier of Li atoms in Si is decreasing from 0.62 eV to 0.47 eV when an adjacent Li atom is present due to the Li–Li electrostatic repulsion.[84] This electrostatic repulsion suggests that Li interstitials in Si tend to isolate themselves rather than clustering together.[84] To the best of our knowledge, there are no barriers available for higher lithiation degrees of bulk Si.

Tritsaris et al. calculated the energy barrier for jumps of Li between tetrahedral interstitial sites of crystalline Si (0.55 eV).[109] For amorphous Si, the same authors found energy barriers ranging from 0.1 eV to 2.4 eV for elemental hops of Li between equilibrium sites.[109] In amorphous Si, not all diffusion pathways contribute equally in mediating the Li diffusion.[109] The calculated long-range Li diffusion is comparable in crystalline and amorphous Si (≈10^{-12} cm^2 s^{-1}).[109] Ding et al. estimated a similar range of (10^{-13} to 10^{-12}) cm^2 s^{-1} from electrochemical measurements (GITT, EIS, and cyclic voltammetry) for nano-Si.[110] We like to note that these data should be considered with care as the conventional analysis of kinetic data only applies to single-phase materials.

Several attempts to increase the Si anode performance and overcome the existing challenges were reported. Different Si morphologies and nanostructures were examined in order to overcome the large volume expansion during the lithiation process, which eventually leads to the electrode fracture and pulverization of the active material and ease the diffusion of Li. Quiroga-González et al. presented a silicon microwire anode embedded at one end in a copper current collector. When comparing the microwire anode to other Si anode structures, higher areal capacities and charge density rates were achieved.[111] A coral-like network of porous silicon nanowires interconnected by a thin carbon layer was synthesized by Wang et al. and used for high-energy and high-power Li-ion batteries. The interconnected structure enables fast ion/electron diffusion along with a short ion diffusion path resulting from the porous Si nanowires. High specific capacities were presented at high charging rates of 7C, reaching over 500 charge–discharge cycles.[112] Yu et al. showed the use of thin Si layers, which were previously reported as a successful solution for the volume expansion issue,[113] on an elastomeric substrate in high-performance Li-ion batteries. The use of this multilayered structure resulted in a stable and high coulombic efficiency of up to 500 cycles.[114] Manipulating the composition of the Si bulk can also improve the Si characteristics as displayed for heavily boron-doped Si anodes proving enhanced Li^+ transport in the bulk and at the interface. Using this active material led to an increased rate performance even at high current rates (893 mA h g^{-1} at 8C).[115]

Silicon–carbon composites present an approach to overcome the drawbacks of sluggish electronic and ionic transport in pure silicon anodes. Thereby, the addition of carbon can improve the lithium diffusion coefficient by up to two orders of magnitude.[116] This increases the fast-charging capability compared to pure silicon.[117] Nevertheless, such composites are still hampered by low energy densities of the resulting full cells and high fabrication costs.[118]

Li Diffusion in Silicene Sheets: Silicene, the Si analogue of graphene, was investigated theoretically via first-principles calculations by Tritsaris et al.[119] The authors found that the diffusion barrier for adsorbed Li on free-standing single-layer silicene (Li_xSi_{1-x}) sheets is 0.23 eV and 0.24 eV for $x = 0.11$ and $x = 0.47$, respectively.[119] For double layer silicene, the diffusion barriers are 0.75 eV and 0.25 eV for $x = 0.06$ and $x = 0.41$, respectively,[119] that is, the diffusion is enhanced for the higher Li content. The diffusion of Li through silicene double layers (0.56 eV) is favored over single layers (1.07 eV).[119] In contrast to Si bulk material, lithiated silicene does most likely not suffer from irreversible structural changes, and the expected volume change is most likely in the order of <25%.[119]

Li Diffusion in Silicon Nanowires: For single Li atoms inside Si nanowires, Zhang et al. found that the Li binding energy increases gradually with the nanowires' diameter until they reach the value for bulk Si (1.36 eV).[89] For example, the Li binding energy at core sites of Si nanowires with the long axis along the [110] direction with (1.5, 2.0, and 2.5) nm diameter are (1.22, 1.34, and 1.35) eV, respectively.[89]

Figure 4c shows the calculated barriers of Li diffusion into Si[110] nanowires of 1.5 nm diameter.[89] The barrier for the surface-to-surface diffusion is the lowest ((0.12–0.20) eV), followed by core-to-core diffusion (0.58 eV), however, the rate-determining step is the transition of Li into the Si nanowire (≈0.9 eV).[89] This result is consistent with the experimentally observed core–shell phase distribution for Si nanowires.[120]

Li Diffusion in Lithium Titanates: Tielens et al. calculated the energetic barrier for Li^+ diffusion in Li_xTiO_2 for $x < 0.5$.[121] Interestingly, the authors found that the diffusion barrier decreased with higher Li content from 1.31 to 0.67 eV.[121] This means that the intercalation should be faster with increasing x in Li_xTiO_2, in contrast to the trend observed for Li_xC_6 (see **Figure 5**). We like to note that TiO_2 and $Li_4Ti_5O_{12}$ have very low electronic conductivity and the assumption that the chemical diffusion coefficient of Li can be replaced by that of Li^+ is oversimplifying. Upon lithium insertion, the partial electronic conductivity increases, which also gives rise to a strong increase of $\widetilde{D}_{\mathrm{Li}}$.

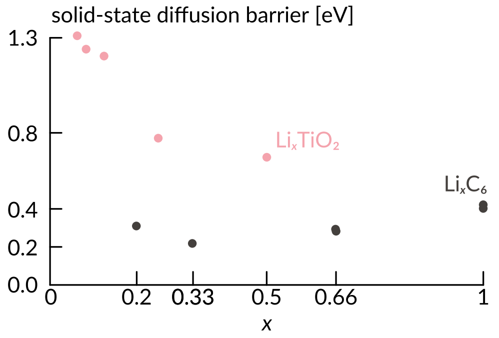

Figure 5. Comparison of activation energies of solid-state chemical diffusion coefficients for Li_xC_6[98,99] and Li_xTiO_2.[121]

The fast-charging capability of cells with LTO anodes[122] is much better than with graphite, although the diffusion barriers are higher. This might be related to the general use of nanosizing and nano-structuring of LTO materials[123–126] leading to shorter solid-state diffusion paths. Recently, the low activation barriers in LTO were reported to originate from kinetic pathways formed by distorted face-sharing Li polyhedra at the two-phase boundaries between the stable end members $Li_4Ti_5O_{12}$ and $Li_7Ti_5O_{12}$. In the metastable intermediates, which are accessible at high rates and formed because of low interfacial energy in the material, the diffusion barrier was found to only be 0.216 eV ($Li_5Ti_5O_{12}$) compared to 0.343 eV and 0.455 eV in $Li_4Ti_5O_{12}$ and $Li_7Ti_5O_{12}$, respectively. This might thus be the actual reason for the improved fast-charging capability of LTO.[127]

Li Diffusion in Bulk Tin: The diffusion barrier for a single Li atom in Sn as calculated by Chou et al. and Wang et al. is 0.39 eV.[84,88] Similarly to Li diffusion in Si, the diffusion barrier is decreased to 0.33 eV for Sn if a second Li atom is present near the diffusing atom.[84] This barrier reduction was found to be proportional to the Li–Li electrostatic repulsion.[84]

A comparison of the Li diffusion barrier in Si and in Sn while using the same calculation method resulted in 0.62 eV and 0.39 eV, respectively.[84] The lower barrier for Sn results from the higher flexibility of the lattice and the larger atomic size of Sn that allows for easier lattice expansion and therefore easier passage of Li atoms.[84]

Li^+ Diffusion in Niobium Tungsten Oxides: Lithium niobium tungsten oxides ($Li_xNb_{16}W_5O_{55}$ and $Li_xNb_{18}W_{16}O_{93}$) were reported as alternative anode materials for fast-charging applications by offering low diffusion barriers in the range (0.10–0.30) eV.[128] Compared to LTO, they operate at similar potentials (on average 1.57 V vs Li^+/Li) while offering significantly lower diffusion barriers without the need for nanoscaling. Instead, they rely on an oxide superstructure enabling fast diffusion and stability.[128]

Li^+ Diffusion in Organic Anode Materials: Organic materials are discussed as possible resource-saving alternatives to state-of-the-art materials and have a potential for biodegradability.[129] Different groups performed first-principles calculations on the Li^+ diffusion in organic anode materials. Exemplary barriers are 0.12 eV and 0.21 eV for lithium terephthalate[130] and di-lithium

terephthalate,[131] respectively. These values are low compared to the value range of graphite,[80,98,99] indicating a good fast-charging capability, however, the specific energies of organic anode materials investigated so far are very low.

SEI and Artificial SEI: The composition and structure of the SEI layer limit the charge transfer. The ideal SEI for fast-charging applications should be thin, homogeneous, long-term stable, and show high ionic and low electronic conductivity. All those characteristics can be obtained by forming an artificial SEI layer. When the SEI layer is formed during cycling, its properties are directly related, among others, to the electrolyte and anode material content.[132] Most of these methods of in situ SEI alteration are based on electrolyte properties and will therefore be discussed in Section 5. Here, we will focus on how modification of the anode can improve SEI characteristics. Although many studies have been performed on electrolyte additives to modify the SEI layer properties,[59] recent studies offer to conduct a pretreatment process using various techniques, which results in an artificial SEI layer possessing the desired properties.[8,133]

A straightforward process presented by Wang et al. includes vigorous stirring of commercial graphite powder in aqueous solutions with different content of glucose (w = (2.5–7.5)%) followed by a pyrolysis procedure. The samples coated with the glucose solution (w = 5%) presented a high reversible capacity of ≈340 mA h g^{-1} (at 60 mA g^{-1} for 45 cycles) alongside excellent rate capabilities.[134] Another artificial SEI coating containing polyethylene glycol *tert*-octyl-phenyl ether (PEGPE) and polyallylamine (PAAm) was applied to different anode materials, including natural graphite (NG). The plateau associated with the SEI formation was not observed when comparing the treated and untreated NG active materials' cycling profiles. At high rates (10C), the treated NG presented an extremely high capacity of 336 mA h g^{-1} along with a retained capacity of 93% even after 100 cycles.[135]

Moreover, chemical and thermal vapor deposition (CVD and TVD, respectively) are widely used as techniques to coat graphite particles with a homogeneous carbon-based artificial SEI layer resulting in a core–shell structure composite.[133,136] For example, Yoshio and coworkers presented a TVD process of toluene at 1000 °C. The carbon coating thickness was monitored by the feed time of the toluene vapor into the reaction tube. As the concentration of carbon coating on the graphite increases (w = (0–17.6)%), the irreversible capacity loss obtained decreases while the coulombic efficiency increases.[137]

Particle Size Distribution: The active material particle size distribution (PSD) affects the overall particle arrangement in the electrode microstructure while presenting varying Li solid-state diffusion lengths. The influence of the PSD on the high rate performance of the full cell was evaluated using various commercial graphite materials.[138] Under fast-charging conditions, Li$^+$ ions arrive with a high flux at the anode material's surfaces, leading to lithiation gradients inside the particles, that is, the local lithiation degree is higher at the particle surfaces compared to the particle core.[139] These lithiation gradients lead to stress evolution, for example, due to the Si particles' volume expansion,[140] which can in turn lead to particle cracking.[141] Larger particles are more prone to cracking[142] due to the longer diffusion lengths. Furthermore, larger particles typically reach lower charge capacities at high C-rates suggesting a limitation by slow solid-state Li$^+$ diffusion in graphite.[143] However, a smaller mean particle size leads to higher specific surface areas and, therefore, to higher capacity losses during formation[143] as well as to higher reaction rates with the electrolyte.[144]

When similar flat lamellae-shaped graphites with different particle sizes ((6–44) μm) were examined, a more facile and complete deintercalation process took place for the small-sized active material. In contrast, only partial lithiation occurred for the 44 μm particles, confirming the considerations in section Single-Phase Intercalation Electrodes. During the high C-rate evaluations, not enough time is given for the Li$^+$ ions to intercalate into the graphite structure, directly leading to lower capacities.[145]

Several computational studies addressed the influence of porosity and particle size on Li-ion battery performance and degradation. Röder and colleagues have presented the PSD impact (using the Weibull distribution) on the electrode capacity. Their numerical calculations, also confirmed by experimental work, demonstrated a decrease in the electrode capacity with larger mean radius. The higher internal resistance caused by longer diffusion pathways in larger particles can explain the results obtained, especially for high C-rates.[146] Thus, in any case the mean particle size should satisfy the condition given in Equation (18).

Moreover, during cycling, the particles may crack due to degradation processes (e.g., in the case of Si), leading to reduced particle size alongside the particles' electrical disconnection. Therefore, although the diffusion pathway shortens due to the decrease in the mean particle size, the electrode performance drops considerably, especially for high discharge rates, due to the active material's disconnection.[146]

Porosity of Particles: High diffusion resistance values alongside low rate capacities are only some of the difficulties caused by the long diffusion distances of Li$^+$ ions in graphite particles. One of the existing solutions to the long diffusion length is producing porous graphite active material that enables high charging rates.

An etching process using 1 mol L^{-1} potassium hydroxide solution followed by drying at 80 °C and an annealing process at 800 °C in nitrogen gas for two hours resulted in nanometer-scale pores.[147] The specific capacities obtained by the etched graphite were higher than the pristine material, in particular for high current densities.[147] A nickel-catalyzed steam gasification process was also proven to result in a porous graphite structure.[148] The synthesized active material exhibited a longer cycling life at high charging rates (5C) in addition to the higher reversible capacity (at 35 mA g^{-1}).[148]

3.1.2. Limitation of Fast Charging on Electrode Level

The need for high rates and increased energy densities led researchers to develop different anode electrode compositions and microstructures to address existing challenges. Although the study of the material itself led to significant improvements in the overall performance, the engineering approach must not be neglected. Controlling the electrode thickness, increasing the electrode's porosity, reducing its tortuosity, and decreasing the content of non-active additives (such as the

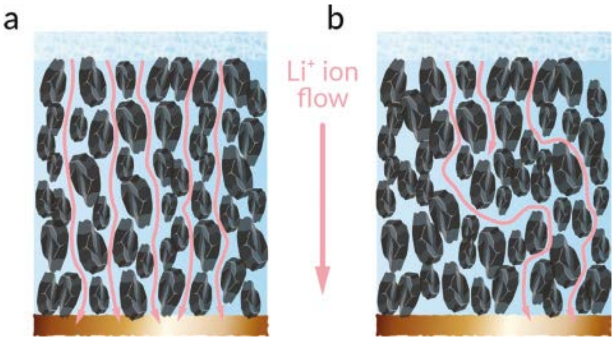

Figure 6. a) Efficient ionic pathways and b) dead-end pores alongside nonefficient pathways resulting in increased tortuosity.

binder and conductive carbon) have already presented promising results, even when using well-known anode materials such as graphite.

Effects of the Electrode Microstructure: *Anode Tortuosity*: The anode fabrication process begins with the preparation of a multi-component-containing slurry. Later, the mixture goes through the casting and calendaring processes, creating tortuous diffusion paths in the porous active material layer, in which the charge carriers are transported. Tortuosity can be defined as the ion transport path length due to the porous microstructure existing in the electrode.[16,149] A direct ionic pathway (**Figure 6**a), therefore, has a tortuosity value of $\tau = 1$. Several reports correlated the electrode's porosity and tortuosity both by calculations alongside experimental work to reach an optimization in the electrode structure parameters.[18] Also, impedance studies were found to quantify electrode tortuosity, allowing meaningful experimental results that support the numerical calculations.[16,17] Although closely connected to porosity, tortuosity describes the effective ionic pathways, whereas porosity describes the fraction of voids. Therefore, highly porous electrodes do not necessarily have low tortuosity values, for example in the case of a high fraction of dead-end pores, as presented in Figure 6b.

When thick, highly loaded electrodes are used, the high rates are limited by the diffusion paths inside the electrode's microstructure.[19,150–153] High tortuosity values are a significant limitation that directly influences the battery's ability to sustain high cycling rates alongside higher power densities. Reduction in the ion's path lengths in the electrodes will eventually result in faster and more efficient diffusion (reduction of the parameter β), increasing the limiting current density j_{lim}, which directly influences the electrolyte overpotential on the anode side $\Delta\varphi_{\text{EL}}^{\text{a}}$, as detailed in Section 2.2.1. The slow migration rates related to high tortuosity values can lead to significant ohmic and concentration polarization, which eventually prevents utilizing the whole available active material. Eventually, the overpotential for ion transport due to the sluggish electrode kinetics of the anode can lead to capacity fade and lithium deposition on the electrode surface close to the separator.[154,155]

Various studies focus on improving transport limitations by using three-dimensional electrode architectures where the controlled electrode particle shape and orientation results in preferential paths with low tortuosity for the Li^+ ions. It is crucial to compare structured and unstructured electrodes with the same loadings to assess the effect of tortuosity correctly. Studies conducted using a mesoporous anatase microstructure, presenting uniform and connected pores, resulted in improved performance compared to the optimal result previously reported for anatase nanoparticles.[156] Moreover, calculations performed for magnetically aligned graphite flakes (see Figure 6a) indicated a reduction in the out-of-plane tortuosity by a factor of nearly four.[157] Additionally, the rate capability test presented three times higher specific charge, more defined potential plateau, and much lower overpotential when aligned graphite flakes were used.

A co-extrusion process followed by a sintering method resulting in controlled tortuosity while maintaining the electrode porosity and thickness was previously reported by Bae and coworkers.[158] Alternative approaches, such as laser patterning, manage to manipulate the electrode structure after fabrication, creating an array of vertical channels serving as linear diffusion paths.[159,160]

Anode Porosity: The porosity of the anode is crucial for proper electrode performance since the penetration of electrolyte into the electrode bulk is directly affected by the voids present between the active material particles. The control of porosity during electrode manufacturing is a compromise between electronic and ionic conductivity.[161] While a higher porosity is favorable for the ionic conductivity, it also reduces the areal capacity for the same anode coating thickness. Anodes with higher porosity and the same areal capacity result in a thicker active material layer, leading to a lower energy density on cell level. For example, Colclasure et al. showed that the full cell volumetric energy density achieved for an electrode of 4 mA h cm^{-2} with 40% porosity is less than for a 3 mA h cm^{-2} anode with 30% porosity.[19] Increasing the porosity to high levels is, therefore, not an effective strategy to improve the fast-charging capability.

The ongoing growth of the SEI layers on the anode surface[162] is a well-known aging mechanism leading to clogging of the electrode pores[163] and therefore reducing the porosity during battery life. A microkinetic Li-ion battery model predicted the aging characteristics resulting from the continuous clogging of electrode pores due to SEI formation (see **Figure 7**).[164] A significant electrolyte overpotential is generated after ≈3000 cycles, enabling the deposition of lithium metal.[164] The positive feedback caused by the lithium metal deposition and the decrease in porosity accelerates the aging process and can lead to a sudden drop in cell capacity.[164]

Theoretical and experimental studies have previously discussed optimizing the electrode porosity, depending on the chemical composition of the electrodes. Zheng and coworkers have presented the connection between the electrode inactive components and its porosity, resulting in an optimum mass fraction (w) of 8% of inert material while calendaring the electrode to at least 30% porosity.[20] The same group has also reported optimal performance while using a combination of PVDF (w = 8%) with acetylene black (w = 7%) while calendaring the electrodes to (30–40)% porosity.[21] Another study presented a decrease in the first and second cycle capacity alongside higher irreversible capacity loss when increasing the graphite anode density from 0.9 g cm^{-3} (where optimal results were obtained) to 1.38 g cm^{-3}.[165] Therefore, when deciding

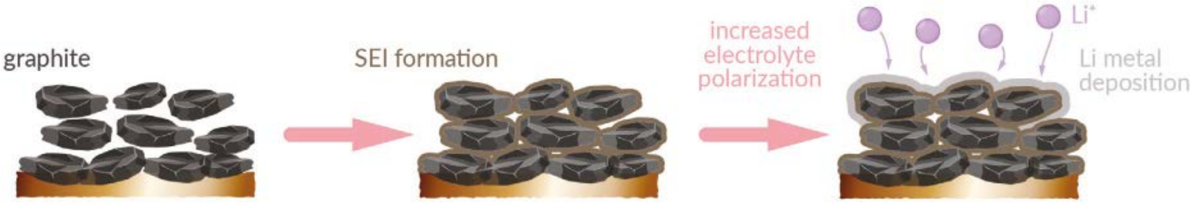

Figure 7. Illustration of SEI growth and pore-clogging during cycling inducing polarization and therefore promoting Li metal deposition.

on the electrode porosity, facile Li^+ ion penetration alongside the inactive material's content and the rates applied should be considered.

Anode Coating Thickness: An effective way to increase the fast-charging capability, which is also applied in state-of-the-art commercial cells[166,167] are thin anode coatings.[19,138] However, in the case of low coating thicknesses, the active to inactive material ratio is unfavorable in terms of specific energies and low energy densities, resulting in increased costs.[13]

One effective method to increase the volume ratio of active and inactive materials is increasing the electrode thickness.[166] In commercial cells, the single-sided coating thicknesses are currently up to ≈100 µm.[166] However, various studies went to much higher values. Numerical models were created to study the relation between thickness and applied charging C-rate. The advantages of thick electrodes with respect to energy density were compromised by the internal cell polarization and low utilization of the active material resulting in a critical thickness.[152,168]

Sivakkumar et al. studied Li/graphite half cell behavior at high current densities (up to 60C) while using different graphite anode thicknesses ((12–100) µm). Thinner electrode coatings presented superior performance while applying a C/10 intercalation rate alongside varying deintercalation currents (up to 60C). When the same rate, 20C, was used for the intercalation and deintercalation processes, the 100 µm thick coating presented a sharp drop resulting in only 2% gravimetric deintercalation capacity retention.[138]

Gallagher and colleagues presented a correlation between the electrode loading and various parameters such as current density, electrolyte transport, and overall cell performance while using numerical calculations and experimental results.[151] The analyses presented a significant drop in the areal capacity utilization due to salt depletion. On the other hand, when proper current densities, which allow for full access to the available capacity while avoiding lithium deposition, were chosen, stable cycling was achieved.[151]

Effects of Anode Potential: Unfavorable deposition of lithium metal on the anode becomes thermodynamically possible if the anode potential becomes lower than 0 V versus Li^+/Li,[103,169–171] corresponding to an overpotential of (0.065–0.2) V in the case of graphite.[171] This condition is more likely to be fulfilled in front of the anode surface (near the separator) due to higher Li^+ activity[105] and less likely near the current collector due to depletion of Li^+ ions.[153] For pouch cells, Li metal deposition on the anode surface leads to measurable thickness changes.[172] Simulations taking the anode microstructure into account show that the lithium deposition condition is first fulfilled on the anode surface.[170] Consistent with this, post-mortem analysis after cycling showed that lithium metal is mostly deposited on the anode surface.[173–175] The anode potential and therefore the tendency of lithium metal deposition is affected by electrolyte additives,[176] anode active materials,[177] the anode coating thickness,[38] operating parameters such as temperature, C-rate, and SOC[38,103–105,177] as well as the ratio of the areal capacities between anode and cathode (N/P ratio).[19,178–181]

The N/P ratio is typically in the range of 1.1 to 1.2.[19,178–182] N/P ratios < 1 lead to Li metal deposition, since the areal capacity of the cathode exceeds that of the anode. Mao et al. described the N/P ratio as a function of the C-rate for charging graphite/$LiNi_{0.8}Co_{0.1}Mn_{0.1}O_2$ (NCM811) pouch cells.[37] As an example, the authors found for their electrodes optimum N/P ratios of 1.15, 1.00, and 0.5 for C/10, 3C, and 4C, respectively.[37]

The anode potential is further related to properties on the material level. For example, larger particles and higher barriers for Li migration into the active material and for solid-state diffusion within the active material show a higher tendency of lithium metal deposition due to stronger polarization effects. In contrast, high anode potentials as in the case of LTO materials avoid lithium metal deposition while decreasing the cell voltage and therefore the specific energy and energy density on cell level.

By preparing anodes with different ratios of graphite and hard carbon ((0–100)% hard carbon), Chen et al. found a significant improvement of capacity retention after 500 cycles with 4C and 6C for 50% graphite/hard carbon.[183] The authors used industrially relevant areal densities (3 mA h cm^{-2}) and multi-layer pouch full cells. The improvement was attributed to enhanced homogeneity of the reaction within the anode and mitigation of Li plating.

For the special case of LMAs, lithium metal is deposited directly on lithium metal or a suitable current collector. Here, lithium plating is not an issue anymore, but a desired feature. In combination with SEs stable against lithium metal this opens the possibility of fast-charging capable SSBs. Bad contact between the two solid phases is still an issue, however, among others, which will be further detailed in Section 5.2.2. Along with the aforementioned limited vacancy diffusion leading to dendrite propagation this poses major challenges for fast charging of LMAs.[90]

3.1.3. Degradation of Anode Induced by Fast Charging

The main degradation modes related to fast charging are i) Li deposition on the anode and subsequent reaction with electrolyte as well as the formation of "dead Li," ii) increased reaction rates resulting from heating of the cell due to current flow, and iii) particle cracks.

In literature, the mechanism of lithium metal deposition is mostly investigated for graphite anodes,[102,105,172–175,177,184,185] although it is also studied in Si/C composite anodes.[186] The phenomenon of lithium metal deposition on anodes is highly critical since it can reduce safety by dendrite growth[187] and exothermic reactions.[175,188] On graphite anodes, lithium metal deposition is favored during charging at low temperatures,[38,102,103,185] high charging C-rates,[103,185] and high SOCs,[103] as well as their combination.[104,185] These effects can be counteracted by avoiding negative anode potentials, for example, by optimized charging protocols[103–105] or by internal heating of cells during charging.[189]

Additionally, cell heating due to current flow during charging can have significant influence on the anode potential. Tippmann et al. showed by simulations with and without a coupled thermal model (i.e., with and without heating due to the charging current) that the anode potential is shifted to higher values.[103] Therefore, larger cells, which usually show a stronger heating due to current flow,[166,182] are likely to show a lower tendency to lithium metal deposition compared to smaller cells.

In the case of fast charging at high ambient temperatures or strong cell heating due to high charging currents, different aging mechanisms come into play. High temperatures are known to suppress lithium deposition; however, SEI growth is favored at elevated temperatures.[162]

The graphite laminated structure (interlayer spacing of 0.335 nm[137]) enables Li^+ intercalation. Simultaneously, solvent co-intercalation may occur, especially at high charging rates, causing volume expansion and exfoliation (≈10%) followed by structural degradation of graphite.[190] When fast charging rates are applied, rapid Li^+ intercalation is required. Due to the existing charge-transfer limitations, a large concentration gradient can be created, leading to an inhomogeneous stress distribution among the graphite particles. Cracks in the material and electrode microstructure, leading to isolation of graphite particles and even disconnection of the active material from the current collector, can occur. Graphite lattice rearrangement can cause further mechanical degradation and defects during the intercalation process.[59]

When alloy metal host materials are being used as negative electrodes, severe volume expansion can be obtained. Winter and coworkers have shown that massive volume changes can be prevented by keeping a small particle size of the host material ((10–20) nm for Sn_2Fe and $SnFe_3C$ intermetallic phases, for example[191]).

3.2. Advantages and Disadvantages of Existing Materials Fulfilling Fast-Charging Capability

As discussed above, many obstacles can hinder the Li-ion battery's abilities when high C-rates are applied. Several studies have been conducted to improve Li^+ ion migration inside the active material by various modifications performed on the active material itself as well as on the electrode level. **Table 1** summarizes numerous improvements of well-known anode Li-ion materials and their performance at high rates.

Figure 8a correlates the diffusion barriers in different anode active materials (Section Solid-State Li^+ Diffusion Inside Active Materials) with the specific capacities on the material level. A nearly linear correlation is obtained for Si, Sn, graphene, graphite, and organic materials, thus materials with higher specific capacity often show worse fast-charging capability. On the other hand, lower C-rates already lead to higher absolute currents for high capacity materials.

LTO does not fit into the correlation in Figure 8a since it combines a low specific capacity with a high diffusion barrier. However, for LTO mostly nanoscale materials are utilized[123–126,205] and therefore the shorter diffusion paths compensate the higher barriers. Furthermore, nanosized materials usually cause higher initial capacity losses due to higher surface area where SEI is formed. This is not the case for LTO due to its higher anode potential, which is inside the stability window of the electrolyte. Therefore, the higher surface area does not lead to a new SEI layer formation in each cycle. However, the higher anode potential contributes to the drawback of lower specific energy for LTO.

On the material level, the goal is to combine materials with higher specific capacities and energies alongside lower diffusion barriers, as well as lower charge-transfer barriers. Figure 8a suggests that these requirements seem to exclude each other; however, the exception of LTO shows that there is hope to find such materials.

Another approach is the use of smaller particles, for instance nanosized materials. The shorter diffusion paths of Li^+ ions in nanoparticles enables improved solid-state diffusion and therefore a better utilization of the materials during fast-charging (see Figure 8d). However, this is limited by higher irreversible losses[143] and increased tortuosity. Therefore, a further target for improved fast-charging capability is nanosized materials with high specific energy and energy density, however, without high irreversible losses.

Figure 8c shows a similar trend on the cell level for commercially available cells as Figure 8a for materials. In Figure 8c, cells with LTO anodes fit into the linear correlation together with graphite and Si/graphite since the smaller particle size of LTO is already included in the evaluation on cell level. The target on the cell level is reaching a higher specific energy while preserving the short charging time. The key is not only on the material level, however optimization on the electrode level is required as well.

On the electrode level, the increased specific energy and lower costs are usually achieved by thicker electrode coatings,[13,19,166,167] however, this leads to lower utilization of the negative electrode and favors Li deposition as illustrated in Figure 8e. The aim is to construct electrodes with both higher loading and higher fast-charging capability and lower susceptibility to Li deposition. In Figure 8b, the effect of particle shape on tortuosity is shown.[19] In this example, spherical and potato-shaped particles on material level lead to a lower and higher tortuosity on electrode level, respectively.[19] Alternative approaches use aligned particles[157] or holes on the anode coating to improve the tortuosity.[159,160] It is, however, always critical to cross-check whether such approaches lead to a decrease in energy density, for example, by removing active material. In the case that active materials are removed in modified electrodes, they must be compared with untreated electrodes with the same loading.

Table 1. Several active materials and their modifications for fast-charging applications.

Active material	Material limitations	Material modifications for high-rate applications	Active material loading	Performance reported (number of cycles, capacity, current density)	Ref.
Graphite/graphene	Unstable SEI layer due to the extansion and contraction of the graphite leading to high ICL; sluggish intercalation kinetics and low lithiation voltage resulting in metallic lithium deposition	Mildly oxidized graphite resulting in extended *d*-spacing while conserving good electrical conductivity		No significant decrease in capacity from the value obtained at 0.1C up until 10C; the capacity value was maintained close to the $Q_{0.1C}$ up until 50C	[192]
		Magnetically aligned graphite	9.1 mg cm^{-2}	Higher capacities were obtained for the aligned material at C/2–2C; the specific charge capacity achieved was higher (by the factor of 1.6) than the reference material (at 1C for 50 cycles)	[157]
		Graphene-like graphite prepared by an oxidation process using $KClO_3$ and HNO_3, followed by a heating treatment	5 mg cm^{-2}	Capacity retention of 79% and 39% at 6C (100 cycles) for GLG and graphite, respectively	[193]
		3D interconnected porous nitrogen-doped graphene foam (NGF) with encapsulated Ge quantum dot@ nitrogen-doped graphene yolk–shell nanoarchitecture (Ge-QD@NG/NGF)	1.8 mg cm^{-2}	Over 800 mA h g^{-1} at 40C (200 cycles) alongside extended cycling capability (≈96% reversible capacity retention up to 1000 cycles)	[194]
		Hybrid anodes with a uniform mixture of graphite and hard carbon	≈3 mA h cm^{-2} anode areal capacity loading (depending on the graphite/hard carbon blend ratio)	Anodes containing $w = 50\%$ graphite retain 87% (4C) and 82% (6C) of their initial specific energy after 500 cycles	[183]
		Nanoscale turbostratic carbon-coated graphite	1.0 mA h cm^{-2} anode areal capacity loading	A significant improvement in initial Coulombic efficiency, specific capacity, and rate performance	[106]
Hard carbons	A lower density and initial coulombic efficiency in comparison to graphite; large irreversible capacity, low packing density, and hysteresis in the voltage profile	Polyacrylonitrile (PAN) hard carbon	5.2 mg cm^{-2}	The PAN hard carbon presents a charge capacity of 135.4 mA h g^{-1} at 3C (100 cycles), exceeding the graphite electrode's value (106.0 mA h g^{-1})	[195]
		Siloxane-grafted nano-$SiO_{0.26}$/hard-carbon composite	1.2 mg cm^{-2}	(916–750) mA h g^{-1} at 0.2C (100 cycles); ≈650 mA h g^{-1} at 10C (100 cycles)	[196]
Li	Fragile SEI layer leads to Li dendrite growth during cycling; the cyclability is possible for most Li anodes only under low current densities (<1 mA cm^{-2})	Pretreatment of the Li anode surface using a thin silicon wafer ([20–30] µm), resulting in a thin, highly ionically conductive Li_xSi film		Specific capacity of ≈390 mA h g^{-1} at 2 mA cm^{-2} (150 cycles)	[197]
		An over-lithiation process of mesoporous AlF_3 resulting in a nanocomposite of Li/Al_4Li_9-LiF (LAFN)		Specific capacities of (140, 131, 113, and ≈80) mA h g^{-1} at (0.2, 1, 4, and 10)C, respectively (≈10 cycles); long term cyclability at 1C resulted in ≈130 mA h g^{-1} (100 cycles)	[198]
Si	Electrode disintegration and high charge-transfer resistance due to the extreme volume change during cycling (>300%) alongside low electrical conductivity (≈10^{-4} S^{-1})	An edge-plane activated graphite with an-Si nanolayer (SEAG) prepared by nickel-catalyzed hydrogenation followed by a chemical vapor deposition (CVD) process using acetylene and silane gas		Less Li deposition after applying high charging currents avoiding the drastic capacity degradation	[199]

Table 1. Continued.

Active material	Material limitations	Material modifications for high-rate applications	Active material loading	Performance reported (number of cycles, capacity, current density)	Ref.
		A composite layer-by-layer silicon/reduced graphene oxide (Si/RGO) anode material with a post-laser-shock (LS) compression treatment	(0.1–1) mg cm^{-2}	≈1850 mA h g^{-1} at 6 A g^{-1} after 200 cycles; ≈1200 mA h g^{-1} at 15 A g^{-1} after 1000 cycles	[117]
LTO	Low electrical conductivity (≈(10^{-8}–10^{-13}) S cm^{-1}) and slow Li^{+} ion diffusion (≈(10^{-8}–10^{-13}) cm^{2} s^{-1})	LTO porous particles filled up with N-doped carbons	10 mg cm^{-2}	Better capacity retention in comparison to commercial LTO while applying 1C, 45 °C (300 cycles)	[200]
Conversion materials	Poor cycle stability due to large structural reorganization leading to massive volume changes; extremely high Coulombic inefficiencies and large irreversible capacity and voltage hysteresis between discharge and charge steps	α-Fe$_2$O$_3$ hollow spheres with sheet-like sub-units		Reversible capacity of 710 mA h g^{-1} at 200 mA g^{-1} (100 cycles)	[201]
		Carbon-decorated Fe$_3$O$_4$ nanowires		≈830 mA h g^{-1} at 0.1C (50 cycles); when higher charge rates were applied (5C), the carbon decorated Fe$_3$O$_4$ nanowires delivered a high capacity of 600 mA h g^{-1}	[202]
		CoO/graphene nanocomposite: ultrafine CoO nanocrystals densely attached to the graphene nanosheets		≈1018 mA h g^{-1} at 200 mA g^{-1} (520 cycles); the synthesized material presents good rate capability—at high rates (1600 mA g^{-1}), a favorable specific capacity was obtained (531.2 mA h g^{-1})	[203]
Organic materials	Low capacity of the conducting polymer, low electronic conductivity, and dissolution of conjugated carbonyl compounds	2D covalent organic framework (COF) based on covalently connected polyporphyrin with 4-thiophenephenyl groups (TThPP)	0.2 mg cm^{-2}	Good rate capability resulted in (666, 519, 384, 271, and 195) mA h g^{-1} when (0.2, 0.5, 1, 2, and 4) A g^{-1} rates were applied; cycling performance evaluations resulted in ≈400 mA h g^{-1} at 1 A g^{-1} (200 cycles)	[204]

3.3. Requirements on Material and Electrode Level

As deduced from theoretical considerations in Section 2 and corroborated with experimental data in the current Section 3, improved anode materials with high fast-charging capability should ideally show the following properties:

i) low energetic barriers for Li^{+} transfer into the material;
ii) low energy barriers for Li solid-state diffusion inside the active material. According to Equation (18), this directly results in
iii) small particle size with rather narrow PSD, for example, nanoparticles, while sustaining processability and low irreversible losses.

Furthermore, high long-term stability in contact to the electrolyte and in a wide temperature range is required. In addition, high energy density and specific energy are needed, while safety must be sufficiently high.

Improved negative electrodes with high fast-charging capability should ideally show the following properties:

i) a tortuosity value near one, which is difficult since the preferred small particles adversely affect the tortuosity;
ii) an optimized porosity regarding electronic and ionic conductivity of the electrode layer;
iii) an electrode expansion as small as possible.

Combined, these properties can result in a very low or even negligible tendency of lithium metal deposition, that is, in anode potentials above 0 V versus Li^{+}/Li. However, the anode potential should not be too high in order to retain high specific energies. Furthermore, without changing the properties above, the areal capacity must be high enough, that is, by high electrode loading to increase the ratio of active to inactive material and therefore lower costs.

On cell level, fast-charging capability needs to be improved regarding cell heating due to current flow and charging strategies: i) At low ambient temperatures, cell heating is desired to improve migration and diffusion kinetics and to hinder Li deposition on the anode. Examples are cell designs with internal heating.[155,189,206] ii) At high ambient temperatures, cell heating should be hindered by cell designs for improved heat dissipation. iii) Charging strategies to prevent Li deposition by preventing negative anode potentials versus Li^{+}/Li.

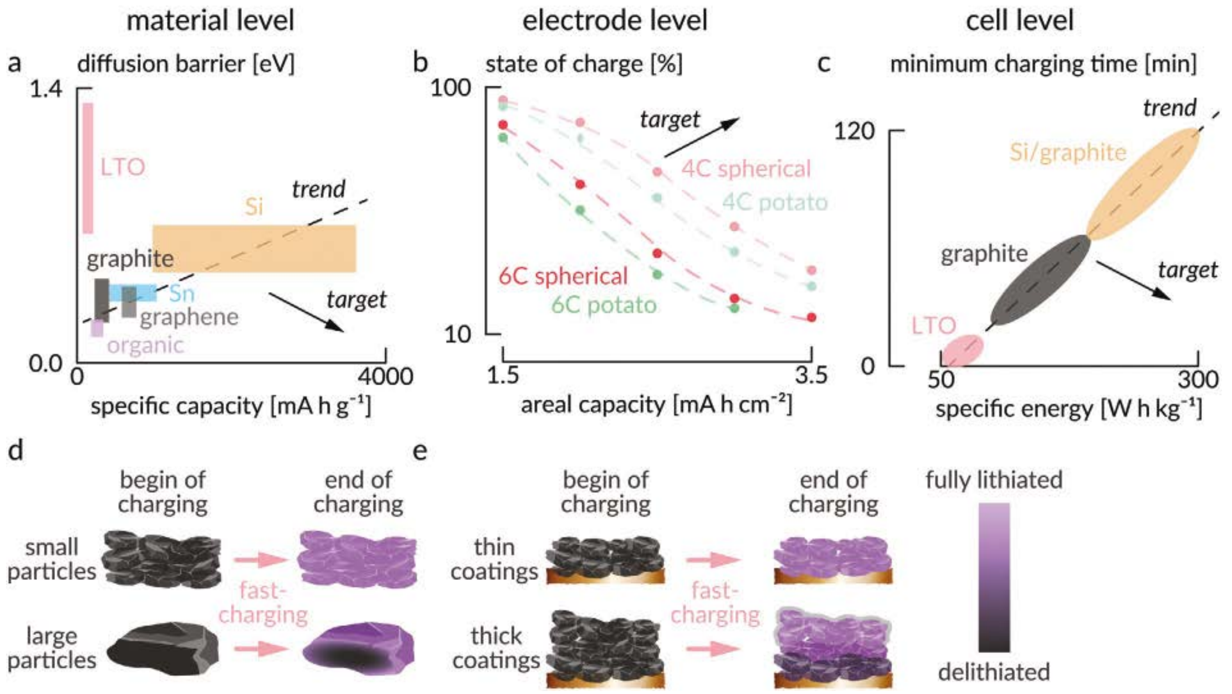

Figure 8. General trends for fast-charging capability from material to cell level: a) Solid-state diffusion barriers of Li in different anode active materials as a function of specific capacity on the material level. b) Calculation of charged capacity after 4C and 6C CC charging to 4.2 V as a function of anode loading. Spherical (lower electrode tortuosity) and potato-shaped (higher electrode tortuosity) particles were used. Data (redrawn) from ref. [19]. c) Minimum charging time (C-rate^{-1}) as specified in data sheets from commercial cells for LTO (Toshiba SCiB cells), graphite, and Si/graphite composite anodes as a function of specific energy on cell level. Illustration of material utilization for d) small/large active material particles and e) thin/thick anode coatings.

4. Cathode

In this section, the kinetic aspects associated with Li$^+$ transport in/at the cathode are reviewed and rated according to their relevance for fast charging. A simple way to obtain insights into the kinetics of battery electrodes, thus their fast-charging capability during operation is to monitor the voltage or potential.[2,22,77,207] For a battery cell, the overvoltages and voltage hysteresis, that is, the voltage/potential difference between the obtained charge and discharge curves, reveals the overall internal resistance of the cell as exemplarily shown in **Figure 9**a.[58,208] Moreover, with the support of a reference electrode,[209] the individual contribution of both electrodes, cathode and anode, on the overall internal resistance can be distinguished via the respective electrode potentials (overpotentials and/or potential hysteresis $\Delta\varphi^c$ and $\Delta\varphi^a$).[210,211,212] Simple electrochemical techniques allow for a systematic investigation of kinetic aspects for various cathode active materials as exemplarily shown in Figure 9b.[34,213] Typically, cathodes contribute

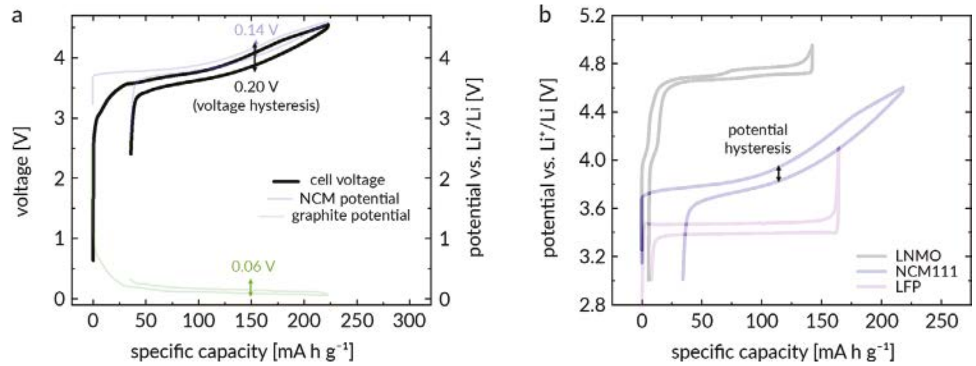

Figure 9. a) Initial charge/discharge cycle of an NCM||graphite full cell setup including a reference electrode for monitoring the potential behavior of individual electrodes. The voltage hysteresis (here: $\Delta\varphi = 0.20$ V) as an indication for overall internal cell resistance is the sum of the potential hysteresis of both, the cathode (here: $\Delta\varphi^c = 0.14$ V) and anode (here: $\Delta\varphi^a = 0.06$ V). Data (redrawn) from refs. [210,214]. b) The overall kinetic aspects of a single electrode, for example, a cathode with varied CAMs can consequently be simply indicated by monitoring the cathode potential during operation. Data (redrawn) from refs. [215–217].

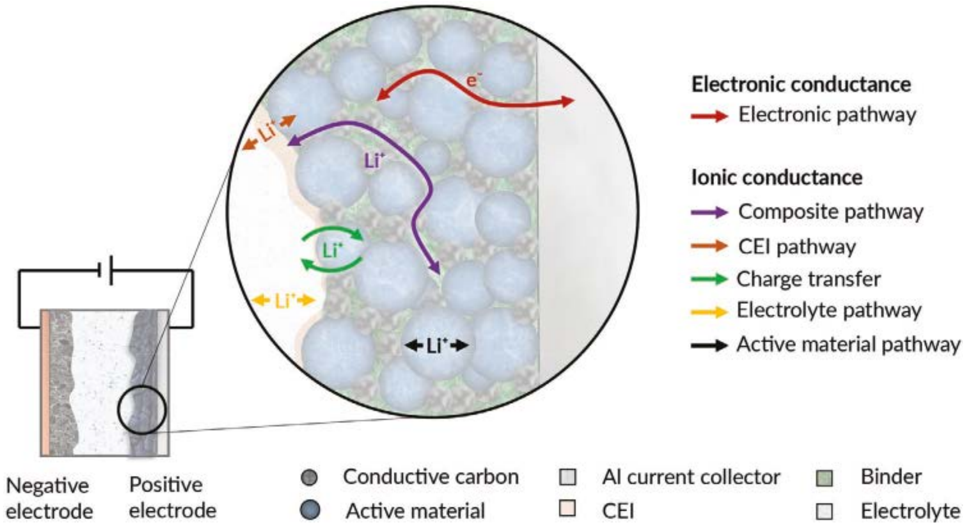

Figure 10. Schematic illustration of various Li$^+$ and e$^-$ pathways, which can impact the internal resistance. Relevance and implication of the individual contributions to the overall internal resistance and fast charge capability are discussed in the main text. Redrawn from ref. [22].

most to the internal cell resistance as also seen in the example of Figure 9a, where the voltage hysteresis amounts to 0.14 V for the NCM cathode contrary to 0.06 V for the graphite anode.

The cathode as a particle-type composite electrode includes inactive ingredients, that is, a binder for mechanical robustness/structural integrity as well as conductive carbon for improved electronic conductance and electrolyte uptake.[218] Consequently, the complex nature of the cathode, both on the material level and on the composite electrode level, involves several processes and charge pathways, which contribute to the cathode's internal resistance as shown in **Figure 10**.[22]

4.1. Limitation of Fast Charging on the Material Level

4.1.1. Influences of the Crystal Structure

Insight into relevant factors controlling the internal resistance, which were already deduced fundamentally in Section 2.1.1, can also be obtained from in situ monitoring of kinetics during the charge process, that is, through changes in overpotentials. The charge profiles of $LiNi_{1/3}Co_{1/3}Mn_{1/3}O_2$ (NCM111) as an exemplary CAM for various specific charge currents are depicted in **Figure 11**a (compare also Figure 2a). The accompanied increase in overpotentials $\Delta\varphi^{c}_{AM}$ is not constant, but rather SOC dependent with a minimum at a specific charge capacity of ≈140 mA h g^{-1}, corresponding to an Li$^+$ extraction ratio of ≈50% and to step II in Figure 2. At this SOC, the maximal *c*-parameter (proportional to the Li$^+$ interlayer distance) of NCM111 is observed, as shown in Figure 11b. This implies a direct relation with the development of overpotentials in the entire cathode. In other words, the kinetic aspect and internal resistance overwhelmingly depend on the used CAM and changes associated with the CAM. In line with this, changes of solely the CAMs, for example, $LiFePO_4$ (LFP), NCM111, or $LiNi_{0.5}Mn_{1.5}O_4$ (LNMO), lead to significant changes of the cathodes' overpotential as shown in Figure 9b, while the other aspects obviously play only a minor role.

The SOC dependence of the overpotential $\Delta\varphi^{c}_{AM}$ can be related to the crystal structure of state-of-the-art CAMs, that is, layered oxides (example: NCM111), which is depicted in **Figure 12**,

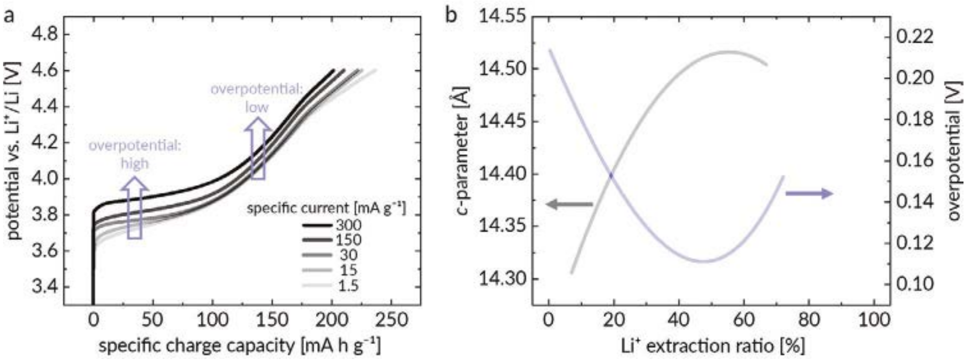

Figure 11. a) Initial charge curves of NCM111 for varied specific charge currents demonstrating SOC dependence of the overpotential $\Delta\varphi^{c}_{AM}$. Adapted with permission.[22] Copyright 2016, IOP Publishing. b) The overpotential behavior can be related with the *c*-parameter of the NCM111 structure. At approximately 50% Li$^+$ extraction ratio, the maximum *c*-parameter and lowest overpotential (=best kinetics) is observed, which can be attributed to the widest Li$^+$ interlayer distance, thus to maximized Li$^+$ mobility. Hence, the cathode overpotentials can predominantely be assigned to the Li$^+$ pathway within the active material. Data (redrawn) from ref. [22].

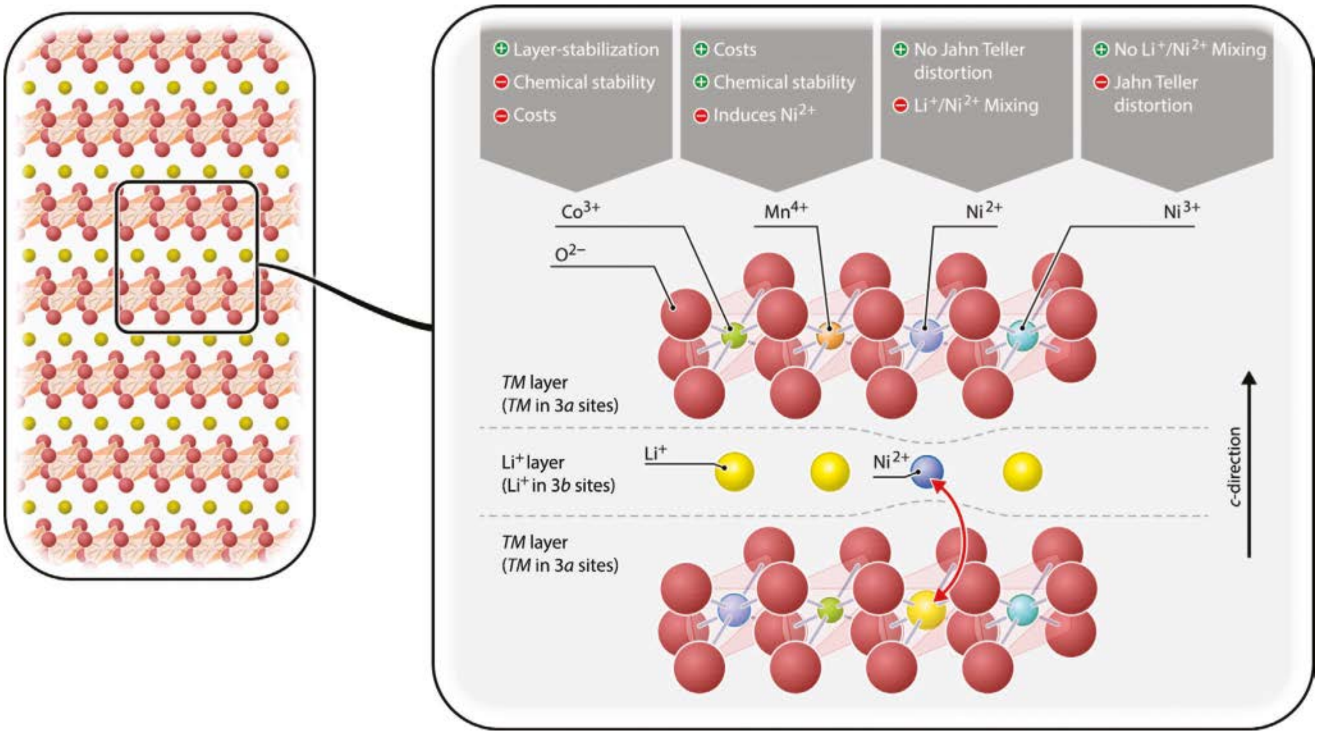

Figure 12. Crystal structure of the state-of-the-art CAM, that is, layered oxides like NCM. Each transition metal contribution has pros and cons rendering compromises necessary. Particularly the Li^+/Ni^{2+} mixing effect is relevant for fast charge as it dictates cathode kinetics via decreasing the chemical diffusion coefficient within the CAM as a rate-limiting aspect. Adapted with permission.[215] Copyright 2017, John Wiley and Sons.

where the functionality of each transition metal is included. While the transition metals reside in the 3*a* layer, the Li^+ resides in the 3*b* layer ("Li^+ layer"), which provides the slab space for the 2D Li^+ pathway.[219] The changes in Coulombic interactions during charge within the crystal are intertwined with changes in the *c*-axis, thus the Li^+ interlayer distances, which consequently affect Li^+ mobility and in turn the SOC dependent overpotential.[22–26] In addition, a phase transformation, which occurs depending on the SOC in NCM, has to be considered, as demonstrated in detail in section Phase-Transformation and Conversion-Type Electrodes. Thereby, the dependence of the cathode overpotential $\Delta\varphi^{\mathrm{c}}_{\mathrm{AM}}$ on the SOC—and thus also the presence of the different phases H2 and H3—is shown in Figure 2c,d. Obviously, these parameters, which affect the Li^+ mobility within the CAM, are the key parameters for the internal resistance, thus for the CAM's fast-charging capability.[22]

The related Li^+ chemical diffusion coefficient ($\tilde{D}_{\mathrm{Li}^+}$) is a crucial indicator for the evaluation of CAMs for fast-charging applications.[22] For example, layered sulfide-based CAMs with high $\tilde{D}_{\mathrm{Li}^+}$, for example, $LiTiS_2$ ($\tilde{D}_{\mathrm{Li}^+} = 10^{-8}$ cm^2 s^{-1}), also reveal superior rate performance.[220] The same relation can be also observed for layered oxides, where LCO reveals the highest $\tilde{D}_{\mathrm{Li}^+}$ ($\tilde{D}_{\mathrm{Li}^+} = 10^{-9}$ cm^2 s^{-1}) and best rate performance among this structure type of CAMs.[22,23] For NCM811, $\tilde{D}_{\mathrm{Li}}$ can reach 10^{-9} cm^2 s^{-1} at 50% SOC, while it is decreased for higher and lower lithiation degrees.[221] The Li^+ chemical diffusion coefficient can be improved, for example, by introducing concentration gradients of Ni, Mn, or Co in the NCM or NCA particles. For gradients of Ni and Co in NCM523 ($LiNi_{0.5}Co_{0.2}Mn_{0.3}O_2$), $\tilde{D}_{\mathrm{Li}^+}$ was increased by one order of magnitude.[222,223]

Recently, single-crystalline CAMs have been actively investigated since they can offer improved cycling stability compared to polycrystal-based secondary particles.[221,224,225] The increased particle size in the case of single crystals leads to significantly longer diffusion paths within the primary particles, however, decreasing the fast-charging capability of single crystals initially. During the lifetime of the battery cell, polycrystalline particles decompose faster, though, resulting in faster kinetics for single crystals after prolonged cycling.[225]

4.1.2. *Surface Modification of Cathode Active Materials*

In addition to the research on NCM cathode materials, a whole range of studies have attempted to meet the demand for fast-charging cathode materials either by modification of already-reported cathodes[223,226–234] or by the synthesis of new cathode materials.[235–238] The most common technique for modifying conventional cathode materials for fast-charging applications is through surface modifications. By changing the surface environment, researchers were able to enhance the Li^+ ion (charge) transfer during cycling and to get higher capacities during operation at high rates.[223,226–234]

LCO, one of the most commonly used cathode materials in rechargeable batteries used for portable electronics, has been the subject of such surface modification. Yasuhara et al., following previous research by Teranishi et al., were able to significantly improve the cyclability and high-rate chargeability of LCO cathode thin films by supporting them with ferroelectric $BaTiO_3$ nanodots.[226,227] The decoration of the cathode material surface with $BaTiO_3$ nanodots, which have a thickness of less than 3 nm, diameter of 35 nm, and less than 5% coverage, creates what the authors refer to as a "triple-phase interface" (TPI) (cathode–nanodots–electrolyte). This interface presumably enhances the Li^+ intercalation/deintercalation in its vicinity due to the formation of an "electric field concentration" by the high dielectric constant material $BaTiO_3$. Using this approach, the authors were able to obtain impressive capacity retention of more than 90% of the first cycle after 800 cycles at 5C. In a subsequent study, the group was able to determine a similar permittivity of the dielectric layer and the electrolyte as the underlying reason for improved charge transfer.[239] Analyzing bare LCO, LCO decorated with TiO_2, and LCO decorated with $BaTiO_3$, all resulting in different permittivity of the dielectric surface layer, in combination with electrolytes based on DMC (low permittivity) and EC:DEC (high permittivity), the authors found a correlation between the capacity retention at high charging rates (10C) and the dielectric constant of the dielectric layer. For DMC, the bare LCO surface exhibiting the lowest permittivity showed improved capacity retention. In the case of EC:DEC, the behavior was reversed, with $BaTiO_3$ (high dielectric constant) resulting in the highest capacity retention. This was explained with improved adsorption and desolvation on the dielectric layer compared to the bare LCO. For similar permittivity of dielectric and solvent, desolvation of Li^+ preferentially occurs at the dielectric surface, followed by diffusion to the TPI and transfer to the electrode. Thereby, even cycling at 50C was enabled.[239]

Another recent attempt at modifying the surface of LCO cathode material was reported by Wang et al.[228] In this study, the authors coated the LCO cathode material with $Li_{1.6}Mg_{1.6}Sn_{2.8}O_8$ showing a double-layer structure, which has similar oxygen packing to that of LCO and is inactive in the voltage window of the cathode. The $Li_{1.6}Mg_{1.6}Sn_{2.8}O_8$ coating was formed in situ on the surface of cathode particles using the reaction between SnO_2 and Mg-doped LCO. The coating improved the stability of the cathode surface by serving as a protective layer and increased the electronic conductivity by oxidizing some of the Co^{3+} in the pristine LCO and formation of mixing valence of Co^{3+}/Co^{4+}. The coated LCO exhibited better capacity retention than its uncoated counterpart under high-rate cycling and retained a capacity of 175 mA h g^{-1} at 10C (upper cutoff potential 4.5 V).

One frequently used cathode material that has been subjected to various surface modifications for the purpose of achieving superior rate performance is spinel-structured LNMO. MgF_2, ZrO_2, SiO_2, and V_2O_5 coatings have been proven to be beneficial for the rate capability and cycling stability of LNMO.[229–232] Wu et al. showed by analyzing dQ/dV plots that MgF_2 coating of LNMO reduces the electrode polarization. This phenomenon, in their opinion, may explain the observed facilitation of ion transfer through the cathode–electrolyte interface. Their calculations of the apparent chemical diffusion coefficient agree with their dQ/dV analysis and suggested that the coated cathode has better kinetic properties than the uncoated one.

4.1.3. *Effects of Morphology*

Morphology or "dimension" modification is another common approach to improve the high-rate performance of well-known cathode materials. For example, LiV_3O_8 cathode material has shown better high-rate capabilities with the morphology of nanowires and nanorods compared to the conventional nanoparticle cathode structure.[233,234] Xu et al. synthesized LiV_3O_8 nanorods with a diameter of (0.5–1.0) µm and a length of (4–8) µm using the nonionic triblock surfactant Pluronic-F127 as a structure directing agent. The nanorod structure of the particles of the cathode assisted in having faster kinetics of Li^+ ion transfer that result in a better rate performance and cycling stability compared to particles with the nanoparticles structure. Thanks to that, the LiV_3O_8 nanorods exhibited a capacity of 138.4 mA h g^{-1} at high current density of 6.4 A g^{-1} (≈21C). Also, common NCM cathode material can be improved for better operation at high rates when using a nanorod structure.[223] Noh et al. prepared NCM with a full concentration gradient of Ni and Co within the rod-shaped particles, while the Mn concentration was kept constant throughout. Thus, the Li^+ chemical diffusion coefficient could be increased by one order of magnitude compared to conventional NCM523, improving the discharge capacity from 136 to 155 mA h g^{-1} at 5C. Similar experiments were performed on NCA.[222] Introducing concentration gradients of Ni and Mn in the material also led to rod-shaped primary particles, improving the reversible capacity and capacity retention.

4.1.4. *Development of New Cathode Active Materials*

Another recent strategy to obtain Li-ion batteries that are suitable for fast-charging is the development of novel organic cathode materials, with the advantages of being transition metal free and mechanically flexible.[235] In a recent study, Otteny et al. demonstrated that factors such as the polymer structure, the amount of π-interactions between redox-active groups, and the morphology of the composite electrode have a significant impact on the rate capability and cycling performances of phenothiazine-based polymers.[236] Their study shows that directly linked poly(3-norbornylphenothiazine) cathode material, with a redox potential of 3.5 V versus Li^+/Li, had good cycling stability and rate capability. It reached a maximum specific capacity of 64 mA h g^{-1} after 850 cycles at 100C rate, and retained 73% (47 mA h g^{-1}) of this capacity after 10 000 cycles, which is 55% of the theoretical value. The same group reported a cross-linked phenoxazine poly(vinylene) as cathode active material. This organic CAM has a high discharge potential of 3.52 V versus Li^+/Li.[237] After 10 000 cycles at 100C rate, a capacity of 70 mA h g^{-1} was still obtained (74% of the first discharge capacity at 100C and 58% of the theoretical value).

Conductive metal-organic frameworks (MOFs) with redox metal centers are another class of materials that have been considered as potential cathode materials and might be suitable for fast-charging capabilities.[235] Gu et al. investigated the MOF $Cu_3(2,3,6,7,10,11\text{-hexahydroxytriphenylene})_2$ as a cathode material for Li-ion batteries.[238] This MOF, with the Cu^{2+}/Cu^+ redox center responsible for the Li^+ ion accommodation between the layers, has intrinsically high electrical conductivity and exhibits an open porous layered framework that makes it efficient for Li^+ ion transfer during cycling at high rates. At a rate of 20C, the MOF cathode had a capacity of 85 mA h g^{-1} after 500 cycles with capacity retention of 85%.

4.2. Limitation of Fast Charging on Electrode Level

While e$^-$ transport proceeds mainly through the CAM and the conductive carbon toward/from the Al current collector,[240] Li$^+$ transport pathways are more complex and proceed through the bulk electrolyte, the electrolyte-soaked composite electrode, the CEI, and CAM including intertwined charge-transfer processes as shown in Figure 10.[22] The rating of each aspect according to its relevance and significance for the total internal resistance, thus for the fast-charging capability, is discussed as follows.[22]

A relevant contribution of the e$^-$ pathway to the cell resistance can rather be excluded.[22,23,241] The intrinsic electronic conductivity of common layered oxide based CAMs like NCM is between (10^{-3} and 10^{-5}) S cm^{-1}, which depends on the SOC under normal operation and composition of the transition metals.[23,242] After the addition of already small concentrations (w = 1%) of conductive agent, for example, conductive carbon, the electronic conductivity of the cathode composite increases up to 10^{-1} S cm^{-1}, which is two orders of magnitude higher than the ionic conductivity of common organic solvent based electrolytes, thus sufficiently high.[21,22,243,244] The relevance of the electrolyte conductivity on internal resistance and fast charge aspects will be discussed in Section 5.[22] An insightful additional proof for the negligible kinetic limitation due to electronic conductivity is the well-known example of the addition of Co to $LiNiO_2$, thus the formation of $LiNi_{0.8}Co_{0.2}O_2$.[23] Even though the electronic conductivity of the resulting material decreases by an order of magnitude, the rate performance increases and demonstrates that other factors are relevant for fast charging, which will be discussed in the next sections.[23,245]

According to literature, the impact of the cathode composite characteristics (e.g., porosity, mass fraction of inactive materials, mass loading, etc.) on the Li$^+$ transport is not as important as it is for anodes.[21,22] The porosity as a crucial parameter for the density of Li$^+$ pathways within composite electrodes is minimized via calendaring for reasons of improved mechanical and energy density aspects.[246] Despite calendaring, rate performance is only affected for porosity values below 20%, and this only if combined with high CAM loading > 30 mg cm^{-2} (roughly corresponding to >5 mA h cm^{-2}). This combination of electrode properties is, however, far from application.[21,212,247] Moreover, the inactive materials can theoretically have an impact on Li$^+$ transport and be kinetically problematic, but only below a conductive carbon to binder ratio of 0.6:1 and at inactive material mass loadings greater than 5% (relative to the active material amount), which is both not the case in present LIBs.[243]

Finally, aspects related to Li$^+$ transport within a CAM, for example, material, particle size, particle morphology, etc., should also be of particular focus for fast charging. It is speculated that the crystal structure and associated Li$^+$ diffusion may be stressed in the course of fast charging via inhomogeneous delithiation and accompanied phase changes.[248] These inhomogeneities can lead to secondary and primary particle cracking with an undesired raise of CAM surface, that is, electrolyte contact, which can affect the internal resistance and the fast-charging behavior,[249] as will be discussed in Section 5. Crack formation increases with the SOC, the Ni content, and, just like for anodes,[142] the size of the secondary particles.[250]

It should be also noted that fast charging may also have a beneficial effect on cathode stability as it counteracts undesired crystal-intrinsic decomposition by a shorter time for the thermodynamic-driven phase changes of layered oxides at higher SOC. As shown in **Figure 13**a for NCM111, when charged to equal SOC (e.g., an 85% Li$^+$ extraction ratio), the specific capacity losses are lower after faster charge. A similar relation can be deduced for the charge/discharge cycling performance of NCM111, as shown in Figure 13b. The CAM obviously remains more stable during faster charge than during slower charge and this considerably affects the subsequent cycling performance, when again, equal charge conditions are used. As shown in Figure 13b, the specific charge current variation in the initial three cycles has a significant impact on subsequent cycle life under high-voltage conditions.[251]

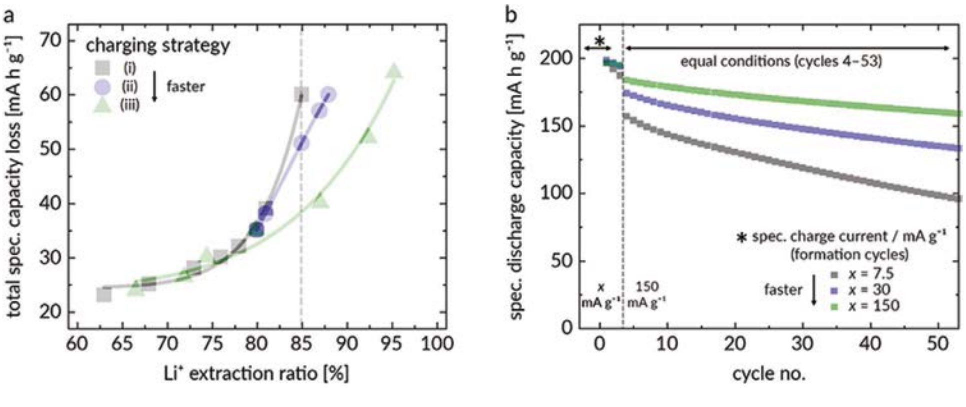

Figure 13. a) Specific capacity losses of the initial charge/discharge cycle versus the Li$^+$ extraction ratio of NCM111. The faster the charge, the lower the specific capacity loss. Adapted with permission.[22] Copyright 2016, IOP Publishing. b) Specific discharge capacities as a function of cycle number of NCM111, with three formation cycles followed by charge/discharge cycling at 150 mA g^{-1} (≈1C). The variation of the specific charge current only in the formation cycles has a significant influence on the subsequent cycling performed under equal conditions, that is, fast charge during formation leads to better performance. Adapted with permission.[251] Copyright 2017, Elsevier.

5. Electrolyte

5.1. Liquid Electrolytes

Among the different electrolyte systems currently under consideration for LIBs, liquid organic solvent based electrolytes show a most favorable combination of cost and performance properties.[252] The (total) ionic conductivities of state-of-the-art liquid electrolytes, that is, 1.0 mol L^{-1} $LiPF_6$ in a solvent mixture based on EC and linear carbonates like DMC, DEC, and/or ethyl methyl carbonate (EMC) reach values of up to 10^{-2} S cm^{-1} at room temperature (RT).[253] While t_{Li^+} typically is only between 0.2 and 0.4,[253] resulting in an Li^+ conductivity of less than half of the total conductivity, these values are more than sufficient for LIB application at RT and below. Even decreasing the concentration down to 0.2 mol L^{-1} $LiPF_6$, the ionic conductivity is still 3 mS cm^{-1}.[244] As shown in **Figure 14**a for NCM111, no changes in charge/discharge behavior can be deduced for different salt concentrations, also at faster charge conditions. The charge profiles remain similar, that is, without additional overpotentials at lower salt concentration, which demonstrates that not the bulk ionic conductivity of the electrolyte within the separator but rather other cell parameters are rate-determining, as discussed in Sections 3 and 4.

However, at the anode side, transport in the electrolyte is considered the rate-limiting step, as already overpotentials < 100 mV induce lithium plating. Such overpotentials are easily achieved if the current density approaches j_{lim}. Gallagher et al. observed cell failure of NCM622/graphite full cells due to lithium plating at currents > 1C for approximately the targeted capacity of 3.3 mA h cm^{-2} and an N/P ratio of around 1.2 (**Figure 15**a).[151] Based on Equation (38), we calculated j_{lim} for such cells, assuming an ion transference number of 0.4, lithium-ion concentration of 1 mol L^{-1}, separator—and thus electrolyte—thickness of 30 µm and diffusion coefficients in the range (1–5) × 10^{-6} cm^2 s^{-1}, which represents the typical range for diffusion coefficients of concentrated lithium electrolytes. If the porosity is between 30% and 40% (typical values), β would be 5–10 for realistic electrodes.[47] Therefore, according to Figure 15b, the target current density of 12 mA cm^{-2} (4C) would be around the limiting current. We note that according to Equation (40) the overpotential is quite substantial even below the limiting current. Therefore, although 4C charging would be possible, the high overpotential would result in lithium plating at the anode.

The reason behind this is that although high currents are possible, the reaction becomes confined at those parts of the electrodes that are easily accessed by the electrolyte (i.e., close to the separator). The lithium-ion concentration in the electrolyte of those electrode regions, which are hardly accessed by the electrolyte (i.e., close to the current collector) is depleted.[152] This confinement of the reaction leads to a substantial local potential drop. Therefore, growth of lithium dendrites is mostly observed originating from the tip of the graphite electrode. Hence, we assume that lithium plating as a result of reaction confinement in the anode is the rate-limiting step in practical battery full cells. A strategy to overcome such issue would, for example, involve a higher lithium diffusion coefficient (or also lithium-ion transference number) as this lifts the limiting current density significantly. Such issue can also be circumvented by increasing the temperature during cell charging. Another possibility is the application of a porous layer in contact to the electrode, of which the surface is functionalized with groups exhibiting high Li^+ affinity. Thus, the concentration of Li^+ within the pores is increased, reducing concentration polarization in the electrolyte. Additionally, electrokinetic effects, such as electroosmosis and surface conduction, enhance Li^+ transport within the pores, significantly increasing the limiting current density, which enables cycling at higher rates.[254]

Besides ionic conduction in the bulk, the electrolyte may impact the internal resistance of the cell also in other ways, in particular via charge-transfer processes at the interfaces as detailed in Section 2.1.2. It is known from the anode side that the intercalation of Li^+ into, for example, graphite during the

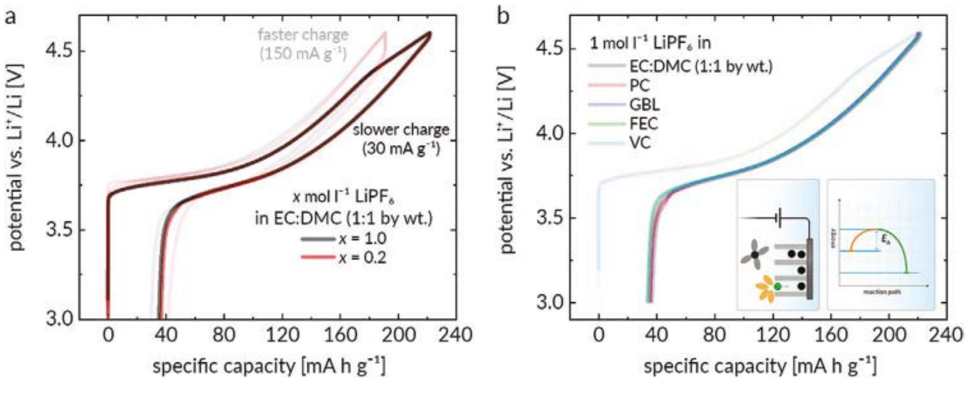

Figure 14. a) Initial charge/discharge cycle of NCM111 at different specific currents using an electrolyte with a conventional Li salt concentration (1.0 mol L^{-1}), and a decreased Li salt concentration (0.2 mol L^{-1}), thus decreased ionic conductivity. The charge profile is similar for both Li salt concentrations, even for elevated specific currents, which points to a rather insignificant impact of the electrolyte bulk ionic conductivity on internal cell resistances. b) Initial charge/discharge cycle of an NCM111 electrode using $LiPF_6$ in various solvents and solvent mixtures. A possible solvent impact on the charge performance, that is, delithiation kinetics, cannot be noticed. The impact of the cation desolvation process on performance, at least for the used cathodes, appears also negligible as the discharge curves behave similar. Still, any effect of kinetically hindered desolvation should not be disregarded during charge of anodes. Adapted with permission.[22] Copyright 2016, IOP Publishing.

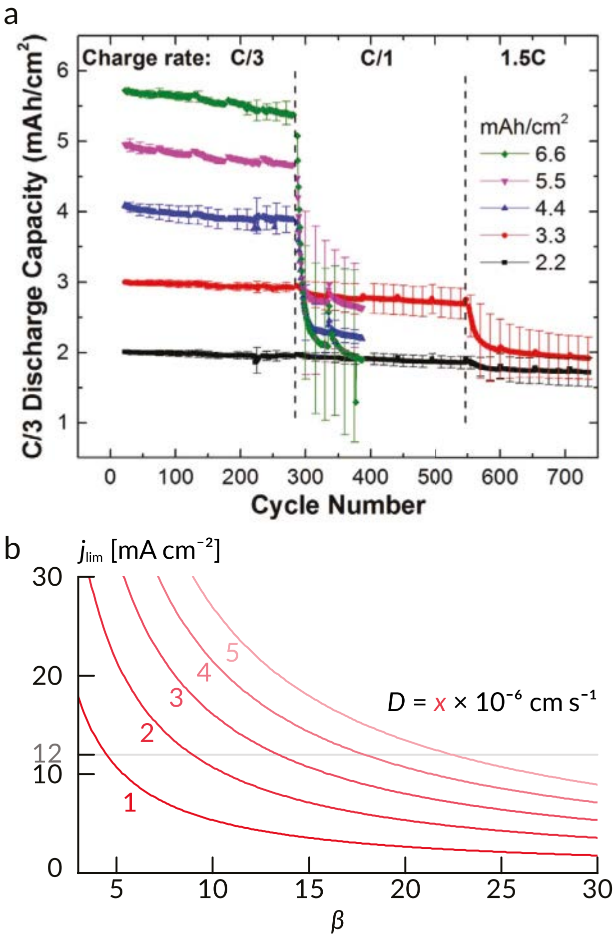

Figure 15. a) Capacity of NCM622/graphite full cells with different loading of active material (N/P ratio of around 1.2). Upon increasing charge rate, cells with high loading fail as a result of lithium plating. Reproduced under the terms of the CC BY-NC-ND 4.0 license.[151] Copyright 2016, The Authors. Published by IOP Publishing, Ltd. b) Diffusion-limited current density j_{lim} as a function of the electrode structure (parameter β) and with different chemical diffusion coefficients calculated from Equation (38) based on the experimental parameters of the cells shown in (a).

charge process requires Li^+ desolvation from the solvent shell, which is regarded as a rate-determining process during charge (see Section Barriers for Migration of Li^+ Ions from Electrolyte into Anode Active Materials).[78,255] In the typically used carbonate solvent based electrolyte mixtures, naturally the highly polar EC is the preferable solvating solvent component. Moreover, given its large activation energy (E_A) values, the Li^+ desolvation process is also assumed to contribute to internal resistances of the cathode, though in this case in the discharge process.[75,77,256] These conclusions are drawn from theoretical considerations.[257] It is claimed, that the kinetics of Li^+ desolvation sensitively depends on the coordination strength of Li^+ with the respective solvent molecules constituting the solvent shell.[258]

To check this claim under practical experimental conditions, $LiPF_6$ dissolved in various solvents including γ-butyrolactone (GBL), propylene carbonate (PC), fluoroethylene carbonate (FEC), and vinylene carbonate (VC) was investigated with respect to overpotentials on the cathode side.[22] The discharge curves display similar shapes for all electrolytes as shown in Figure 14b. In addition, also any solvation effects during charge on the kinetics can also be excluded on cell level as also the charge profile behaves similar for all investigated solvents.[22] The salt, however, can have an influence on charge transfer as a recent study indicates.[259] Thereby, the addition of lithium bis(trifluoromethanesulfonyl imide) (LiTFSI) to $LiPF_6$ in DMC electrolyte increased the cathode exchange current density by about two orders of magnitude. Thus, the charge-transfer resistance was decreased to 6% of its value without LiTFSI. Using molecular dynamics simulations, the $TFSI^-$ anions were found to preferentially solvate Li^+, which—combined with the lower binding energy to the Li^+ ion—enables faster interface kinetics.[259] Thus, different conducting salts next to (or in combination with) conventional $LiPF_6$ are worth investigating.

Finally, the impact of the electrolyte at electrode|electrolyte interfaces in LIB cells will be discussed.[22,260] On graphite-based anodes, the electrolyte electrochemically decomposes and forms a protective layer, the SEI.[261] Its chemical composition and thickness significantly contribute to the internal resistances, which thus can be significantly tailored via reasonable electrolyte formulation, for example, via electrolyte additives.[246,262] For graphite anodes with $LiPF_6$ in a mixture of EC, EMC, and methyl propionate (MP), the addition of lithium bis(fluorosulfonyl)imide (LiFSI) reduced the charge-transfer resistance and activation barrier of the SEI compared to the pure solvent mixture, for example.[263] Another method is changing the solvent. A recent study used 1,4-dioxane, which is only weakly solvating while still retaining sufficient solubility for the LiFSI conducting salt. Thereby, ion pairs prevail even at low salt concentration leading to a mainly inorganic SEI, which offers fast interfacial charge transfer and high stability, improving the fast-charging capability.[264]

In contrast, the CEI, particularly on commonly used layered oxide based cathodes (e.g., NCM, NCA, LCO)[265] considerably differs from the SEI. Organic carbonate-based electrolytes are more oxidatively stable than commonly believed[215,216,251,265–269] However, the CEI composition and behavior on the cathode is affected by the so-called “native” cathode surface, which exists prior to application in form of Li_2CO_3 and/or LiOH.[216,217,253,266–270] Alteration of the CEI can already proceed after simple electrolyte contact, particularly at elevated temperatures, thus in a chemical manner, in addition to CEI formation by electrochemical oxidation of instable electrolyte components.[271,272] As mentioned in Section 4, Li^+ transport within the CAM is the rate-limiting step in/at the cathode. Nevertheless, the impact of the CEI on performance can get significant during cycle and calendar life in the course of aging and can be tailored via the electrolyte.[272]

5.2. Inorganic Solid-State Electrolytes

Solid electrolytes behave quite different compared to liquid electrolytes when it comes to fast charging. As typical polymer electrolytes show relatively low lithium-ion conductivity, they are hardly suited for fast-charging applications and we focus on inorganic solid electrolytes (ISEs) in this section. Typically, ISEs exhibit single-ion conduction, due to the rigidity of the anion polyhedron framework. Thus, lithium transference numbers are almost equal to unity, assuming electronic charge transport can be neglected. Although the ionic conductivity of most ISEs is lower than the total ionic conductivity of liquid electrolytes (10 mS cm^{-1}), their single ion conducting character makes them competitive. The conductivity of a specific charge carrier is obtained by the product of the respective transference number and the total conductivity. Assuming a transference number of $t_{\mathrm{Li}} = 0.4$, the lithium-ion conductivity of liquid electrolytes amounts to about 4 mS cm^{-1}. This value has already been achieved and even surpassed by several ISEs, such as $Li_{9.54}Si_{1.74}P_{1.44}S_{11.7}Cl_{0.3}$,[68] $Li_{6.6}P_{0.4}Ge_{0.6}S_5I$,[273] and $Li_{6.6}Si_{0.6}Sb_{0.4}S_5I$.[274] Complementary to a higher single-ion conductivity, no concentration polarization effects are observed in inorganic solid electrolytes (compare Section 2.2.2). At high current densities, which are a necessity to enable fast charging, the contribution of the overpotential $\Delta\varphi_{\mathrm{EL}}$ that originates in the motion of ions in the solid-state electrolyte follows Ohms law, that is, Equation (42).

Superionic solid electrolytes show no anion migration and typically have very high charge carrier concentrations, which leads to a deviation from the Nernst–Einstein equation. The migration of the lithium ions takes place simultaneously throughout the whole material. This can also be described in terms of cooperative transport processes.[275] Inorganic solid electrolytes are either ceramics, glasses, or glass-ceramics, which makes them much more stable at higher temperatures than liquid electrolytes based on carbonates and other organic solvents. This is a key advantage, as higher operating temperatures can be achieved.

The ionic motion in solid electrolytes is based on the migration of lithium ions through empty lattice sites (vacancies) or interstitial sites. In ceramic solid electrolytes, these lattice sites are usually either tetrahedrally or octahedrally coordinated. For this migration, an activation energy has to be provided, to overcome the binding energies of the stable ground state. Consequently, the ionic conductivity follows an Arrhenius-like behavior, resulting in an increased ionic conductivity at higher temperatures. Fast charging of Li-based solid-state batteries can thus be accelerated by an increased temperature during charging. Typically, Joule heating already increases the temperature within an LIB if high current densities are provided.[276] To avoid uncontrolled decomposition and evaporation of the liquid electrolyte, advanced cooling systems have to be employed, decreasing the specific energy and power density. These cooling systems might be omitted in solid-state systems, because the increasing temperature may not only be not harmful, but it may further accelerate the charging, due to increased ionic conductivity of the solid electrolyte. Overpotentials originating from the solid electrolyte itself can, therefore, easily be reduced to a bare minimum. Kato et al. reported by using a superionic conductor that SSB cells could be cycled at temperatures as high as 100 °C repeatedly, as is depicted in **Figure 16**. Additionally, discharge rates of up to 1500C (discharging in 2.4 s) were demonstrated.[68] Although the experiments were conducted at 100 °C and only showed the high discharge capability, they also demonstrated that extremely high current densities (1 A cm^{-2}) are enabled by ISEs.

Additionally, solid electrolytes do not suffer from low temperature phase transitions, which might result in the solidification of liquid electrolytes. Choi et al. could show that even at the deep freezing conditions of −30 °C, thiophosphate-based solid electrolytes can provide sufficient ionic conductivity to operate an SSB cell.[277]

5.2.1. Solid Electrolytes in Composite Cathodes

On the cathode side, the charge-transfer resistance between, for example, NCM and SEs is a problem, since it is increased compared to LEs by one order of magnitude.[48] This is a result of irreversible degradation reactions at the interface between CAM and SE (CEI formation).[48,278] Another disadvantage of solid electrolytes is their rigidity, resulting in decreased contact between active materials and solid electrolytes. While liquid electrolytes can easily infiltrate the porous composite cathodes, particularly ISEs do not exhibit a “wetting” behavior of the CAM surface.[48] This makes, for instance, processing quite challenging, as good interfacial contact is a necessity to reduce interfacial overpotentials. Not only the charge-transfer resistance will be influenced, but also the diffusion within the cathode active material itself becomes limiting, as extraction of lithium ions can only take place at a few contact points. This behavior most likely becomes even worse over the course of cycling. Cracking of the active material can be caused by electro-chemo-mechanical stresses.[279] Reasons can be gradients in lattice parameters due to different Li-ion concentrations in the bulk and at the surface of the cathode active materials. While a liquid electrolyte can penetrate the newly formed cracks and, thus, further decrease ionic diffusion lengths, a solid electrolyte cannot do the same.[221] It may hence be necessary to inhibit cracking of the cathode active material, for instance by transitioning from secondary particles to single crystals, especially when aiming for high Ni compounds. Another factor influencing the fast-charging behavior of solid-state composite cathodes is the microstructure of the cathode. As mentioned above, a liquid electrolyte can easily penetrate pores of the cathodes. Here, the viscosity of the liquid as well as the wetting angle of the solid–liquid interface are important material properties. While these material properties may, within certain boundaries, be used in solid polymer electrolyte systems, they do not apply to ISE systems. Here, good mixing of the powders is essential to achieve sufficient charge transport pathways.

In an ideal microstructure, both, ionic and electronic pathways, are percolating throughout the whole composite cathode. This means that tortuosity factors, which correlate volume fractions and bulk conductivities of the participating components to the effective total conductivity, are as low as possible. Numerous studies have targeted the microstructure of solid-state composite cathodes.[280] Kaiser et al. used electrochemical as well as tomographic methods to investigate the ionic charge transport within thiophosphate-based composite cathodes. They found that composition of the composite cathode plays a central role for total ionic conductivities and will thus strongly influence the fast-charging behavior of SSBs.[281,282] Recently, Shi et al. determined that the ratio between ISE particle size and CAM particle size is crucial for an improved rate performance.[283] In general, it

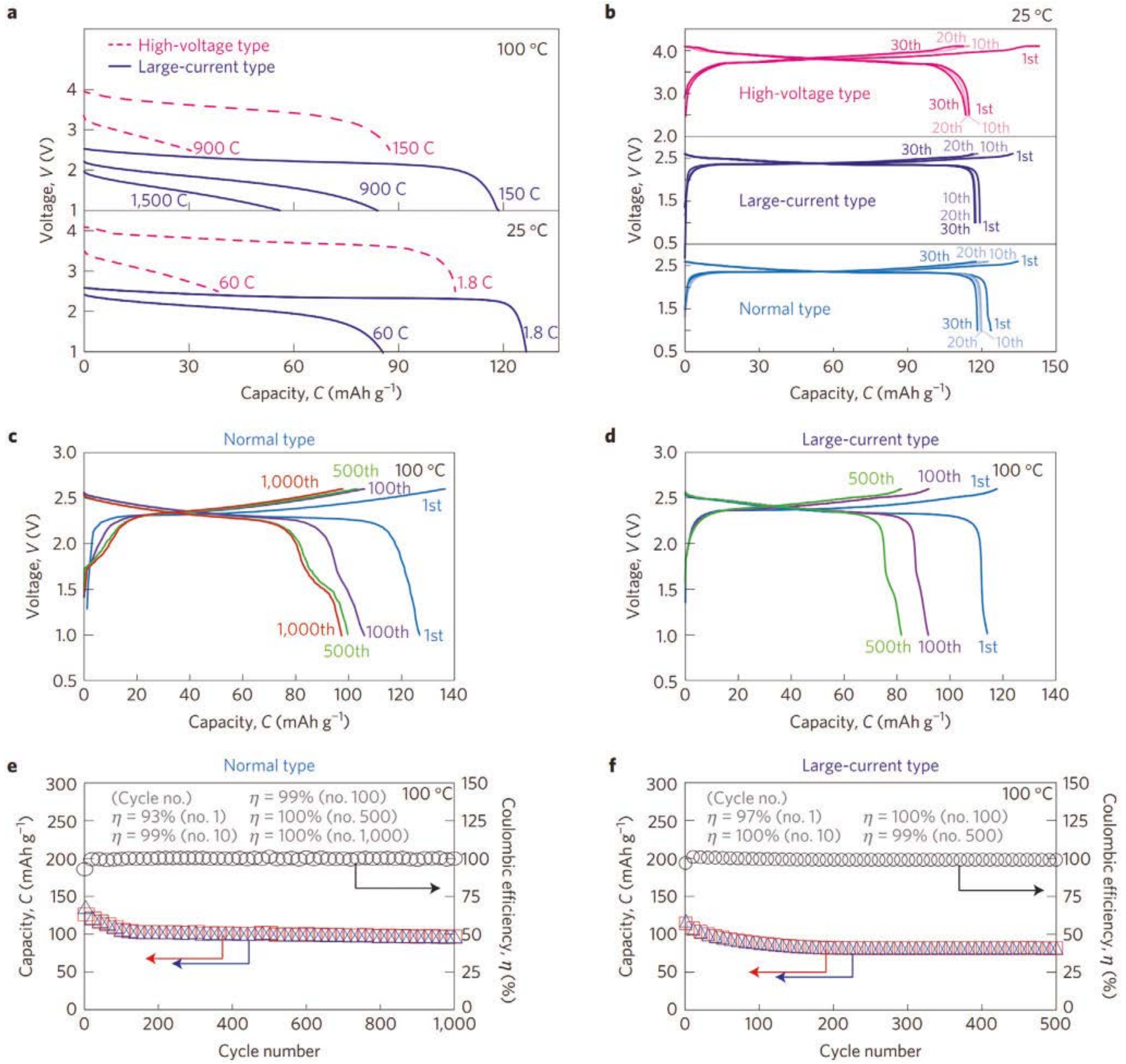

Figure 16. Solid-state battery performance at 100 °C. The high temperature increases the ionic conductivity without increasing safety hazards. C-rates of 1500C have been demonstrated, enabled by a superior temperature stability at 100 °C (discharge in 2.4 s). a) Comparison of discharge curves at (25 and 100) °C. b) Charge and discharge curves at 0.1C and 25 °C. Charge and discharge curves at 18C and 100 °C for c) normal-type and d) large current type cells. Development of Coulombic efficiency (black) as well as discharge (red) and charge (blue) capacity at 100 °C as a function of cycle number for e) normal-type and f) large current type cells, respectively. Reproduced with permission.[68] Copyright 2016, Springer Nature.

can be assumed that the ionic tortuosity of SE-based composite cathodes is higher than in LE-based ones.[16,282,284] As a consequence, the ionic conductivity of the solid electrolyte needs to be higher than that of the liquid electrolyte. **Figure 17** displays that ionic conductivities of more than 10 mS cm^{-1} are necessary for fast charging a simulated solid-state cathode with a tortuosity of $\tau = 2$ and an active material content of $\varphi = 70\%$.[71]

Clearly, high ionic conductivities of more than 10 mS cm^{-1} are necessary in order to achieve high rates (>4C) and simultaneously high energy densities, meaning thick cathodes and high-power densities, meaning low overpotentials. Recently, Minnmann et al. reported high tortuosity factors for both ionic and electronic conduction in thiophosphate/NCM based cathode composites, demonstrating that the effective ionic conductivity in cathode composites can be much lower than the bulk electrolyte conductivity.[70] It is, therefore, crucial to improve the tortuosity of solid-state cathodes as well as to increase the (bulk) ionic conductivity.

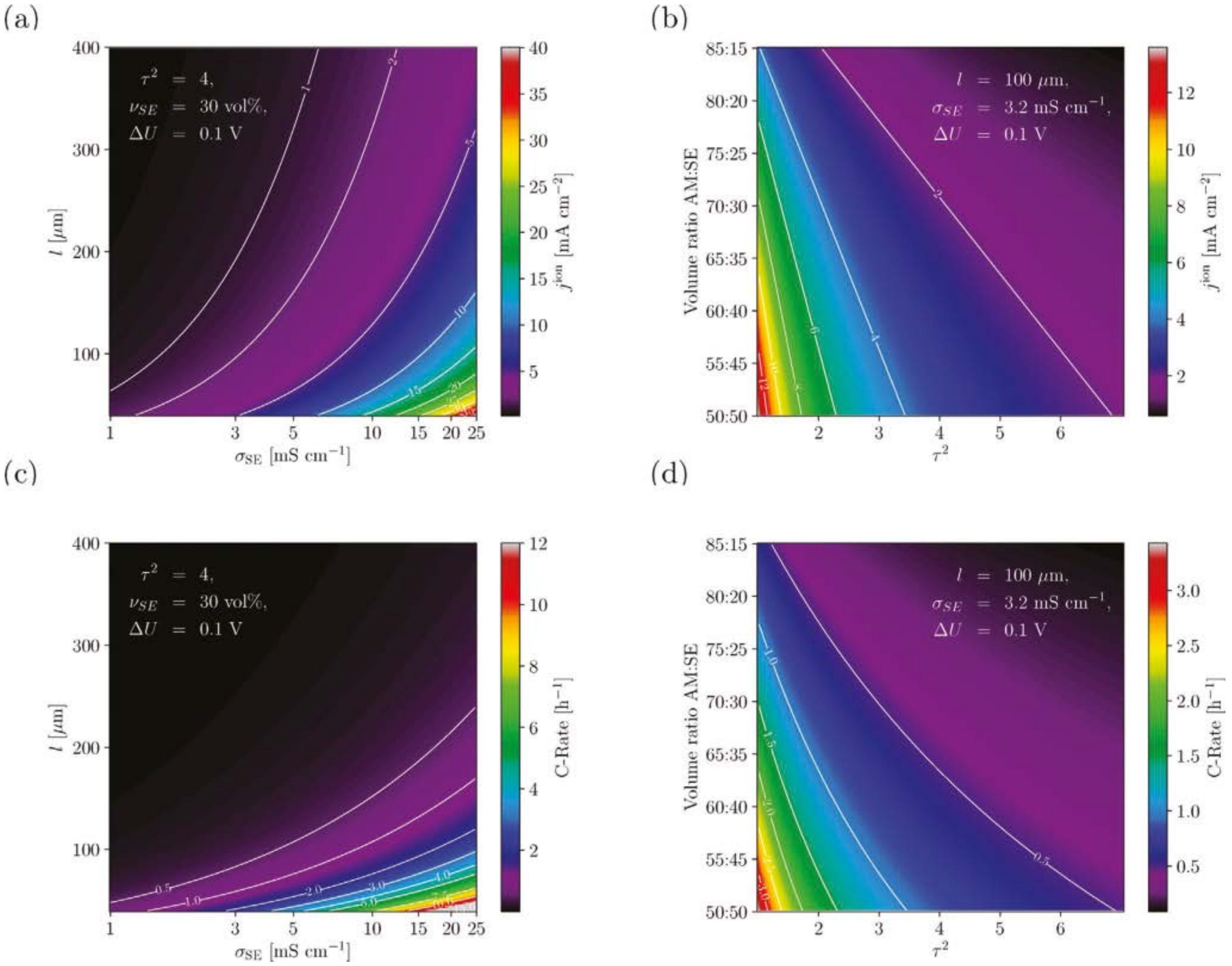

Figure 17. Simulated areas of fast-charging capability for thiophosphate-based composite cathodes with a,c) varying thickness and ISE conductivity as well as b,d) CAM volume fractions and tortuosity factors. The colors represent the area of a certain current density (a, b) and C-rate (c, d), respectively. For the fast-charging capability, a maximum allowed overpotential of 100 mV is assumed. Reproduced with permission.[71] Copyright 2020, American Chemical Society.

5.2.2. Contact between Solid Electrolytes and Anodes

Fast charging requires the implementation of an anode material with low charge-transfer resistance and, ideally, no diffusion limitation. Typically, LMAs are considered as the most desired concept, as they provide the highest energy and power density that can be achieved. Recently, Krauskopf et al. could demonstrate that the interfacial charge-transfer resistance between an LMA and the solid electrolyte $Li_{6.25}Al_{0.25}La_3Zr_2O_{12}$ (LLZO) is negligible.[285] This would make LMAs also favorable for fast charging, as the charge-transfer overpotentials will be minimal and no incorporation into a host material is necessary. However, LMAs have several other issues that need to be overcome. Contrary to a liquid electrolyte, it is necessary to provide and maintain a good mechanical contact between the solid electrolyte and the LMA. It is evident that decreasing contact area will increase the area specific resistance (ASR) of the cell ultimately influencing the overpotential. Because ISEs are typically (sintered) powders, a certain roughness toward the LMA will always remain. It is, thus, essential to achieve a good uniform contact by plastic deformation of either the ISE, the LMA, or both. Additionally, stack pressure becomes important in order to remain a good contact upon lithium removal and plating. However, Doux et al. reported that high stack pressures could also lead to mechanical failure of the cell, since lithium can creep through the solid electrolyte.[286] The influence of stack pressure is not fully resolved yet and is still discussed. Influential factors, such as solid electrolyte morphology, mechanical properties, and thickness of the employed lithium metal anode have to be considered.

Fast charging means cathodic load. Hence, lithium is removed from the cathode and plated at the anode side. Ideally, this process produces a homogeneous and even surface. However, high current densities, which are a feature of fast charging, often result in inhomogeneous Li deposition and dendrite formation takes place. ISEs have the advantage to provide a "mechanical resistance" to dendrite growth, making Young's modulus, fracture toughness, and shear modulus important parameters. Recently, porous solid electrolytes were reported to show increased dendrite resistance by drastic reduction of the current density, which was caused by an increased contact area between lithium and ISE.[287] Krauskopf et al. have published a detailed review on the physicochemical concept of lithium metal anodes, in which all major concepts are being discussed.[90]

6. Limitation and Improvement of Fast Charging on Cell Level

Limited heat dissipation and conventional CC–CV charging hinders fast-charging applications on the cell level. The operating temperature strongly affects the energy, capacity, reliability, and durability of the batteries. High temperatures accelerate capacity degradation and shorten battery life.[162,288] Various studies presented the (25–40) °C range as optimum temperature to achieve the best LIB performance.[38,177,289] When high rates are required, efficient thermal management systems (TMS) are essential due to the massive heat produced, especially at high ambient temperatures.

Ye and coworkers performed numerical modeling predicting the temperature reached by a battery undergoing a charging process at 10C when thermal contact resistance is taken into consideration. When a liquid cold plate cooling system is applied in the simulation, the maximum battery temperature may reach 64.6, 38.2 °C higher than the case without thermal contact resistance.[290] The transfer of Li^+ ions across the activation energy barrier at the electrode interface results in a loss in the kinetic energy contributing to (30–40)% of the heat losses under practical operation conditions.[291]

So far, three different categories of TMSs were studied, including air cooling, liquid cooling, and phase change materials (PCMs) cooling systems.[292] Recently, advanced systems were developed in order to overcome the increasing need for high battery operation rates. Silica liquid cooling plates (SLCP) attached to both sides of a Li-ion battery were tested as a heat dissipation system for high-current systems. A various number of channels were investigated while applying different discharge C-rates. It was concluded that an increased number of channels manages to keep the maximum temperature inside the cell below 39.1 °C (Discharge rate of 3C and liquid flow rate of $0.1\ m\ s^{-1}$).[293]

Furthermore, an innovative fast-charging Li-ion battery pack that combines both liquid cooling and PCM cooling has presented promising simulation results. The temperature of an 8C charging process was maintained at a maximum value below 40 °C. In this case, the PCM heat adsorption accounts for less than 10%, while the liquid cooling takes 80% of the general heat.[294]

The extended charging time required for the Li-ion battery nowadays compromises their popularity in the automotive industry worldwide. A typical charging process is conducted using a constant current (CC) step followed by a constant voltage (CV) one.[295] Lithium metal deposition on the anode surface is prone to occur when increasing the current applied during the fast-charging process due to the significant polarization formed on the electrode|electrolyte interface.[7] Although the time required to reach the cut-off voltage decreases while increasing the applied current, more time will be necessary to obtain the desired current value during the CV phase. Therefore, the charging time is not significantly reduced.[296]

Innovative charging procedures such as pulsed or tapered current techniques were studied to decrease the concentration polarization.[296–299] By doing so, better utilization of the active material along with shorter charging time and increased cell life can be achieved. Different charging models considering the ion concentration on the electrode surface alongside the degradation processes taking place during cycling have reduced the charging time by (60–70)% compared to the classical CC–CV charging technique.[105,295,297]

Lu et al. presented a charging method that takes into consideration the stress induced in electrode particles by diffusion, which later on may result in mechanical failure and a considerable effect on the battery's electrochemical performance. An exponential current (EC) method where the charging process initiates in a maximum current density, followed by an exponential continuous decrease, avoiding any sudden changes, was found to prevent stress undulation in addition to acceleration of the charging process. Due to the direct connection between the stress evolution and the heat generated in the cell this method could also improve the battery's thermal performance.[300]

The impact of different pulse charging protocols was evaluated in various studies while considering the electrolyte polarization, stress evolution, heat generation, and the battery cycle life.[299,301] Most studies presented an improved battery performance, higher cycling number, and slower battery aging and degradation process than the conventional CC–CV charging method. Therefore, the charging protocol can significantly affect the overall battery performance, especially when a short charging period is required.

7. Conclusions

In this review, we focus on the issues hindering fast charging of today's LIBs from a physicochemical and materials' point of view. Complemented by an overview of studies analyzing different cells regarding their fast-charging ability, a detailed picture of the requirements for fast-charging enabling materials is drawn. Fast Li ion diffusivity in the active materials is identified as one of the major factors needed for fast charging. Improved anode materials should offer low barriers for migration into them as well as for diffusion within the material itself. Thus, lithium plating—a major obstacle observed on graphite anodes—can be reduced as well. Once diffusion is not fast enough, particle size becomes an important factor in enabling fast charging, partially able to counteract low lithium diffusivity. For active materials with strong diffusion anisotropy, like, for example, the layered compounds, the particle morphology becomes another important factor, and particle morphology control may lead to faster charging rates on the material level. This leads to the electrode level, where a particular microstructure with low tortuosity factors and optimized porosity balancing both, electronic and ionic conductivity, is needed.

For the cathode, a slightly different behavior is observed. While the characteristics of the cathode composite do have a certain impact on the electrode's fast-charging ability, for application-relevant cathode composites their influence is small. Instead, the characteristics of the CAM itself were identified to greatly affect cathode overpotentials, in line with the varying Li$^+$ chemical diffusion coefficients and crystal structures of different CAMs. In addition, phase changes depending on SOC have to be considered, since state-of-the-art layered oxides like NCM undergo a phase transition with changing lithiation degree, for example.

Transport within the bulk liquid electrolyte was found to play a less important role in determining a given battery cell's fast-charging ability. Its ionic conductivity is high enough to not slow down lithium transport nearly as much as the electrodes. At those, specifically at the anode side, transport in the liquid electrolyte becomes rate-limiting, though. For typical electrode properties, the current density targeted for fast-charging applications is close to the limiting current density. This causes a high overpotential leading to lithium plating at the anode. In addition, the compatibility of the electrolyte with active materials is of interest, as degradation occurs on both, the anode and the cathode side, leading to SEI and CEI formation, respectively. Thereby, the SEI properties can be tuned by the electrolyte composition, allowing for optimization regarding low charge-transfer resistances. For solid electrolytes, the limited ionic conductivity—resulting from high tortuosity and contact issues—does become an issue, though. Therefore, also the microstructure of the cathode composite gets increasingly important when applying solid instead of liquid electrolytes. The increased thermal stability of SEs allows for operation at increased temperature, however, which greatly improves diffusion coefficients and reaction kinetics, mitigating the disadvantages of reduced ionic conductivity.

Yet, operation at higher temperatures does demand more intricate designs on cell level, which is shortly outlined in the final part of this review. Thermal management systems have to be applied for optimum heat dissipation to reduce degradation and elongate the battery lifetime. In addition, improvements to the charging protocol should be considered, since pulsed charging and stepwise reduction of the charging current was shown to exhibit benefits over the traditional CC–CV method, not only resulting in better performance but also reduced degradation.

We hope that, with the collected suggestions for improvements in fast-charging materials and the depicted comparison of advantages and disadvantages of existing materials, this review will spark new exciting research in this crucial field, possibly leading to widespread adoption of electric vehicles in the future.

Acknowledgements

The authors thank Joachim Sann (JLU) for fruitful discussions and Raimund Koerver (BMW AG), Dominik Weber (Volkswagen AG), and Andreas Fischer (BASF SE) for critical comments on the manuscript. Financial support is highly appreciated and acknowledged from the following entities and foundations: the German Federal Ministry for Education and Research (BMBF) within GIBS 4 bi-national workshop, ELONGATE (03XP0248), FestBatt (03XP0180), LiMetalFreeSSiBAT (03XP0141), and by the Federal Ministry for Economic Affairs and Energy (BMWi) within the Structur.e (03ETE018E) project, the Israeli Ministry of Science and Technology (MOST), the Planning & Budgeting Committee/Israel Council for Higher Education (CHE), and Fuel Choice Initiative (Prime Minister Office) within the framework of "Israel National Research Center for Electrochemical Propulsion" (INREP 2) and by the Grand Technion Energy Program (GTEP).

Open access funding enabled and organized by Projekt DEAL.

Conflict of Interest

The authors declare no conflict of interest.

Keywords

cell degradation, fast-charging batteries, lithium chemical diffusion, lithium plating, lithium-ion batteries

Received: April 8, 2021
Revised: May 28, 2021
Published online: July 19, 2021

---

[1] a) J. M. Tarascon, M. Armand, *Nature* **2001**, *414*, 359; b) A. Yoshino, K. Sanechika, T. Nakajima (Asahi Kasei Corp), US 4668595, **1986**.
[2] J. B. Goodenough, K.-S. Park, *J. Am. Chem. Soc.* **2013**, *135*, 1167.
[3] A. Eftekhari, *ACS Sustainable Chem. Eng.* **2019**, *7*, 3684.
[4] a) J. Janek, W. G. Zeier, *Nat. Energy* **2016**, *1*, 16141; b) A. Manthiram, X. Yu, S. Wang, *Nat. Rev. Mater.* **2017**, *2*, 16103.
[5] H. J. Gores, J. Barthel, S. Zugmann, D. Moosbauer, M. Amereller, R. Hartl, A. Maurer, in *Handbook of Battery Materials* (Eds: C. Daniel, J. O. Besenhard), Wiley-VCH, Weinheim, Germany **2011**, pp. 525–626.
[6] A. Adam, J. Wandt, E. Knobbe, G. Bauer, A. Kwade, *J. Electrochem. Soc.* **2020**, *167*, 130503.
[7] A. Tomaszewska, Z. Chu, X. Feng, S. O'Kane, X. Liu, J. Chen, C. Ji, E. Endler, R. Li, L. Liu, Y. Li, S. Zheng, S. Vetterlein, M. Gao, J. Du, M. Parkes, M. Ouyang, M. Marinescu, G. Offer, B. Wu, *eTransportation* **2019**, *1*, 100011.
[8] Y. Liu, Y. Zhu, Y. Cui, *Nat. Energy* **2019**, *4*, 540.
[9] P. Entwistle, B. Schaper, *Porsche Taycans use IONITY High-Power Charging Stations on International Media Ride and Drive Event*, **2019**, http://ionity.eu/_Resources/Persistent/cffc5959e6c98afcbca7d0abe575502911a3b26c/20190911_IONITY_Posche_Taycan_EN.pdf (accessed: March 2021).
[10] L. Ulrich, *IEEE Spectrum* **2020**, *57*, 30.
[11] C. Kim, A. Lennon, World Premiere of the Porsche Taycan: The Sports Car for a Sustainable Future. PR No. 73/19, **2019**, http://press.porsche.com/prod/presse_pag/PressResources.nsf/Content?ReadForm&languageversionid=1021391 (accessed: March 2021).
[12] a) M. Holland, Supercharger V3. Shocking Power & Smart Strategy By Tesla (Charts!), cleantechnica.com/2019/03/08/supercharger-v3-shocking-power-smart-strategy-by-tesla-charts/ (accessed: November 2020); b) M. Holland, Tesla Model 3 On SuperCharger V3. Adds 50% Range In Under 12 Minutes! (Charts!), cleantechnica.com/2019/06/24/tesla-model-3-on-supercharger-v3-adds-50-range-in-under-12-minutes-charts/ (accessed: November 2020).
[13] S. Ahmed, I. Bloom, A. N. Jansen, T. Tanim, E. J. Dufek, A. Pesaran, A. Burnham, R. B. Carlson, F. Dias, K. Hardy, M. Keyser, C. Kreuzer, A. Markel, A. Meintz, C. Michelbacher, M. Mohanpurkar, P. A. Nelson, D. C. Robertson, D. Scoffield, M. Shirk, T. Stephens, R. Vijayagopal, J. Zhang, *J. Power Sources* **2017**, *367*, 250.
[14] K. Du, H. Xie, G. Hu, Z. Peng, Y. Cao, F. Yu, *ACS Appl. Mater. Interfaces* **2016**, *8*, 17713.

[15] a) J. Li, A. R. Cameron, H. Li, S. Glazier, D. Xiong, M. Chatzidakis, J. Allen, G. A. Botton, J. R. Dahn, *J. Electrochem. Soc.* **2017**, *164*, A1534; b) J. E. Harlow, X. Ma, J. Li, E. Logan, Y. Liu, N. Zhang, L. Ma, S. L. Glazier, M. M. E. Cormier, M. Genovese, S. Buteau, A. Cameron, J. E. Stark, J. R. Dahn, *J. Electrochem. Soc.* **2019**, *166*, A3031; c) Y. Liu, J. Harlow, J. Dahn, *J. Electrochem. Soc.* **2020**, *167*, 020512.

[16] J. Landesfeind, J. Hattendorff, A. Ehrl, W. A. Wall, H. A. Gasteiger, *J. Electrochem. Soc.* **2016**, *163*, A1373.

[17] S. Malifarge, B. Delobel, C. Delacourt, *J. Electrochem. Soc.* **2017**, *164*, E3329.

[18] I. V. Thorat, D. E. Stephenson, N. A. Zacharias, K. Zaghib, J. N. Harb, D. R. Wheeler, *J. Power Sources* **2009**, *188*, 592.

[19] A. M. Colclasure, A. R. Dunlop, S. E. Trask, B. J. Polzin, A. N. Jansen, K. Smith, *J. Electrochem. Soc.* **2019**, *166*, A1412.

[20] H. Zheng, G. Liu, X. Song, P. Ridgway, S. Xun, V. S. Battaglia, *J. Power Sources* **2010**, *157*, A1060.

[21] H. Zheng, L. Tan, G. Liu, X. Song, V. S. Battaglia, *J. Power Sources* **2012**, *208*, 52.

[22] J. Kasnatscheew, U. Rodehorst, B. Streipert, S. Wiemers-Meyer, R. Jakelski, R. Wagner, I. C. Laskovic, M. Winter, *J. Electrochem. Soc.* **2016**, *163*, A2943.

[23] M. S. Whittingham, *Chem. Rev.* **2004**, *104*, 4271.

[24] B. L. Ellis, K. T. Lee, L. F. Nazar, *Chem. Mater.* **2010**, *22*, 691.

[25] J. K. Ngala, N. A. Chernova, M. Ma, M. Mamak, P. Y. Zavalij, M. S. Whittingham, *J. Mater. Chem.* **2004**, *14*, 214.

[26] J.-M. Kim, H.-T. Chung, *Electrochim. Acta* **2004**, *49*, 937.

[27] A. Kraytsberg, Y. Ein-Eli, *J. Solid State Electrochem.* **2017**, *21*, 1907.

[28] F. Wu, G. Yushin, *Energy Environ. Sci.* **2017**, *10*, 435.

[29] L. Li, R. Jacobs, P. Gao, L. Gan, F. Wang, D. Morgan, S. Jin, *J. Am. Chem. Soc.* **2016**, *138*, 2838.

[30] T. P. Heins, N. Harms, L.-S. Schramm, U. Schröder, *Energy Technol.* **2016**, *4*, 1509.

[31] C.-F. Chen, P. P. Mukherjee, *Phys. Chem. Chem. Phys.* **2015**, *17*, 9812.

[32] A. Tokranov, R. Kumar, C. Li, S. Minne, X. Xiao, B. W. Sheldon, *Adv. Energy Mater.* **2016**, *6*, 1502302.

[33] L. M. Riegger, R. Schlem, J. Sann, W. G. Zeier, J. Janek, *Angew. Chem., Int. Ed.* **2021**, *60*, 6718.

[34] T. R. Jow, M. B. Marx, J. L. Allen, *J. Electrochem. Soc.* **2012**, *159*, A604.

[35] W. Weppner, R. A. Huggins, *Annu. Rev. Mater. Sci.* **1978**, *8*, 269.

[36] a) T. Waldmann, B.-I. Hogg, M. Wohlfahrt-Mehrens, *J. Power Sources* **2018**, *384*, 107; b) V. Kabra, M. Parmananda, C. Fear, F. L. E. Usseglio-Viretta, A. Colclasure, K. Smith, P. P. Mukherjee, *ACS Appl. Mater. Interfaces* **2020**, *12*, 55795; c) M.-T. F. Rodrigues, K. Kalaga, S. E. Trask, D. W. Dees, I. A. Shkrob, D. P. Abraham, *J. Electrochem. Soc.* **2019**, *166*, A996.

[37] C. Mao, R. E. Ruther, J. Li, Z. Du, I. Belharouak, *Electrochem. Commun.* **2018**, *97*, 37.

[38] X.-G. Yang, C.-Y. Wang, *J. Power Sources* **2018**, *402*, 489.

[39] a) S. S. Zhang, *J. Energy Chem.* **2020**, *41*, 135; b) R. Jung, M. Metzger, F. Maglia, C. Stinner, H. A. Gasteiger, *J. Electrochem. Soc.* **2017**, *164*, A1361; c) D. Streich, C. Erk, A. Guéguen, P. Müller, F.-F. Chesneau, E. J. Berg, *J. Phys. Chem. C* **2017**, *121*, 13481; d) B. Strehle, K. Kleiner, R. Jung, F. Chesneau, M. Mendez, H. A. Gasteiger, M. Piana, *J. Electrochem. Soc.* **2017**, *164*, A400.

[40] R. Usiskin, J. Maier, *Adv. Energy Mater.* **2021**, *11*, 2001455.

[41] R. Amin, Y.-M. Chiang, *J. Electrochem. Soc.* **2016**, *163*, A1512.

[42] C. Heubner, M. Schneider, A. Michaelis, *Adv. Energy Mater.* **2020**, *10*, 1902523.

[43] R. E. Usiskin, J. Maier, *Phys. Chem. Chem. Phys.* **2018**, *20*, 16449.

[44] W. Weppner, R. A. Huggins, *J. Electrochem. Soc.* **1977**, *124*, 1569.

[45] C. J. Wen, B. A. Boukamp, R. A. Huggins, W. Weppner, *J. Electrochem. Soc.* **1979**, *126*, 2258.

[46] A. Honders, J. M. der Kinderen, A. H. van Heeren, J. H. W. de Wit, G. H. J. Broers, *Solid State Ionics* **1985**, *15*, 265.

[47] M. Doyle, J. Newman, *J. Appl. Electrochem.* **1997**, *27*, 846.

[48] R. Ruess, S. Schweidler, H. Hemmelmann, G. Conforto, A. Bielefeld, D. A. Weber, J. Sann, M. T. Elm, J. Janek, *J. Electrochem. Soc.* **2020**, *167*, 100532.

[49] a) S. Cui, Y. Wei, T. Liu, W. Deng, Z. Hu, Y. Su, H. Li, M. Li, H. Guo, Y. Duan, W. Wang, M. Rao, J. Zheng, X. Wang, F. Pan, *Adv. Energy Mater.* **2016**, *6*, 1501309; b) A. van der Ven, G. Ceder, *J. Power Sources* **2001**, *97-98*, 529; c) M. D. Levi, D. Aurbach, *J. Phys. Chem. B* **1997**, *101*, 4641; d) M. D. Levi, E. Markevich, D. Aurbach, *J. Phys. Chem. B* **2005**, *109*, 7420.

[50] J. C. Bachman, S. Muy, A. Grimaud, H.-H. Chang, N. Pour, S. F. Lux, O. Paschos, F. Maglia, S. Lupart, P. Lamp, L. Giordano, Y. Shao-Horn, *Chem. Rev.* **2016**, *116*, 140.

[51] S. P. Culver, R. Koerver, T. Krauskopf, W. G. Zeier, *Chem. Mater.* **2018**, *30*, 4179.

[52] R. J. D. Tilley, *Defects in Solids*, Wiley, Hoboken, NJ **2008**.

[53] a) B. E. Francisco, C. R. Stoldt, J.-C. M'Peko, *Chem. Mater.* **2014**, *26*, 4741; b) H. Sato, in *Topics in Applied Physics* (Ed: S. Geller), Vol. *21*, Springer, Berlin, Heidelberg **1977**, pp. 3–39.

[54] M. D. Levi, E. Markevich, D. Aurbach, *Electrochim. Acta* **2005**, *51*, 98.

[55] A. Funabiki, M. Inaba, T. Abe, Z. Ogumi, *J. Electrochem. Soc.* **1999**, *146*, 2443.

[56] Y. Zhu, C. Wang, *J. Phys. Chem. C* **2010**, *114*, 2830.

[57] L. de Biasi, B. Schwarz, T. Brezesinski, P. Hartmann, J. Janek, H. Ehrenberg, *Adv. Mater.* **2019**, *31*, 1900985.

[58] W. Dreyer, J. Jamnik, C. Guhlke, R. Huth, J. Moskon, M. Gaberscek, *Nat. Mater.* **2010**, *9*, 448.

[59] W. Cai, Y.-X. Yao, G.-L. Zhu, C. Yan, L.-L. Jiang, C. He, J.-Q. Huang, Q. Zhang, *Chem. Soc. Rev.* **2020**, *49*, 3806.

[60] P. L. Taberna, S. Mitra, P. Poizot, P. Simon, J.-M. Tarascon, *Nat. Mater.* **2006**, *5*, 567.

[61] M. Schönleber, C. Uhlmann, P. Braun, A. Weber, E. Ivers-Tiffée, *Electrochim. Acta* **2017**, *243*, 250.

[62] a) A. M. Colclasure, R. J. Kee, *Electrochim. Acta* **2010**, *55*, 8960; b) T. F. Fuller, M. Doyle, J. Newman, *J. Electrochem. Soc.* **1994**, *141*, 1.

[63] A. J. Bard, L. R. Faulkner, *Electrochemical Methods: Fundamentals and Applications*, 2nd ed., Wiley, New York **2000**.

[64] a) C. Li, H. P. Zhang, L. J. Fu, H. Liu, Y. P. Wu, E. Rahm, R. Holze, H. Q. Wu, *Electrochim. Acta* **2006**, *51*, 3872; b) P. Guan, L. Zhou, Z. Yu, Y. Sun, Y. Liu, F. Wu, Y. Jiang, D. Chu, *J. Energy Chem.* **2020**, *43*, 220; c) T. Nakamura, K. Amezawa, J. Kulisch, W. G. Zeier, J. Janek, *ACS Appl. Mater. Interfaces* **2019**, *11*, 19968.

[65] Y. Li, Y. Qi, *Energy Environ. Sci.* **2019**, *12*, 1286.

[66] D. Liu, C. Zhang, G. Zhou, W. Lv, G. Ling, L. Zhi, Q.-H. Yang, *Adv. Sci.* **2018**, *5*, 1700270.

[67] J. Landesfeind, H. A. Gasteiger, *J. Electrochem. Soc.* **2019**, *166*, A3079.

[68] Y. Kato, S. Hori, T. Saito, K. Suzuki, M. Hirayama, A. Mitsui, M. Yonemura, H. Iba, R. Kanno, *Nat. Energy* **2016**, *1*, 16030.

[69] a) A. M. Colclasure, T. R. Tanim, A. N. Jansen, S. E. Trask, A. R. Dunlop, B. J. Polzin, I. Bloom, D. Robertson, L. Flores, M. Evans, E. J. Dufek, K. Smith, *Electrochim. Acta* **2020**, *337*, 135854; b) W. Mai, F. L. Usseglio-Viretta, A. M. Colclasure, K. Smith, *Electrochim. Acta* **2020**, *341*, 136013; c) F. Usseglio-Viretta, W. Mai, A. M. Colclasure, M. Doeff, E. Yi, K. Smith, *Electrochim. Acta* **2020**, *342*, 136034.

[70] P. Minnmann, L. Quillman, S. Burkhardt, F. H. Richter, J. Janek, *J. Electrochem. Soc.* **2021**, *168*, 040537.

[71] A. Bielefeld, D. A. Weber, J. Janek, *ACS Appl. Mater. Interfaces* **2020**, *12*, 12821.

[72] Y. Kato, S. Shiotani, K. Morita, K. Suzuki, M. Hirayama, R. Kanno, *J. Phys. Chem. Lett.* **2018**, *9*, 607.

[73] A. Bielefeld, D. A. Weber, J. Janek, *J. Phys. Chem. C* **2019**, *123*, 1626.

[74] Z. Ogumi, *Electrochemistry* **2010**, *78*, 319.

[75] Y. Yamada, Y. Iriyama, T. Abe, Z. Ogumi, *Langmuir* **2009**, *25*, 12766.

[76] Z. Ogumi, T. Abe, T. Fukutsuka, S. Yamate, Y. Iriyama, *J. Power Sources* **2004**, *127*, 72.
[77] T. Abe, H. Fukuda, Y. Iriyama, Z. Ogumi, *J. Electrochem. Soc.* **2004**, *151*, A1120.
[78] K. Xu, A. von Cresce, U. Lee, *Langmuir* **2010**, *26*, 11538.
[79] F. Yao, F. Güneş, H. Q. Ta, S. M. Lee, S. J. Chae, K. Y. Sheem, C. S. Cojocaru, S. S. Xie, Y. H. Lee, *J. Am. Chem. Soc.* **2012**, *134*, 8646.
[80] S. Thinius, M. M. Islam, P. Heitjans, T. Bredow, *J. Phys. Chem. C* **2014**, *118*, 2273.
[81] K. Zaghib, G. Nadeau, K. Kinoshita, *J. Electrochem. Soc.* **2000**, *147*, 2110.
[82] T. Kar, J. Pattanayak, S. Scheiner, *J. Phys. Chem. A* **2001**, *105*, 10397.
[83] P. Kaghazchi, *Appl. Phys. Lett.* **2013**, *102*, 093901.
[84] C.-Y. Chou, H. Kim, G. S. Hwang, *J. Phys. Chem. C* **2011**, *115*, 20018.
[85] H. Kim, K. E. Kweon, C.-Y. Chou, J. G. Ekerdt, G. S. Hwang, *J. Phys. Chem. C* **2010**, *114*, 17942.
[86] O. I. Malyi, T. L. Tan, S. Manzhos, *Appl. Phys. Express* **2013**, *6*, 027301.
[87] W. Wan, Q. Zhang, Y. Cui, E. Wang, *J. Phys.: Condens. Matter* **2010**, *22*, 415501.
[88] Z. Wang, Q. Su, H. Deng, W. He, J. Lin, Y. Q. Fu, *J. Mater. Chem. A* **2014**, *2*, 13976.
[89] Q. Zhang, W. Zhang, W. Wan, Y. Cui, E. Wang, *Nano Lett.* **2010**, *10*, 3243.
[90] T. Krauskopf, F. H. Richter, W. G. Zeier, J. Janek, *Chem. Rev.* **2020**, *120*, 7745.
[91] a) J. Asenbauer, T. Eisenmann, M. Kuenzel, A. Kazzazi, Z. Chen, D. Bresser, *Sustainable Energy Fuels* **2020**, *4*, 5387; b) I. L. Spain, A. R. Ubbelohde, D. A. Young, *Philos. Trans. R. Soc. London* **1967**, *262*, 345.
[92] S. Suh, H. Choi, K. Eom, H.-J. Kim, *J. Alloys Compd.* **2020**, *827*, 154102.
[93] X. Zeng, M. Li, D. Abd El-Hady, W. Alshitari, A. S. Al-Bogami, J. Lu, K. Amine, *Adv. Energy Mater.* **2019**, *9*, 1900161.
[94] J. Wolfenstine, U. Lee, J. L. Allen, *J. Power Sources* **2006**, *154*, 287.
[95] P. Heitjans, A. Korblein, H. Ackermann, D. Dubbers, F. Fujara, H.-J. Stockmann, *J. Phys. F: Met. Phys.* **1985**, *15*, 41.
[96] M. Wang, J. B. Wolfenstine, J. Sakamoto, *Electrochim. Acta* **2019**, *296*, 842.
[97] A. Masias, N. Felten, R. Garcia-Mendez, J. Wolfenstine, J. Sakamoto, *J. Mater. Sci.* **2019**, *54*, 2585.
[98] K. Persson, V. A. Sethuraman, L. J. Hardwick, Y. Hinuma, Y. S. Meng, A. van der Ven, V. Srinivasan, R. Kostecki, G. Ceder, *J. Phys. Chem. Lett.* **2010**, *1*, 1176.
[99] K. Persson, Y. Hinuma, Y. S. Meng, A. van der Ven, G. Ceder, *Phys. Rev. B* **2010**, *82*, 125416.
[100] T. L. Kulova, A. M. Skundin, E. A. Nizhnikovskii, A. V. Fesenko, *Russ. J. Electrochem.* **2006**, *42*, 259.
[101] A. Funabiki, M. Inaba, Z. Ogumi, S. Yuasa, J. Otsuji, A. Tasaka, *J. Electrochem. Soc.* **1998**, *145*, 172.
[102] H. Lin, D. Chua, M. Salomon, H.-C. Shiao, M. Hendrickson, E. Plichta, S. Slane, *J. Electrochem. Soc.* **2001**, *4*, A71.
[103] S. Tippmann, D. Walper, L. Balboa, B. Spier, W. G. Bessler, *J. Power Sources* **2014**, *252*, 305.
[104] T. Waldmann, B.-I. Hogg, M. Kasper, S. Grolleau, C. G. Couceiro, K. Trad, B. P. Matadi, M. Wohlfahrt-Mehrens, *J. Electrochem. Soc.* **2016**, *163*, A1232.
[105] B.-I. Hogg, T. Waldmann, M. Wohlfahrt-Mehrens, *J. Electrochem. Soc.* **2020**, *167*, 090525.
[106] W. Cai, C. Yan, Y.-X. Yao, L. Xu, R. Xu, L.-L. Jiang, J.-Q. Huang, Q. Zhang, *Small Struct.* **2020**, *1*, 2000010.
[107] C. Uthaisar, V. Barone, *Nano Lett.* **2010**, *10*, 2838.
[108] Y. W. Koh, S. Manzhos, *MRS Commun.* **2013**, *3*, 171.
[109] G. A. Tritsaris, K. Zhao, O. U. Okeke, E. Kaxiras, *J. Phys. Chem. C* **2012**, *116*, 22212.
[110] N. Ding, J. Xu, Y. X. Yao, G. Wegner, X. Fang, C. H. Chen, I. Lieberwirth, *Solid State Ionics* **2009**, *180*, 222.
[111] E. Quiroga-González, J. Carstensen, H. Föll, *Energies* **2013**, *6*, 5145.
[112] B. Wang, J. Ryu, S. Choi, X. Zhang, D. Pribat, X. Li, L. Zhi, S. Park, R. S. Ruoff, *ACS Nano* **2019**, *13*, 2307.
[113] T. Takamura, S. Ohara, M. Uehara, J. Suzuki, K. Sekine, *J. Power Sources* **2004**, *129*, 96.
[114] C. Yu, X. Li, T. Ma, J. Rong, R. Zhang, J. Shaffer, Y. An, Q. Liu, B. Wei, H. Jiang, *Adv. Energy Mater.* **2012**, *2*, 68.
[115] X. Han, Z. Zhang, H. Chen, L. Luo, Q. Zhang, J. Chen, S. Chen, Y. Yang, *J. Mater. Chem. A* **2021**, *9*, 3628.
[116] D. A. Lozhkina, A. M. Rumyantsev, E. V. Astrova, *Semiconductors* **2020**, *54*, 383.
[117] B. Deng, R. Xu, X. Wang, L. An, K. Zhao, G. J. Cheng, *Energy Storage Mater.* **2019**, *22*, 450.
[118] X. Shen, Z. Tian, R. Fan, L.e Shao, D. Zhang, G. Cao, L. Kou, Y. Bai, *J. Energy Chem.* **2018**, *27*, 1067.
[119] G. A. Tritsaris, E. Kaxiras, S. Meng, E. Wang, *Nano Lett.* **2013**, *13*, 2258.
[120] C. K. Chan, H. Peng, G. Liu, K. McIlwrath, X. F. Zhang, R. A. Huggins, Y. Cui, *Nat. Nanotechnol.* **2008**, *3*, 31.
[121] F. Tielens, M. Calatayud, A. Beltrán, C. Minot, J. Andrés, *J. Electroanal. Chem.* **2005**, *581*, 216.
[122] TOSHIBA, SCiB Rechargeable battery, www.scib.jp (accessed: December **2020**).
[123] S.-T. Myung, J. Kim, Y.-K. Sun, in *Batteries. Present and Future Energy Storage Challenges* (Eds: S. Passerini, D. Bresser, A. Moretti), Wiley-VCH, Weinheim, Germany **2020**, p. 196.
[124] A. Ghicov, M. Yamamoto, P. Schmuki, *Angew. Chem., Int. Ed.* **2008**, *47*, 7934.
[125] M. Fehse, S. Cavaliere, P. E. Lippens, I. Savych, A. Iadecola, L. Monconduit, D. J. Jones, J. Rozière, F. Fischer, C. Tessier, L. Stievano, *J. Phys. Chem. C* **2013**, *117*, 13827.
[126] M. Pfanzelt, P. Kubiak, M. Fleischhammer, M. Wohlfahrt-Mehrens, *J. Power Sources* **2011**, *196*, 6815.
[127] W. Zhang, D.-H. Seo, T. Chen, L. Wu, M. Topsakal, Y. Zhu, D. Lu, G. Ceder, F. Wang, *Science* **2020**, *367*, 1030.
[128] K. J. Griffith, K. M. Wiaderek, G. Cibin, L. E. Marbella, C. P. Grey, *Nature* **2018**, *559*, 556.
[129] L. Picard, T. Gutel, in *Batteries. Present and Future Energy Storage Challenges* (Eds: S. Passerini, D. Bresser, A. Moretti), Wiley-VCH, Weinheim, Germany **2020**, p. 783.
[130] Q. Zhao, C. Guo, Y. Lu, L. Liu, J. Liang, J. Chen, *Ind. Eng. Chem. Res.* **2016**, *55*, 5795.
[131] Y. Y. Zhang, Y. Y. Sun, S. X. Du, H.-J. Gao, S. B. Zhang, *Appl. Phys. Lett.* **2012**, *100*, 091905.
[132] S. T. Taleghani, B. Marcos, K. Zaghib, G. Lantagne, *J. Electrochem. Soc.* **2017**, *164*, E3179.
[133] H. Li, H. Zhou, *Chem. Commun.* **2012**, *48*, 1201.
[134] C. Wang, H. Zhao, J. Wang, J. Wang, P. Lv, *Ionics* **2013**, *19*, 221.
[135] F.-S. Li, Y.-S. Wu, J. Chou, M. Winter, N.-L. Wu, *Adv. Mater.* **2015**, *27*, 130.
[136] H. Wang, M. Yoshio, T. Abe, Z. Ogumi, *J. Electrochem. Soc.* **2002**, *149*, A499.
[137] M. Yoshio, H. Wang, K. Fukuda, Y. Hara, Y. Adachi, *J. Electrochem. Soc.* **2000**, *147*, 1245.
[138] S. R. Sivakkumar, J. Y. Nerkar, A. G. Pandolfo, *Electrochim. Acta* **2010**, *55*, 3330.
[139] X.-G. Yang, S. Ge, T. Liu, Y. Leng, C.-Y. Wang, *J. Power Sources* **2018**, *395*, 251.
[140] a) A. Sarkar, P. Shrotriya, A. Chandra, *J. Electrochem. Soc.* **2017**, *164*, E3606; b) S. Kalnaus, K. Rhodes, C. Daniel, *J. Power Sources* **2011**, *196*, 8116.

[141] X. H. Liu, L. Zhong, S. Huang, S. X. Mao, T. Zhu, J. Y. Huang, *ACS Nano* **2012**, *6*, 1522.
[142] M. Zhu, J. Park, A. M. Sastry, *J. Electrochem. Soc.* **2012**, *159*, A492.
[143] K. Zaghib, X. Song, A. Guerfi, R. Kostecki, K. Kinoshita, *J. Power Sources* **2003**, *124*, 505.
[144] D. D. MacNeil, D. Larcher, J. R. Dahn, *J. Electrochem. Soc.* **1999**, *146*, 3596.
[145] T. D. Tran, J. H. Feikert, R. W. Pekala, K. Kinoshita, *J. Appl. Electrochem.* **1996**, *26*, 1161.
[146] F. Röder, S. Sonntag, D. Schröder, U. Krewer, *Energy Technol.* **2016**, *4*, 1588.
[147] J. Kim, S. M. Nithya Jeghan, G. Lee, *Microporous Mesoporous Mater.* **2020**, *305*, 110325.
[148] T. Deng, X. Zhou, *J. Solid State Electrochem.* **2016**, *20*, 2613.
[149] M. Ebner, V. Wood, *J. Electrochem. Soc.* **2015**, *162*, A3064.
[150] M. Singh, J. Kaiser, H. Hahn, *J. Electrochem. Soc.* **2015**, *162*, A1196.
[151] K. G. Gallagher, S. E. Trask, C. Bauer, T. Woehrle, S. F. Lux, M. Tschech, P. Lamp, B. J. Polzin, S. Ha, B. Long, Q. Wu, W. Lu, D. W. Dees, A. N. Jansen, *J. Electrochem. Soc.* **2016**, *163*, A138.
[152] T. Danner, M. Singh, S. Hein, J. Kaiser, H. Hahn, A. Latz, *J. Power Sources* **2016**, *334*, 191.
[153] L. S. Kremer, A. Hoffmann, T. Danner, S. Hein, B. Prifling, D. Westhoff, C. Dreer, A. Latz, V. Schmidt, M. Wohlfahrt-Mehrens, *Energy Technol.* **2020**, *8*, 1900167.
[154] W. Huang, P. M. Attia, H. Wang, S. E. Renfrew, N. Jin, S. Das, Z. Zhang, D. T. Boyle, Y. Li, M. Z. Bazant, B. D. McCloskey, W. C. Chueh, Y. Cui, *Nano Lett.* **2019**, *19*, 5140.
[155] C.-Y. Wang, T. Xu, S. Ge, G. Zhang, X.-G. Yang, Y. Ji, *J. Electrochem. Soc.* **2016**, *163*, A1944.
[156] Y. Ren, L. J. Hardwick, P. G. Bruce, *Angew. Chem., Int. Ed.* **2010**, *49*, 2570.
[157] J. Billaud, F. Bouville, T. Magrini, C. Villevieille, A. R. Studart, *Nat. Energy* **2016**, *1*, 16097.
[158] C.-J. Bae, C. K. Erdonmez, J. W. Halloran, Y.-M. Chiang, *Adv. Mater.* **2013**, *25*, 1254.
[159] K.-H. Chen, M. J. Namkoong, V. Goel, C. Yang, S. Kazemiabnavi, S. M. Mortuza, E. Kazyak, J. Mazumder, K. Thornton, J. Sakamoto, N. P. Dasgupta, *J. Power Sources* **2020**, *471*, 228475.
[160] L. Kraft, J. B. Habedank, A. Frank, A. Rheinfeld, A. Jossen, *J. Electrochem. Soc.* **2020**, *167*, 013506.
[161] Y.-H. Chen, C.-W. Wang, X. Zhang, A. M. Sastry, *J. Power Sources* **2010**, *195*, 2851.
[162] M. Broussely, S. Herreyre, P. Biensan, P. Kasztejna, K. Nechev, R. Staniewicz, *J. Power Sources* **2001**, *97*, 13.
[163] J. Vetter, P. Novák, M. R. Wagner, C. Veit, K.-C. Möller, J. O. Besenhard, M. Winter, M. Wohlfahrt-Mehrens, C. Vogler, A. Hammouche, *J. Power Sources* **2005**, *147*, 269.
[164] X.-G. Yang, Y. Leng, G. Zhang, S. Ge, C.-Y. Wang, *J. Power Sources* **2017**, *360*, 28.
[165] J. Shim, K. A. Striebel, *J. Power Sources* **2003**, *119*, 934.
[166] J. B. Quinn, T. Waldmann, K. Richter, M. Kasper, M. Wohlfahrt-Mehrens, *J. Electrochem. Soc.* **2018**, *165*, A3284.
[167] M. J. Lain, J. Brandon, E. Kendrick, *Batteries* **2019**, *5*, 64.
[168] Z. Du, D. L. Wood, C. Daniel, S. Kalnaus, J. Li, *J. Appl. Electrochem.* **2017**, *47*, 405.
[169] P. Arora, M. Doyle, R. E. White, *J. Electrochem. Soc.* **1999**, *146*, 3543.
[170] S. Hein, A. Latz, *Electrochim. Acta* **2016**, *201*, 354.
[171] N. Legrand, B. Knosp, P. Desprez, F. Lapicque, S. Raël, *J. Power Sources* **2014**, *245*, 208.
[172] B. Bitzer, A. Gruhle, *J. Power Sources* **2014**, *262*, 297.
[173] N. Ghanbari, T. Waldmann, M. Kasper, P. Axmann, M. Wohlfahrt-Mehrens, *J. Phys. Chem. C* **2016**, *120*, 22225.
[174] N. Ghanbari, T. Waldmann, M. Kasper, P. Axmann, M. Wohlfahrt-Mehrens, *ECS Electrochem. Lett.* **2015**, *4*, A100.
[175] T. Waldmann, J. B. Quinn, K. Richter, M. Kasper, A. Tost, A. Klein, M. Wohlfahrt-Mehrens, *J. Electrochem. Soc.* **2017**, *164*, A3154.
[176] Q. Q. Liu, R. Petibon, C. Y. Du, J. R. Dahn, *J. Electrochem. Soc.* **2017**, *164*, A1173.
[177] T. Waldmann, M. Wilka, M. Kasper, M. Fleischhammer, M. Wohlfahrt-Mehrens, *J. Power Sources* **2014**, *262*, 129.
[178] P. Arora, R. E. White, M. Doyle, *J. Electrochem. Soc.* **1998**, *145*, 3647.
[179] S. Liu, L. Xiong, C. He, *J. Power Sources* **2014**, *261*, 285.
[180] C.-S. Kim, K. M. Jeong, K. Kim, C.-W. Yi, *Electrochim. Acta* **2015**, *155*, 431.
[181] S. Krueger, R. Kloepsch, J. Li, S. Nowak, S. Passerini, M. Winter, *J. Electrochem. Soc.* **2013**, *160*, A542.
[182] T. Waldmann, R.-G. Scurtu, K. Richter, M. Wohlfahrt-Mehrens, *J. Power Sources* **2020**, *472*, 228614.
[183] K.-H. Chen, V. Goel, M. J. Namkoong, M. Wied, S. Müller, V. Wood, J. Sakamoto, K. Thornton, N. P. Dasgupta, *Adv. Energy Mater.* **2021**, *11*, 2003336.
[184] a) D. Anseán, M. Dubarry, A. Devie, B. Y. Liaw, V. M. García, J. C. Viera, M. González, *J. Power Sources* **2017**, *356*, 36; b) T. C. Bach, S. F. Schuster, E. Fleder, J. Müller, M. J. Brand, H. Lorrmann, A. Jossen, G. Sextl, *J. Energy Storage* **2016**, *5*, 212; c) C. Birkenmaier, B. Bitzer, M. Harzheim, A. Hintennach, T. Schleid, *J. Electrochem. Soc.* **2015**, *162*, A2646; d) M. Ecker, P. Shafiei Sabet, D. U. Sauer, *Appl. Energy* **2017**, *206*, 934; e) C. von Lüders, V. Zinth, S. V. Erhard, P. J. Osswald, M. Hofmann, R. Gilles, A. Jossen, *J. Power Sources* **2017**, *342*, 17; f) V. Zinth, C. von Lüders, M. Hofmann, J. Hattendorff, I. Buchberger, S. Erhard, J. Rebelo-Kornmeier, A. Jossen, R. Gilles, *J. Power Sources* **2014**, *271*, 152.
[185] J. C. Burns, D. A. Stevens, J. R. Dahn, *J. Electrochem. Soc.* **2015**, *162*, A959.
[186] K. Richter, T. Waldmann, N. Paul, N. Jobst, R.-G. Scurtu, M. Hofmann, R. Gilles, M. Wohlfahrt-Mehrens, *ChemSusChem* **2020**, *13*, 529.
[187] Z. Li, J. Huang, B. Yann Liaw, V. Metzler, J. Zhang, *J. Power Sources* **2014**, *254*, 168.
[188] a) M. Fleischhammer, T. Waldmann, G. Bisle, B.-I. Hogg, M. Wohlfahrt-Mehrens, *J. Power Sources* **2015**, *274*, 432; b) T. Waldmann, M. Wohlfahrt-Mehrens, *Electrochim. Acta* **2017**, *230*, 454.
[189] X.-G. Yang, T. Liu, Y. Gao, S. Ge, Y. Leng, D. Wang, C.-Y. Wang, *Joule* **2019**, *3*, 3002.
[190] J. L. Tirado, *Mater. Sci. Eng., R* **2003**, *40*, 103.
[191] M. Winter, J. O. Besenhard, *Electrochim. Acta* **1999**, *45*, 31.
[192] T.-H. Kim, E. K. Jeon, Y. Ko, B. Y. Jang, B.-S. Kim, H.-K. Song, *J. Mater. Chem. A* **2014**, *2*, 7600.
[193] Q. Cheng, Y. Okamoto, N. Tamura, M. Tsuji, S. Maruyama, Y. Matsuo, *Sci. Rep.* **2017**, *7*, 14782.
[194] R. Mo, D. Rooney, K. Sun, H. Y. Yang, *Nat. Commun.* **2017**, *8*, 13949.
[195] X. Rao, Y. Lou, J. Chen, H. Lu, B. Cheng, W. Wang, H. Fang, H. Li, S. Zhong, *Front. Energy Res.* **2020**, *8*, 652.
[196] H.-J. Kim, J.-S. Kim, S.-W. Song, *J. Solid State Chem.* **2019**, *270*, 479.
[197] T. Xu, P. Gao, P. Li, K. Xia, N. Han, J. Deng, Y. Li, J. Lu, *Adv. Energy Mater.* **2020**, *10*, 1902343.
[198] H. Wang, D. Lin, Y. Liu, Y. Li, Y. Cui, *Sci. Adv.* **2017**, *3*, 1701301.
[199] N. Kim, S. Chae, J. Ma, M. Ko, J. Cho, *Nat. Commun.* **2017**, *8*, 812.
[200] J.-C. Daigle, Y. Asakawa, M. Beaupré, V. Gariépy, R. Vieillette, D. Laul, M. Trudeau, K. Zaghib, *Sci. Rep.* **2019**, *9*, 16871.
[201] B. Wang, J. S. Chen, H. B. Wu, Z. Wang, X. W. Lou, *J. Am. Chem. Soc.* **2011**, *133*, 17146.
[202] T. Muraliganth, A. Vadivel Murugan, A. Manthiram, *Chem. Commun.* **2009**, *45*, 7360.
[203] Y. Sun, X. Hu, W. Luo, Y. Huang, *J. Phys. Chem. C* **2012**, *116*, 20794.
[204] H. Yang, S. Zhang, L. Han, Z. Zhang, Z. Xue, J. Gao, Y. Li, C. Huang, Y. Yi, H. Liu, Y. Li, *ACS Appl. Mater. Interfaces* **2016**, *8*, 5366.

[205] J. Haetge, P. Hartmann, K. Brezesinski, J. Janek, T. Brezesinski, *Chem. Mater.* **2011**, *23*, 4384.

[206] a) X.-G. Yang, G. Zhang, S. Ge, C.-Y. Wang, *Proc. Natl. Acad. Sci. USA* **2018**, *115*, 7266; b) H. Ruan, J. Jiang, B. Sun, X. Su, X. He, K. Zhao, *Appl. Energy* **2019**, *256*, 113797; c) J. Zhang, H. Ge, Z. Li, Z. Ding, *J. Power Sources* **2015**, *273*, 1030.

[207] a) J. B. Goodenough, Y. Kim, *J. Power Sources* **2011**, *196*, 6688; b) J. B. Goodenough, Y. Kim, *Chem. Mater.* **2010**, *22*, 587; c) B. Kang, G. Ceder, *Nature* **2009**, *458*, 190; d) P. Gao, G. Yang, H. Liu, L. Wang, H. Zhou, *Solid State Ionics* **2012**, *207*, 50; e) J. Kasnatscheew, M. Börner, B. Streipert, P. Meister, R. Wagner, I. Cekic Laskovic, M. Winter, *J. Power Sources* **2017**, *362*, 278; f) G. Homann, P. Meister, L. Stolz, J. P. Brinkmann, J. Kulisch, T. Adermann, M. Winter, J. Kasnatscheew, *ACS Appl. Energy Mater.* **2020**, *3*, 3162.

[208] K. Mizushima, P. C. Jones, P. J. Wiseman, J. B. Goodenough, *Mater. Res. Bull.* **1980**, *15*, 783.

[209] R. Nölle, K. Beltrop, F. Holtstiege, J. Kasnatscheew, T. Placke, M. Winter, *Mater. Today* **2020**, *32*, 131.

[210] J. Kasnatscheew, T. Placke, B. Streipert, S. Rothermel, R. Wagner, P. Meister, I. C. Laskovic, M. Winter, *J. Electrochem. Soc.* **2017**, *164*, A2479.

[211] a) Y. Watanabe, S. Kinoshita, S. Wada, K. Hoshino, H. Morimoto, S. Tobishima, *J. Power Sources* **2008**, *179*, 770; b) A. V. Churikov, *Electrochim. Acta* **2001**, *46*, 2415; c) P. Novák, D. Goers, L. Hardwick, M. Holzapfel, W. Scheifele, J. Ufheil, A. Würsig, *J. Power Sources* **2005**, *146*, 15; d) P. Novák, J.-C. Panitz, F. Joho, M. Lanz, R. Imhof, M. Coluccia, *J. Power Sources* **2000**, *90*, 52; e) C.-H. Chen, F. Brosa Planella, K. O'Regan, D. Gastol, W. D. Widanage, E. Kendrick, *J. Electrochem. Soc.* **2020**, *167*, 080534.

[212] K. Amine, J. Liu, I. Belharouak, S.-H. Kang, I. Bloom, D. Vissers, G. Henriksen, *J. Power Sources* **2005**, *146*, 111.

[213] a) J. Kasnatscheew, S. Röser, M. Börner, M. Winter, *ACS Appl. Energy Mater.* **2019**, *2*, 7733; b) S. J. An, J. Li, C. Daniel, S. Kalnaus, D. L. Wood, *J. Electrochem. Soc.* **2017**, *164*, A1755; c) Y. Sun, C. Ouyang, Z. Wang, X. Huang, L. Chen, *J. Electrochem. Soc.* **2004**, *151*, A504; d) K. Kang, Y. S. Meng, J. Bréger, C. P. Grey, G. Ceder, *Science* **2006**, *311*, 977; e) D. Aurbach, *J. Power Sources* **2003**, 119, *497*.

[214] J. Kasnatscheew, M. Evertz, B. Streipert, R. Wagner, R. Klöpsch, B. Vortmann, H. Hahn, S. Nowak, M. Amereller, A.-C. Gentschev, P. Lamp, M. Winter, *Phys. Chem. Chem. Phys.* **2016**, *18*, 3956.

[215] J. Kasnatscheew, M. Evertz, R. Kloepsch, B. Streipert, R. Wagner, I. Cekic Laskovic, M. Winter, *Energy Technol.* **2017**, *5*, 1670.

[216] J. Kasnatscheew, B. Streipert, S. Röser, R. Wagner, I. Cekic Laskovic, M. Winter, *Phys. Chem. Chem. Phys.* **2017**, *19*, 16078.

[217] B. Streipert, L. Stolz, G. Homann, P. Janßen, I. Cekic-Laskovic, M. Winter, J. Kasnatscheew, *ChemSusChem* **2020**, *13*, 5301.

[218] a) X. Qi, B. Blizanac, A. DuPasquier, M. Oljaca, J. Li, M. Winter, *Carbon* **2013**, *64*, 334; b) S. F. Lux, F. Schappacher, A. Balducci, S. Passerini, M. Winter, *J. Electrochem. Soc.* **2010**, *157*, A320.

[219] a) Y. Wei, J. Zheng, S. Cui, X. Song, Y. Su, W. Deng, Z. Wu, X. Wang, W. Wang, M. Rao, Y. Lin, C. Wang, K. Amine, F. Pan, *J. Am. Chem. Soc.* **2015**, *137*, 8364; b) A. Kraytsberg, Y. Ein-Eli, *Adv. Energy Mater.* **2012**, *2*, 922.

[220] J. B. Goodenough, K. Mizuchima, US 4302518, **1980**.

[221] E. Trevisanello, R. Ruess, G. Conforto, F. H. Richter, J. Janek, *Adv. Energy Mater.* **2021**, *11*, 2003400.

[222] B.-B. Lim, S.-T. Myung, C. S. Yoon, Y.-K. Sun, *ACS Energy Lett.* **2016**, *1*, 283.

[223] H.-J. Noh, Z. Chen, C. S. Yoon, J. Lu, K. Amine, Y.-K. Sun, *Chem. Mater.* **2013**, *25*, 2109.

[224] S. Lee, Y. Cho, H.-K. Song, K. T. Lee, J. Cho, *Angew. Chem., Int. Ed.* **2012**, *51*, 8748.

[225] S. Klein, P. Bärmann, O. Fromm, K. Borzutzki, J. Reiter, Q. Fan, M. Winter, T. Placke, J. Kasnatscheew, *J. Mater. Chem. A* **2021**, *9*, 7546.

[226] S. Yasuhara, S. Yasui, T. Teranishi, K. Chajima, Y. Yoshikawa, Y. Majima, T. Taniyama, M. Itoh, *Nano Lett.* **2019**, *19*, 1688.

[227] T. Teranishi, Y. Yoshikawa, R. Sakuma, H. Hashimoto, H. Hayashi, A. Kishimoto, T. Fujii, *Appl. Phys. Lett.* **2014**, *105*, 143904.

[228] M. Wang, X. Feng, H. Xiang, Y. Feng, C. Qin, P. Yan, Y. Yu, *Small Methods* **2019**, *3*, 1900355.

[229] Q. Wu, X. Zhang, S. Sun, N. Wan, D.u Pan, Y. Bai, H. Zhu, Y.-S. Hu, S. Dai, *Nanoscale* **2015**, *7*, 15609.

[230] U. Nisar, R. Amin, R. Essehli, R. A. Shakoor, R. Kahraman, D. K. Kim, M. A. Khaleel, I. Belharouak, *J. Power Sources* **2018**, *396*, 774.

[231] U. Nisar, S. A. J. A. Al-Hail, R. K. Petla, R. A. Shakoor, R. Essehli, R. Kahraman, S. Y. AlQaradawi, D. K. Kim, I. Belharouak, M. R. Amin, *ACS Appl. Energy Mater.* **2019**, *2*, 7263.

[232] J.-J. Pan, B. Chen, Y. Xie, N. Ren, T.-F. Yi, *Mater. Lett.* **2019**, *253*, 136.

[233] Z. Chen, F. Xu, S. Cao, Z. Li, H. Yang, X. Ai, Y. Cao, *Small* **2017**, *13*, 1603148.

[234] X. Xu, Y.-Z. Luo, L.-Q. Mai, Y.-L. Zhao, Q.-Y. An, L. Xu, F. Hu, L. Zhang, Q.-J. Zhang, *NPG Asia Mater* **2012**, *4*, e20.

[235] Y. Lu, J. Chen, *Nat. Rev. Chem.* **2020**, *4*, 127.

[236] F. Otteny, G. Studer, M. Kolek, P. Bieker, M. Winter, B. Esser, *ChemSusChem* **2020**, *13*, 2232.

[237] F. Otteny, V. Perner, D. Wassy, M. Kolek, P. Bieker, M. Winter, B. Esser, *ACS Sustainable Chem. Eng.* **2020**, *8*, 238.

[238] S. Gu, Z. Bai, S. Majumder, B. Huang, G. Chen, *J. Power Sources* **2019**, *429*, 22.

[239] T. Teranishi, K. Kozai, S. Yasuhara, S. Yasui, N. Ishida, K. Ishida, M. Nakayama, A. Kishimoto, *J. Power Sources* **2021**, *494*, 229710.

[240] E. Krämer, T. Schedlbauer, B. Hoffmann, L. Terborg, S. Nowak, H. J. Gores, S. Passerini, M. Winter, *J. Electrochem. Soc.* **2013**, *160*, A356.

[241] a) N. Imanishi, M. Fujiyoshi, Y. Takeda, O. Yamamoto, M. Tabuchi, *Solid State Ionics* **1999**, *118*, 121; b) S. Levasseur, M. Ménétrier, E. Suard, C. Delmas, *Solid State Ionics* **2000**, *128*, 11.

[242] F. Croce, F. Nobili, A. Deptula, W. Lada, R. Tossici, A. D'Epifanio, B. Scrosati, R. Marassi, *Electrochem. Commun.* **1999**, *1*, 605.

[243] G. Liu, H. Zheng, S. Kim, Y. Deng, A. M. Minor, X. Song, V. S. Battaglia, *J. Electrochem. Soc.* **2008**, *155*, A887.

[244] A. Nyman, M. Behm, G. Lindbergh, *Electrochim. Acta* **2008**, *53*, 6356.

[245] I. Saadoune, C. Delmas, *J. Mater. Chem.* **1996**, *6*, 193.

[246] S. Klein, K. Borzutzki, P. Schneider, O. Fromm, J. Reiter, Q. Fan, T. Placke, M. Winter, J. Kasnatscheew, *Chem. Mater.* **2020**, *32*, 6279.

[247] X. Liu, G. Zhu, K. Yang, J. Wang, *J. Power Sources* **2007**, *174*, 1126.

[248] a) L. Zou, W. Zhao, Z. Liu, H. Jia, J. Zheng, G. Wang, Y. Yang, J.-G. Zhang, C. Wang, *ACS Energy Lett.* **2018**, *3*, 2433; b) S. Hwang, E. Jo, K. Y. Chung, K. S. Hwang, S. M. Kim, W. Chang, *J. Phys. Chem. Lett.* **2017**, *8*, 5758.

[249] a) H. Liu, M. Wolf, K. Karki, Y.-S. Yu, E. A. Stach, J. Cabana, K. W. Chapman, P. J. Chupas, *Nano Lett.* **2017**, *17*, 3452; b) J.-M. Lim, T. Hwang, D. Kim, M.-S. Park, K. Cho, M. Cho, *Sci. Rep.* **2017**, *7*, 39669; c) D. J. Miller, C. Proff, J. G. Wen, D. P. Abraham, J. Bareño, *Adv. Energy Mater.* **2013**, *3*, 1098; d) E.-J. Lee, Z. Chen, H.-J. Noh, S. C. Nam, S. Kang, D. H. Kim, K. Amine, Y.-K. Sun, *Nano Lett.* **2014**, *14*, 4873.

[250] a) H.-H. Ryu, K.-J. Park, C. S. Yoon, Y.-K. Sun, *Chem. Mater.* **2018**, *30*, 1155; b) W. Li, H. Y. Asl, Q. Xie, A. Manthiram, *J. Am. Chem. Soc.* **2019**, *141*, 5097; c) A. O. Kondrakov, A. Schmidt, J. Xu, H. Geßwein, R. Mönig, P. Hartmann, H. Sommer, T. Brezesinski, J. Janek, *J. Phys. Chem. C* **2017**, *121*, 3286; d) Y. Mao, X. Wang, S. Xia, K. Zhang, C. Wei, S. Bak, Z. Shadike, X. Liu, Y. Yang, R. Xu, P. Pianetta, S. Ermon, E. Stavitski, K. Zhao, Z. Xu, F. Lin, X.-Q. Yang, E. Hu, Y. Liu, *Adv. Funct. Mater.* **2019**, *29*, 1900247; e) S. Xia, L. Mu, Z. Xu, J. Wang, C. Wei, L. Liu, P. Pianetta, K. Zhao, X. Yu, F. Lin, Y. Liu, *Nano Energy* **2018**, *53*, 753.

[251] J. Kasnatscheew, M. Evertz, B. Streipert, R. Wagner, S. Nowak, I. Cekic Laskovic, M. Winter, *J. Power Sources* **2017**, *359*, 458.
[252] M. Winter, B. Barnett, K. Xu, *Chem. Rev.* **2018**, *118*, 11433.
[253] K. Xu, *Chem. Rev.* **2004**, *104*, 4303.
[254] a) G. Li, Z. Liu, Q. Huang, Y. Gao, M. Regula, D. Wang, L.-Q. Chen, D. Wang, *Nat. Energy* **2018**, *3*, 1076; b) G. Li, Z. Liu, D. Wang, X. He, S. Liu, Y. Gao, A. AlZahrani, S. H. Kim, L.-Q. Chen, D. Wang, *Adv. Energy Mater.* **2019**, *9*, 1900704; c) G. Li, *Adv. Energy Mater.* **2021**, *11*, 2002891.
[255] K. Xu, A. von Cresce, *J. Mater. Chem.* **2011**, *21*, 9849.
[256] a) T. Abe, F. Sagane, M. Ohtsuka, Y. Iriyama, Z. Ogumi, *Electrochim. Acta* **2005**, *152*, A2151; b) Y. Yamada, F. Sagane, Y. Iriyama, T. Abe, Z. Ogumi, *J. Phys. Chem. C* **2009**, *113*, 14528; c) T. Doi, Y. Iriyama, T. Abe, Z. Ogumi, *Anal. Chem.* **2005**, *77*, 1696; d) I. Yamada, T. Abe, Y. Iriyama, Z. Ogumi, *Electrochem. Commun.* **2003**, *5*, 502; e) I. Yamada, Y. Iriyama, T. Abe, Z. Ogumi, *J. Power Sources* **2007**, *172*, 933.
[257] a) S. Yanase, T. Oi, *J. Nucl. Sci. Technol.* **2002**, *39*, 1060; b) T. Fukushima, Y. Matsuda, H. Hashimoto, R. Arakawa, *J. Phys. Chem. A* **2001**, *4*, A127.
[258] Y. Matsuda, T. Fukushima, H. Hashimoto, R. Arakawa, *J. Power Sources* **2002**, *149*, A1045.
[259] B. Wen, Z. Deng, P.-C. Tsai, Z. W. Lebens-Higgins, L. F. J. Piper, S. P. Ong, Y.-M. Chiang, *Nat. Energy* **2020**, *5*, 578.
[260] a) J. Kasnatscheew, R. Wagner, M. Winter, I. Cekic-Laskovic, in *Topics in Current Chemistry Collections* (Ed: M. Korth), Springer, Cham **2018**, pp. 23–51; b) G. Homann, L. Stolz, K. Neuhaus, M. Winter, J. Kasnatscheew, *Adv. Funct. Mater.* **2020**, *30*, 2006289; c) G. Homann, L. Stolz, M. Winter, J. Kasnatscheew, *iScience* **2020**, *23*, 101225; d) G. Homann, L. Stolz, J. Nair, I. C. Laskovic, M. Winter, J. Kasnatscheew, *Sci. Rep.* **2020**, *10*, 4390.
[261] a) A. M. Andersson, K. Edström, *J. Electrochem. Soc.* **2001**, *148*, A1100; b) *Lithium-ion Batteries. Solid-electrolyte Interphase* (Eds: P. B. Balbuena, Y. Wang), World Scientific, Singapore **2004**; c) H. Buqa, R. I. R. Blyth, P. Golob, B. Evers, I. Schneider, M. V. Santis Alvarez, F. Hofer, F. P. Netzer, M. G. Ramsey, M. Winter, J. O. Besenhard, *Ionics* **2000**, *6*, 172; d) S. S. Zhang, *J. Power Sources* **2006**, *162*, 1379; e) S. Zhang, M. S. Ding, K. Xu, J. Allen, T. R. Jow, *J. Electrochem. Soc.* **2001**, *4*, A206; f) J. Kasnatscheew, R. W. Schmitz, R. Wagner, M. Winter, R. Schmitz, *J. Electrochem. Soc.* **2013**, *160*, A1369; g) R. W. Schmitz, P. Murmann, R. Schmitz, R. Müller, L. Krämer, J. Kasnatscheew, P. Isken, P. Niehoff, S. Nowak, G.-V. Röschenthaler, N. Ignatiev, P. Sartori, S. Passerini, M. Kunze, A. Lex-Balducci, C. Schreiner, I. Cekic-Laskovic, M. Winter, *Prog. Solid State Chem.* **2014**, *42*, 65; h) T. Dagger, J. Kasnatscheew, B. Vortmann-Westhoven, T. Schwieters, S. Nowak, M. Winter, F. M. Schappacher, *J. Power Sources* **2018**, *396*, 519.
[262] a) P. Niehoff, S. Passerini, M. Winter, *Langmuir* **2013**, *29*, 5806; b) L. J. Fu, H. Liu, C. Li, Y. P. Wu, E. Rahm, R. Holze, H. Q. Wu, *Solid State Sci.* **2006**, *8*, 113; c) V. Eshkenazi, E. Peled, L. Burstein, D. Golodnitsky, *Solid State Ionics* **2004**, *170*, 83.
[263] a) T. R. Jow, S. A. Delp, J. L. Allen, J.-P. Jones, M. C. Smart, *J. Electrochem. Soc.* **2018**, *165*, A361; b) J.-P. Jones, M. C. Smart, F. C. Krause, B. V. Ratnakumar, E. J. Brandon, *ECS Trans.* **2017**, *75*, 1.
[264] Y.-X. Yao, X. Chen, C. Yan, X.-Q. Zhang, W.-L. Cai, J.-Q. Huang, Q. Zhang, *Angew. Chem., Int. Ed.* **2021**, *60*, 4090.
[265] R. Schmuch, R. Wagner, G. Hörpel, T. Placke, M. Winter, *Nat. Energy* **2018**, *3*, 267.
[266] J. Kasnatscheew, M. Evertz, B. Streipert, R. Wagner, S. Nowak, I. Cekic Laskovic, M. Winter, *J. Phys. Chem. C* **2017**, *121*, 1521.
[267] D. Aurbach, M. D. Levi, E. Levi, H. Teller, B. Markovsky, G. Salitra, U. Heider, L. Heider, *J. Electrochem. Soc.* **1998**, *145*, 3024.
[268] Y. Park, S. H. Shin, H. Hwang, S. M. Lee, S. P. Kim, H. C. Choi, Y. M. Jung, *J. Mol. Struct.* **2014**, *1069*, 157.
[269] Y. Park, S. H. Shin, S. M. Lee, S. P. Kim, H. C. Choi, Y. M. Jung, *J. Mol. Struct.* **2014**, *1069*, 183.
[270] M. Balasubramanian, H. S. Lee, X. Sun, X. Q. Yang, A. R. Moodenbaugh, J. McBreen, D. A. Fischer, Z. Fu, *J. Electrochem. Soc.* **2002**, *5*, A22.
[271] a) F. Lin, I. M. Markus, D. Nordlund, T.-C. Weng, M. D. Asta, H. L. Xin, M. M. Doeff, *Nat. Commun.* **2014**, *5*, 3529; b) Y. Matsuo, R. Kostecki, F. McLarnon, *J. Electrochem. Soc.* **2001**, *148*, A687; c) S. Röser, A. Lerchen, L. Ibing, X. Cao, J. Kasnatscheew, F. Glorius, M. Winter, R. Wagner, *Chem. Mater.* **2017**, *29*, 7733.
[272] P. Janssen, J. Kasnatscheew, B. Streipert, C. Wendt, P. Murmann, M. Ponomarenko, O. Stubbmann-Kazakova, G.-V. Röschenthaler, M. Winter, I. Cekic-Laskovic, *J. Electrochem. Soc.* **2018**, *165*, A3525.
[273] M. A. Kraft, S. Ohno, T. Zinkevich, R. Koerver, S. P. Culver, T. Fuchs, A. Senyshyn, S. Indris, B. J. Morgan, W. G. Zeier, *J. Am. Chem. Soc.* **2018**, *140*, 16330.
[274] L. Zhou, A. Assoud, Q. Zhang, X. Wu, L. F. Nazar, *J. Am. Chem. Soc.* **2019**, *141*, 19002.
[275] A. Marcolongo, N. Marzari, *Phys. Rev. Mater.* **2017**, *1*, 025402.
[276] R. Srinivasan, A. Carson Baisden, B. G. Carkhuff, M. H. Butler, *J. Power Sources* **2014**, *262*, 93.
[277] S. Choi, M. Jeon, B.-K. Kim, B.-I. Sang, H. Kim, *Chem. Commun.* **2018**, *54*, 14116.
[278] a) R. Koerver, I. Aygün, T. Leichtweiß, C. Dietrich, W. Zhang, J. O. Binder, P. Hartmann, W. G. Zeier, J. Janek, *Chem. Mater.* **2017**, *29*, 5574; b) S.-K. Jung, H. Gwon, S.-S. Lee, H. Kim, J. C. Lee, J. G. Chung, S. Y. Park, Y. Aihara, D. Im, *J. Mater. Chem. A* **2019**, *7*, 22967.
[279] R. Koerver, W. Zhang, L. de Biasi, S. Schweidler, A. O. Kondrakov, S. Kolling, T. Brezesinski, P. Hartmann, W. G. Zeier, J. Janek, *Energy Environ. Sci.* **2018**, *11*, 2142.
[280] M. Falco, S. Ferrari, G. B. Appetecchi, C. Gerbaldi, *Mol. Syst. Des. Eng.* **2019**, *4*, 850.
[281] D. Hlushkou, A. E. Reising, N. Kaiser, S. Spannenberger, S. Schlabach, Y. Kato, B. Roling, U. Tallarek, *J. Power Sources* **2018**, *396*, 363.
[282] N. Kaiser, S. Spannenberger, M. Schmitt, M. Cronau, Y. Kato, B. Roling, *J. Power Sources* **2018**, *396*, 175.
[283] T. Shi, Q. Tu, Y. Tian, Y. Xiao, L. J. Miara, O. Kononova, G. Ceder, *Adv. Energy Mater.* **2019**, *2*, 1902881.
[284] a) S. Choi, M. Jeon, J. Ahn, W. D. Jung, S. M. Choi, J.-S. Kim, J. Lim, Y.-J. Jang, H.-G. Jung, J.-H. Lee, B.-I. Sang, H. Kim, *ACS Appl. Mater. Interfaces* **2018**, *10*, 23740; b) T. Asano, S. Yubuchi, A. Sakuda, A. Hayashi, M. Tatsumisago, *J. Electrochem. Soc.* **2017**, *164*, A3960; c) J. Landesfeind, A. Eldiven, H. A. Gasteiger, *J. Electrochem. Soc.* **2018**, *165*, A1122.
[285] T. Krauskopf, B. Mogwitz, H. Hartmann, D. K. Singh, W. G. Zeier, J. Janek, *Adv. Energy Mater.* **2020**, *10*, 2000945.
[286] J.-M. Doux, H. Nguyen, D. H. S. Tan, A. Banerjee, X. Wang, E. A. Wu, C. Jo, H. Yang, Y. S. Meng, *Adv. Energy Mater.* **2020**, *10*, 1903253.
[287] C. Yang, L. Zhang, B. Liu, S. Xu, T. Hamann, D. McOwen, J. Dai, W. Luo, Y. Gong, E. D. Wachsman, L. Hu, *Proc. Natl. Acad. Sci. U. S. A.* **2018**, *115*, 3770.
[288] Y. Ye, L. H. Saw, Y. Shi, A. A. O. Tay, *Appl. Therm. Eng.* **2015**, *86*, 281.
[289] Y. Ye, Y. Shi, A. A. O. Tay, *J. Power Sources* **2012**, *217*, 509.
[290] Y. Ye, L. H. Saw, Y. Shi, K. Somasundaram, A. A. O. Tay, *Electrochim. Acta* **2014**, *134*, 327.
[291] M. Keyser, A. Pesaran, Q. Li, S. Santhanagopalan, K. Smith, E. Wood, S. Ahmed, I. Bloom, E. Dufek, M. Shirk, A. Meintz, C. Kreuzer, C. Michelbacher, A. Burnham, T. Stephens, J. Francfort, B. Carlson, J. Zhang, R. Vijayagopal, K. Hardy, F. Dias, M. Mohanpurkar, D. Scoffield, A. N. Jansen, T. Tanim, A. Markel, *J. Power Sources* **2017**, *367*, 228.
[292] D. Chen, J. Jiang, G.-H. Kim, C. Yang, A. Pesaran, *Appl. Therm. Eng.* **2016**, *94*, 846.
[293] C. Wang, G. Zhang, L. Meng, X. Li, W. Situ, Y. Lv, M. Rao, *Int. J. Energy Res.* **2017**, *41*, 2468.

[294] Y. Zheng, Y. Shi, Y. Huang, *Appl. Therm. Eng.* **2019**, *147*, 636.
[295] S.-Y. Choe, X. Li, M. Xiao, *World Electr. Veh. J.* **2013**, *6*, 782.
[296] S. S. Zhang, *J. Power Sources* **2006**, *161*, 1385.
[297] Z. Guo, B. Y. Liaw, X. Qiu, L. Gao, C. Zhang, *J. Power Sources* **2015**, *274*, 957.
[298] A. Aryanfar, D. Brooks, B. V. Merinov, W. A. Goddard, A. J. Colussi, M. R. Hoffmann, *J. Phys. Chem. Lett.* **2014**, *5*, 1721.
[299] J. Amanor-Boadu, A. Guiseppi-Elie, E. Sánchez-Sinencio, *Energies* **2018**, *11*, 2162.
[300] B. Lu, Y. Zhao, Y. Song, J. Zhang, *Electrochim. Acta* **2018**, *288*, 144.
[301] a) B. Kwak, M. Kim, J. Kim, *Electronics* **2020**, *9*, 227; b) N. Majid, S. Hafiz, S. Arianto, R. Y. Yuono, E. T. Astuti, B. Prihandoko, *J. Phys.: Conf. Ser.* **2017**, *817*, 012008.

Manuel Weiss received his M.Sc. degree in Advanced Materials from Justus Liebig University Giessen. Afterward, he obtained his Ph.D. in the field of physical chemistry under supervision of Prof. Jürgen Janek. Currently, he is working as a postdoctoral researcher in Prof. Janek's group, investigating interfacial processes between different ionic conductors, liquid electrolytes for metal–oxygen batteries, and structure–property relationships in solid electrolytes.

Johannes Kasnatscheew studied chemistry at University of Münster and was granted an M.Sc. degree in 2012 under the supervision of Prof. Martin Winter. He continued his research in Prof. Winter's group in the department of "Münster's Electrochemical Energy Technology" (MEET) and obtained his Ph.D. in Physical Chemistry in 2017. That same year he joined the Helmholtz-Institute Münster (HIMS) "Ionics in Energy Storage" (IEK-12), an institute branch of Research Center Jülich, as a Post-Doc in Prof. Winter's group. His research focuses on failure diagnosis within Li-Ion batteries (LIBs) and all-solid-state-batteries at harsh conditions, in particular on electrolyte- and cathode materials.

Yehonatan Levartovsky received his B.Sc. in Chemistry from Tel-Aviv University in 2015, and his M.Sc. in Chemistry from the Hebrew University in Jerusalem in 2018. He is about to complete his Ph.D. in Chemistry under the guidance of Prof. Doron Aurbach at Bar-Ilan University, and then he will begin a fellowship at the UCL Electrochemical Innovation Lab. Currently, he is working on the design and synthesis of high-energy cathode materials for electric vehicles.

Natasha Ronith Levy received her B.Sc. degrees in Materials Science and Engineering (2016) and Chemistry (2016) and M.S. degree (2018) in Material Science and Engineering, all from the Technion-Israel Institute of Technology, Haifa, Israel. She started a Ph.D. in the Electrochemistry and Energy Storage field under the supervision of Prof. Y. Ein-Eli in 2018. Her research interests are focused on developing innovative air cathodes and study nonaqueous electrolytes for aluminum–air batteries.

Thomas Waldmann studied chemistry at Ulm University and received his Ph.D. degree in 2012. He joined the Zentrum für Sonnenenergie- und Wasserstoff-Forschung Baden-Württemberg (ZSW) in 2011 where he started working on degradation mechanisms of Li-ion batteries. His interests are focused on fast-charging, unraveling of aging mechanisms, especially on Li plating, knowledge-based extension of battery life-time, as well as interactions of safety and aging. Since 2018, he is team leader for Post-Mortem analysis and aging mechanisms at ZSW.

Doron Aurbach is full professor at the Department of Chemistry, which he chaired during 2001–2005, leading the electrochemistry group (founded in 1985) at Bar Ilan University and the Israel National Research Center for Electrochemical Propulsion (INREP). Professor Aurbach's group studies the electrochemistry of active metals, non-aqueous electrochemistry, intercalation processes, electronically conducting polymers, and water desalination and develop rechargeable batteries and supercapacitors with high energy density including spectroscopic methods for sensitive electrochemical systems. He has published over 720 papers and 30 patents, cited over 77 000 times. He is technical editor for the Journal of the Electrochemical Society (JES).

Yair Ein-Eli graduated from Bar-Ilan University (1995) and he joined (2001) the Department of Materials Engineering at the Technion-Israel Institute of Technology, after serving 3 years as the VP of R&D of Electric Fuel Ltd. (Israel). Before that (1995–1998), he was a post-doctoral fellow at Covalent Assoc. Inc. (MA, USA). Current research projects of Yair in the field of power sources involve advanced materials for Li-ion batteries, alkaline batteries, metal–air cells, and fuel cells. He is also engaged in research and development of electroplating methods, as well as corrosion inhibitors studies.

Jürgen Janek holds a chair for Physical Chemistry at Justus Liebig University in Giessen (Germany) and is scientific director of BELLA, a joint lab of BASF SE and KIT in Karlsruhe/Germany. He received his doctoral degree in Physical Chemistry and was visiting professor at Seoul National University, Tohoku University, and Université d'Aix-Marseille. His research spans a wide range from transport studies in mixed conductors and at interfaces to in situ studies in electrochemical cells. Current key interests include all-solid state batteries, solid electrolytes, and solid electrolyte interfaces. He is particularly interested in kinetics at interfaces.

Batteries & Supercaps
Articles
doi.org/10.1002/batt.202100148
Chemistry Europe
European Chemical Societies Publishing

Estimation of Li-Ion Degradation Test Sample Sizes Required to Understand Cell-to-Cell Variability**

Philipp Dechent+,*[a, b] Samuel Greenbank+,[c] Felix Hildenbrand,[a, b] Saad Jbabdi,[d] Dirk Uwe Sauer,*[a, e] and David A. Howey*[c]

Ageing of lithium-ion batteries results in irreversible reduction in performance. Intrinsic variability between cells, caused by manufacturing differences, occurs throughout life and increases with age. Researchers need to know the minimum number of cells they should test to give an accurate representation of population variability, since testing many cells is expensive. In this paper, empirical capacity versus time ageing models were fitted to various degradation datasets for commercially available cells assuming the model parameters could be drawn from a larger population distribution. Using a hierarchical Bayesian approach, we estimated the number of cells required to be tested. Depending on the complexity, ageing models with 1, 2 or 3 parameters respectively required data from at least 9, 11 or 13 cells for a consistent fit. This implies researchers will need to test at least these numbers of cells at each test point in their experiment to capture manufacturing variability.

1. Introduction

Lithium-ion batteries have grown in importance over the past decade and are now the key technology underlying applications from electric vehicles to grid energy storage.[1] High specific energy, low internal resistance and long lifetime have already led Li-ion cells to dominate the market for consumer electronics applications. A crucial issue that strongly impacts overall system performance is the intrinsic variability in capacity, resistance and degradation rate between cells, caused by small variations in manufacturing processes.[2–4] Quantifying the typical variability in mature commercially available Li-ion cells is crucial for understanding the trade-offs involved in designing battery packs and estimating pack performance and lifetime on the basis of individual cell performance.

Battery state of health (SOH) is usually defined as the capacity or impedance/resistance of a cell[5] under standard test conditions, and it constrains the useful and safe operation of batteries. State of health changes with time and usage, and is influenced both by external factors (such as voltage, time and temperature) and by internal manufacturing and materials variations.[6] Since it has a direct bearing on the economic value and operation of batteries, the estimation of current and future Li-ion SOH is a popular area of research.[6]

Variability in cell capacity and resistance can create differing loads within a Li-ion battery pack, and depending on its extent, variability will inevitably impact performance, cost and safety.[7–9] There are a variety of sources for this variability, for instance, thermal inhomogeneities influence SOH and increase cell-to-cell variability during usage.[5,10,11] However, manufacturing variability, sometimes described as tolerance, is a significant contributor to cell-to-cell variability.[2,3,12] New, nominally identical cells from the same batch exhibit a spread in capacity before they have been cycled.[4,13,14] Simulations and experiments have demonstrated that this intrinsic manufacturing variability is a contributing factor to differing ageing rates between cells.[2,3,13,15,16]

There are many possible sources of manufacturing variability,[17] such as variability in electrode thickness and density,[18] fraction of active material, liquid-to-solid ratio and coating gap.[19] In this work we assume that all intrinsic variability may be expressed through a single lumped population distribution, for each parameter and dataset. A further contributor to cell-to-cell variability results from variance in experimental conditions, for example location in a given testing chamber.[20]

---

[a] *P. Dechent,+ F. Hildenbrand, D. U. Sauer*
Electrochemical Energy Conversion and Storage Systems Group,
Institute for Power Electronics and Electrical Drives (ISEA), RWTH Aachen University, Germany
E-mail: philipp.dechent@isea.rwth-aachen.de
[b] *P. Dechent,+ F. Hildenbrand*
Jülich Aachen Research Alliance,
JARA-Energy,
Germany
[c] *S. Greenbank,+ D. A. Howey*
Battery Intelligence Lab,
Department of Engineering,
University of Oxford,
UK
E-mail: david.howey@eng.ox.ac.uk
[d] *S. Jbabdi*
Wellcome Centre for Integrative Neuroimaging,
FMRIB, University of Oxford, UK
[e] *D. U. Sauer*
Helmholtz Institute Münster (HI MS),
IEK-12, Forschungszentrum
Jülich, Münster, Germany
E-mail: DirkUwe.Sauer@isea.rwth-aachen.de

[+] *Authors contributed equally*

[**] *A previous version of this manuscript has been deposited on a preprint server (https://arxiv.org/abs/2107.07881)."*

Ageing reduces the performance of a given cell or pack and increases variability between cells.[10,13,14,21–23] To compound this, no significant correlation between initial health and ageing rates and subsequent ageing rates in later life has been found experimentally,[2,13,23,24] although features derived from early cycle life can be used to accurately predict lifetime.[25,26] Some authors have found that initial battery health is sometimes bi-modal.[27,28] It has also been found that Weibull distributions, common in failure analysis, may be used to quantify battery end of life statistics.[2,21,29,30]

In summary, cell-to-cell variability is a significant factor influencing the performance and value of batteries. As a result, modelling of battery ageing data is complicated by the question of how many cells should be tested at each experimental condition so as to adequately capture the intrinsic variability. Battery testing involves cost, in time and number of test channels, and therefore optimising the amount of information obtained from a test is a key consideration. The literature seems to have largely ignored the issue of how many cells should be tested to capture intrinsic variability, and for practical reasons, most ageing studies use only a small number of cells (e.g. 1–3) at each test condition. In this paper we address this question directly by fitting models to ageing data. There are many options for modelling battery capacity through life, from empirical curve fits[31] through to physical models[32] and machine learning approaches.[6,33] Since our aim was to investigate intrinsic rather than extrinsic variability, we chose as our modelling approach to use simple empirical curve fits of health versus time. We examined the consistency of the resulting model parameters as we added data drawn from increasing numbers of cells within each dataset, using five different battery ageing datasets. An estimate of required sample size was drawn for each parameter in every model for every available dataset.

2. Datasets and models

2.1. Data

To study cell-to-cell variability, ideally we need data from a very large number of cells, perhaps thousands. The costs of such large scale testing would be prohibitive, requiring many battery test channels for multiple years, and no such datasets are openly available. As a compromise, however, some ageing datasets are available with order 10–100 cells cycled identically (or very similarly). We selected five datasets for analysis based on the requirement of wanting as many cells as possible to have been tested within each dataset. Two of these are open source, and three are from our own experiments. Each individual dataset used identical commercially available Li-ion cells, albeit having different manufacturers, chemistries and cell sizes from dataset to dataset. All datasets used 18650 cylindrical cells, although the methods discussed below can equally be applied to other form factors. Some of the datasets featured identical experimental conditions, i.e. each cell was tested in exactly the same way, whereas others varied the testing conditions slightly beyond the expected uncontrollable experimental variability. The datasets are as follows:

1. **Baumhöfer-2014**[3] consists of 48 Sanyo/Panasonic UR18650E NMC/graphite 1.85 Ah cells in a cycle ageing test each under the same operating conditions. Data available at [34].
2. **Dechent-2020** consists of 22 Samsung INR18650-35E NCA/graphite cells each with a nominal capacity of 3.4 Ah. The cells were cycled with C/2 constant current and a 20% cycle depth around an average SOC of 50%. Data available at [35].
3. **Dechent-2017** consists of 21 Samsung NR18650-15 L1 1.5 Ah NMC/graphite cells. Six of the cells were cycled with 1 C charge and 6 C discharge current between 3.3 V and 4.1 V (90% cycle depth), and 15 additional cells were cycled with the same voltage range but current rates varied by up to 15%. Data available at [36].
4. **Severson-2019** consists of 124 cells made by A123 APR18650 M1 A with LFP/graphite chemistry, each with nominal capacity 1.1 Ah. For this work a subset 67 of these cells with similar load profiles but slightly varying charging currents was chosen. Data available via.[25] The cells in this dataset are from three different experimental batches so will have been subjected to higher variance in testing conditions than the other datasets.
5. **Attia-2020** replicates Severson-2019, but with a fixed charging window of 10 minutes. There are 45 cells in this set. Data available via [37].

Three of these datasets, namely Baumhöfer-2014, Severson-2019 and Attia-2020, exhibit an onset of rapid degradation in later life, sometimes called the 'knee-point'.[3,26] The other two datasets show only linear degradation over usage. The data prior to the knee-point in the Attia-2020 and Severson-2019 sets was separately extracted to produce two additional linear ageing datasets.

2.2. Models

The models and the corresponding datasets that they were fitted to are shown in Table 1. Here, Linear-1 and Linear-2 refer to the two linear models, having one and two parameters respectively. Alternatively, LinExp is a combined linear and exponential model that was used to capture the knee-point and later life health decay, where this was evident in the data.

Table 1. The dataset and empirical model combinations used here. Linear-1 is a single parameter linear model, Linear-2 a two parameter linear model, and LinExp a 3 parameter linear plus exponential model.

Dataset	Linear-1	Linear-2	LinExp	Ref.
Dechent-2017	X	X		[36]
Dechent-2020	X	X		[35]
Baumhöfer-2014			X	[3]
Severson-2019	X	X	X	[25]
Attia-2020	X	X	X	[37]

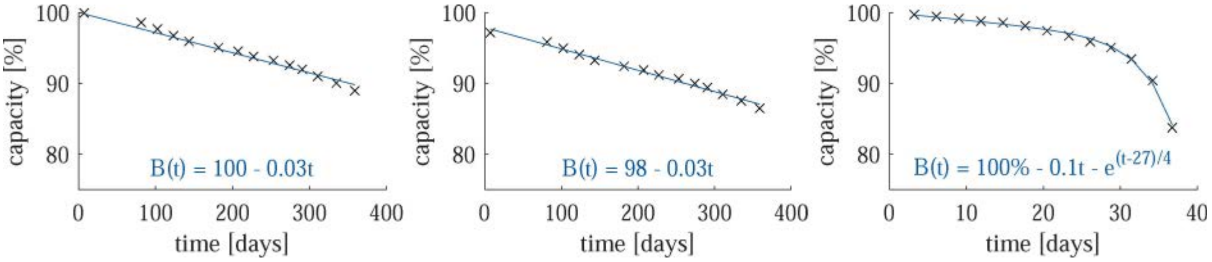

Figure 1. Examples of data and fitted curves. Left to right: Linear-1 model on a cell from Dechent-2020; Linear-2 model on a cell from Dechent-2020; LinExp model on a cell from Severson-2019.

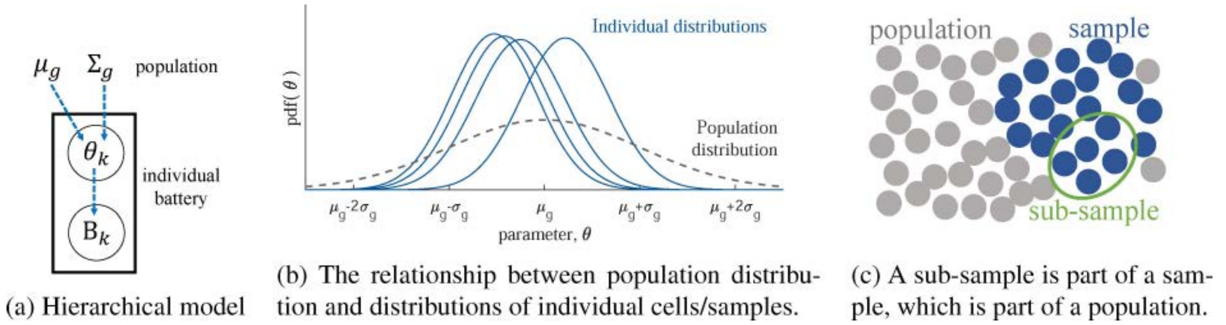

(a) Hierarchical model

(b) The relationship between population distribution and distributions of individual cells/samples.

(c) A sub-sample is part of a sample, which is part of a population.

Figure 2. A hierarchical approach was used to infer population statistics.

The three models are given by the following expressions, where t is time, B is capacity, and all other parameters $(c_1, c_2, c_3, B_0, t_f, \tau)$ were fitted to the data:

$$\text{Linear}-1: \quad B(t) = 100\% + c_1 \times t \tag{1}$$

$$\text{Linear}-2: \quad B(t) = B_0 + c_2 \times t \tag{2}$$

$$\text{LinExp}: \quad B(t) = 100\% + c_3 \times t - \exp[(t - t_f)/\tau] \tag{3}$$

Linear-1 and Linear-2 differ only by the addition of the initial capacity B_0 as a fitted parameter in the latter. The cell capacities were normalised according to which model was in use. For Linear-1 and LinExp, the capacities were normalised relative to the initial capacity of each cell. Linear-2 used capacity curves normalised relative to the nominal capacity. In the LinExp model, the initial linear capacity decrease is followed by a faster exponential decrease with onset time t_f and time constant τ, as shown in Figure 1.

3. Methodology

To quantify cell-to-cell variability, we used an approach called multi-level Bayes (MLB), also known as hierarchical Bayes, where the parameters of an individual cell model are assumed to be drawn from a population distribution, as depicted in Figure 2a. In this framework, the first level of inference is on the parameters of an individual battery cell model, and the second level of inference is on the parameters of the underlying population distribution.[38–40] Given some data sub-sampled from the datasets described above, this approach provides an estimate of the individual (θ_k) and the population (μ_g, Σ_g) parameter values as well as their associated uncertainties, as depicted in Figure 2(a) and (b). Therefore one can explore the trade off between the number of cells' data used for fitting the models versus the stability and variance (or standard deviation) of the resulting population parameter estimates. As additional data from more cells is included in the estimation, the variance of the population mean and variance decreases (i.e. we become more certain of the population model). As illustrated in Figure 3, we considered the population estimates to be stable when the standard deviation of the population standard deviation estimate began to steadily decrease as a function of sub-sample size $(\sim \frac{1}{N})$. We set the condition of an acceptable variability as being within a threshold, α, of the stable

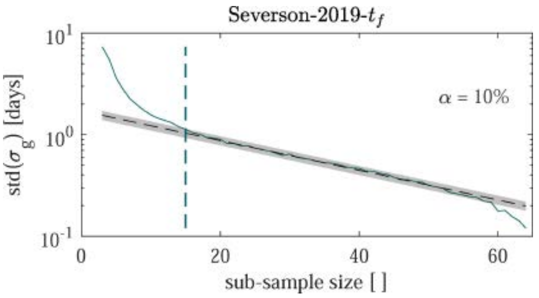

Figure 3. Example showing the decreasing standard deviation of the population standard deviation estimate as the number of sub-samples used for model fitting is increased. A threshold for an acceptable estimate is shown (vertical dashed line). Example taken from the t_f parameter for Severson-2019.

decreasing region. The value of α was set at 10% as shown by the grey shaded region in Figure 3.

The following conventions are used throughout the remainder of this work. Figure 2(c) shows the definitions of population, sample and subsample used. The 'population' means the very large (but unavailable) group of all possible similar batteries produced in the same manufacturing batch, from which a subset were tested in a lab. (Therefore, we expect the population statistics to be different for each dataset that was introduced in the previous section.) A 'sample' refers to all the available full data in a specific dataset. Therefore, a sample is drawn from a population. Conversely, any time a smaller subset was drawn from a full test dataset, it is referred to here as a 'sub-sample'. Summary sample statistics are denoted with the Latin alphabet, while population estimates are written using the Greek alphabet. For example, mean and variance are (m, s^2) and (μ, σ^2) respectively. The letter k is used to denote value(s) for a specific cell, and K denotes the total number of cells. Probabilities and distributions are written in capitals: P, N. Battery capacities are represented by the letter B.

3.1. Multi-Level Bayes

The parameters of an individual cell degradation model are assumed to be drawn from a population distribution that is unique for each dataset, with unknown population mean and variance. Let B_k denote the capacity of cell k over a number of measurements (i.e. B_k is a vector) and θ_k denote the model parameters determining the time evolution of capacity. For example, for the LinExp model, $\theta_k = (c_k, t_{f,k}, \tau_k)^T$. Assuming additive and Gaussian measurement noise,

$$B_k = f(\theta_k) + \varepsilon_k, \tag{4}$$

where $\varepsilon_k \sim \mathrm{N}\left(0, \sigma^2_{\mathrm{n,k}}\right)$ and f is one of the three models introduced above.

The parameters of an individual cell model k are themselves drawn from a population distribution, assumed here to be Gaussian,

$$\theta_k \sim \mathrm{N}\left(\mu_{\mathrm{g}}, \sigma^2_{\mathrm{g}}\right), \tag{5}$$

where μ_g is the group (i.e. population) mean and σ^2_g the group variance. These population parameters are vectors of one, two, or three elements depending on whether the generative model is Linear-1, Linear-2, or LinExp, respectively.

To complete the specification of this generative model in the Bayesian framework requires prior distributions to be assumed. We used wide Gaussian priors (zero mean, 10^4 variance) on the population means μ_g, and uniform distributions on the population variances. The noise parameters $\sigma_{n,k}$ were assumed to follow a Jeffrey's prior, $\mathrm{P}\left(\sigma^2_{\mathrm{n,k}}\right) \sim 1/\sigma^2_{n,k}$, and were integrated out analytically.

To infer the posterior distributions of the population parameters μ_g and σ_g, we used a two step process. In the first step (first level inference), we fitted individual cell parameters θ_k using Markov chain Monte Carlo (MCMC) sampling to obtain samples from $\mathrm{P}(\mathrm{B_k}|\theta_\mathrm{k}) = \int \mathrm{P}(\mathrm{B_k}|\theta_\mathrm{k}, \sigma_{\mathrm{n,k}})\mathrm{P}(\sigma_{\mathrm{n,k}})d\sigma_{n,k}$. We then approximated the distributions for each cell with a Gaussian using their summary statistics (means μ_k and variances σ^2_k), which were then used in a second step (second level inference). This allowed the full posterior distribution of the population parameters to be written as follows:

$$\mathrm{P}(\mu_\mathrm{g}, \sigma_\mathrm{g}|\{\mathrm{B_k}\}) = \int \dots \int \mathrm{P}(\mathrm{B_k}|\theta_\mathrm{k})\mathrm{P}(\theta_\mathrm{k}|\mu_\mathrm{g}, \sigma_\mathrm{g})\mathrm{P}\left(\mu_\mathrm{g}, \sigma_\mathrm{g}\right)d\theta_1 \dots d\theta_K \tag{6}$$

The above multivariate integral can be evaluated analytically, owing to the Gaussian approximation to the first level inference. This yields:

$$\mathrm{P}(\mu_\mathrm{g}, \sigma_\mathrm{g}|\{\mathrm{B_k}\}) \propto \prod_{k=1}^{K} \mathrm{N}\left(\mu_\mathrm{k}, \sigma^2_\mathrm{k} + \sigma^2_\mathrm{g}\right)\mathrm{P}\left(\mu_\mathrm{g}, \sigma_\mathrm{g}\right) \tag{7}$$

Intuitively, this last expression shows that the posterior population mean is a Gaussian centred around the weighted average of the individual cell parameters, where the weights combine the first level variances (uncertainty on the fitting of each cell) and the group variance (mixed effect model). After this, we again used MCMC to draw samples from this posterior distribution to calculate its summary statistics.

The MLB approach was used to fit the parameters of all the model/dataset combinations shown in Table 1. That fitting was performed at all sub-sample sizes from minimum 3 cells, up to 3 less than the full number of cells in each dataset, with 1,000 repeats performed at each sub-sample size using random selection with replacement. A population distribution was deemed to have a stable fit if the standard deviation of the estimate of σ_g settled to follow a function $\log y = ax + b$ where x is sub-sample size, y is the standard deviation of σ_g and a, b are arbitrary slope and offset parameters. As a comparison, the equivalent result was also plotted when using a simple sub-sample distribution (SSD) by taking the mean, m_g, and variance, s^2_g, of a given sub-sample:

$$m_g = \frac{1}{K}\sum_{k=1}^{K} \theta_k, \quad s_g = \sqrt{\frac{\sum_{k=1}^{K}\left(\theta_k - m_g\right)^2}{K-1}} \tag{8}$$

4. Results

As a reminder, the objective is to quantify the number of battery cells that are required for a stable fit of a population model, when cells are selected at random from a population. In particular, we wish to infer both the parameters of the capacity fade model for each cell, and the parameters of the underlying population, including their uncertainties. We now examine both aspects in succession across the various datasets and models.

In most cases, the parameter values estimated by MLB for the population level distributions match that of the sample distributions. Figure 4 shows two examples of well matched population and sample distributions, namely from Severson-2019- c_1 and and Attia-2020- τ. The parameter distribution in the sample is approximately Gaussian in both cases, matching an important assumption in the MLB derivation.

There was very little correlation between parameter distributions for any dataset/model combinations. The only significant case was for the Baumhöfer-2014-LinExp model, where Pearson's rank coefficients of 0.94 were found between all of c_1, t_f and τ. Severson-2019 had correlation coefficients of ~0.6, suggestive of a weak relationship between the parameters of the LinExp model.

The MLB results were subject to significant variability when fitting a single incidence at each sub-sample size. Figure 5 demonstrates a typical set of parameter estimates where it was hard to interpret the values at small sub-sample sizes. The mean estimates appeared to be well fit at small values, but the population distributions only settled when the majority of the sample was used.

The summary results from 1,000 repeats, with replacement, were much smoother. The estimated standard deviation of σ_g for the Linear-1 models rapidly dropped with increasing numbers of cells in a sub-sample for all datasets as shown in Figure 6. The SSD approach produced a lower variance at all sub-sample sizes, but appears insensitive to small sub-samples.

The results for Linear-2 and LinExp were very similar as shown in Figures 7 and 8, although there were distinctly less stable fit for Baumhöfer-2014- τ. All three models shared a reduced standard deviation of σ_g when using SSD.

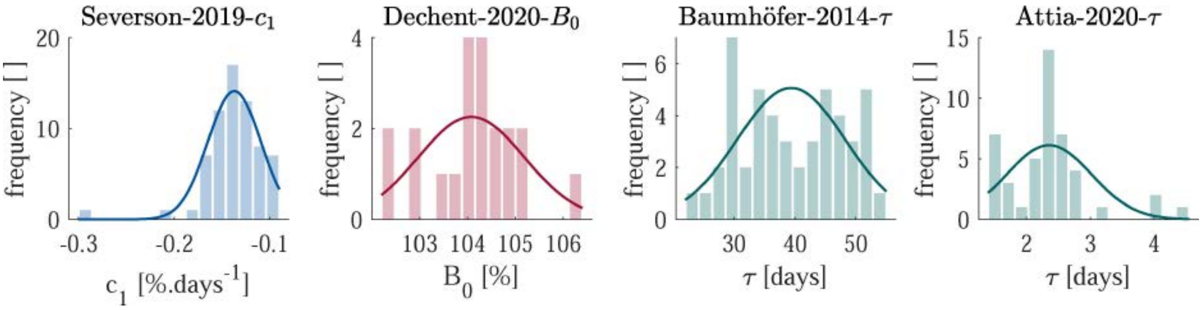

Figure 4. Generally, the inferred population distributions (lines) and sample distributions (bars) are similar, but there are some exceptions.

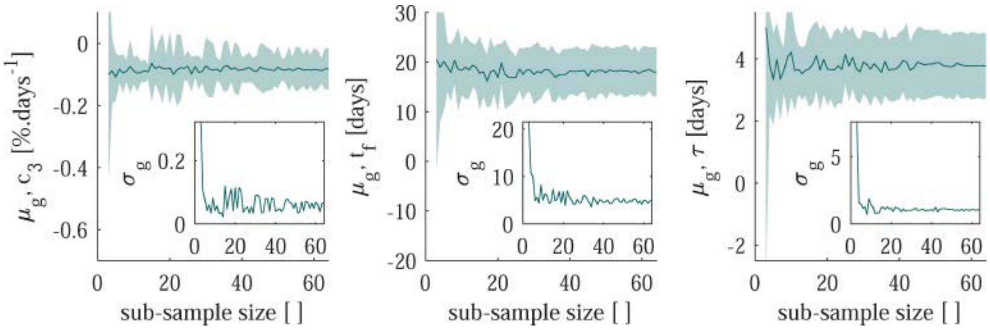

Figure 5. MLB results when fitting a single sub-sample draw have significant variability, shown here using Severson-2019 with the LinExp model. Lines show mean parameter estimates, shaded region is 1-σ about that mean, inset is σ_g.

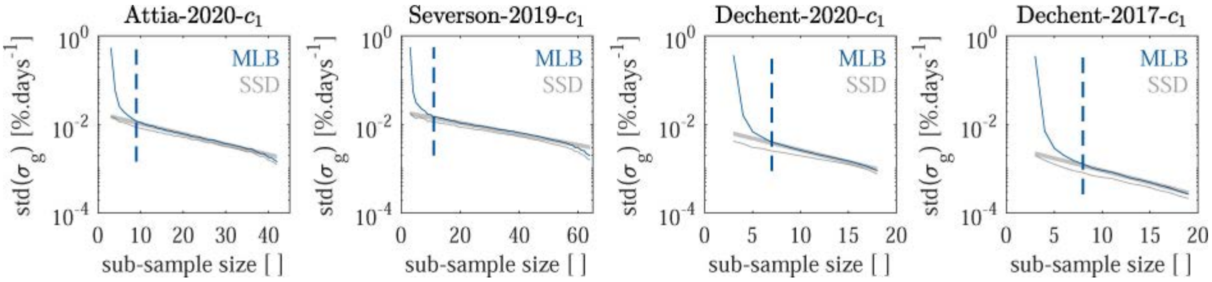

Figure 6. Smooth standard deviations are estimated by taking 1,000 random subsamples (with replacement), shown here with the Linear-1 model. MLB is Multi-Level-Bayes, SSD is sub-sample distribution, over the number of cells in the sample.

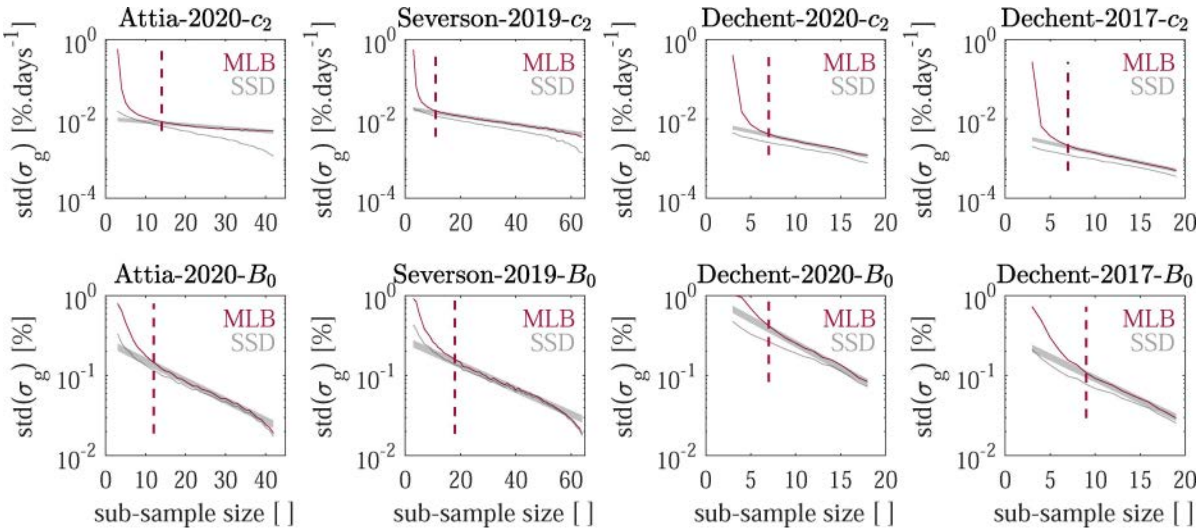

Figure 7. The standard deviations of the population-level standard deviation estimates for the Linear-2 model. MLB shows the Multi-Level-Bayes and SSD the sub-sample distribution results over the number of cells in the sub-sample.

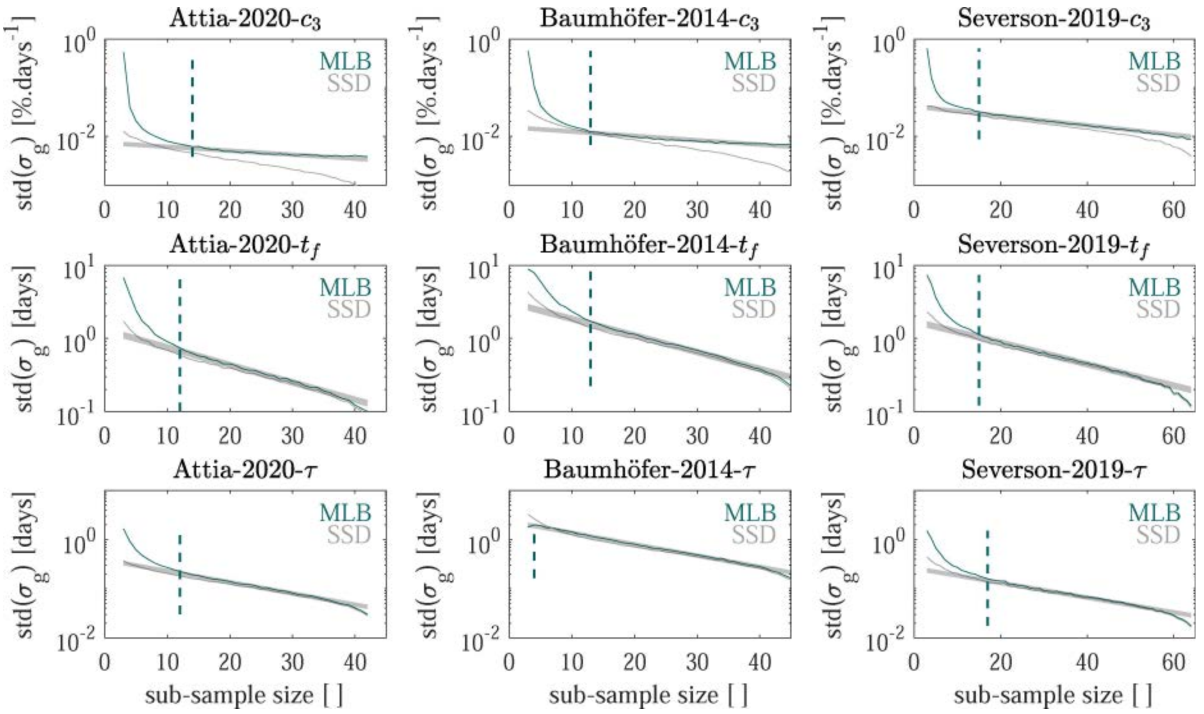

Figure 8. The standard deviations of the population-level standard deviation estimates for the LinExp model. MLB shows the Multi-Level-Bayes and SSD the sub-sample distribution results over the number of cells in the sub-sample.

The linear relationship between sub-sample size and the log of the standard deviations was deemed to represent a consistent fit. It was subsequently used to determine when an 'effective' sub-sample size had been reached. A model was considered well fit when the standard deviation of σ_g was within $\alpha = 10\%$ of this stable section, found using a linear extrapolation (as plotted in the figures).

Figure 9 shows the relationship between the number of cells required to achieve 'stable' population estimates, vs. the number of model parameters. The number is shown for all model, dataset and parameter combinations. The mean required sub-sample sizes for a consistent fit were 9, 11 and 13 for the 1, 2 and 3 parameter models respectively.

5. Discussion

The number of cells required to fit the various models presented here and capture a stable estimate of the population variability is of order 10. For the simplest model, Linear-1, the

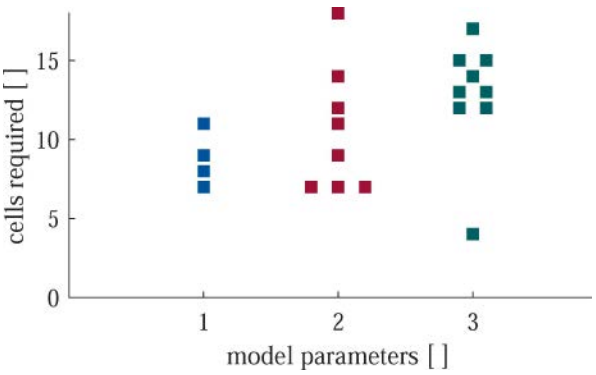

Figure 9. Testing with order 10 cells is required to achieve stable population estimates, with the number increasing as the model complexity increases. (Offset x-axis values were used to show identical results.)

number was 9 cells, and for the most complex LinExp model, the number increases to 13. The results understandably suggest that increased model complexity leads to an increase in the number of cells required to be tested to achieve a stable estimate of the population variability.

The multi-level Bayesian approach produced consistent parameter estimates from sub-samples. Given that cell-to-cell variability is an important phenomenon impacting battery performance, the estimated distributions are an invaluable tool to use in empirical modelling. Simple sample distribution techniques are limited to estimates of spread within the domain of the sample and hence showed less sensitivity to sub-sample size here when using random selection. The number of cells required to estimate population variability was fairly consistent across the datasets investigated here and was a stronger function of the model complexity than of the dataset. However, future work could test the robustness of this conclusion across a wider range of datasets.

The standard deviation of the σ_g estimates reduced as sub-sample sizes were increased. In most cases, the SSD and MLB results also approached the same values as sub-sample sizes increased because the two techniques will return similar results at high sub-sample sizes. At low sub-sample sizes SSD was limited to the variability of the sub-sample, whereas MLB was less certain, resulting in higher values for both σ_g and its standard deviation. In this case, SSD appears to have been artificially confident as an estimate of the population distribution.

The chosen threshold condition for a well fit σ_g parameter resulted in consistent results. The same consistency was also found when using other threshold values of α. The hypothesis that sub-sample size increases with model complexity appears to be supported. However, it would be useful to explore this in more depth using larger datasets.

In the derivation of the MLB approach, we assumed there to be no correlations between parameters in the prior probability distributions. That assumption was found to be questionable in two cases here. Future work should explore the impact of this on population modelling.

MLB was found to be a robust fitting mechanism when researching this work. For example, outliers were successfully ignored in Figure 4 where the sample distribution was not easily described as Gaussian. Our current approach assumes a Gaussian distribution at the population level. In the case of a bi-modal (or multi-modal) population distribution, we expect that the MLB method would respond by estimating a wide standard deviation, but this has not been tested. Extending the method proposed in this paper to other population distributions would be an interesting subject for future study.

Various ageing mechanisms are likely responsible for the degradation datasets considered in this paper. In the case of the Severson dataset, it is likely that degradation was largely caused by lithium plating,[25] while on the Dechent-2020 dataset, covering layer formation and jellyroll deformation are key to degradation.[41]

Between the datasets small differences were found. For the Linear-2 model the datasets Attia-2020 and Severson-2019 show a higher cell number threshold required for population estimation. The reasons for the trends we see are varied. The underlying mechanisms may be caused by increased variation of cycling conditions within the dataset. In order to capture higher usage variation in addition to intrinsic variability the number of cells will likely need to be increased. Future research could look into quantifying both use variability and manufacturing variability at the same time.

The fact that more complex models required more cells to be tested at each test point is challenging for battery lifetime experiments, since it could increase greatly the number of test channels and cells required in long term ageing experiments. We did not extrapolate to higher numbers of parameters or to other models, but it is reasonable to assume that the issues explored here will be present in other, more complex cases.

One challenge with the technique used here is that it relied on limited size samples from the population. Future work could explore whether larger sample sizes lead to similar results as found here.

Finally, further work is required to investigate the impacts of cell-to-cell variability using more complex physics-based models of battery ageing,[32] which can have 5–10 or more parameters in addition to the 20+ parameters of the required underlying electrochemical model. Openly available ageing datasets are at present too small to enable meaningful calculation of population parameter variability for such complex models using the methods we outline, since the number of parameters is significantly more than 1–3. One approach in a future study could be using synthetic datas to study more complex models with more parameters and test parameter identifiability.[42]

6. Conclusions

Simple empirical battery capacity fade models were fitted to a variety of ageing datasets to quantify the number of cells required to estimate the variability of the underlying population. The number of cells required to give a stable population variance estimate was found to vary according to the number of parameters in a given model. Respectively, 9, 11 and 13 cells are estimated to be required for models with 1, 2 and 3 parameters. Both sample statistics and population estimates were shown to stabilise with under 20 cells in most cases but this relied on there existing a Gaussian distribution of parameters within the sample, otherwise 20 cells were required.

For capacity curve fitting, perhaps the biggest challenge going forward is the selection of appropriate ageing model order and structure. This should be done not just by looking to what functions fit the capacity profiles best, but which functions produce the most reliable parameter distributions when looking at a dataset as a whole.

There was insufficient data here to test these results and conclusions as a function of variability caused by differences in usage, but this would be an interesting future exploration topic. Also, model selection across larger datasets is a challenging problem. For example, some of the battery capacity fade trajectories in this study fitted well to a linear degradation stage followed by an exponential decay starting from some knee point. However some of the resultant sample distributions cannot be confidently used to calculate basic summary statistics.

Understanding and quantifying battery cell-to-cell manufacturing variability is an open research topic, and this work represents an initial step. These results form a useful order of magnitude guide, for those undertaking long term battery ageing experiments, of what is needed to capture manufacturing variability.

Author contributions

P.D. and S.G.: conceptualisation, software, data curation, writing – original draft, visualisation. F.H.: software, writing – review and editing. S.J.: methodology, software, writing – review and editing. D.U.S.: supervision, funding acquisition. D.A.H.: conceptualisation, supervision, funding acquisition, writing – review and editing.

Acknowledgment

The authors would like to thank P.M. Attia, K. Severson and coworkers [25] and [37] S.G. is funded by EPSRC, UK, and Siemens Ltd. F.H gratefully acknowledges the financial support of Engie. P.D., F.H. and D.U.S gratefully acknowledge the financial support by Bundesministerium für Bildung und Forschung (BMBF 03XP0302C, 03XP0320A) and Engie. Open Access funding enabled and organized by Projekt DEAL.

Conflict of Interest

The authors declare no conflict of interest.

Keywords: ageing · Bayesian approach · degradation · lithium-ion batteries · modeling

[1] Nobel Committee. Press release: The Nobelprize in chemistry 2019. https://www.nobelprize.org/prizes/chemistry/2019/press-release/, 2019.
[2] S. J. Harris, D. J. Harris, C. Li, *J. Power Sources* **2017**, *342*, 589–597.
[3] T. Baumhöfer, M. Brühl, S. Rothgang, D. U. Sauer, *J. Power Sources* **2014**, *247*, 332–338.
[4] Markus Schindler, Johannes Sturm, Sebastian Ludwig, Julius Schmitt, Andreas Jossen, *eTransportation* **2021**, 100102.
[5] K. Rumpf, M. Naumann, A. Jossen, *J. Energy Storage* **2017**, *14*, 224–243.
[6] Y. Li, Kailong Liu, A. M. Foley, A. Zülke, M. Berecibar, E. Nanini-Maury, J.Van Mierlo, H. E. Hoster, *Renewable Sustainable Energy Rev.* **2019**, *113*, 109254.
[7] S. Santhanagopalan, R. E. White, *International Journal of Electrochemistry* **2012**, 1–10.
[8] M. Dahmardeh, Z. Xi, *ASCE-ASME J Risk and Uncert in Engrg Sys Part B Mech Engrg* **2019**, *5*, (020909).
[9] S. Orcioni, A. Ricci, L. Buccolini, C. Scavongelli, M. Conti, In *2017 13th Workshop on Intelligent Solutions in Embedded Systems (WISES)*, pages 15–21, June **2017**.
[10] X. Liu, W. Ai, M. N. Marlow, Y. Patel, B. Wu, *Appl. Energy* **2019**, *248*, 489–499.
[11] S. Paul, C. Diegelmann, H. Kabza, W. Tillmetz, *J. Power Sources* **2013**, *239*, 642–650.
[12] D. Shin, M. Poncino, E. Macii, N. Chang, *IEEE Transactions on Computer-Aided Design of Integrated Circuits and Systems* **2015**, *34*, 252–265.
[13] S. Rothgang, T. Baumhofer, D. U. Sauer, *2014 IEEE Vehicle Power and Propulsion Conference (VPPC)* **2014**, 1–6.
[14] M. Baumann, L. Wildfeuer, S. Rohr, M. Lienkamp, *J. Energy Storage* **2018**, *18*, 295–307.
[15] B. Kenney, K. Darcovich, D. D. MacNeil, I. J. Davidson, *J. Power Sources* **2012**, *213*, 391–401.
[16] M. Dubarry, C. Pastor-Fernández, G. Baure, T. F. Yu, W. D. Widanage, J. Marco, *J. Energy Storage* **2019**, *23*, 19–28.
[17] D. Beck, P. Dechent, M. Junker, D. U. Sauer, M. Dubarry, *Energies* **2021**, 14, 3276.
[18] G. Lenze, H. Bockholt, C. Schilcher, L. Froböse, D. Jansen, U. Krewer, A. Kwade, *J. Electrochem. Soc.* **2018**, *165*, A314–A322, 2018.
[19] M. Duquesnoy, I. Boyano, L. Ganborena, P. Cereijo, E. Ayerbe, A. A. Franco, *Energy and AI* **2021**, *5*, 100090.
[20] M. Elliott, L. G. Swan, M. Dubarry, G. Baure, *J. Energy Storage* **2020**, *32*, 101873, 12.
[21] S. F. Schuster, M. J. Brand, P. Berg, M. Gleissenberger, A. Jossen, *J. Power Sources* **2015**, *297*, 242–251.
[22] I. Zilberman, S. Ludwig, A. Jossen, *J. Energy Storage* **2019**, *26*, 100900.
[23] A. Devie, G. Baure, M. Dubarry, *Energies* **2018**, *11*, 1031.
[24] M. Lucu, E. Martinez-Laserna, I. Gandiaga, K. Liu, H. Camblong, W. D. Widanage, J. Marco, *J. Energy Storage* **2020**, *30*, 101410.
[25] K. A. Severson, P. M. Attia, N. Jin, N. Perkins, B. Jiang, Z. Yang, M. H. Chen, M. Aykol, P. K. Herring, D. Fraggedakis, M. Z. Bazant, S. J. Harris, W. C. Chueh, R. D. Braatz, *Nat. Energy* **2019**.
[26] P. Fermín-Cueto, E. McTurk, M. Allerhand, E. Medina-Lopez, M. F. Anjos, J. Sylvester, G. dos Reis, *Energy and AI* **2020**, *1*, 100006.
[27] S. Lehner, *Reliability Assessment of Lithium-Ion Battery Systems with Special Emphasis on Cell Performance Distribution*. Shaker, PhD thesis, RWTH Aachen University, 1 edition, March **2017**.
[28] F. An, L. Chen, J. Huang, J. Zhang, P. Li, *Sci. Rep.* **2016**, *6*, 35051.
[29] C. I. Ossai, N.agarajan Raghavan, *Batteries* **2017**, *3*, 32.
[30] Y. Jiang, J. Jiang, C. Zhang, W. Zhang, Y. Gao, Q. Guo, *J. Power Sources* **2017**, *360*, 180–188.
[31] M. Ecker, J. B. Gerschler, J. Vogel, S. Käbitz, F. Hust, P. Dechent, D. U. Sauer, *J. Power Sources* **2012**, *215*, 248–257.
[32] J. M. Reniers, G. Mulder, D. A. Howey, *Journal of The Electrochemical Society* **2019**, *166*, A3189–A3200.
[33] X. Hu, L. Xu, X. Lin, M. Pecht, *Joule* **2020**, S2542435119305859.
[34] D. U. Sauer, Time-series cyclic aging data on 48 commercial nmc/graphite Aanyo/Panasonic UR18650E cylindrical cells, **2021**, doi.org/10.18154/RWTH-2021-04545.
[35] P. Dechent, L. Willenberg, M. Eckert, D. U. Sauer. Time series data on cycle tests on Samsung NR18650-35E, **2021**, doi.org/10.18154/RWTH-2021-07965.

[36] P. Dechent, S. Lehner, D. U.Sauer, Time series data on cycle tests on Samsung NR18650-15L1, **2021**, doi.org/10.18154/RWTH-2021-08740.

[37] P. M. Attia, A. Grover, N. Jin, K. A. Severson, T. M. Markov, Y.-H. Liao, M. H. Chen, B. Cheong, N. Perkins, Z. Yang, P. K. Herring, M. Aykol, S. J. Harris, R. D. Braatz, S. Ermon, W. C. Chueh, *Nature* **2020**, *578*, 397–402.

[38] M. W. Woolrich, T. E. J. Behrens, C. F. Beckmann, M. Jenkinson, S. M. Smith, *NeuroImage* **2004**, *21*, 1732–1747.

[39] K. P. Murphy, *Machine learning: a probabilistic perspective.* Adaptive computation and machine learning series. MIT Press, Cambridge, MA, **2012**.

[40] S. Theodoridis, Chapter 13 - Bayesian Learning: Approximate Inference and Nonparametric Models. In Sergios Theodoridis, editor, *Machine Learning (Second Edition)*, pages 647–730. Academic Press, January **2020**.

[41] L. Willenberg, P. Dechent, G. Fuchs, M. Teuber, M. Eckert, M. Graff, N. Kürten, D. U. Sauer, E. Figgemeier, *J. Electrochem. Soc.* **2020**, *167*, 120502.

[42] A. Aitio, S. G. Marquis, P. Ascencio, D. Howey, *IFAC-PapersOnLine* **2020**, *53*, 12497–12504.

Manuscript received: July 5, 2021
Revised manuscript received: August 4, 2021
Version of record online: September 24, 2021

A High-Energy NASICON-Type Cathode Material for Na-Ion Batteries

Jingyang Wang, Yan Wang, Dong-Hwa Seo, Tan Shi, Shouping Chen, Yaosen Tian, Haegyeom Kim, and Gerbrand Ceder**

Over the last decade, Na-ion batteries have been extensively studied as low-cost alternatives to Li-ion batteries for large-scale grid storage applications; however, the development of high-energy positive electrodes remains a major challenge. Materials with a polyanionic framework, such as Na superionic conductor (NASICON)-structured cathodes with formula $Na_xM_2(PO_4)_3$, have attracted considerable attention because of their stable 3D crystal structure and high operating potential. Herein, a novel NASICON-type compound, $Na_4MnCr(PO_4)_3$, is reported as a promising cathode material for Na-ion batteries that deliver a high specific capacity of 130 mAh g^{-1} during discharge utilizing high-voltage $Mn^{2+/3+}$ (3.5 V), $Mn^{3+/4+}$ (4.0 V), and $Cr^{3+/4+}$ (4.35 V) transition metal redox. In addition, $Na_4MnCr(PO_4)_3$ exhibits a high rate capability (97 mAh g^{-1} at 5 *C*) and excellent all-temperature performance. In situ X-ray diffraction and synchrotron X-ray diffraction analyses reveal reversible structural evolution for both charge and discharge.

1. Introduction

The abundance and widespread distribution of sodium make Na-ion batteries a significantly less expensive alternative to Li-ion batteries, which is particularly attractive for large-scale grid storage applications.[1] Nevertheless, to make Na-ion batteries competitive, the development of high-energy cathode materials is crucial.[2] Extensive efforts have thus been devoted to the investigation of Na-ion cathode materials, especially sodium-layered oxides and polyanionic compounds.[3] Despite the high specific capacity of layered compounds,[4] they often lack structural stability in the highly charged state and require a low discharge cutoff voltage to achieve enough capacity.[5] In contrast, polyanionic compounds usually have a 3D robust framework that provides better cycling stability and a flatter voltage profile compared with those of layered oxides. In addition, owing to the inductive effect of the polyanion group (e.g., $(PO_4)^{3-}$, $(P_2O_7)^{4-}$, and $(SO_4)^{2-}$), a higher operating voltage can be achieved,[6] making these compounds interesting candidates for stable, high-energy-density cathode materials for Na-ion batteries.

The most studied polyanionic Na-ion cathode materials are the vanadium-containing phosphate $Na_3V_2(PO_4)_3$ (NVP)[7,8] and the fluorophosphate $Na_3V_2(PO_4)_2F_3$ (NVPF).[9] NVPF has a theoretical capacity of 128 mAh g^{-1} (two electrons per formula unit) at 3.9 V, with specific energy reaching 500 Wh kg^{-1}. Moreover, the electrochemical properties of NVPF can be tuned by substituting F anions by O, forming the complete solid solution $Na_3V_2(PO_4)_2F_{3-2y}O_{2y}$ $(0 \leq y \leq 1)$.[10] For example, Bianchini et al. showed that at the low-voltage end, an additional Na can be inserted in $Na_3V_2(PO_4)_2O_2F$ to produce $Na_4V_2(PO_4)_2O_2F$ upon discharge, which enables three-electron cycling between $Na_4V_2(PO_4)_2O_2F$ and $NaV_2(PO_4)_2O_2F$.[11] However, the extraction of the third Na from $NaV_2(PO_4)_2F_3$ to $V_2(PO_4)_2F_3$ has not yet been demonstrated to be practical because of the high Na extraction potential (predicted to be ≈4.9 V), which is beyond the stability window of organic Na-ion electrolytes.[12] Cation substitution has been considered in an effort to lower this high Na extraction voltage; however, only a few metal cations, such as Al, can substitute for V in the NVPF structure, with their solubility limited to 0.2.[11,13]

NVP has a Na superionic conductor (NASICON)-type structure. Na-ion cathode materials with the NASICON structure tend to have high multielectron capacity, a stable framework, and fast Na diffusion.[14] NVP has the general chemical formula $Na_xMM'\,(PO_4)_3$, where M and M′ represent transition metals and x can vary between 1 and 4.[15,16] The 3D host framework of NVP is built up by interlinking $[MO_6]$ octahedra and $[PO_4]$ tetrahedra via corner-shared oxygen; the strong covalent bonding results in good thermal stability and long cycle life. This open framework also provides 3D channels for fast Na-ion diffusion, yielding excellent rate performance.[17,18] Numerous

---

J. Wang, Dr. T. Shi, S. Chen, Dr. Y. Tian, Dr. H. Kim, Prof. G. Ceder
Materials Sciences Division
Lawrence Berkeley National Laboratory
Berkeley, CA 94720, USA
E-mail: gceder@berkeley.edu

J. Wang, Dr. T. Shi, S. Chen, Dr. Y. Tian, Prof. G. Ceder
Department of Materials Science and Engineering
University of California
Berkeley, CA 94720, USA

Dr. Y. Wang, Prof. D.-H. Seo
Advanced Material Lab
Samsung Research America
Burlington, MA 01803, USA
E-mail: eric.wangyan@samsung.com

The ORCID identification number(s) for the author(s) of this article can be found under https://doi.org/10.1002/aenm.201903968.

DOI: 10.1002/aenm.201903968

NASICON-type compounds with different metal cation combinations (V_2, MnV, MnTi, MnZr, VCr, VGa, NiV, FeV, etc.) have been synthesized and studied,[15,16,19–24] giving rise to a much more diverse chemical space and tunable electrochemical properties in contrast to NVPF. Though NASICON-type compounds have a large Na reservoir with potentially up to four extractable Na (i.e., a theoretical capacity of ≈220 mAh g^{-1}), reversible extraction/insertion of more than 2Na can rarely be achieved. NVP delivers a discharge capacity of 110 mAh g^{-1} with an average voltage of 3.4 V based on the $V^{3+/4+}$ redox. Partially substituting Al, Ga, or Cr for V can slightly increase the energy density by activating the high-voltage $V^{4+/5+}$ redox;[8,21,22] nevertheless, the capacity remains limited to a 2Na capacity. Replacing one V with Mn leads to another well-known NASICON-type compound, $Na_4MnV(PO_4)_3$ (NMVP), from which 3Na can be electrochemically extracted when charged to 4.3 V versus Na metal.[25,26] However, a recent in situ X-ray diffraction (XRD) study performed by Chen et al. revealed that NMVP undergoes an irreversible structural change after 3Na deintercalation and that only ≈2Na can be intercalated back, with poor cycling stability observed for the second and subsequent cycles.[25] Other Mn-based NASICONs such as $Na_3MnZr(PO_4)_3$ (NMZP) and $Na_3MnTi(PO_4)_3$ (NMTP)[19,27] exhibit stable cycling based on $Mn^{2+/3+}$ and $Mn^{3+/4+}$ redox; however, the theoretical capacities are also limited to 2Na because Zr and Ti are not electrochemically active at a useful cathode potential. Recently, Zhu et al. reported that NMTP can be initially discharged to 1.5 V, uptaking one more Na from the electrolyte/Na metal anode, with 3Na cycling achieved between the $Na_4MnTi(PO_4)_3$ and $NaMnTi(PO_4)_3$ phases; while the voltage based on $Ti^{3+/4+}$ redox is too low (2.1 V).[28] Therefore, to further increase the energy density of NASICON-type cathodes, the discovery of a new compound is needed to activate 3Na cycling at high voltage.

In this work, we computationally designed and experimentally synthesized a novel NASICON-type compound $Na_4MnCr(PO_4)_3$ (NMCP), achieving for the first time reversible 2.35Na (de)intercalation at the highest average voltage (3.59 V) among NASICON-type cathodes to date. Reversible transition metal redox ($Mn^{2+/3+}$, $Mn^{3+/4+}$, and $Cr^{3+/4+}$) is confirmed by X-ray absorption spectroscopy. Moreover, in situ XRD and synchrotron XRD analyses reveal a combined single-phase, two-phase, and single-phase reversible Na (de)intercalation mechanism during cycling of this novel NASICON-type compound.

2. Results

The feasibility of synthesizing the Mn/Cr-based NMCP was evaluated and compared with that of $Na_xMnM(PO_4)_3$ (M = Ti and Zr) with the same NASICON structure using density functional theory (DFT) calculations. Ground-state phase diagram was computed by generating the respective quaternary convex hulls constrained with all the competing phases present in the Materials Project.[29] The calculated phase stabilities are summarized in Table S1 (Supporting Information). The Mn/Cr-based NMCP compound has a relatively low energy above the hull (<25 meV $atom^{-1}$) across the full Na1–Na4 region, suggesting synthetic accessibility and good structural stability upon Na extraction/reinsertion. **Figure 1** presents the DFT-calculated voltage profile of $Na_xMnM(PO_4)_3$ (M = Cr, Ti, Zr, x = 0, 1, 2, 3, 4) averaged between the discrete Na compositions.[30] The combination of $Mn^{2+/3+}$, $Mn^{/3+/4+}$, and $Cr^{3+/4+}$ redox couples in NMCP is predicted to provide an average voltage close to 4 V and a theoretical capacity of 165 mAh g^{-1}, which is the highest capacity among $Na_xMnM(PO_4)_3$ (M = Cr, Ti, and Zr) materials.

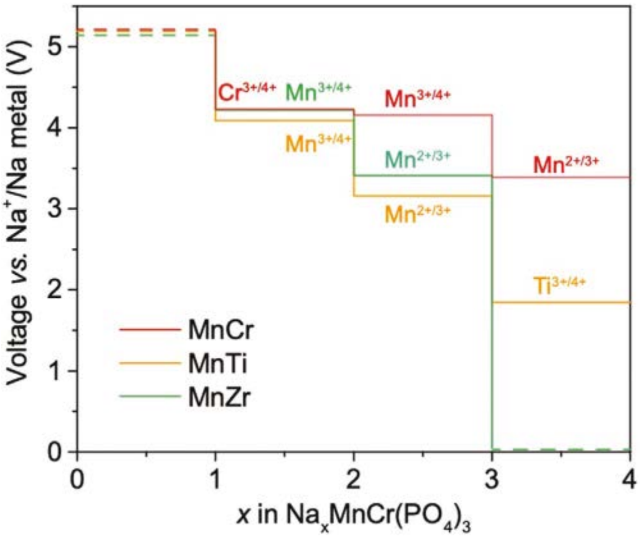

Figure 1. Calculated voltage profiles for $Na_xMnM(PO_4)_3$ (M = Cr, Ti, Zr; x = 0, 1, 2, 3, and 4) obtained using DFT calculations. The dashed lines are considered inaccessible voltages according to the phase stability analysis (Supporting Information).

The NMCP compounds were synthesized by mixing the precursors through a sol–gel method followed by preheating the product at 400 °C and annealing at 650 °C in an argon atmosphere (Experimental Section). The synchrotron XRD data for NMCP is presented in **Figure 2**a with no obvious impurity phases observed. The as-synthesized NMCP has the typical NASICON structure (Figure 2b) with rhombohedral space group $R\text{-}3c$ and lattice parameters $a = b = 8.9228(5)$ Å, $c = 21.471(1)$ Å as obtained from Rietveld refinement, yielding a volume $V = 1480.4(1)$ Å^3 per unit cell. The values of a and c are slightly smaller than those reported for NMVP,[16] consistent with the smaller ionic radius of Cr^{3+} (0.615 Å) relative to that of V^{3+} (0.64 Å). There are two distinct sodium sites in the structure as shown in Figure 2b, the 6b site with sixfold coordination (Na_1) and the 18e site with eightfold coordination (Na_2). The Na occupancies obtained from the Rietveld refinement are 1 for Na_1 and 0.999 for Na_2 (Table S2, Supporting Information), which confirms that both Na sites are fully occupied and in good agreement with the nominal composition $Na_4MnCr(PO_4)_3$. Detailed crystallographic data from the Rietveld refinement are provided in Table S2 (Supporting Information). Figure 2c presents a high-angle annular dark-field (HAADF) scanning transmission electron microscopy (STEM) image of a single NMCP particle. The corresponding energy-dispersive X-ray spectroscopy (EDX) elemental mapping demonstrates a uniform distribution of Na, Mn, and Cr.

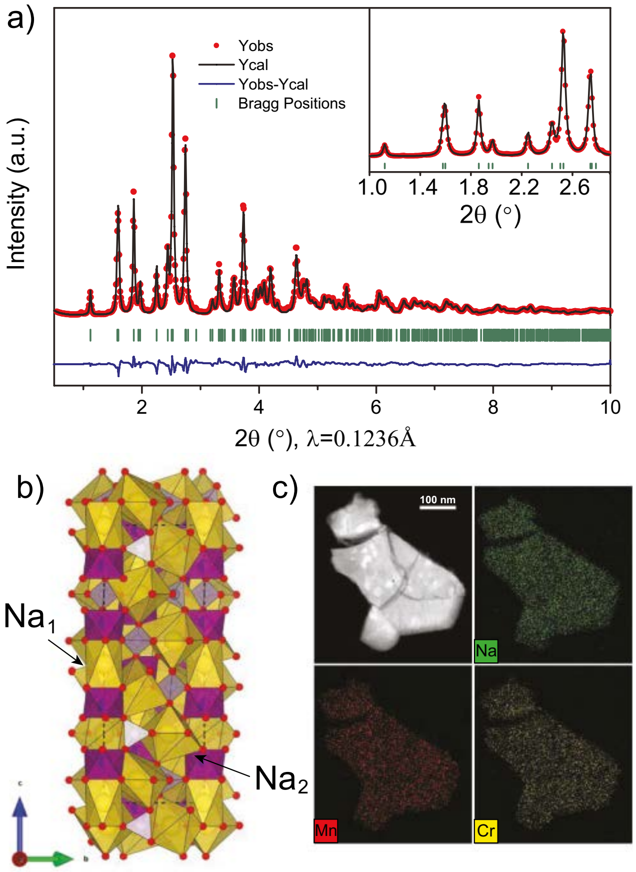

Figure 2. a) Rietveld refinement of synchrotron XRD data of as-synthesized $Na_4MnCr(PO_4)_3$. b) Structure of $Na_4MnCr(PO_4)_3$ obtained from Rietveld refinement of synchrotron XRD data, with the purple units representing $[(Mn/Cr)O_6]$ octahedra and the light purple $[PO_4]$ tetrahedra and yellow units representing the coordination of Na. c) HAADF image of an NMCP particle and corresponding EDX mapping obtained using STEM.

The size and morphology of the as-synthesized NMCP were characterized using scanning electron microscopy (SEM), as shown in Figure S1a,b (Supporting Information), revealing that the particle size of NMCP is not evenly distributed and ranges from several to tens of micrometers. The large particle size implies that the electrochemical performance of NMCP can possibly be improved by morphology optimization.

The electrochemical performance of NMCP as a positive electrode was tested in a Na half-cell. **Figure 3**a presents the voltage versus capacity curve of NMCP for the first two cycles between 1.5 and 4.5 V at $C/20$ ($1C$ = 110 mAh g^{-1}). NMCP delivers a large first charge capacity of 141 mAh g^{-1} and discharge capacity of 130 mAh g^{-1}, corresponding to 2.6Na extraction and 2.35Na reinsertion. Distinct plateaus appear in the voltage profile during charge (discharge) at 3.6 V (3.5 V), 4.2 V (4.1 V), and 4.4 V (4.35 V), as confirmed by the three oxidation and reduction peaks observed in the differential capacity ($dQ\ dV^{-1}$) curve (inset). When further discharged to 1.0 V, an additional low-voltage tail appears, and the overall discharge capacity reaches 157 mAh g^{-1}, with a Coulombic efficiency of ≈100% (Figure 3b). This low-voltage capacity is highly reversible in the subsequent cycles.

The cycling performance of NMCP in different voltage windows is summarized in Figure 3c. When cycled between 1.5 and 4.5 V, the discharge capacity of NMCP fades to 90 mAh g^{-1} after 20 cycles, whereas the Coulombic efficiency gradually increases from 91% to 97%. The capacity retention can be improved by decreasing the high-voltage cutoff to 4.35 V (88% retention after 20 cycles), although the initial discharge capacity is reduced to 96 mAh g^{-1}. These results indicate that the capacity fading of NMCP may originate from the capacity loss in the high-voltage region. At this point, we do not know if this capacity loss at high voltage is due to electrolyte failure or an intrinsic degradation of the material.

The Na diffusion kinetics of NMCP was investigated by means of the galvanostatic intermittent titration (GITT) and rate testing. Figure 3d presents the GITT curve for the second cycle. A small overpotential (20–30 mV) is observed during most of the charge and discharge, demonstrating good kinetics for Na diffusion, especially at high voltage when the composition has low Na content (red). A larger overpotential is present in the lower-voltage regions, marked by the orange and blue regions in the time versus voltage plot (inset) respectively. At the end of discharge, the overpotential for Na insertion is 324 mV, and 200 mV for Na extraction when the charge is started. The rate performance of NMCP was tested in a half-cell cycled between 1.5 and 4.5 V. As shown in Figure 3e, NMCP exhibits excellent rate capability with discharge capacities of 105 and 97 mAh g^{-1} at 2 and 5 C, respectively, corresponding to 81% and 75% of the discharge capacity at $C/20$. Interestingly, the capacity loss at increased rate is mainly associated with the low-voltage region, and the high-voltage plateaus are better maintained upon increasing the current (Figure 3f). This rate test confirms the finding in the GITT experiment that Na diffusion kinetics is very good in the Na-deficient phase. Even though the cathode particles are microsized, this rate performance is comparable to that of other reported nanosized NASICONs.[19,28,31]

The electrochemical performance of the NMCP|Na metal half-cell was then investigated at temperatures well above and below room temperature (RT). A capacity cutoff (100 mAh g^{-1}, ≈2Na) was applied during charge to ensure that the samples at different temperatures were deintercalated to the same Na content, and a 1.5 V voltage cutoff was applied during discharge. The charge and discharge curves at −10, 20, and 50 °C in **Figure 4**a can be divided into a low-voltage region (≈3.6 V) and a high-voltage region (≈4.2 V). The capacity of the low-voltage region increases substantially with increasing temperature, whereas the trend for the high-voltage region is clearly reversed: from −10 to 20 °C and then to 50 °C the charge capacity of the low-voltage region is extended, whereas the discharge capacity of high-voltage region is decreased. This observation suggests that at low temperature, during discharge, more capacity is delivered at high voltage. This finding is unusual as improved electrochemical performance is expected at high temperature because of the improved Na kinetics; however, the performance of NMCP at −10 °C is as good as that at high temperature and even better in terms of energy density. The inset of Figure 4a clearly shows that the high-voltage discharge capacity at −10 °C is almost twice that at 50 °C. Same behavior is observed using a 4.5 V voltage cutoff (Figure S5, Supporting Information). The cycling performance at −10, 20,

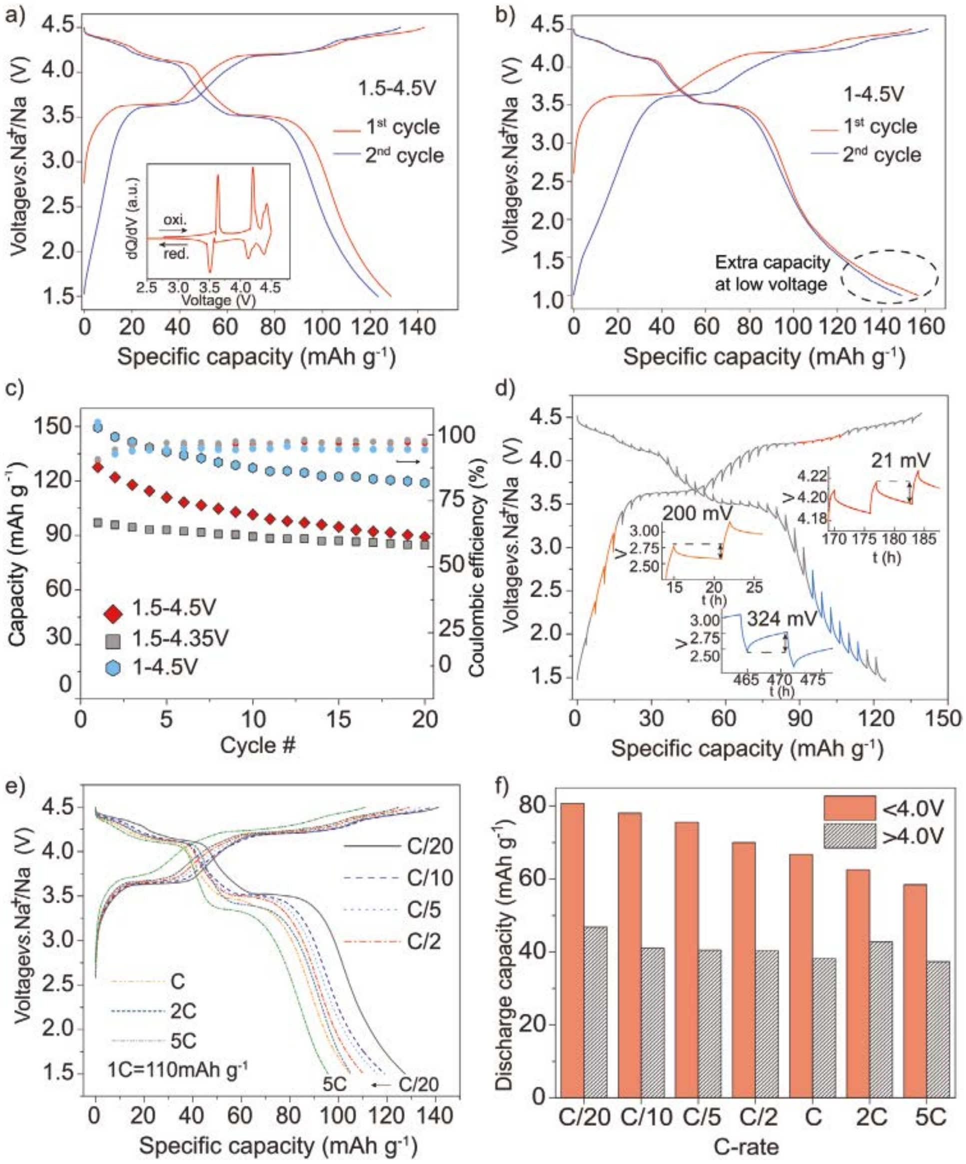

Figure 3. Electrochemical charge and discharge of an NMCP|Na metal half-cell cycled a) between 1.5 and 4.5 V and b) between 1 and 4.5 V at *C*/20 (1*C* = 110 mAh g^{-1}). c) Cycling performance and Coulombic efficiency of NMCP in different voltage windows. d) GITT curve of NMCP|Na metal half-cell during second cycle. Charging was performed at *C*/30 for 1 h, followed by a relaxation time of 6 h. Voltage versus time plots are presented as insets to highlight the relaxation intervals. e) Rate performance of NMCP charged and discharged at *C*-rates ranging from *C*/20 to 5*C* between 1.5 and 4.5 V. Note that we use 1*C* = 110 mAh g^{-1} (2Na) but not the theoretical capacity 166 mAh g^{-1} (3Na) to better compare with other NASICONs. f) Discharge capacity of NMCP for voltages >4 V (red) and <4 V (shaded) at various *C*-rates.

and 50 °C is summarized in Figure 4b. NMCP exhibits negligible capacity loss with nearly 100% Coulombic efficiency at all the temperatures after ten cycles, indicating its stable all-temperature electrochemical performance.

Because of the poor electrical conductivity of NMCP, the electrochemical performance is greatly affected by the carbon content. Cathode films with different carbon contents were prepared and tested under identical conditions (Figure S2, Supporting Information). As the active material:carbon:polytetrafluoroethylene (PTFE) ratio changes from 70:30:0 to 70:30:5 and then to 70:20:10, the discharge capacity first remains relatively constant from 131 to 130 mAh g^{-1} and finally drops to 112 mAh g^{-1}, indicating that the electrical conductivity of the cathode composite is a limiting factor. Moreover, the largest discharge capacity, 131 mAh g^{-1} (1.5–4.5 V) was achieved using a 70:30 active material to carbon ratio without any PTFE binder (Experimental Section), which is electronically insulating, yielding a high energy density of ≈470 Wh kg^{-1}.

X-ray absorption spectroscopy (XAS) analysis was conducted to investigate the redox mechanism of NMCP. Several ex situ samples were prepared at different charge and discharge states as shown in Figure S3 (Supporting Information). **Figure 5**a and Figure 5b show the X-ray absorption near-edge structure (XANES) for the Mn K-edge and Cr K-edge, respectively. Both the Mn and Cr K-edges shift to higher energy during charge and return almost to their initial positions when discharged

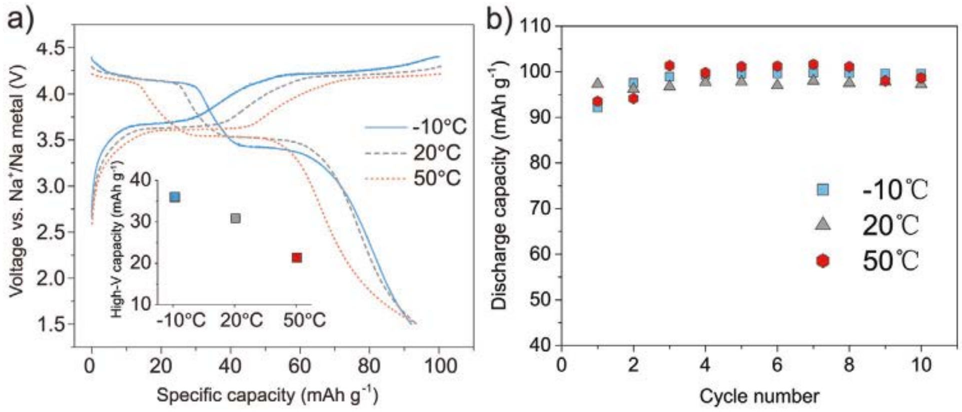

Figure 4. a) NMCP|Na metal half-cell cycled at –10, 20, and 50 °C at $C/10$. The charge capacity is limited to 100 mAh g^{-1}. The inset shows the discharge capacities of the high-voltage plateau cycled at different temperatures. b) Capacity retention of NMCP during first ten cycles at $C/10$. The charge capacity is limited to 100 mAh g^{-1}, and the voltage cutoff for discharge is 1.5 V.

back to 1.5 V, indicating that both Mn and Cr are electrochemically active and reversible during cycling. Specifically, Mn redox and Cr redox occur in sequence: Mn is only active from the open-circuit voltage (OCV) to somewhere between 3.9 and 4.3 V, as the Mn K-edge spectra at 4.3 and 4.5 V are almost identical. Cr is active from somewhere between 3.9 and 4.3 V to 4.5 V but not at lower voltage. While it is possible that within a small voltage region near 4.3 V, Mn and Cr redox could be both active, as the calculated voltages of $Mn^{3+/4+}$ and $Cr^{3+/4+}$ redox are extremely similar (Figure 1), it has been experimentally

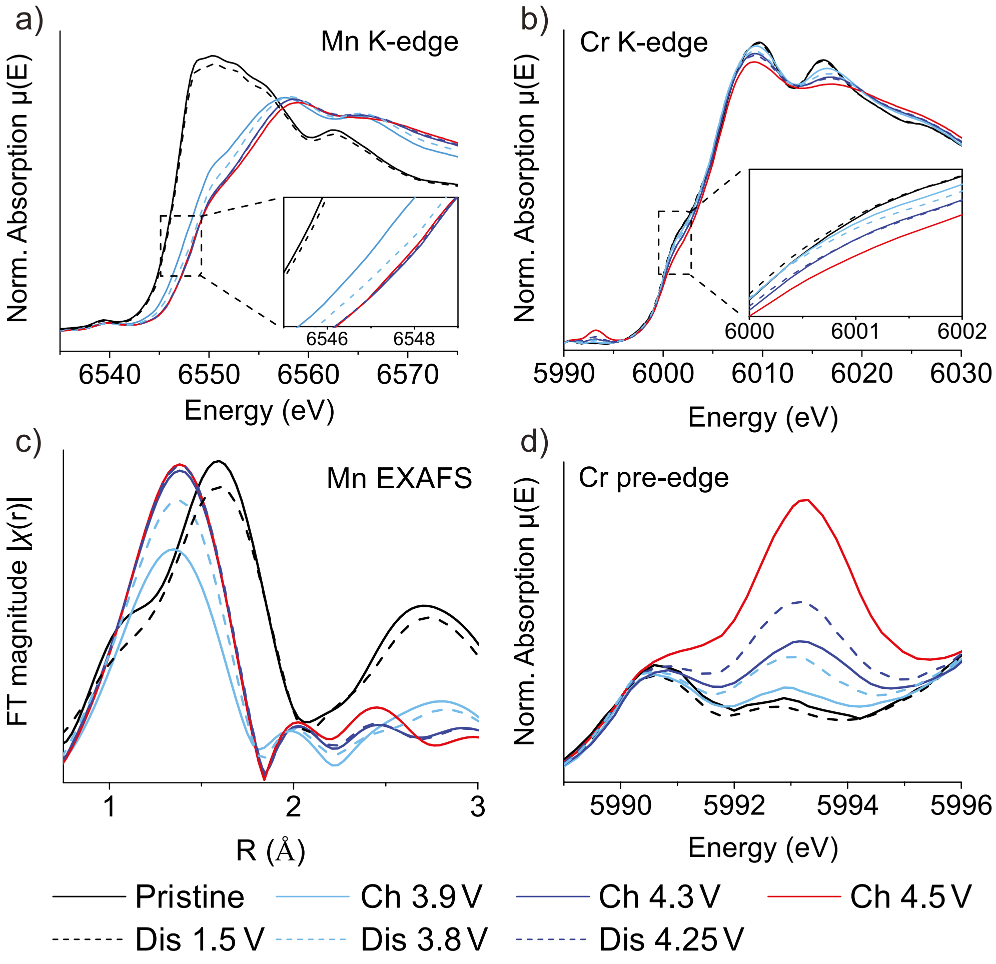

Figure 5. XAS spectra of NMCP at different charge/discharge states: a) Mn K-edge shift and b) Cr K-edge shift. c) k^2-weighted Fourier transform magnitudes of Mn K-edge EXAFS spectra. d) Pre-edge feature of Cr K-edge.

reported that Cr redox in NASICON framework tends to be higher than Mn redox.[20] Therefore, it is likely that the Mn redox contributes to the first two plateaus in the charge profile (Figure 3a) of NMCP, whereas the Cr redox mainly contributes to the third. The capacities of the first two plateaus are almost equal to two electrons per formula unit, so it is plausible to assume that double redox $Mn^{2+/3+}$ and $Mn^{3+/4+}$ are active. This observation is also consistent with the computational predictions in Table S3 (Supporting Information), which indicate that $Mn^{2+/3+}$ and $Mn^{3+/4+}$ redox are active from Na4 to Na2 and that the $Cr^{3+/4+}$ redox is active from Na2 to Na1.

The extended X-ray absorption fine structure (EXAFS) of Mn for samples at various charge states is presented in Figure 5c, where the first peak reflects the Mn—O bond length variation. As the pristine material is charged to 3.9 V, the first peak (Mn—O bond) shifts to the left and its intensity decreases. The reduced Mn—O bond length is consistent with the oxidation of Mn^{2+} to Mn^{3+}, and the decrease in peak intensity can be attributed to the Jahn–Teller distortion of Mn^{3+} that reduces the octahedral symmetry. Upon charging from 3.9 to 4.3 V, the Mn—O peak intensity increases again, indicating restored octahedral symmetry and Mn^{3+} ion is oxidized to Mn^{4+}. Note that the Mn—O peak position does not show obvious change between Mn^{3+} and Mn^{4+}, which is consistent with several previous studies.[23,32] When the sample is further oxidized to 4.5 V, both the intensity and position of the first peak barely change, consistent with the conclusion from the XAS data in Figure 5a that Mn is not active at higher voltage (>4.3 V). The EXAFS spectrum of the sample after one cycle does not perfectly overlap with that of the pristine sample, indicating a slight change of the Mn local structure as not all the Na extracted during charge is intercalated back when the material is discharged to 1.5 V.

Figure 5d shows the variation of the Cr pre-edge feature, providing insight into the Cr oxidation state. The spectrum taken in the pristine state remains unchanged upon charge to 3.9 V with only a single peak at ≈5590.05 eV. Upon further charge to 4.3 V, another peak at higher energy appears and continues to grow before returning to the pristine spectrum after one cycle. This prominent pre-edge peak results from the 1s–3d quadrupole transition, indicating the existence of Cr^{4+}.[20] As Cr^{4+} with the d^2 electron configuration usually has a distorted octahedral symmetry, the probability of Cr–3d and O–2p orbital mixing increases, thus increasing the probability of a 1s–3d transition; this transition is forbidden when Cr is present as Cr^{3+} which has a symmetric octahedral coordination.[33] In addition, the intensity of this pre-edge peak is less than 10% of the edge height, as shown in Figure 5b, thereby excluding the existence of Cr^{6+}, as tetrahedrally coordinated Cr^{6+} increases the pre-edge peak intensity dramatically (≈80% of the edge height). This pre-edge feature confirms that Cr is indeed oxidized to Cr^{4+} during charge.

To investigate the structural evolution during charge/discharge, in situ XRD analysis was performed and the results are plotted in **Figure 6**. The four observed peaks for the uncharged sample at $x = 4$ can be assigned as the (024), (211), (116), and (300) Bragg peaks of the pristine NMCP. Between $x = 4$ and $x \approx 3.5$, all four peaks shift slightly toward higher angle with no additional peak emerging, indicating that in this composition range NMCP forms a solid solution. Between $x \approx 3.5$ and $x \approx 3.2$, Na is further extracted by a two-phase mechanism as evidenced by the discrete position change of the (024) and (116) peaks and the disappearance of the (211) and (300) peaks. In addition, a new peak appears at 16.2°. From $x \approx 3.2$ to the top of charge, NMCP undergoes further single-phase desodiation since the (116) and (300) peaks continuously shift to higher angle, reaching a composition of $Na_{1.27}MnCr(PO_4)_3$ at 4.5 V. The discharge of NMCP follows the same but inverse sequence: single phase, two phases, and single phase. This reversible structural evolution is also observed for the subsequent cycle, as confirmed by the in situ diffraction data of two full cycles in Figure S4 (Supporting Information).

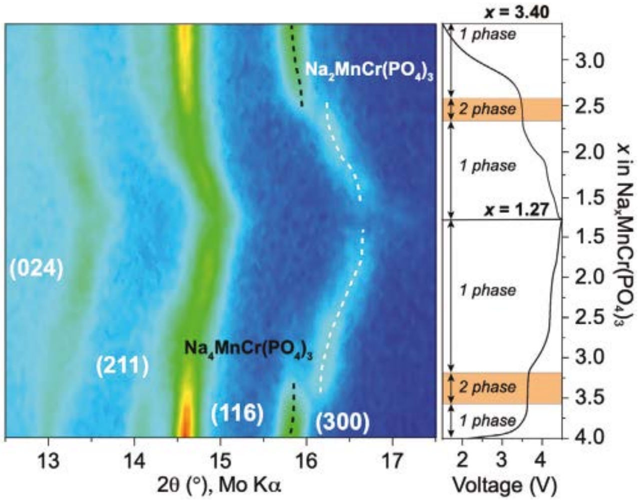

Figure 6. In situ XRD pattern of NMCP cycled between 1.5 and 4.5 V. The current rate was *C*/24, and an X-ray scan was performed every hour. The corresponding voltage profile is presented on the right, where the Na content was calculated from the capacity, assuming no electrolyte decomposition contribution.

The structural evolution of NMCP was further studied using ex situ synchrotron XRD. **Figure 7**a presents the diffraction patterns of samples at different states of charge with the extracted lattice parameters summarized in Figure 7b. The patterns for the pristine sample and sample after one cycle are almost identical, except for a slightly lower intensity for the cycled sample. In the single-phase region, between $x = 4$ and $x = 3.5$, the lattice parameters a (= b) and c both decrease negligibly ($|\Delta a/a| \approx 0.17\%$, $|\Delta c/c| \approx 0.37\%$), resulting in a small overall decrease in the unit cell volume ($|\Delta V/V| = 0.7\%$). The second phase appears at 3.9 V, of which the (2–10), (113), and (300) diffraction peaks are marked by the dashed line. They continue to shift to higher angle to the top of charge. Note that at 3.9 V, (2–10) and (104) peaks are so closed to each other that they are not clearly distinguished. Upon further Na removal, (2–10) peak shifts to higher angle faster than (104) peak. As a consequence, two peaks are observed separately at 4.5 V. In this region, NMCP endures a slightly larger lattice change, with the a and b lattice parameters decreasing ($|\Delta a/a| = 1.18\%$) and the c lattice parameter increasing ($|\Delta c/c| = 1.8\%$). The increase in c lattice parameter is prominent between $x \approx 2$ and $x \approx 1$ (Figure 7b), indicating that the third Na is likely extracted from the Na_1 site (Figure 2b) where the absence of Na leads to large electrostatic repulsion between adjacent $[(Mn/Cr)O_6]$

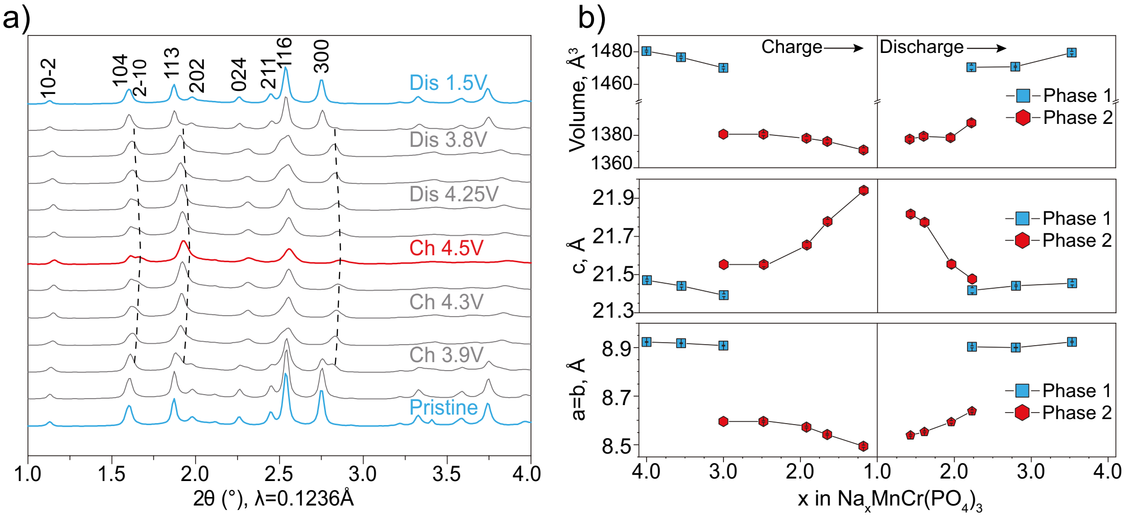

Figure 7. a) Ex situ synchrotron XRD patterns of NMCP at various states of charge. The black dashed line denotes the appearance and disappearance of the $Na_2MnCr(PO_4)_3$ phase. The samples were prepared as shown in Figure S3 (Supporting Information). b) Corresponding lattice parameters.

octahedra. The calculated lattice parameter changes are summarized in **Table 1** for comparison.

3. Discussion

The NASICON structure is able to accommodate different transition metal cations and is synthetically accessible with various Na contents, leading to a rich chemical space and tunable electrochemical performance.[16,18,22,23,34] Among all the redox-active metals, V and Mn have been favored because they can provide double redox at high voltage ($V^{3+/5+}$ and $Mn^{2+/4+}$). However, reversible 3Na (de)intercalation has not been possible in $Na_4MnV(PO_4)_3$ because an irreversible structural change occurs after the extraction of 3Na.[25] Mn is more preferable than V from a cost and energy density perspective because the $Mn^{2+/3+}$ (3.6 V) and $Mn^{3+/4+}$ (4.2 V)[19] redox potentials are higher than those of $V^{3+/4+}$ (3.4 V) and $V^{4+/5+}$ (≈4 V),[28] respectively. Hence, a Mn-based NASICON-type compound was preferred in our composition design. We show below that by systematically considering three types of Mn-based compositions, the MnCr appears naturally as the preferred compound. 1) The first compositional category contains the $Na_3Mn^{2+}M^{4+}(PO_4)_3$ compounds, which utilize $Mn^{2+/3+}$ and $Mn^{3+/4+}$ redox and possibly achieve the insertion of one more Na based on the $M^{3+/4+}$ redox; however, the reduction potential of the +4 metal is often very low (e.g., NMTP, $Ti^{3+/4+}$ ≈ 2.1 V), and an additional Na source such as a Na metal anode or a sacrificial salt (NaN_3 or NaP_3) is needed in practical application. 2) $Na_3Mn^{3+}M^{3+}(PO_4)_3$ compounds, which make use of $Mn^{3+/4+}$ and $M^{3+/4+}$ redox, have also been considered; however, they also require an additional Na source in a full cell to use $Mn^{3+/2+}$. In addition, it is relatively difficult to synthesize NASICON compounds with Mn^{3+} rather than with Mn^{2+} in the pristine material because of the reducing environment from the carbon source used during the synthesis created. 3) Finally, $Na_4Mn^{2+}M^{3+}(PO_4)_3$ can be considered; this compound type can use $Mn^{2+/3+}$, $Mn^{3+/4+}$, and $M^{3+/4+}$ redox, and the pristine material contains 4Na, which is optimal for achieving electrode balance in the full cell. Therefore, a NASICON-type compound with the composition $Na_4Mn^{2+}M^{3+}(PO_4)_3$, in principle, has three-electron redox at high voltage, and the trivalent metal can be Cr^{3+}, Fe^{3+}, Co^{3+}, or Ni^{3+}. The redox potentials of $Co^{3+/4+}$ and $Ni^{3+/4+}$ might be too high to access in the polyanionic framework[35] and the $Fe^{3+/4+}$ redox potential is around 3 V which is less attractive.[36] $Cr^{3+/4+}$ redox has been demonstrated to occur ≈4.5 V in NASICON-type $Na_3Cr_2(PO_4)_3$, which is within the electrolyte stability window, though significant capacity decay is observed in this compound.[20] However, in this work we demonstrate that based on the synergetic effect of Mn and Cr, $Na_4MnCr(PO_4)_3$ achieves a reasonable cyclability at a high operating voltage, and the highest energy density among all reported NASICON-type Na-ion cathodes (**Figure 8**).

Table 1. DFT calculated lattice parameters for $Na_xMnCr(PO_4)_3$.

Composition	$a = b$ [Å]	c [Å]
Na4	9.08	21.35
Na3	8.86	21.64
Na2	8.69	21.80
Na1	8.55	21.87

It is instructive to compare NMCP with another Mn^{2+}, M^{3+} compound in this category, NMVP. Although NMVP also has enough redox-active transition metal, it experiences an irreversible phase transformation when the third Na is extracted,[25] evidenced by the asymmetry behavior in the charge and discharge. A single-phase as well as two-phase structural transformation occurs in sequence in the charge of NMVP, whereas the discharge follows a single solid-solution mechanism with no two-phase region being observed. This structural irreversibility results in a low Coulombic efficiency of ≈74%, and the subsequent charge and discharge of NMVP occur via a single solid-solution mechanism with significant capacity fade.[25] In contrast, we observe in the present work that NMCP has a symmetric voltage profile, i.e., the charge and discharge curves both have three distinct plateaus, with the solid-solution and

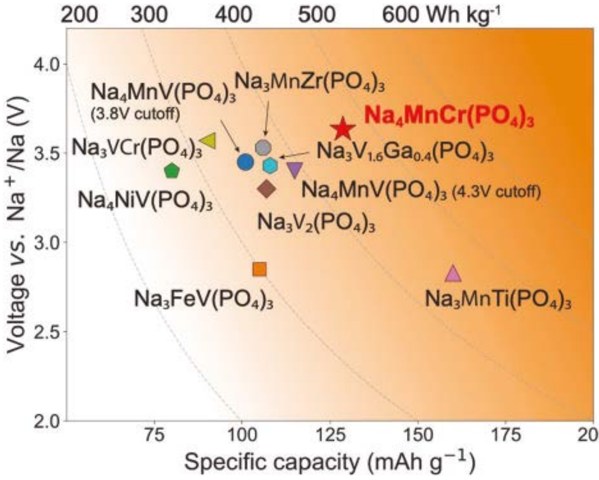

Figure 8. Capacity versus voltage plot of reported NASICON-type Na cathode materials.

two-phase reactions reversibly taking place during charge and discharge. This reversible structural evolution leads to a larger discharge capacity (130 mAh g^{-1}) at high voltage and higher Coulombic efficiency (≈91.5%) compared with NMVP. Our ex situ synchrotron XRD results also suggest that NMCP undergoes less volume change from Na2 to Na1 than NMVP (NMCP: $|\Delta a/a| = 1.18\%$, $|\Delta c/c| = 1.8\%$; NMVP: $|\Delta a/a| = 6.1\%$, $|\Delta c/c| = 2.4\%$[25]).

Because capacity fading is observed for both NMCP and NMVP after the extraction of 3Na, we computationally investigate the structural stability of the NASICON framework in the highly desodiated state by calculating the energy penalty of transition metal (TM) migration at a Na content of $x = 1$. As shown in Table S4 (Supporting Information), the calculated energy penalty associated with the migration of a Cr^{4+} (V^{5+}) cation to the adjacent unoccupied Na_2 site (Figure 2b) is 2.47 eV per defect (3.01 eV per defect), which is much higher than the M defect formation energy in layered Na_xMO_2 materials, which are known to suffer from structure instability at high voltage due to TM migration.[37] In addition, having Na reoccupied the TM site (TM/Na antisite) does not necessarily reduce the energy penalty. Our calculation suggests that TM migration is unlikely in the NASICON structure even at Na content $x = 1$; therefore, the origin of capacity fading at high voltage requires further investigation.

The electrochemical tests at various temperatures indicate that NMCP has a higher energy density at −10 °C than at RT and 50 °C if a capacity cutoff of 100 mAh g^{-1} is applied. This difference is observed because the temperature affects the capacity from the low-voltage and high-voltage regions differently, i.e., during discharge, low temperature increases the high-voltage capacity but decreases the low-voltage capacity. **Figure 9**a presents the voltage profile of the first two cycles of NMCP at 50 °C followed by a third cycle at 9 °C. Although the high-voltage discharge region is shortened at 50 °C, the capacity is regained during the following cycle at 9 °C, indicating that the high-voltage capacity reduction occurring at 50 °C is not an irreversible process. Ex situ XRD patterns of NMCP cycled at 50 and 9 °C are presented in Figure 9b, with no obvious difference observed at the top of charge, i.e., the charged crystal structures at 50 and 9 °C are the same. This observation indicates that the different voltage profiles may result from the different Na (de)intercalation pathways at various temperatures rather than to any structural aspect at the top of charge. As revealed by the in situ diffraction results, the Na (de)intercalation mechanism differs at the two plateaus: for the low-voltage plateau, NMCP is desodiated via a two-phase reaction, whereas a solid-solution mechanism is observed for the high-voltage one (Figure 6) so that it should probably be referred to as a "pseudoplateau" consistent with the fact that the GITT-relaxed voltages in this region are not constant (Figure 3d). As a two-phase reaction occurs through the nucleation and motion of an interface, extra kinetic barriers need to be overcome. High temperature will accelerate the nucleation and growth as these processes have a higher activation energy than diffusion, resulting in the elongation of the two-phase region (low-voltage region). Figure 9a clearly shows that the voltages in the low-voltage region at 50 °C are constant (two-phase reaction), while they do not become constant (solid solution) at 9 °C. Malik et al.[38] report a similar behavior of $LiFePO_4$ cathode, of which a nonequilibrium single-phase delithiation pathway is trigged by high rate to bypass

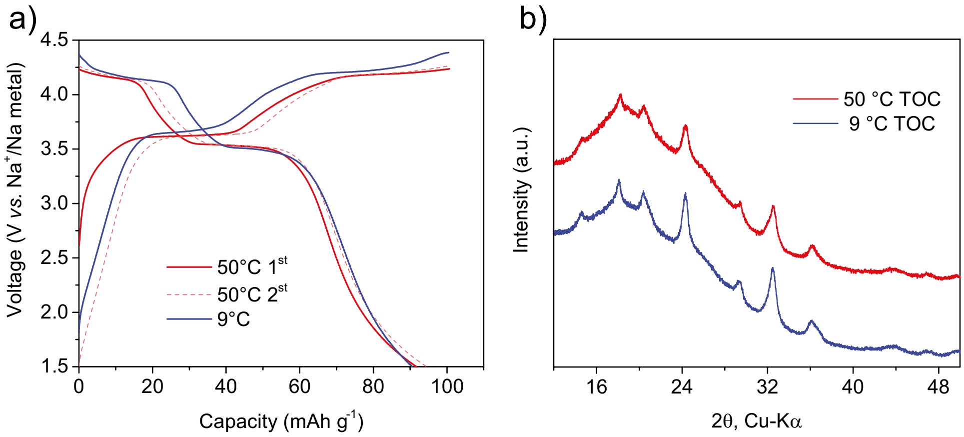

Figure 9. a) Voltage profile of NMCP|Na metal half-cell using a 100 mAh g^{-1} charge cutoff and 1.5 V discharge cutoff, at 50 °C, C/10 for the first two cycles (red), followed by a third cycle at 9 °C, C/10 (blue). b) Ex situ X-ray diffraction patterns of NMCP|C_{sp}|PTFE electrode cycled at 50 °C (red) and 9 °C (blue) at top of charge (100 mAh g^{-1}). X-ray diffraction was taken at RT immediately after cycled at different temperatures.

the equilibrium two-phase reaction. However, in our case, direct evidence such as in situ XRD at various temperatures is needed to confirm this speculation. We also plot in Figure S5 (Supporting Information) the voltage profile of NMCP cycled at low temperature (9 °C) and high temperature (50 °C) using a voltage cutoff (1.5–4.5 V). Though the charge capacity at high temperature is substantially larger than that at low temperature, the discharge capacities are similar because high temperature introduces more capacity degradation at high voltage.

In conclusion, we computationally predicted the phase stability and voltage profile of a novel NASICON-type compound, $Na_4MnCr(PO_4)_3$, which is synthesized via a sol–gel-assisted solid-state method. Electrochemically, NMCP delivers a capacity of 130 mAh g^{-1} when cycled between 1.5 and 4.5 V, with a high energy density of 470 Wh kg^{-1}. XAS analysis revealed a reversible redox mechanism based on $Mn^{2+/3+}$, $Mn^{3+/4+}$, and $Cr^{3+/4+}$ redox. Reversible and symmetric structural evolution during cycling was confirmed using in situ XRD and ex situ synchrotron XRD. The compound also has the remarkable property that it delivers higher energy density at low temperature than at high temperature.

4. Experimental Section

First-principles calculations were performed using DFT as implemented in the Vienna ab initio simulation package.[39] A kinetic energy cutoff of 520 eV was selected for the plane-wave basis set, and a 2 × 2 × 1 *k*-point grid was used in all the calculations. The Perdew–Burke–Ernzerhof (PBE) generalized gradient approximation (GGA) exchange-correlation functional with the rotationally invariant scheme of Hubbard-U correction[40] was applied to calculate the voltages. The values of $U_{\text{eff}} =$ 5.09 and 3.7 eV were employed for Mn and Cr, respectively, consistent with previous ab initio studies of the intercalation voltage of MnZr NASICONs and Mn phosphates.[19,41] Desodiated structures with Na/vacancy orderings were prescreened using an electrostatic energy criterion followed by DFT geometry optimizations. Na ions were extracted in the sequence from three Na ions at the Na_2 sites to one Na ion at the Na_1 site, which was consistent with previous findings in other NASICON structures.[34,42]

Material Synthesis: $Na_4MnCr(PO_4)_3$ was synthesized via a sol–gel-assisted solid-state method. First, manganese(II) acetate tetrahydrate (Aldrich, 99%) and chromium(III) nitrate nonahydrate (Sigma-Aldrich, 99%) in a 1:1 ratio were dissolved in deionized water. Then, citric acid (Sigma-Aldrich, ≥99.5%) was added using a 3:2 (transition metal) ratio. The solution was heated at 60 °C for 2 h with magnetic stirring before stoichiometric amounts of sodium phosphate monobasic (Sigma-Aldrich, ≥99%) and sodium acetate (Sigma-Aldrich, ≥99%) were added sequentially to the solution, which was then thoroughly stirred at 90 °C overnight to evaporate the solvent. The resulting gel-like mixture was collected, ground, and fired at 400 °C for 6 h in argon and then re-ground and fired at 650 °C for 8 h in argon.

Structural Characterization: High-energy X-ray powder diffraction data were collected at beamline 6-ID-D at the Advanced Photon Source, Argonne National Laboratory with a wavelength of $\lambda = 0.1236$ Å. The samples were sealed in Kapton capillaries with the measurements performed using a 0.1 s exposure time for 30 s. Ex situ synchrotron XRD samples were prepared using a 70:30 ratio of active material:C_{sp} and cycled to various states of charge at *C*/20 before the powder was recovered, washed, centrifuged, and collected. Lab XRD data were collected using a Rigaku MiniFlex 600 diffractometer. Data analysis was performed using Rietveld refinement[43] (as-synthesized material) and the Le Bail method[44] (ex situ samples) using FullProf software.[45] Structure visualization was performed with VESTA.[46]

SEM images were captured using a Zeiss Gemini Ultra-55 analytical field-emission microscope at the Molecular Foundry at Lawrence Berkeley National Laboratory.

High-angle annular dark-field scanning transmission electron microscopy and EDX mapping were performed using an FEI TitanX 60–300 at the Molecular Foundry at Lawrence Berkeley National Laboratory.

XAS data were collected at beamline 20 BM at the Advanced Photon Source, Argonne National Laboratory. Samples were prepared with a 70:30:5 active material:C_{sp}:PTFE ratio and cycled to various states of charge at *C*/20 before the powder was recovered, rinsed, and collected. All the samples were sealed with Kapton tape for XAS measurements. Data reduction, normalization, and analysis were performed using the Demeter package.[47]

In situ electrochemical tests were performed with a customized cell with a beryllium window allowing X-ray penetration. The experiments were conducted on a Bruker D8 diffractometer using Bragg–Brentano geometry with Mo Kα radiation. Each scan was performed for 1 h while the cell was cycled at *C*/24 for two full cycles.

Electrochemical Methods: To prepare the cathode film, the $Na_4MnCr(PO_4)_3$ powder and carbon black (Timcal, Super P) were first mixed using a Fritsch Pulverisette ball mill (with one steel sphere) for 20 min at 20 s^{-1}. The powder was then recovered and PTFE (Dupont, Teflon 8C) was added and mixed using a mortar and pestle before the sample was rolled into a thin film inside an argon-filled glove box. The weight ratio of active material:C_{sp}:PTFE was 70:30:5. To assemble a coin cell for electrochemical tests, 1 M $NaPF_6$ in a 1:1 solution of ethylene carbonate (Sigma-Aldrich, 99%, anhydrous) and diethyl carbonate (Sigma-Aldrich, ≥99%, anhydrous) was used as the electrolyte, and Na metal was used as the negative electrode. The CR2032 coin cells were assembled inside an argon-filled glove box and tested on an Arbin instrument at room temperature in galvanostatic mode.

Supporting Information

Supporting Information is available from the Wiley Online Library or from the author.

Acknowledgements

This work was supported by the Samsung Advanced Institute of Technology. Work at the Molecular Foundry, LBNL was supported by the Office of Science, Office of Basic Energy Sciences of the U.S. Department of Energy under Contract No. DE-AC02-05CH11231. Use of the Advanced Photon Source at Argonne National Laboratory was supported by the U.S. Department of Energy, Office of Science, Office of Basic Energy Sciences under Contract No. DE-AC02-06CH11357. The authors acknowledge Dr. Hyunchul Kim, Dr. Guobo Zeng, and Dr. Jianping Huang for valuable discussions; Zijian Cai for assistance with the XAS measurements; and Dr. Douglas Robinson for assistance at APS.

Conflict of Interest

The authors declare no conflict of interest.

Keywords

Na-ion batteries, Na-ion cathode materials, NASICON

Received: December 2, 2019

[1] a) B. L. Ellis, L. F. Nazar, *Curr. Opin. Solid State Mater. Sci.* **2012**, *16*, 168; b) H. Pan, Y.-S. Hu, L. Chen, *Energy Environ. Sci.* **2013**, *6*, 2338; c) J.-M. Tarascon, *Nat. Chem.* **2010**, *2*, 510.
[2] X. Xiang, K. Zhang, J. Chen, *Adv. Mater.* **2015**, *27*, 5343.
[3] a) S. W. Kim, D. H. Seo, X. Ma, G. Ceder, K. Kang, *Adv. Energy Mater.* **2012**, *2*, 710; b) K. Kubota, S. Komaba, *J. Electrochem. Soc.* **2015**, *162*, A2538; c) D. Kundu, E. Talaie, V. Duffort, L. F. Nazar, *Angew. Chem., Int. Ed.* **2015**, *54*, 3431; d) M. D. Slater, D. Kim, E. Lee, C. S. Johnson, *Adv. Funct. Mater.* **2013**, *23*, 947; e) N. Yabuuchi, K. Kubota, M. Dahbi, S. Komaba, *Chem. Rev.* **2014**, *114*, 11636.
[4] a) I. Hasa, S. Passerini, J. Hassoun, *J. Mater. Chem. A* **2017**, *5*, 4467; b) L. Liu, X. Li, S. H. Bo, Y. Wang, H. Chen, N. Twu, D. Wu, G. Ceder, *Adv. Energy Mater.* **2015**, *5*, 1500944; c) N. Yabuuchi, M. Kajiyama, J. Iwatate, H. Nishikawa, S. Hitomi, R. Okuyama, R. Usui, Y. Yamada, S. Komaba, *Nat. Mater.* **2012**, *11*, 512.
[5] a) M. H. Han, E. Gonzalo, G. Singh, T. Rojo, *Energy Environ. Sci.* **2015**, *8*, 81; b) N. Ortiz-Vitoriano, N. E. Drewett, E. Gonzalo, T. Rojo, *Energy Environ. Sci.* **2017**, *10*, 1051.
[6] a) C. Masquelier, L. Croguennec, *Chem. Rev.* **2013**, *113*, 6552; b) Q. Ni, Y. Bai, F. Wu, C. Wu, *Adv. Sci.* **2017**, *4*, 1600275.
[7] Z. Jian, W. Han, X. Lu, H. Yang, Y. S. Hu, J. Zhou, Z. Zhou, J. Li, W. Chen, D. Chen, *Adv. Energy Mater.* **2013**, *3*, 156.
[8] F. Lalère, V. Seznec, M. Courty, R. David, J. Chotard, C. Masquelier, *J. Mater. Chem. A* **2015**, *3*, 16198.
[9] R. Gover, A. Bryan, P. Burns, J. Barker, *Solid State Ionics* **2006**, *177*, 1495.
[10] a) Y. U. Park, D. H. Seo, H. Kim, J. Kim, S. Lee, B. Kim, K. Kang, *Adv. Funct. Mater.* **2014**, *24*, 4603; b) P. Serras, V. Palomares, A. Goñi, I. G. de Muro, P. Kubiak, L. Lezama, T. Rojo, *J. Mater. Chem.* **2012**, *22*, 22301.
[11] M. Bianchini, P. Xiao, Y. Wang, G. Ceder, *Adv. Energy Mater.* **2017**, *7*, 1700514.
[12] M. Xu, P. Xiao, S. Stauffer, J. Song, G. Henkelman, J. B. Goodenough, *Chem. Mater.* **2014**, *26*, 3089.
[13] H. Yi, M. Ling, W. Xu, X. Li, Q. Zheng, H. Zhang, *Nano Energy* **2018**, *47*, 340.
[14] a) S. Chen, C. Wu, L. Shen, C. Zhu, Y. Huang, K. Xi, J. Maier, Y. Yu, *Adv. Mater.* **2017**, *29*, 1700431; b) Z. Jian, Y.-S. Hu, X. Ji, W. Chen, *Adv. Mater.* **2017**, *29*, 1601925; c) S. Li, Y. Dong, L. Xu, X. Xu, L. He, L. Mai, *Adv. Mater.* **2014**, *26*, 3545; d) C. Zhu, K. Song, P. A. van Aken, J. Maier, Y. Yu, *Nano Lett.* **2014**, *14*, 2175.
[15] C. Delmas, F. Cherkaoui, A. Nadiri, P. Hagenmuller, *Mater. Res. Bull.* **1987**, *22*, 631.
[16] W. Zhou, L. Xue, X. Lü, H. Gao, Y. Li, S. Xin, G. Fu, Z. Cui, Y. Zhu, J. B. Goodenough, *Nano Lett.* **2016**, *16*, 7836.
[17] Y. Yu, X. Zhang, X. Rui, D. Chen, H. T. Tan, D. Yang, S. Huang, *Nanoscale* **2019**, *11*, 2556.
[18] Y. Jiang, J. Shi, M. Wang, L. Zeng, L. Gu, Y. Yu, *ACS Appl. Mater. Interfaces* **2016**, *8*, 689.
[19] H. Gao, I. D. Seymour, S. Xin, L. Xue, G. Henkelman, J. B. Goodenough, *J. Am. Chem. Soc.* **2018**, *140*, 18192.
[20] K. Kawai, W. Zhao, S.-i. Nishimura, A. Yamada, *ACS Appl. Energy Mater.* **2018**, *1*, 928.
[21] R. Liu, G. Xu, Q. Li, S. Zheng, G. Zheng, Z. Gong, Y. Li, E. Kruskop, R. Fu, Z. Chen, K. Amine, Y. Yang, *ACS Appl. Mater. Interfaces* **2017**, *9*, 43632.
[22] Q. Hu, J.-Y. Liao, X.-D. He, S. Wang, L.-N. Xiao, X. Ding, C.-H. Chen, *J. Mater. Chem. A* **2019**, *7*, 4660.
[23] A. Leclaire, M.-M. Borel, A. Grandin, B. Raveau, *Acta Crystallogr., Sect. A: Found. Crystallogr.* **1989**, *45*, 699.
[24] R. V. Panin, O. A. Drozhzhin, S. S. Fedotov, N. R. Khasanova, E. V. Antipov, *Electrochim. Acta* **2018**, *289*, 168.
[25] F. Chen, V. M. Kovrugin, R. David, O. Mentré, F. Fauth, J.-N. Chotard, C. Masquelier, *Small Methods* **2018**, *3*, 1800218.
[26] M. V. Zakharkin, O. A. Drozhzhin, I. V. Tereshchenko, D. Chernyshov, A. M. Abakumov, E. V. Antipov, K. J. Stevenson, *ACS Appl. Energy Mater.* **2018**, *1*, 5842.
[27] H. Gao, Y. Li, K. Park, J. B. Goodenough, *Chem. Mater.* **2016**, *28*, 6553.
[28] T. Zhu, P. Hu, X. Wang, Z. Liu, W. Luo, K. A. Owusu, W. Cao, C. Shi, J. Li, L. Zhou, L. Mai, *Adv. Energy Mater.* **2019**, *9*, 1803436.
[29] A. Jain, S. P. Ong, G. Hautier, W. Chen, W. D. Richards, S. Dacek, S. Cholia, D. Gunter, D. Skinner, G. Ceder, *APL Mater.* **2013**, *1*, 011002.
[30] M. K. Aydinol, *J. Electrochem. Soc.* **1997**, *144*, 3832.
[31] K. Saravanan, C. W. Mason, A. Rudola, K. H. Wong, P. Balaya, *Adv. Energy Mater.* **2013**, *3*, 444.
[32] a) Z. Lun, B. Ouyang, D. A. Kitchaev, R. J. Clément, J. K. Papp, M. Balasubramanian, Y. Tian, T. Lei, T. Shi, B. D. McCloskey, *Adv. Energy Mater.* **2019**, *9*, 1802959; b) L. Baggetto, K. J. Carroll, R. R. Unocic, C. A. Bridges, Y. S. Meng, G. M. Veith, *ECS Trans.* **2014**, *58*, 47.
[33] M. L. Peterson, G. E. BrownJr., G. A. Parks, C. L. Stein, *Geochim. Cosmochim. Acta* **1997**, *61*, 3399.
[34] O. Tillement, J. Angenault, J. C. Couturier, M. Quarton, *Solid State Ionics* **1991**, *44*, 299.
[35] a) P. R. Kumar, H. B. Yahia, I. Belharouak, M. T. Sougrati, S. Passerini, R. Amin, R. Essehli, *J. Solid State Electrochem.* **2020**, *24*, 17; b) M. Nose, K. Nobuhara, S. Shiotani, H. Nakayama, S. Nakanishi, H. Iba, *RSC Adv.* **2014**, *4*, 9044.
[36] a) R. Rajagopalan, B. Chen, Z. Zhang, X. L. Wu, Y. Du, Y. Huang, B. Li, Y. Zong, J. Wang, G. H. Nam, *Adv. Mater.* **2017**, *29*, 1605694; b) H. Kim, I. Park, S. Lee, H. Kim, K.-Y. Park, Y.-U. Park, H. Kim, J. Kim, H.-D. Lim, W.-S. Yoon, K. Kang, *Chem. Mater.* **2013**, *25*, 3614.
[37] a) X. Li, Y. Wang, D. Wu, L. Liu, S.-H. Bo, G. Ceder, *Chem. Mater.* **2016**, *28*, 6575; b) S. Kim, X. Ma, S. P. Ong, G. Ceder, *Phys. Chem. Chem. Phys.* **2012**, *14*, 15571.
[38] R. Malik, F. Zhou, G. Ceder, *Nat. Mater.* **2011**, *10*, 587.
[39] G. Kresse, J. Furthmüller, *Phys. Rev. B* **1996**, *54*, 11169.
[40] S. L. Dudarev, G. A. Botton, S. Y. Savrasov, C. J. Humphreys, A. P. Sutton, *Phys. Rev. B* **1998**, *57*, 1505.
[41] F. Zhou, M. Cococcioni, C. A. Marianetti, D. Morgan, G. Ceder, *Phys. Rev. B* **2004**, *70*, 235121.
[42] S. Y. Lim, H. Kim, R. A. Shakoor, Y. Jung, J. W. Choi, *J. Electrochem. Soc.* **2012**, *159*, A1393.
[43] H. Rietveld, *J. Appl. Crystallogr.* **1969**, *2*, 65.
[44] A. Altomare, M. C. Burla, M. Camalli, G. L. Cascarano, C. Giacovazzo, A. Guagliardi, A. G. Moliterni, G. Polidori, R. Spagna, *J. Appl. Crystallogr.* **1999**, *32*, 115.
[45] J. Rodriguez-Carvajal, *Phys. B* **1993**, *192*, 55.
[46] K. Momma, F. Izumi, *J. Appl. Crystallogr.* **2011**, *44*, 1272.
[47] B. Ravel, M. Newville, *J. Synchrotron Radiat.* **2005**, *12*, 537.

ADVANCED ENERGY MATERIALS
www.advenergymat.de

High Active Material Loading in All-Solid-State Battery Electrode via Particle Size Optimization

*Tan Shi, Qingsong Tu, Yaosen Tian, Yihan Xiao, Lincoln J. Miara, Olga Kononova, and Gerbrand Ceder**

Low active material loading in the composite electrode of all-solid-state batteries (SSBs) is one of the main reasons for the low energy density in current SSBs. In this work, it is demonstrated with both modeling and experiments that in the regime of high cathode loading, the utilization of cathode material in the solid-state composite is highly dependent on the particle size ratio of the cathode to the solid-state conductor. The modeling, confirmed by experimental data, shows that higher cathode loading and therefore an increased energy density can be achieved by increasing the ratio of the cathode to conductor particle size. These results are consistent with ionic percolation being the limiting factor in cold-pressed solid-state cathode materials and provide specific guidelines on how to improve the energy density of composite cathodes for solid-state batteries. By reducing solid electrolyte particle size and increasing the cathode active material particle size, over 50 vol% cathode active material loading with high cathode utilization is able to be experimentally achieved, demonstrating that a commercially-relevant, energy-dense cathode composite is achievable through simple mixing and pressing method.

1. Introduction

All-solid-state batteries (SSBs) have become an exciting energy storage technology to replace conventional lithium-ion batteries.[1,2] They improve safety by removing organic carbonate-based liquid electrolytes and can potentially increase energy density by utilizing a Li-metal anode.[3] However, while proof of concept of SSBs has been shown, multiple hurdles still have to be overcome before they can truly compete with today's commercialized Li-ion cells in terms of energy density.[4] In this paper, we focus on active material loading in the cathode as one of these challenges. Composite cathodes for SSBs are typically made up of the cathode active material (CAM), a solid electrolyte (SE), and carbon, and can be fabricated in multiple ways, the simplest one of them consisting of mixing the three components and then pressing or sintering them together with the bulk SE/separator layer.[5–8] However, because of the large solid-electrolyte fraction (30–50 wt%) typically required in cathode composites to provide sufficient ionic diffusion,[5,6,9,10] the volume fraction of cathode (cathode loading) of current SSBs is low, resulting in low energy density. Considering that the cathode loading of liquid cells is typically greater than 90 wt% (or 50 vol%),[11,12] achieving full capacity in an energy-dense electrode (with >50 vol% cathode loading) is vital for SSBs to be competitive with conventional lithium-ion batteries. An optimal composite cathode morphology should have minimal void space and good cathode/SE contact, and include the minimum amount of SE needed to ensure sufficient Li diffusion between the CAM and bulk electrolyte. Several studies have separately demonstrated that the CAM and SE particle sizes affect the morphology of a cold-pressed cathode composite as well as the full-cell performance.[7,13–16]

Using experiments and modeling, we demonstrate in this work that, somewhat surprisingly, very high volume fractions of the cathode can be fully utilized in a composite cathode as long as the ratio of the SE to cathode particle size is controlled. We find that the most critical factor in obtaining high energy density is to keep the SE particle size smaller than that of the active cathode material. By reducing the conductor particle size by a factor 2–3 the cathode, utilization can improve from 20% to 100% even at high total cathode loading. The higher the volume loading of the cathode, the smaller the ratio of SE to cathode size needs to be.

Our modeling results are verified using Li_2O–ZrO_2 (LZO)-coated $LiNi_{0.5}Mn_{0.3}Co_{0.2}O_2$ (NMC) as the CAM and amorphous $75Li_2S$–$25P_2S_5$ (LPS) as the SE. Using small-particle-size LPS ($\bar{D}_{SE} \approx 1.5$ μm) and large-particle-size NMC ($\bar{D}_{CAM} \approx 12$ μm), we are able to dramatically increase cathode loading towards a commercially viable level without sacrificing specific capacity.

T. Shi, Dr. Q. Tu, Y. Tian, Y. Xiao, Dr. O. Kononova, Prof. G. Ceder
Department of Materials Science and Engineering
University of California
Berkeley, CA 94720, USA
E-mail: gceder@berkeley.edu

Y. Xiao, Prof. G. Ceder
Materials Sciences Division
Lawrence Berkeley National Laboratory
Berkeley, CA 94720, USA

Dr. L. J. Miara
Advanced Materials Lab
Samsung Research America
3 Van de Graaff Drive, Burlington, MA 01803, USA

The ORCID identification number(s) for the author(s) of this article can be found under https://doi.org/10.1002/aenm.201902881.

DOI: 10.1002/aenm.201902881

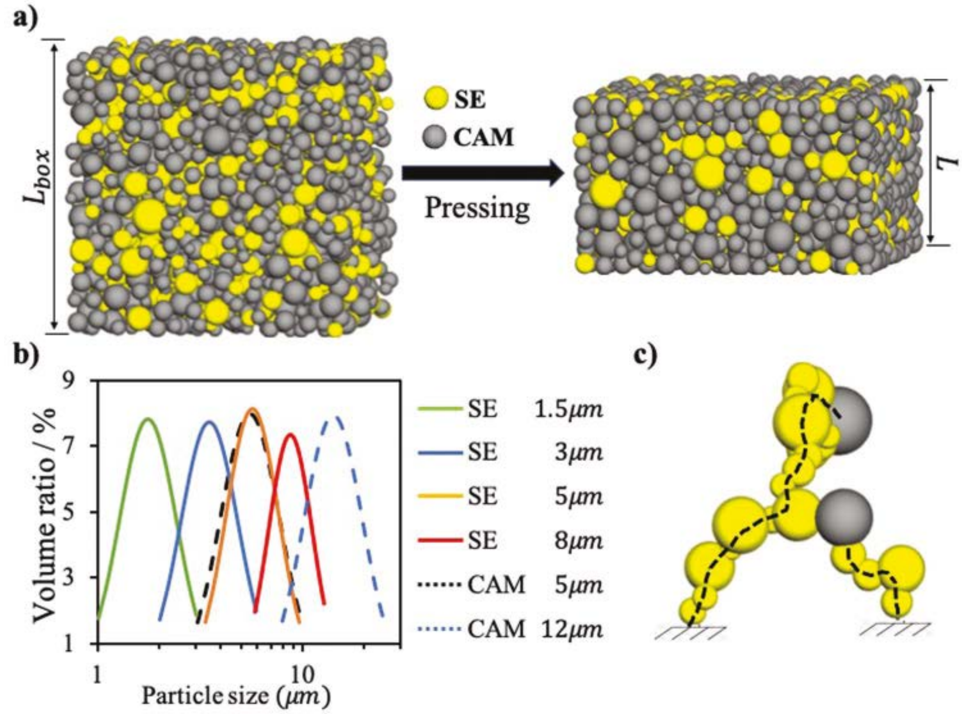

Figure 1. a) Example microstructures showing the composite cathode from its initial cubic shape (top-left, with box size L_{box}) to its final compact shape (bottom-left, with height L) under a pressing pressure of 200 MPa. The model was built using the following parameters: $f_{\text{CAM}} =$ 80 wt%, $\overline{D}_{\text{SE}} = 5$ µm, $\overline{D}_{\text{CAM}} = 5$ µm. b) Particle size distributions used in the simulation. The average particle diameters and standard deviations measured from the SEM images were used as inputs in the log-normal distributions. c) Ionic percolating paths for two typical CAM particles (black dash lines). The paths connect CAM particles to the composite cathode/bulk SE interface (bottom of the simulation box).

Our results provide simple design guidelines to improve the energy density of solid-state batteries by achieving high CAM loading in the composite cathode.

2. Computational and Experimental Methods

2.1. Microstructural Modeling

We systematically studied the relation between cathode loading (f_{CAM}), cathode utilization (θ_{CAM}), and the particle size of the CAM and the SE through a basic model for the composite cathode. Numerical representations of 3D electrode microstructures are generated by randomly inserting spherical CAM and SE particles into a cubic simulation domain (V_{Box}), as shown in **Figure 1**a. Electronic conductive agents such as carbon nanofibers (CNFs) are not included in the model as the current study focuses on ionic percolation in the cathode composite. The weight fractions of CAM and SE are defined as $f_{\text{CAM}} = \frac{0.95 M_{\text{CAM}}}{M_{\text{CAM}} + M_{\text{SE}}}$ and $f_{\text{SE}} = \frac{0.95 M_{\text{SE}}}{M_{\text{CAM}} + M_{\text{SE}}}$, where M_{CAM} and M_{SE} are the weights of the CAM and SE, respectively. The prefactor (0.95) is used to account for the 5 wt% CNF used in our experimental cells, but not explicitly included in our model. The standard log-normal particle size distributions used in the simulation have average particle diameter $\overline{D}_c$ and standard deviation σ_c (c is either the CAM or the SE), and are shown in Figure 1b. They match the scanning electron microscopy (SEM) measurements of our experimental material as close as possible and are of similar form to what have been used in other studies.[7,17]

A discrete element method (DEM) implemented in the open-source package LIGGGHTS was used to simulate the pressing process in the experiment.[18–20] Granular contact walls were placed at the bottom and all four vertical boundaries of the box. A flat surface was applied at the top of the simulation box and moved downward at a prescribed velocity until the system reaches a specified pressure of 200 MPa. Pressure was then held constant until the system reaches static equilibrium (i.e., the kinetic energy of the system decayed to zero).[21] The Hertzian granular contact potential was used to describe the normal and tangential interactions and damping forces[22] as well as the frictional yield (further details are provided in Section S1 in the Supporting Information).[23]

Because Li-ion diffusion is much faster in the SE than in the CAM,[24] we only consider Li-ion percolation pathways through SE particles.[25] A CAM particle is considered to be “active” if at least one Li percolation pathway connects it to the bulk SE layer (as shown in Figure 1c). To analyze whether a CAM particle is active or inactive, we first built networks of CAM particles by connecting each node (CAM or SE particles) with its neighbors and then defined CAM particles as source nodes and SE particles located at the bottom boundary as target nodes.[26] From the network, we extracted the shortest percolating pathway of each active CAM particle to a SE target particle. The cathode utilization (θ_{CAM}) in a cathode composite is the ratio of the volume of the active CAM particles to the total CAM volume

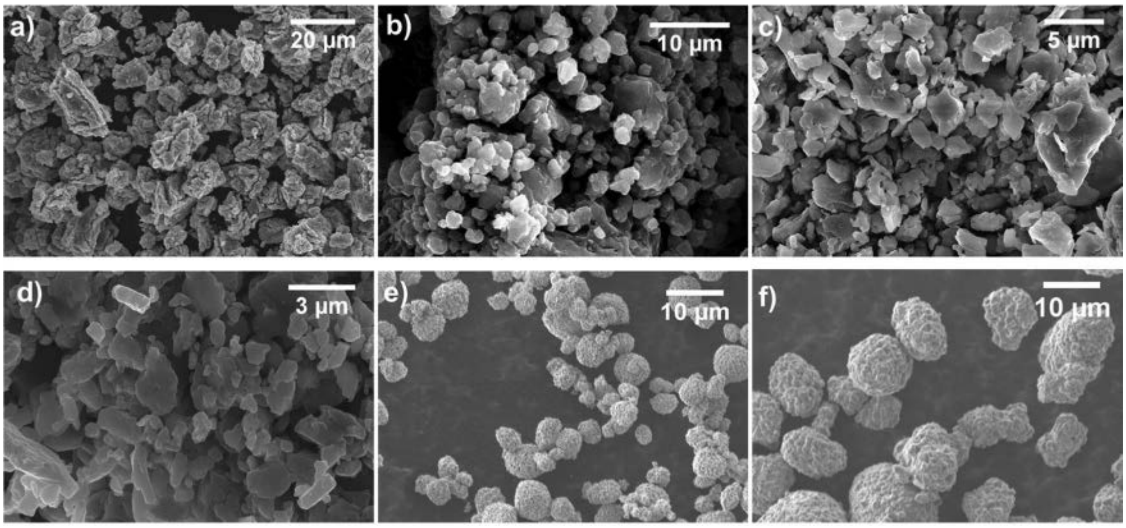

Figure 2. a–d) SEM images of LPS with average particle diameters of a) 8, b) 5, c) 3, and d) 1.5 µm prepared using different wet-ball-milling conditions. e,f) SEM images of LZO-coated NMC cathode particles with average diameters of e) 5 and f) 12 µm.

($\theta_{\mathrm{CAM}} = V_{\mathrm{CAM}}^{\mathrm{active}} / V_{\mathrm{CAM}}$). The result for each condition was averaged using at least three different random initial configurations.

The convergence of the percolation results with the simulation box size is discussed in Section S2 in the Supporting Information. We observed an empirical relation between the minimal initial box size for convergence and the maximal particle size in the model: $L_{\min} \approx 10\bar{D}_{\max}$. Therefore, the box sizes of all the models used in the current study were set to be 1.5-times larger than the critical minimal box size: $L_{\mathrm{box}} = 1.5L_{\min} \approx 15\bar{D}_{\max}$.

2.2. Experimental Details

2.2.1. Materials Synthesis and Characterization

In our experiments, NMC and LPS were used as the cathode (CAM) and SE materials, respectively. Small-sized NMC powder ($\bar{D}_{\mathrm{CAM}} \approx 5$ µm) was provided by Samsung Research Japan, and large-sized NMC powder ($\bar{D}_{\mathrm{CAM}} = \approx 12$ µm) was purchased from MSE Supplies LLC. The 6–8 nm LZO coating was applied to both NMC powders by Samsung Research Japan using the procedure described by Ito et al.[6] The LZO-coated NMC has been shown to minimize the interfacial reaction between NMC and LPS, allowing the current study to mainly focus on the particle size effect. The bulk LPS SE used as the separator was synthesized by ball milling stoichiometric amounts of Li_2S (99.98% Sigma-Aldrich) and P_2S_5 (99% Sigma-Aldrich) in a 50-mL ZrO_2 jar for 200 min using a SPEX 8000M mixer mill. The resulting LPS SE shows an ionic conductivity of 0.39 mS cm^{-1}, consistent with previous reports.[27] The small-particle-size LPS used in the cathode composite was prepared by wet ball milling the LPS SE with heptane and dibutyl ether using a Retsch PM200 ball mill.[7] LPS particles with different average diameters were prepared using ZrO_2 balls ranging in size from 1 to 10 mm under different ball-milling conditions. The detailed preparation conditions and the ionic conductivities of the small particle LPS are provided in Table S3 in the Supporting Information. We note that the ionic conductivities of the LPS decrease with smaller particle sizes. This is likely because of the increased grain boundary (or particle boundary) resistance, which can be worsened by any residual solvent from the wet ball milling process. LPS with four different average particle sizes (8, 5, 3, and 1.5 µm) was tested with LZO-coated NMC particles with average particle sizes of 5 and 12 µm. Representative SEM images of all the particles are presented in **Figure 2**.

The SEM images were obtained using a Zeiss Gemini Ultra-55 analytical field-emission scanning electron microscope, and were used to estimate the particle sizes. For each sample, the diameters of ≈200 random particles were measured, and the average value was recorded.

2.2.2. Cell Fabrication and Testing

Solid-state cells were fabricated in an Ar-filled glovebox ($H_2O < 0.1$ ppm and $O_2 < 0.1$ ppm). The composite cathode was fabricated by first hand-mixing the LZO-coated NMC particles and LPS for ≈10 min and then mixing them for another ≈10 min after adding 5 wt% CNFs (from Samsung Research Japan). The cell was assembled using a custom-made pressure cell consisting of a polyether ether ketone (PEEK) cylinder with an inner diameter of 8 mm and two 8-mm-diameter stainless-steel rods as current collectors. The cell was made by closing one end of the cylinder with a current collector. Bulk LPS electrolyte (35 mg) was added and compressed under ≈100-MPa pressure. The cathode composite (≈5 mg) was then spread evenly on top and compacted under ≈200-MPa pressure. Finally, an 8-mm-diameter piece of In metal was attached as the anode, and ≈200-MPa pressure was again applied. The cell was sealed in an Ar-filled airtight jar and cycled under ≈5-MPa pressure provided by a spring.

Cell cycling was performed using a Bio-Logic VMP300 system. For all the cells, the cycling voltage window and current density were set to 2–3.7 V versus In metal and 0.05 mA cm^{-2}, respectively. Constant current constant voltage (CCCV) charging was used, where the cell was held for 5 h at the top-of-charge state.

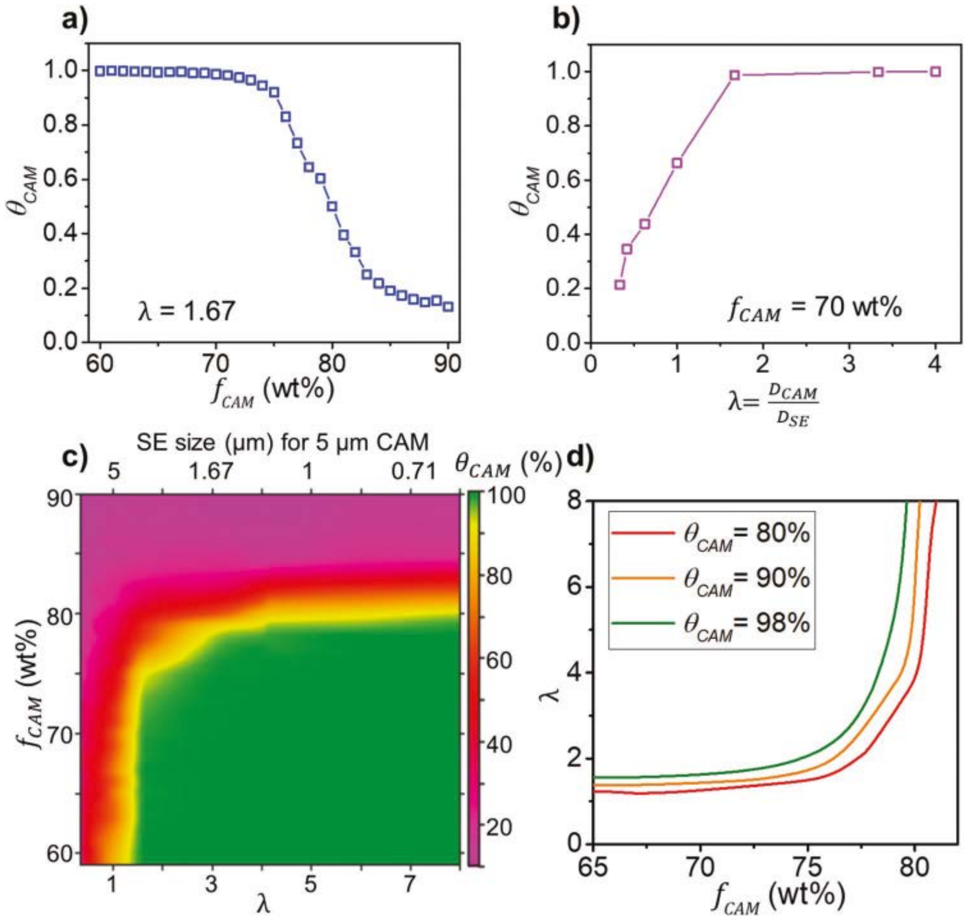

Figure 3. Modeling results showing the effect of a) f_{CAM} and b) λ on θ_{CAM}. c) θ_{CAM} as a function of both λ and f_{CAM}. d) Critical λ needed to achieve $\theta_{\mathrm{CAM}} =$ 80%, 90%, and 98% as a function of f_{CAM}.

3. Results

3.1. Influence of Particle Size Ratio and Cathode Loading on Cathode Utilization

The model results for the effect of cathode loading on the cathode utilization (θ_{CAM}) at fixed relative particle size ($\lambda = 1.67$) are shown in **Figure 3**a. For low f_{CAM} (<70 wt%), the CAM particles are fully utilized ($\theta_{\mathrm{CAM}} = 1$). However, upon increasing the cathode loading above 75 wt%, the cathode utilization decreases drastically. This result is consistent with the idea that Li percolation will weaken as the amount of SE in the composite is reduced. However, for a given λ, there is a corresponding maximum f_{CAM} that still enables full cathode utilization (f_{CAM} ≈70 wt% in this case). We show below that the critical cathode loading at which percolation starts to disappear depends strongly on the SE particle size.

The effect of λ on cathode utilization at fixed f_{CAM} (70 wt%) is shown in Figure 3b. Specifically, we fixed the CAM particle size to 5 μm and determined θ_{CAM} for a series of SE particle sizes (1.5, 3, 5, 8, 12, and 15 μm). Somewhat surprisingly, the cathode utilization can vary between 20% and 100% at fixed cathode loading, by merely changing the SE particle size. Percolation clearly decreases when $\lambda < 1$. An important observation from Figure 3b is that a minimum value of λ is required to achieve full cathode utilization at a given cathode loading ($\lambda = 1.67$ in this case). To confirm that this effect is indeed caused by the change in λ rather than the SE particle size alone, we also calculated similar data using 12 μm CAM particles and obtained the same results (Figure S2, Supporting Information).

Figure 3a,b clearly shows that cathode utilization is affected by both particle size ratio and cathode loading. To quantitatively understand this effect, we varied both λ and f_{CAM} and determined the corresponding value of θ_{CAM}. Our findings are summarized in Figure 3c and indicate that percolation in the cathode composite consistently improves as f_{CAM} decreases (or as the SE weight fraction increases, moving from top to bottom) and as λ increases (moving from left to right). Therefore, to achieve high capacity in an SSB with high cathode loading a large value of λ should be used. In addition, independent of f_{CAM}, percolation always significantly worsens for $\lambda < 1$, stressing that under all circumstances the SE particle size should be kept smaller than the cathode particle size, which is in direct contrast to the desire for high particle size SE in the separator. Additionally, Figure 3c shows that the benefits of λ reduction are very dependent on the cathode loading for which one is trying to optimize: for f_{CAM} = 80 wt%, increasing

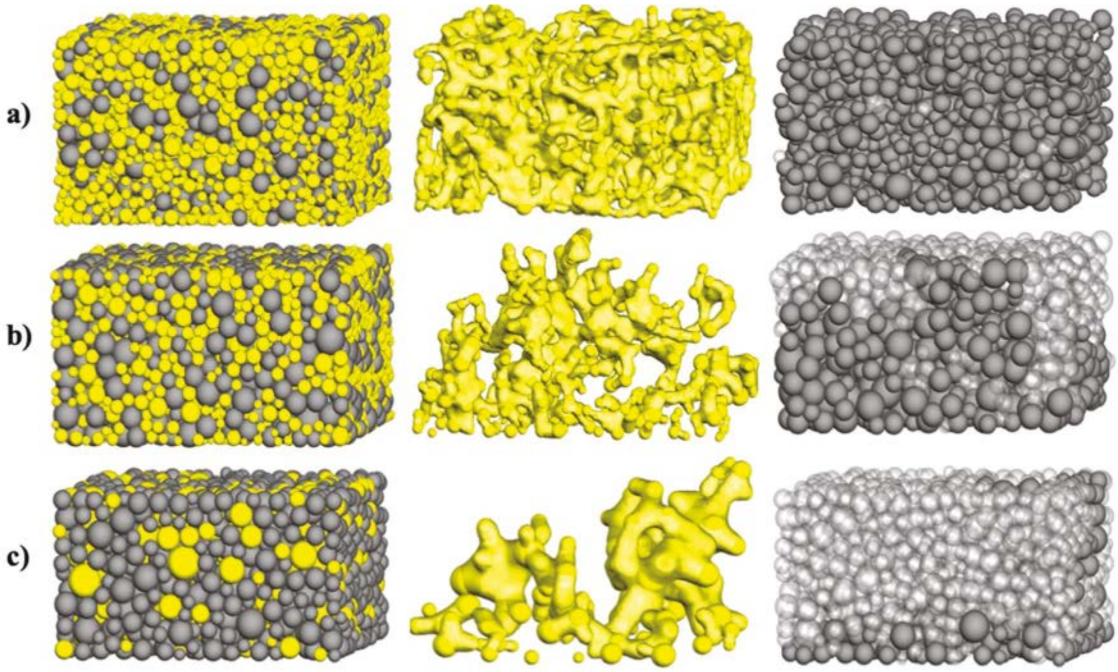

Figure 4. Visualization of models for a) $f_{\mathrm{CAM}} = 70$ wt%, $\bar{D}_{\mathrm{SE}} = 3\ \mu$m, b) $f_{\mathrm{CAM}} = 80$ wt%, $\bar{D}_{\mathrm{SE}} = 3\ \mu$m, and c) $f_{\mathrm{CAM}} = 80$ wt%, $\bar{D}_{\mathrm{SE}} = 5\ \mu$m, with CAM shown in gray and SE showed in yellow ($\bar{D}_{\mathrm{CAM}} = 5\mu$m for all three models). The composite microstructures, isolated SE percolating networks, and isolated CAM particles are shown in the left-hand, middle, and right-hand columns, respectively. The yellow surfaces in the middle column were generated using the QuickSurf method by Gaussian interpolating the SE positions weighted by their diameters.[28] The solid-gray and transparent-gray colors in the right-hand column represent the active and inactive CAM, respectively.

λ from 1 to 3 doubles θ_{CAM} from ≈30% to ≈60%, but at $f_{\mathrm{CAM}} = 85$ wt% increasing λ from 1 to 8 only slightly increases θ_{CAM} from ≈16% to ≈20%.

These simulation results can be summarized in a set of practical design criteria to create high energy density solid-state batteries as shown in Figure 3d. For each desired cathode loading and utilization there is a minimum cathode to SE particle size that needs to be used to create the composite. For example, to achieve 98% cathode utilization with 75wt% loading $\lambda_{\mathrm{min}} = 2.1$. For typical NMC cathode sizes of 5 or 20 µm, this corresponds to a SE particle size of 2.4 and 9.5 µm respectively.

3.2. Visualization of Ionic Percolating Networks

Figure 4 presents visualizations of the composite cathodes and their percolating networks for various cathode loadings and LPS particle sizes, all with $\bar{D}_{\mathrm{CAM}} = 5\ \mu$m.

To demonstrate the SE particle size and cathode loading effect, we isolated the SE percolating network (middle panel) and highlighted the active/inactive CAM particles (right panel). Upon increasing f_{CAM} from 70 wt% (Figure 4a) to 80 wt% (Figure 4b) under constant λ ($\lambda = 1.67$), the SE volume decreases. Consequently, the SE percolating network becomes smaller and less spatially uniform, resulting in a decrease in θ_{CAM} from 98% to 52%.

Comparing Figure 4b,c, where f_{CAM} was fixed at 80 wt% while increasing the SE particle size ($\lambda = 1.67$ and 1 for model b and c, respectively), it is apparent that the SE percolating network becomes smaller upon increasing the SE particle size. Therefore, most of the active CAM in model c is limited to the volume near the separator, leading to a low θ_{CAM} ($\theta_{\mathrm{CAM}} = 52\%$ and 25% for model b and c, respectively).

3.3. Experimental Validation of the Effect of Particle Size Ratio and Cathode Loading on Cathode Utilization

We performed a set of systematic experiments to test the dependence of the cathode utilization on particle size ratio and cathode loading as predicted by the model. **Figure 5**a presents the results for four cells using LPS of different sizes in the cathode composite. The cathode particle size and f_{CAM} were fixed at 5 µm and 60 wt%, respectively. The cells with 8- and 5-µm LPS particles delivered reduced discharge capacities (≈75 and 125 mAh g^{-1}, respectively) compared with those for the 3- and 1.5-µm LPS particles (>150 mAh g^{-1}) (Figure 5a), proving that the use of smaller SE particles (larger λ) indeed improves θ_{CAM}. The good agreement between the experimental and model-predicted specific capacities is shown in Figure 5b. The model-predicted specific capacities were calculated by multiplying the full capacity (largest experimental specific capacity observed, 155 mAh g^{-1}) by the predicted θ_{CAM} (shown in Figure 3c).

We also investigated the change in discharge capacity when λ was modified by only changing the CAM particle size, rather than the SE particle size as above. **Figure 5**c,d presents the variation in discharge capacity when the NMC particle size is increased from 5 to 12 µm while fixing the LPS particle size at either 3 or 1.5 µm (f_{CAM} was fixed at 80 wt%). For both LPS sizes, the cells with 12-µm CAM particles (black curves)

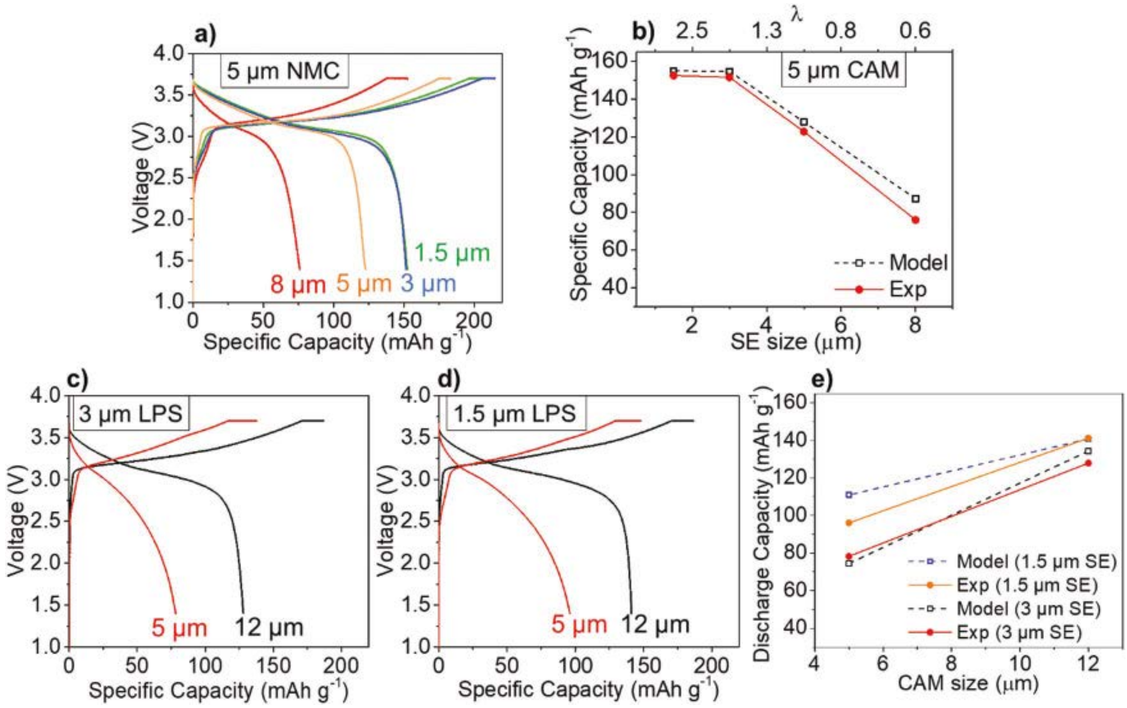

Figure 5. a) First-cycle voltage curves of SSBs using different-sized LPS particles in the cathode composite with fixed NMC size (5 µm) and f_{CAM} (60 wt%). b) Comparison of experimental capacities in with model-predicted capacities. c,d) First-cycle voltage curves of SSBs using different-sized NMC particles (5 and 12 µm) in the cathode composite with fixed LPS size (3 µm for (c) and 1.5 µm for (d)) and f_{CAM} (80 wt%). e) Comparison of experimental capacities in (c) and (d) with model-predicted capacities.

delivered larger discharge capacities than those with 5-µm CAM particles (red curves), further demonstrating that a larger λ benefits θ_{CAM}. The initial discharge capacities of the four cells are compared with the model-predicted specific capacities in Figure 5e and show good agreement.

Finally, the effect of f_{CAM} was validated experimentally by varying f_{CAM} while fixing the LPS and NMC particle sizes. Cells with f_{CAM} = 60, 70, and 80 wt% were tested using 5-µm NMC and 3-µm LPS (λ = 1.67, **Figure 6**a) or 1.5-µm LPS (λ = 3.33, Figure 6c) particles. For f_{CAM} = 60 wt% (blue curves in Figure 6a,c), both LPS sizes fall in the high cathode utilization area (the green region in Figure 3c). Consistent with this prediction, the experimental voltage curves for both cells are almost identical, with both specific discharge capacities greater than 150 mAh g^{-1}. In contrast, for f_{CAM} = 80 wt% (black curves in Figure 6a,c), both LPS sizes fall into the low-θ_{CAM} regions (purple and red regions in Figure 3c), consistent with the dramatically decreased initial discharge capacity. In addition, a comparison of the discharge capacities for f_{CAM} = 70 wt% (orange curves in Figure 6a,c) confirms that increasing λ ensures higher θ_{CAM}. Because λ is larger for the cells with 1.5-µm LPS, f_{CAM} can be increased from 60 wt% to 70 wt% without any capacity decrease. The experimental data show good agreement with the model-predicted specific capacities (Figure 6b,d).

4. Discussion

Solid-state batteries are an important future energy storage technology that may surpass current Li-ion batteries in both energy density and safety. However, high energy density can only be achieved if cathode composites can be made with cathode volume fractions close to those in liquid Li ion cells. Our results show that degradation of capacity at high cathode loading is a percolation problem with only the volume of cathode near the separator being activated when the loading is too high. Somewhat surprisingly, both our modeling and experimental results indicate that percolation depends as much on the cathode volume fraction as on the ratio of the cathode to SE particle size (λ), and that even at high loading the cathode utilization can be dramatically improved by tuning this ratio. Our findings indicate that a larger λ is beneficial for improving cathode utilization and enables higher cathode loading. More specifically, at the fixed cathode and SE volume, the battery capacity can be significantly improved when using SE and CAM particles so that $d_{SE} < d_{CAM}/\lambda$ is satisfied. The higher the weight fraction of cathode, the larger the value of λ is.

Experimentally, we demonstrated that both increasing the CAM particle size and reducing the SE particle size are effective ways to achieve a larger λ and therefore higher f_{CAM}. It may seem counterintuitive that a larger cathode particle size actually improves performance as larger particle sizes are associated with longer diffusion paths. But our result is consistent with Li-percolation to the CAM particles being the limiting factor. Larger cathode particles have a higher surface area and therefore a higher probability of contacting a percolating SE network. This finding shows that experience from liquid Li-ion cells cannot always be translated directly to solid-state batteries.

As shown in Figure 5d, f_{CAM} = 80 wt% can be achieved in the cathode composite with near full CAM utilization when

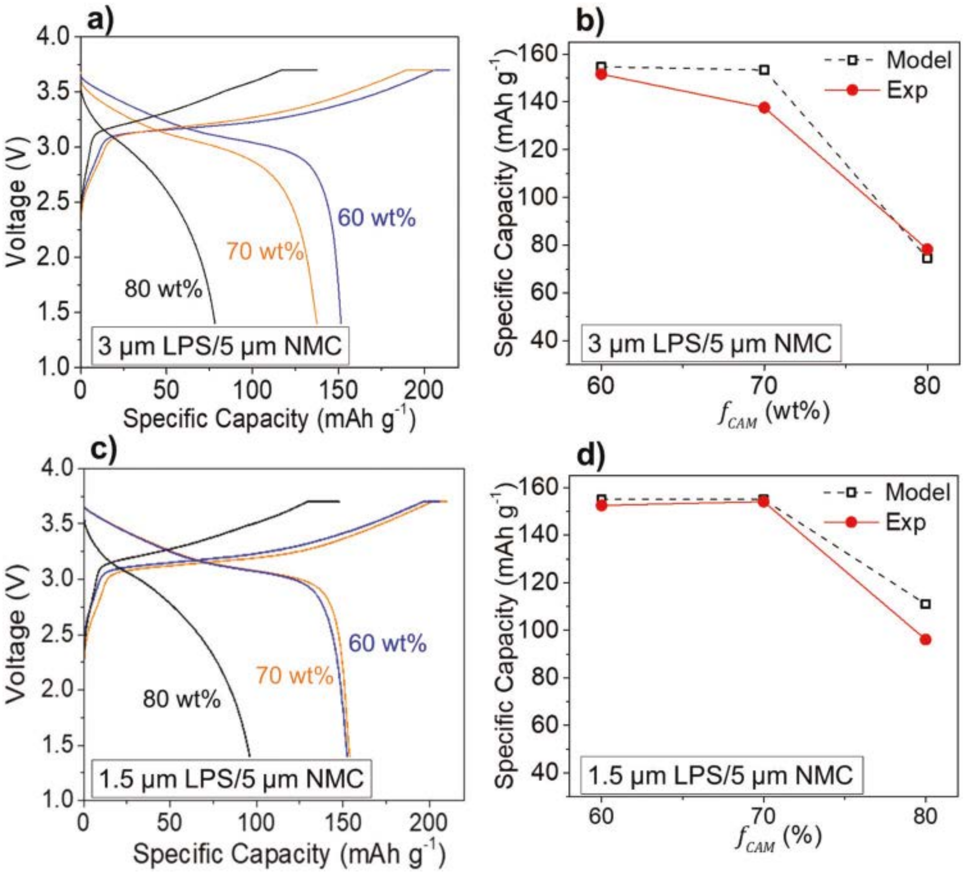

Figure 6. First-cycle voltage profiles of SSBs using a) 3-µm and c) 1.5-µm LPS in the cathode composite. The blue curves represent the cells with 60 wt% NMC, 35 wt% LPS, and 5 wt% CNF (f_{CAM} = 60 wt%), the orange curves represent the cells with 70 wt% NMC, 25 wt% LPS, and 5 wt% CNF (f_{CAM} = 70 wt%), and the black curves represent the cells with 80 wt% NMC, 15 wt% LPS, and 5 wt% CNF (f_{CAM} = 80 wt%). b,d) Comparison of experimental first-cycle discharge capacities with model-predicted capacities. In all the cells, 5-µm NMC particles were used.

λ is increased to ≈8. To put this finding into perspective, we calculate the CAM volume ratio in the cathode composite as a function of cathode loading using previously reported densities and composite cathode porosities (**Figure** 7a).[29] For f_{CAM} = 80 wt%, the volume loading is ≈50 vol%, comparable to that of a common liquid cell cathode (usually >45 vol%).[11,12]

According to our modeling results, higher than 80 wt% cathode loading is possible if λ is further increased. Such large λ will likely require the SE particle size to be reduced to the sub-micron scale. Nano-sized SE particles have been successfully synthesized using solution-based methods in several recent studies, which could potentially lead to even higher cathode loading in the cathode composite.[14,15] Our findings thus motivate further research on the synthesis and application of nano-sized SEs with high ionic conductivity.

It should be noted that although a very large λ can enable high cathode loading and therefore high energy density of a solid-state battery, very large cathode particles or very small SE particles may limit the power density of the cell. A very large CAM particle requires more time to lithiate and delithiate.[24] Reduction of the SE particle size brings other potential issues as a smaller percolation channel width and an increased number of particle/grain boundaries that may increase the impedance within the SE network.[30] In particular, the importance of the grain boundary contribution will depend on the SE selection. Some oxide SEs show much larger grain boundary resistance compared to the sulfide SEs used in the current study, so that in those materials reduction of particle size will slow the ion transport due to the increased number of grain boundaries.[31,32] Hence, whether λ is increased by increasing the cathode particle size or by reducing the SE size should depend on the relative importance of these kinetic contributions. SSBs using cathode materials such as $LiCoO_2$ with good intrinsic Li mobility may be optimized by increasing the cathode particle size, whereas cathode materials with poorer Li-ion transport such as some NMCs may require SE particle size reduction to achieve high loading. Therefore, this trade-off between power and energy density should be considered when determining the optimal λ.

Further refinement of the effect of λ on the ionic diffusivity in the cathode composite would require additional details, such as the Li transport properties across particle boundaries and the contact area between particles. An accurate description of the contact area between particles requires modeling of the plastic deformation of LPS particles, which has been observed experimentally.[29] The degree of the deformation will largely determine the contact area between particles and therefore the resistance at particle boundaries.

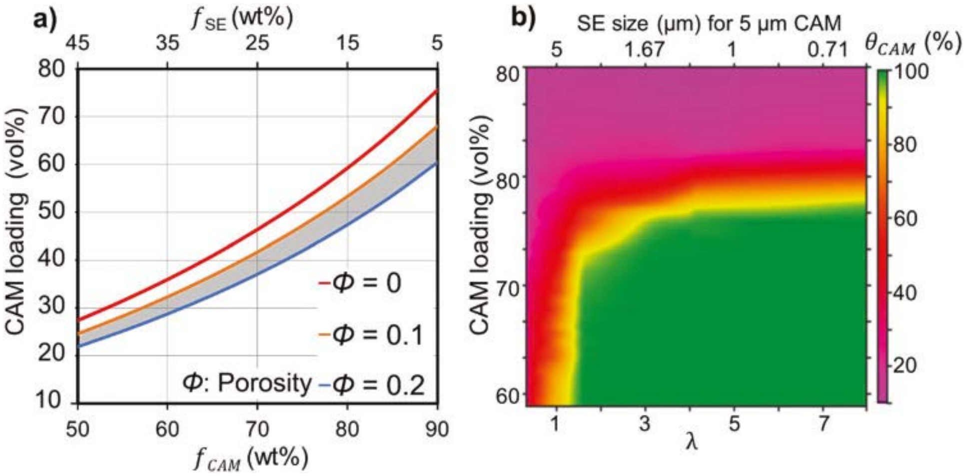

Figure 7. a) CAM volume loading in cathode composite as a function of f_{CAM}. The shaded area represents the experimentally reported porosities for SSB cathode composites (between 0.1 and 0.2).[29] b) θ_{CAM} as a function of both λ and CAM volume loading.

In addition to the Li percolation path provided by the SE, the electron path provided by the conductive carbon additive is also crucial for determining cathode utilization. In the current study, excess (5 wt%) CNF is used to ensure sufficient electron percolation. The electronic percolation can become critical when less or no conductive additive is added. A recent study has shown that without the conductive carbon additive, the electron percolation must be provided through CAM only, and becomes the limiting factor in cathode utilization.[13] This led to a conclusion that a smaller CAM particle size provides better cathode utilization, which seemingly contradicts with our results. However, since the electron percolation provided by the CAM particles is the limiting factor in this case, decreasing the CAM particle size improves the electronic percolation and the cathode utilization according to our model. This further highlights the importance of electronic transport in cathode composite and also demonstrates that our model applies to both electronic and ionic percolations. Adding carbon particles in the model would allow both the Li-ion and electron transport in the cathode composite to be modeled as well as the optimization of both the carbon and SE ratios in the cathode composite. However, the particle sizes of commonly used carbon conductors (e.g., carbon blacks such as Super P and Super C65) are extremely small (tens of nanometers) and would increase the number of particles in our model to the order of 10^{10}, exceeding any computational ability. However, recent findings that the SE degrades at the interface with carbon[33,34] is leading to the preferred use of other morphologies for the additive, such as carbon nanofibers whose high aspect ratio leads to better percolation at lower volume fraction.

Finally, we note that percolation is controlled by the material volume distribution within the composite. Hence, our results can be generalized to other active materials and conductors by converting the data from wt% to vol%. An example of this is shown in Figure 7b. We believe very similar particle size effects will be observed when utilizing other types of SEs, such as $Li_7La_3Zr_2O_{12}$ garnet oxide, since the additional sintering step used in oxide SE processing does not dramatically change the SE percolation network morphology. Additionally, our results should be applicable to SSB anode composites when using traditional anode active materials such as mesocarbon microbeads or $Li_4Ti_5O_{12}$.

5. Conclusion

We have demonstrated the effect of the cathode to SE particle size ratio (λ) on the cathode utilization and loading tolerance in cold-pressed SSBs. Both our modeling and experimental results indicate that cathode utilization in solid-state composites is percolation controlled, and that a larger ratio of the cathode to conductor particle size enables higher cathode loading. In the regime of high cathode volume loading, which is most relevant for creating higher energy density solid-state batteries, the cathode utilization is most critically dependent on this particle size ratio. This leads to the counterintuitive result that in some cases a higher cathode particle size can dramatically improve the capacity of the solid-state battery. We demonstrated the possibility of preparing a solid-state cathode composite with liquid-cell-level cathode volume loading (≈50 vol%) by using large cathode particles (≈12 μm) and small SE particles (≈1.5 μm). Our study provides a quantitative guide for particle size optimization in SSB electrodes, and shows how such optimization can enable commercially relevant cathode loading in SSBs.

Supporting Information

Supporting Information is available from the Wiley Online Library or from the author.

Acknowledgements

T.S. and Q.T. contributed equally to this work. This work was supported by the Samsung Advanced Institute of Technology. The SEM analysis was performed at the Molecular Foundry, Lawrence Berkeley National Laboratory, supported by the Office of Science, Office of Basic Energy Sciences, of the U.S. Department of Energy under Contract No. DE-AC02-05CH11231. This research used the Lawrencium computational cluster resource provided by the IT Division at Lawrence Berkeley National Laboratory (supported by the Director, Office of Science, Office of Basic Energy Sciences, of the U.S. Department of Energy under Contract No. DE-AC02-05CH11231) and the Savio computational cluster resource provided by the Berkeley Research Computing program at the University of California, Berkeley (supported by the UC Berkeley Chancellor, Vice Chancellor for Research, and Chief Information Officer). The authors also gratefully acknowledge Dr. Taku Watanabe, Dr. Yuichi Aihara, Dr. Tomoyuki Tsujimura, and the Samsung R&D Institute of Japan for providing the LZO-coated cathode materials.

Conflict of Interest

The authors declare no conflict of interest.

Keywords

all-solid-state batteries, cathode loading, cathode utilization, ionic percolation

Received: September 3, 2019
Revised: November 1, 2019

[1] A. Manthiram, X. Yu, S. Wang, *Nat. Rev. Mater.* **2017**, *2*, 16103.
[2] J. Li, C. Ma, M. Chi, C. Liang, N. J. Dudney, *Adv. Energy Mater.* **2015**, *5*, 1401408.
[3] J. Liu, Z. Bao, Y. Cui, E. J. Dufek, J. B. Goodenough, P. Khalifah, Q. Li, B. Y. Liaw, P. Liu, A. Manthiram, *Nat. Energy* **2019**, *4*, 180.
[4] J. Janek, W. G. Zeier, *Nat. Energy* **2016**, *1*, 16141.
[5] Y. Kato, S. Hori, T. Saito, K. Suzuki, M. Hirayama, A. Mitsui, M. Yonemura, H. Iba, R. Kanno, *Nat. Energy* **2016**, *1*, 16030.
[6] S. Ito, S. Fujiki, T. Yamada, Y. Aihara, Y. Park, T. Y. Kim, S. Baek, J. Lee, S. Doo, N. Machida, *J. Power Sources* **2014**, *248*, 943.
[7] A. Sakuda, T. Takeuchi, H. Kobayashi, *Solid State Ionics* **2016**, *285*, 112.
[8] Y. J. Nam, D. Y. Oh, S. H. Jung, Y. S. Jung, *J. Power Sources* **2018**, *375*, 93.
[9] Y. Kato, S. Shiotani, K. Morita, K. Suzuki, M. Hirayama, R. Kanno, *J. Phys. Chem. Lett.* **2018**, *9*, 607.
[10] A. Sakuda, K. Kuratani, M. Yamamoto, M. Takahashi, T. Takeuchi, H. Kobayashi, *J. Electrochem. Soc.* **2017**, *164*, A2474.
[11] P. R. Shearing, N. Brandon, J. Gelb, R. Bradley, P. Withers, A. Marquis, S. Cooper, S. Harris, *J. Electrochem. Soc.* **2012**, *159*, A1023.
[12] M. Ebner, F. Geldmacher, F. Marone, M. Stampanoni, V. Wood, *Adv. Energy Mater.* **2013**, *3*, 845.
[13] F. Strauss, T. Bartsch, L. de Biasi, A. Kim, J. Janek, P. Hartmann, T. Brezesinski, *ACS Energy Lett.* **2018**, *3*, 992.
[14] M. Calpa, N. C. Rosero-Navarro, A. Miura, K. Tadanaga, *Electrochim. Acta* **2019**, *296*, 473.
[15] H. Wan, J. P. Mwizerwa, X. Qi, X. Xu, H. Li, Q. Zhang, L. Cai, Y. Hu, X. Yao, *ACS Appl. Mater. Interfaces* **2018**, *10*, 12300.
[16] A. Bielefeld, D. A. Weber, J. Janek, *J. Phys. Chem. C* **2019**, *123*, 1626.
[17] D. Chung, P. R. Shearing, N. P. Brandon, S. J. Harris, R. E. García, *J. Electrochem. Soc.* **2014**, *161*, A422.
[18] C. Kloss, C. Goniva, A. Hager, S. Amberger, S. Pirker, *Prog. Comput. Fluid Dyn. Int. J.* **2012**, *12*, 140.
[19] A. Di Renzo, F. P. Di Maio, *Chem. Eng. Sci.* **2005**, *60*, 1303.
[20] M. P. Schöpfer, S. Abe, C. Childs, J. J. Walsh, *Int. J. Rock Mech. Min. Sci.* **2009**, *46*, 250.
[21] S. A. Roberts, V. E. Brunini, K. N. Long, A. M. Grillet, *J. Electrochem. Soc.* **2014**, *161*, F3052.
[22] L. E. Silbert, D. Ertaş, G. S. Grest, T. C. Halsey, D. Levine, S. J. Plimpton, *Phys. Rev. E* **2001**, *64*, 051302.
[23] H. Zhang, H. Makse, *Phys. Rev. E* **2005**, *72*, 011301.
[24] M. Park, X. Zhang, M. Chung, G. B. Less, A. M. Sastry, *J. Power Sources* **2010**, *195*, 7904.
[25] M. F. Lagadec, R. Zahn, S. Müller, V. Wood, *Energy Environ. Sci.* **2018**, *11*, 3194.
[26] W. Zeng, R. L. Church, *Int. J. Geogr. Inf. Sci.* **2009**, *23*, 531.
[27] A. Hayashi, S. Hama, H. Morimoto, M. Tatsumisago, T. Minami, *J. Am. Ceram. Soc.* **2001**, *84*, 477.
[28] M. Krone, J. E. Stone, T. Ertl, K. Schulten, *EuroVis—Short Papers* **2012**, *2012*, 67.
[29] S. Choi, M. Jeon, J. Ahn, W. D. Jung, S. M. Choi, J. Kim, J. Lim, Y. Jang, H. Jung, J. Lee, *ACS Appl. Mater. Interfaces* **2018**, *10*, 23740.
[30] I. Chu, H. Nguyen, S. Hy, Y. Lin, Z. Wang, Z. Xu, Z. Deng, Y. S. Meng, S. P. Ong, *ACS Appl. Mater. Interfaces* **2016**, *8*, 7843.
[31] J. A. Dawson, P. Canepa, M. J. Clarke, T. Famprikis, D. Ghosh, M. S. Islam, *Chem. Mater.* **2019**, *31*, 5296.
[32] J. Wu, X. Guo, *Phys. Chem. Chem. Phys.* **2017**, *19*, 5880.
[33] T. Hakari, M. Deguchi, K. Mitsuhara, T. Ohta, K. Saito, Y. Orikasa, Y. Uchimoto, Y. Kowada, A. Hayashi, M. Tatsumisago, *Chem. Mater.* **2017**, *29*, 4768.
[34] W. Zhang, T. Leichtweiß, S. P. Culver, R. Koerver, D. Das, D. A. Weber, W. G. Zeier, J. Janek, *ACS Appl. Mater. Interfaces* **2017**, *9*, 35888.

High-Fluorinated Electrolytes for Li–S Batteries

*Jing Zheng, Guangbin Ji, Xiulin Fan, Ji Chen, Qin Li, Haiyang Wang, Yong Yang, Kerry C. DeMella, Srinivasa R. Raghavan, and Chunsheng Wang**

Rechargeable Li–S batteries are regarded as one of the most promising next-generation energy-storage systems. However, the inevitable formation of Li dendrites and the shuttle effect of lithium polysulfides significantly weakens electrochemical performance, preventing its practical application. Herein, a new class of localized high-concentration electrolyte (LHCE) enabled by adding inert fluoroalkyl ether of 1H,1H,5H-octafluoropentyl-1,1,2,2-tetrafluoroethyl ether into highly-concentrated electrolytes (HCE) lithium bis(fluorosulfonyl) imide/dimethoxyether (DME) system is reported to suppress Li dendrite formation and minimize the solubility of the high-order polysulfides in electrolytes, thus reducing the amount of electrolyte in cells. Such a unique LHCE can achieve a high coulombic efficiency of Li plating/stripping up to 99.3% and completely suppressing the shuttling effect, thus maintaining a S cathode capacity of 775 mAh g^{-1} for 150 cycles with a lean electrolyte of 4.56 g A^{-1} h^{-1}. The LHCE reduces the solubility of lithium polysulfides, allowing the Li/S cell to achieve super performance in a lean electrolyte. This conception of using inert diluents in a highly concentrated electrolyte can accelerate commercialization of Li–S battery technology.

1. Introduction

Owing to the high natural abundance of elemental sulfur, high theoretical cell capacity of 1667 mAh g^{-1}, and theoretical cell energy density of 2510 Wh kg^{-1}, rechargeable lithium–sulfur (Li–S) batteries have been regarded as a promising alternative to state-of-the-art lithium-ion batteries (LIBs) for energy storage applications.[1] However, current Li–S batteries still face several serious challenges, including "shuttle" reaction due to the dissolution of polysufides (Li_2S_n, $n > 4$) in electrolytes and dendritic Li growth on Li anode, which significantly lower the cell coulombic efficiency (CE) and cycling performance.[2] In addition, the lithium polysulfides dissolution and Li dendrite growth also require a large amount excess electrolyte to achieve high performance, thus reducing the energy density. Extensive efforts have been devoted to suppress "shuttle" of lithium polysulfide. Among them, encapsulating sulfur cathode into porous host materials including porous carbon,[3] metal oxide/chalcogenide,[4] and conductive polymers[5] are the most effective method for suppressing "shuttle" effect. On the Li anode side, nanostructure design[6] or surface modification[7] has been also developed to suppress the dendritic Li growth.

Different from separately nanostructured design of the electrodes, rational design and optimization of electrolytes are more effective,[8] which simultaneously suppress both lithium polysulfide shuttle and Li dendrite.[9] Recently, highly concentrated electrolyte (HCE) systems with unique solvation structure and functionality have been successfully developed for high performance Li–S batteries. For example, Suo et al. showed a new class of ultrahigh salt concentration electrolyte, which can effectively suppress the lithium dendrite growth and inhibit the polysulfide shuttle phenomenon in Li–S batteries.[2c] Qian et al. reported that the high-concentration electrolytes enabled the high-rate cycling of lithium metal with a high CE up to 99.1% without dendrite growth.[2a] These significant performance improvements were contributed to the strong restraining property for the solvents from the high-concentrated salts in electrolyte that efficiently control the reaction dynamics and Li_2S_n solubility synchronously. These exciting breakthroughs demonstrated that such unique HCE systems can offer new possibilities to address the shuttle effect and dendritic Li growth efficiently and simultaneously.

Nevertheless, the usage of a large amount of expensive lithium salt in the HCE systems also lead to several disadvantages, including high cost, poor wettability, high viscosity, and low ionic conductivity.[10] To address these issues without scarifying the unique characteristics of HCE, a new kind of localized high-concentration electrolyte (LHCE) was proposed by using a rational cosolvent dilution in HCE system. The choice of the cosolvent in LHCE is critical for the performance of Li–S batteries. In Li–S battery electrolytes, ether-based solvents with high donor number were usually employed, which can effectively dissociate the Li^{+} from anion and dissolve Li salts. However, the strong donating ability of such solvents can also facilitate the dissolution of long-chain polysulfide and amplify

---

Dr. J. Zheng, Dr. X. Fan, Dr. J. Chen, Dr. Q. Li, Dr. H. Wang, Dr. Y. Yang,
Dr. S. R. Raghavan, Prof. C. Wang
Department of Chemical and Biomolecular Engineering
University of Maryland
College Park, MD 20742, USA
E-mail: cswang@umd.edu

Dr. J. Zheng, Prof. G. Ji
College of Materials Science and Technology
Nanjing University of Aeronautics and Astronautics
Nanjing 210016, P. R. China

Dr. K. C. DeMella
Department of Chemistry and Biochemistry
University of Maryland
College Park, MD 20742, USA

The ORCID identification number(s) for the author(s) of this article can be found under https://doi.org/10.1002/aenm.201803774.

DOI: 10.1002/aenm.201803774

the negative influence from the "shuttle effect." Therefore, an "inert" cosolvent with low donor ability, permittivity, electrolyte viscosity but high wettability is required for the LHCE, which can maintain the Li^+ solvation structure complexes in HCE and suppress the polysulfide solubility but with significantly reduced salt usage. For example, 1,1,2,2-tetrafluoroethyl-2,2,3,3-tetrafluoropropyl ether (HFE) was employed as the diluent solvent in HCE for Li-based batteries which not only maintain the original Li^+-solvent complex but also lower the electrolyte concentration higher wettability and lower viscosity[11] allowing to use less electrolyte. Furthermore, the choice of the "inert" cosolvent must consider the formation of solid electrolyte interphase (SEI) layer which can significantly affect the cycling performance and lifetime of the battery. As the analogous to HFE, the solvent of 1H,1H,5H-octafluoropentyl-1,1,2,2-tetrafluoroethyl ether (OFE) with lower flammability but higher fluorination degree is identified to better suit for the "inert" solvent requirements, which can be used to dilute the ether-based HCE to obtain the LHCE system for Li–S battery.

In this work, a new "inert" cosolvent, the inert cosolvent of OFE was employed to develop a novel ether-based electrolyte system (lithium bis (fluorosulfonyl) imide (LiFSI)/OFE + dimethoxyether (DME)) for Li–S batteries. By adjusting the volume percentage of OFE in these OFE-based electrolytes, the polysulfide shuttle of Li–S cells can be effectively suppressed. The Li–S cells in a lean 1 M LiFSI/OFE + DME5 electrolyte (4.56 g A^{-1} h^{-1}) show a stable cycle performance with the capacity retention of 775 mAh g^{-1} at 100 mA g^{-1} after 150 cycles. The high average CE of 99.2% for S cathodes and a high stripping/plating CE of 99.3% for Li anodes demonstrate lithium polysulfide dissolution and dendritic Li growth have been effectively suppressed. In addition, 1 M LiFSI/OFE + DME5 electrolyte is nonflammable, which is promising for next generation safe and high-performance Li–S batteries.

2. Results and Discussion

2.1. Physicochemical Properties of Electrolytes

Lithium bis(trifluoromethane sulfonyl) imide (LiTFSI) is the most commonly used metal salt for Li-storage batteries. As the analogous to LiTFSI, LiFSI possesses the similar structures with LiTFSI but better ion mobility/conductivity property and higher labile fluorine, leading to the more formation of F-rich anion-originated interphase. In this work, three OFE-based electrolytes with the LiFSI salt were designed, 1 M LiFSI/OFE + DME with an OFE/DME volume ratio of 50:50, 85:15, and 95:5 were prepared, denoted as DME50, DME15, and DME5, respectively. Traditional 1 M LiTFSI/1,3-dioxolane (DOL) + DME (denoted as DOL + DME) was also employed as the reference electrolyte. The physicochemical properties of ionic conductivity, Li^+ transference number and viscosity for these electrolytes were first investigated, as shown in **Figure 1**a,b. The ionic conductivity of traditional DOL + DME electrolyte is about 9.40 mS cm^{-1},

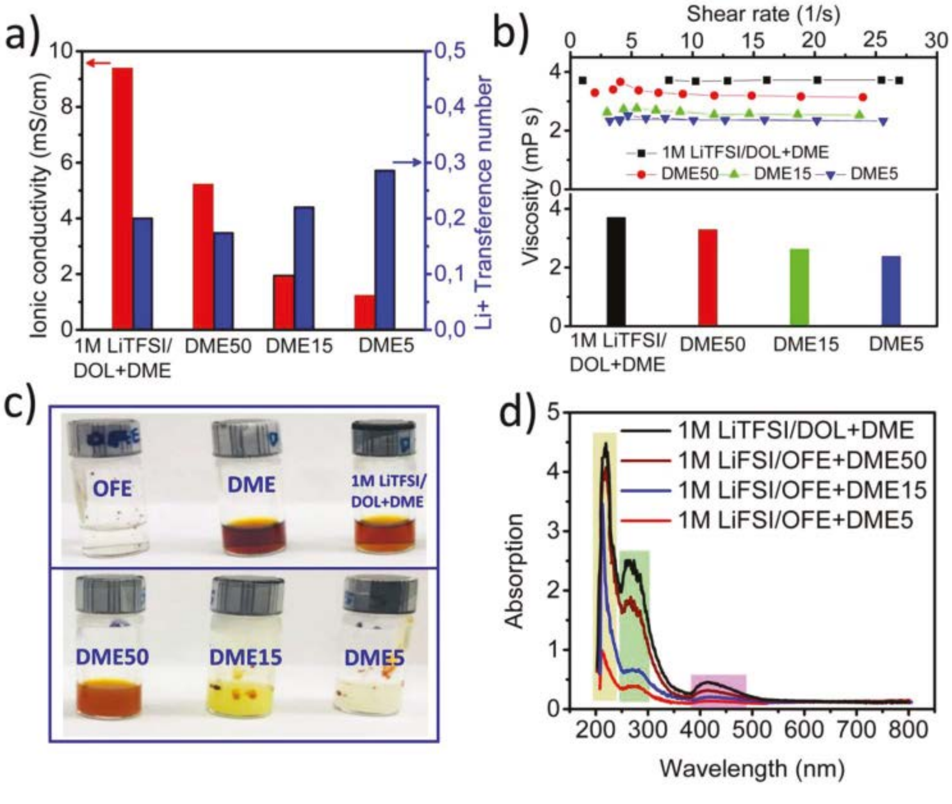

Figure 1. Physicochemical parameters for various electrolytes: a) Li^+ transference number and ionic conductivity. b) Electrolyte viscosities as functions of shear-rate (top) and the corresponding average viscosities (bottom). Property of lithium polysulfide dissolution: c) digital photos for saturate Li_2S_8 in different solutions after 2 weeks standing and d) the corresponding UV–vis absorption spectra.

which is in good agreement with the previous reports.[2c,12] For the OFE-based electrolytes, the ionic conductivity reduced gradually with the increasing volume ratio of OFE, maintaining a value of 5.23 mS cm^{-1} for DME50 electrolyte, 1.94 mS cm^{-1} for DME15 electrolyte, and 1.24 mS cm^{-1} for DME5 electrolyte (Figure 1a). In the mixed solvent of DME and OFE, the Li^+ is preferentially solvated with DME molecules, and the inert OFE solvent is scarcely involved in the solvation with Li^+. Therefore, the dissociation of Li salt and the number of charge carriers in these OFE-based electrolytes increased along with the increased volume ratio of DME from DME5, DME15 to DME50 electrolyte, which is consistent with the previously reported results.[13] Different from ionic conductivity, the Li^+ transference number increases with the decreasing volume ratio of DME in electrolytes from 0.17 for DME50, 0.22 for DME15 to 0.28 for DME5. This tendency was determined by the existential forms of Li^+ in these electrolytes. In the electrolyte with enough DME, the excess DME molecules can replace the bound of FSI^- to form solvent-separated ion pairs (SSIPs), leading to a large existence of free FSI^- anion which effectively suppress the Li^+ transference speed. As the decreasing volume ratio of DME, it exists with different forms of solvate complexes from contact ion pairs (CIPs, an FSI^- coordinating with one Li^+) to the aggregates (AGGs, an FSI^- coordinating with two or more Li^+, no free FSI^-), leading to less resistance of Li^+ migration from the FSI^-.[14] As a result, the increasing Li^+ transference number as the decreasing of DME volume ratio can partially compensate the loss of ion conductivity in the OFE-based electrolytes.

As another important parameter for electrolytes, their viscosities were measured as a function of shear rate, as shown in Figure 1b. The data demonstrate that the viscosities are almost independent of shear rate (top in Figure 1b), indicating that the fluids are Newtonian in their rheological behavior (much like water). Therefore, each electrolyte can be characterized by a single viscosity value, as shown by the bar graph in the bottom of Figure 1b. DOL + DME exhibits the highest viscosity of 3.7 mPa s among all the electrolytes studied; in comparison, the OFE-based electrolytes have lower viscosities and the viscosity of DME5 is the lowest of the lot (2.4 mPa s). The viscosities of DME15 (2.6 mPa s) and DME50 (3.3 mPa s) are also lower than that of DOL + DME. The low viscosity of OFE-based electrolytes ensures high power density and high utilization of active materials in Li–S cells.

Digital photos for the solubility of Li_2S_8 in various solvents and electrolytes are shown in Figure 1c. In line with previous reports,[15] the solubility of Li_2S_8 in the solvent of DME is high, appearing with dark red color; but in OFE, no obvious color can be observed with tiny solubility. Owing to the high solubility of Li_2S_8 in DOL and DME solvents, the color of 1 M LiTFSI/DOL + DME electrolyte mixed with Li_2S_8 also displays the dark red color. Obviously; in the three OFE-based electrolytes, the color gets lighter from dark brown, light yellow, to colorless along with the decreasing ratio of DME, indicating a significant reduce of polysulfide solubility from the DME50, DME15 to DME5 electrolyte. The corresponding UV–vis spectra for these electrolytes with saturated Li_2S_8 are demonstrated in Figure 1d. The characteristic absorption peaks located at about 220 and 270 nm can be attributed to the signal of DME solvent and presence of S_8, respectively; the signals for both DME and S_8 can be observed in all the solvents and electrolytes, which is due to existence of the electrolyte solvent (DME) and raw material (the mixing of Li_2S and S_8) for the preparation of Li_2S_8 polysulfide solution. However, it can be clearly seen that the profile of Li_2S_8 signal at around 424 nm gets smaller and smaller with the decreasing of DME ratio from DME50 to DME15 and totally disappears in DME5 electrolyte. Similarly, Li_2S_8 signal at around 424 nm is also not observed in the inert OFE solvent (Figure S1, Supporting Information). Therefore, these positive results suggest that the dissolution of lithium polysulfide is stepwise controlled by the introduction of inert OFE cosolvent into the LiFSI/DME electrolytes.

2.2. Flammability of OFE-Based Electrolytes

The safety issue such as flammability of the organic ether-based electrolytes in Li–S batteries is also a critical obstacle for the wide application of Li–S batteries. Herein the ignition and combustion behaviors of different solvents and electrolytes are also evaluated, as displayed in **Figure 2** and Video S1 and S2 in the Supporting Information. As displayed in Video S1 in the Supporting Information, the inert fluorinated OFE solvent cannot be ignited, while DME can burn very rapidly once ignited, which can be attributed to the lower vapor pressure (7.42 mmHg) but higher boiling point (≈133 °C) and flash point (45.037 °C) of OFE than that of DME (Table S1, Supporting Information). When removing the heat source from the objectives, there is no observable flame for OFE (Figure 2a) but still exuberant flame for DME (Figure 2b). Figure 2c shows the maximum flame size for each electrolyte, along with its corresponding images of glass fiber after combustion. It can be observed that the flame of OFE-based electrolyte is getting smaller as the increase of OFE content from DME50, DME15 to DME5, indicating that the OFE in these electrolytes improves the nonflammability of the electrolytes. It is so difficult to ignite the electrolyte of DME5, even with multiple tries of ignition; while for the electrolytes of DOL + DME, DME50, and DME15, they can burn very rapidly with much brighter flame (Video S2, Supporting Information). Furthermore, the color of glass fiber after combustion (inset in Figure 2c) is white for the 1 M LiTFSI/DOL + DME reference electrolyte, but it is black for all OFE-based electrolytes. The white color of glass fiber with 1 M LiTFSI/DOL + DME reference electrolyte indicates a complete combustion event of electrolyte occurs with sufficient flammable DME solvent, on the contrast, the black glass-fiber is attributed to the incomplete combustion of the OFE-based electrolytes. It seems that the glass-fiber color in DME50 is slightly more black than that in DME5, which may be owing to the inefficient burning for higher volume ratio DME in DME50 under the same air contact. These results manifest that the introduction of nonflammable OFE can result in maximum difficult burning electrolytes for safe Li–S battery applications.

2.3. Li Metal Plating/Stripping Cycling CE and Stability

Li|Cu cells were then employed to investigate the Li stripping/deposition stability in these electrolytes (**Figure 3**). As demonstrated in Figure S2 in the Supporting Information,

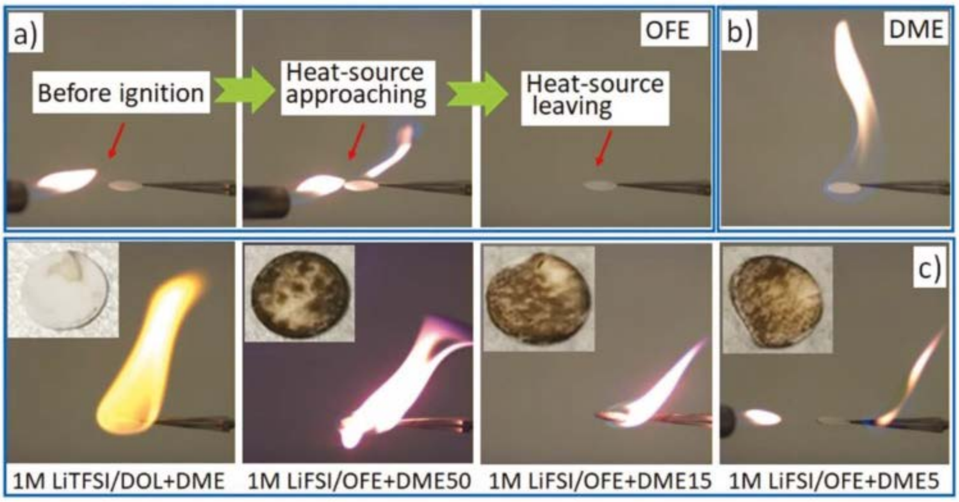

Figure 2. The ignition and combustion experiment: the ignition process for the solvents of a) OFE and b) DME. c) The combustion flammability for various electrolytes on glass-fiber films (inset: the images of glass-fiber films after combustion).

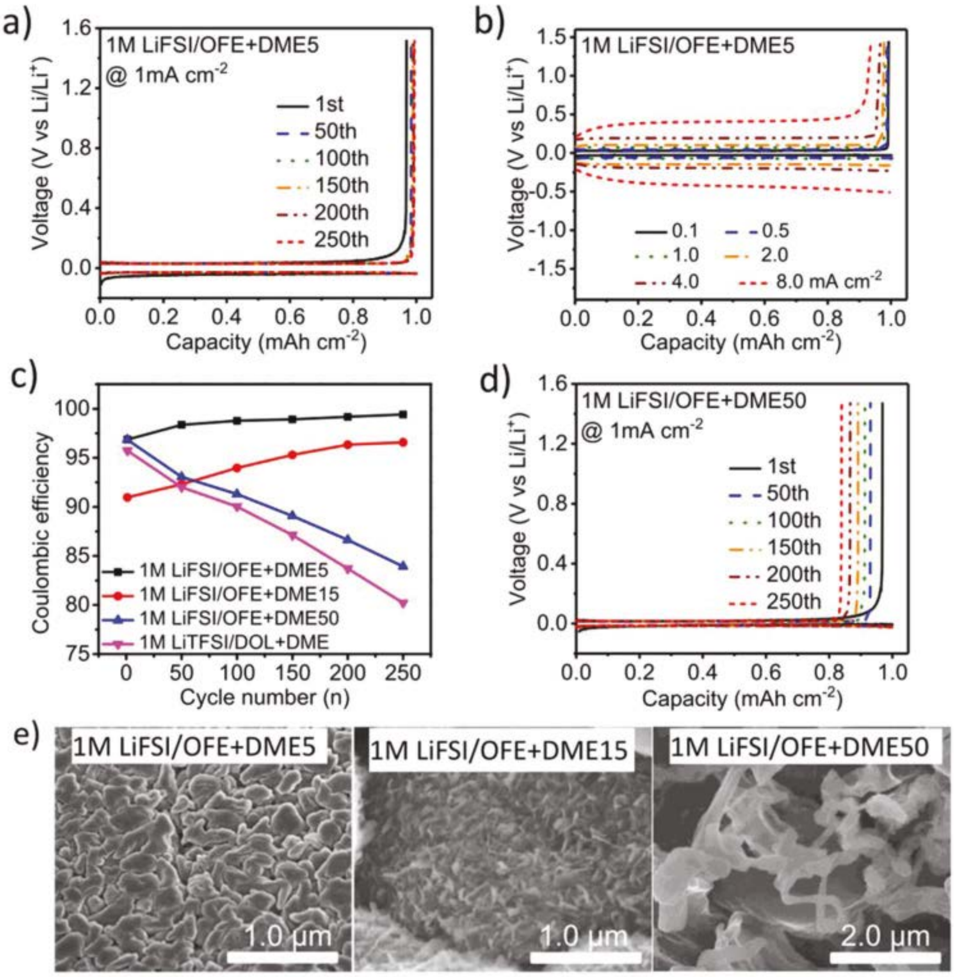

Figure 3. Voltage profiles for Li plating/stripping on Cu working electrode (Li|Cu cell) in 1 M LiFSI/OFE + DME5 electrolyte a) at the current density of 1.0 mA cm^{-2} and b) at different current densities with the deposition capacity of 1.0 mAh cm^{-2}. c) Comparison of Li deposition CE at 1.0 mA cm^{-2} during 250 cycles in different electrolytes. d) Voltage profile of Li metal deposition/stripping at 1.0 mA cm^{-2} with the same deposition capacity of 1.0 mAh cm^{-2} in dilute 1 M LiFSI/OFE + DME50 electrolyte. e) SEM images of the Li metal surface in the OFE-based electrolytes after 100 cycles at the current of 1.0 mA cm^{-2} in Li|Cu cells.

the Li|Cu cells in the LHCE of DME5 show very high CE of 99.3% for 250 cycles at a current of 1 mA cm^{-2} with the deposition capacity of 1.0 mAh cm^{-2}. The voltage profile of Li metal plating/stripping in DME5 at different cycles (Figure 3a) and different current densities (Figure 3b) shows that the Li plating/stripping in DME5 electrolyte is highly stable, and voltage hysteresis just slightly increases with the increasing of current densities. Even at a high current rate of 8 mA cm^{-2}, a stable process for Li stripping/planting also can be received with a high CE of 94.7%. However, under the same current of 1 mA cm^{-2} and the same deposition capacity of 1.0 mAh cm^{-2}, the CE of the dilute DME50 electrolyte is only 83% with rapid fade after 250 cycles (Figure 3c,d). This can be ascribed to the SEI formed from reduction of DME-OFE solvent in DME50 is not robust enough to suppress the Li dendrite growth.

The deposition morphology of Li metal surface after 100 deposition/stripping cycles in Li|Cu cells in the OFE-based electrolytes was examined by scanning electron microscopy (SEM) without exposing to air, as demonstrated in Figure 3e. Obviously, a nodule-like Li deposition surface without any dendrite growth is obtained in the DME5 electrolyte, but some tiny and speculate Li dendritic growths can be obviously observed on the surface of Li metal in the DME15 electrolyte, and much worse in DME50 electrolyte. Moreover, the size of Li nodule in DME5 is larger than the size of Li dendrite in the electrolyte of DME15 and DME50, demonstrating that the SEI formed in DME5 electrolyte successfully suppressed the Li dendrite formation during Li stripping/plating.[10a] The larger particle size with Li smooth nodule in DME5 can effectively reduce contact area with the electrolyte, minimizing the parasitic reactions and prolonging the cycle stability.

Moreover, the polarization test of Li|Li symmetric cells in the OFE-based electrolytes was further performed to investigate the long-term compatibility and cycling stability, as indicated in Figure S3 in the Supporting Information. The cycling performance of Li|Li cells in DME5 electrolyte at a current density of 1 mA cm^{-2} and a deposition capacity of 1.0 mAh cm^{-2} shows a very stable cycling profile without any voltage polarization increment even after 600 h cycling (Figure S3a, Supporting Information). It is worth noting that because the inert solvent of OFE cannot highly coordinate with Li$^+$ ion to obtain solvation-Li$^+$ complex, the overpotential in such an LHCE of DME5 is slightly larger than that of dilute electrolyte at the beginning. However, the enlarged profiles of Li metal plating/stripping exhibit a favorable Li metal exchange with a constant overpotential of ≈0.2 V no matter at the beginning, the middle or the end of cycling (Figure S3b, Supporting Information). In comparison, as displayed in Figure S3c,d in the Supporting Information, the voltage polarization gradually increases during continuous cycling under the same test conditions. Especially for the DME15 electrolyte, the Li|Li cells shows the electrode overpotential is about 0.4 V at 600 h, twice as large as the DME5, indicating an increased interfacial reaction resistances. The comparison results demonstrate that the impedance in DME15 and DME50 electrolytes with a large amount of free DME solvent continuously increased probably due to the remarkable side reactions between electrolyte and Li dendrite, but it was obviously restrained in DME5 electrolyte by suppression of Li dendrite. Besides, because of the introduction of the inert OFE cosolvent, the overpotential for Li plating/stripping cycling in the OFE cosolvent electrolyte system is higher than some published works with dilute electrolyte systems,[16] but the introduction of inert OFE solvent into the HCE system can obtain a new class of LHCE system without breaking the unique Li$^+$ solvation structure complexes of HCE, leading to minimum free active solvent in the LHCE. Therefore, the excellent cycling stability of Li metal plating/stripping along with stable overpotential verifies that the rational introduction of OFE dilution in the electrolyte can effectively suppress the Li dendrite, enabling the stable Li deposition/stripping cycles.

2.4. Mechanisms for Li Dendrite Suppression in Li Deposition/Stripping Cycles

In order to reveal the stable Li deposition/stripping mechanism in such an LHCE of DME5, X-ray photoelectron spectroscopy analysis (XPS) with Ar$^+$ etching technique was performed to analyze the SEI layer on the Li anode surfaces formed in the DME5 and DME50 electrolytes, respectively. The atomic concentration for different elements along with increasing etching time is demonstrated in **Figure** 4a,b and Table S2 in the Supporting Information. It can be clearly found that the chemical composition of SEI layer in the DME5 maintains a higher atomic concentration of F and Li elements when compared with that in DME50 electrolyte. This atom concentration tendency in the SEI layer formed in DME5 electrolyte is similar to that of SEI layer formed in typical HCEs.[15b] Furthermore, the high-resolution Li 1s XPS spectra for DEM5 and DME50 in Figure 4c show an obvious negative shift of the peak position with the etching time increasing from 0 to 1200 s, which should be attributed to the sequential appearance of low-binding-energy Li–O bonds at around 55.5 ± 0.5 eV and lithium metal (Li^0) at around 53.0 ± 0.5 eV along with the increased etching depth. More importantly, it can be clearly observed that the content of Li–F bonds at around 58.0 ± 0.5 eV significantly increased for the SEI layer formed in the DME5 electrolyte, especially at the etching time of 100 and 300 s, while Li–O bond is the dominated type for element Li in the SEI layer formed in the DME50 electrolyte.

The signal of Li—F bond can also be observed in the F1s XPS spectra for the both DME5 and DME50 electrolytes, as shown in Figure 4d. A main peak at about 685.7 eV can be found for both DME5 and DME50 electrolytes, suggesting that the F element in the SEI layer mainly exists in the form of F—Li bond. The peak at around 688.4 eV was assigned to F—C bonds, which should be mainly attributed to the adsorption of the fluorine-rich OFE solvent. Moreover, the intensity of Li—F peak is significantly enhanced for the SEI layer formed in the DME 5 electrolyte when compared with that in DME 50 electrolyte. It can be deduced that a much higher content of inorganic LiF phase in the SEI layer was formed in DME5 electrolyte than that in DME50 electrolyte.

These results indicated that such an LHCE of DME5 can well maintain the similar solvation structure and unique function to typical HCE systems and then promote more F-containing components (such as FSI$^-$ anion and OFE solvent) participating in the formation of SEI layer, resulting to a dense and stable

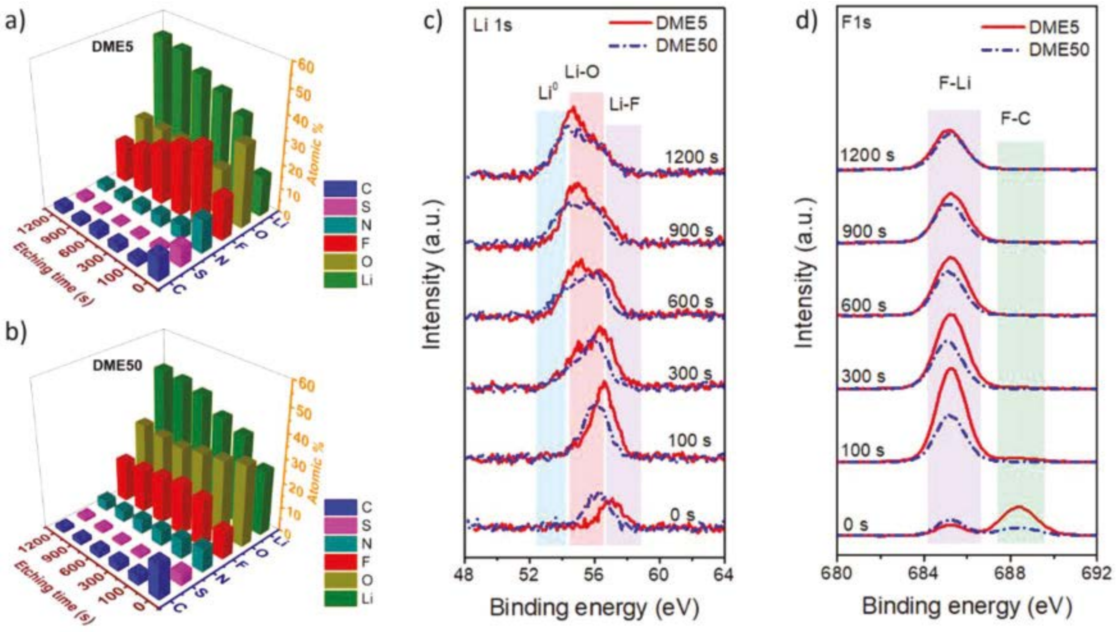

Figure 4. X-ray photoelectron spectroscopy (XPS) analysis for Li metal surface in Li|Cu cells at the current of 100 mA g^{-1} after 50 cycles: atomic concentrations for different elements before and after different etching times in a) 1 M LiFSI/OFE + DME5 and b) 1 M LiFSI/OFE + DME50 electrolytes. High-resolution spectra of c) Li 1s XPS and d) F1s XPS for the lithium metal surface in 1 M LiFSI/OFE + DME5 and 1 M LiFSI/OFE + DME50 electrolytes.

LiF-rich SEI layer which can significantly suppress the Li dendrite growth.[17] In addition, such an LHCE electrolyte of DME5 electrolyte also shows excellent properties of lower cost, lower viscosity, and better wettability than that of typical HCE systems, making it more advantage for practical application in Li–S batteries.

2.5. Electrochemical Behavior of S@C (65.02 wt% for S) Cathodes

In order to further investigate the electrochemical equilibria of S@C cathodes during discharge/charge process in various electrolytes, galvanostatic intermittent titration techniques (GITT) were performed in the voltage window 1–3 V after 15 activation cycles, by applying a short pulses of constant current of 100 mA g^{-1} for 20 min then leaving in open circuit of 2 h for full relaxations to reach equilibrium potential. **Figure** 5a,b represents the GITT profiles of Li–S cells in the DME5 and DME50 electrolytes, respectively. It can be found that the discharge curve of open circuit voltage (OCV) in DME5 electrolyte only has one plateau, and the voltage polarization of S cathode is large but remains almost constant, indicating a deep and direct reduction reaction from solid S_8 to solid-state Li_2S.[18] In contrast, two plateaus regions at about 2.30 and 2.15 V, similar to the S cathodes in a dilute electrolyte, appear in DME50 electrolyte, corresponding to the conversion reaction of solid S_8 to soluble high-order Li_2S_m and then to insoluble low-order Li_2S_2/Li_2S, respectively.[19] Moreover, the voltage polarization of S cathode in DME50 electrolyte increases with state of discharge increased in reaction resistance from soluble liquid low-order lithium polysulfide to insoluble solid Li_2S_2/Li_2S.[20] The voltage polarization of S cathode at the end of the lower voltage region is similar to that in DME5 electrolyte, due to the slow kinetics of solid–solid two phase reduction reaction between Li_2S_2 and Li_2S. More importantly, during charge in the DME50 electrolyte, a large voltage polarization is observed at the initial delithiation from solid Li_2S to solid Li_2S_2 process, then decreasing gradually due to solid–liquid and keeping at a small but constant overpotential in liquid–liquid shuttle reaction, which is the notorious shuttle phenomenon in Li–S batteries. But for the GITT profile in DME5 electrolyte, the state of electrochemical equilibration is reversible without any shuttle. Furthermore, five sequential and stable GITT profile after 15 discharge/charge activation cycles in Figure S4 in the Supporting Information obviously demonstrated the thermodynamically suppression of shuttle phenomenon by the addition of appropriate OFE inert solvent in the DME5.

Furthermore, the self-discharge phenomenon, mainly caused by the shuttle reaction of soluble lithium polysulfides migration from cathode side, is one of the most severe issues that hinder further practical application of Li–S batteries, leading to obvious decrease of OCV and loss of discharge capacity.[21] Thus, the inhibition of the shuttle reaction in turn can reduce the self-discharge rate of Li–S battery, owing to its effective suppression of polysulfides dissolution and migration. Here the self-discharge property of Li–S batteries in different electrolytes was evaluated after 20 activation discharging/charging cycles at the current of 50 mA g^{-1} by fully charging Li–S cells, leaving in open-circuit for a long-term rest period of 60 d, and then discharging at the same current. Figure 5c–e is the comparison of the self-discharge rate of Li–S batteries based on the capacity loss in the OFE-based electrolytes. The battery in the DME5 electrolyte maintains the lowest capacity loss of 16.9% after rest for 60 d (Figure 5c), but a high capacity loss of 29.5% for DME15 (Figure 5d) and a very severe capacity loss of 50.6%

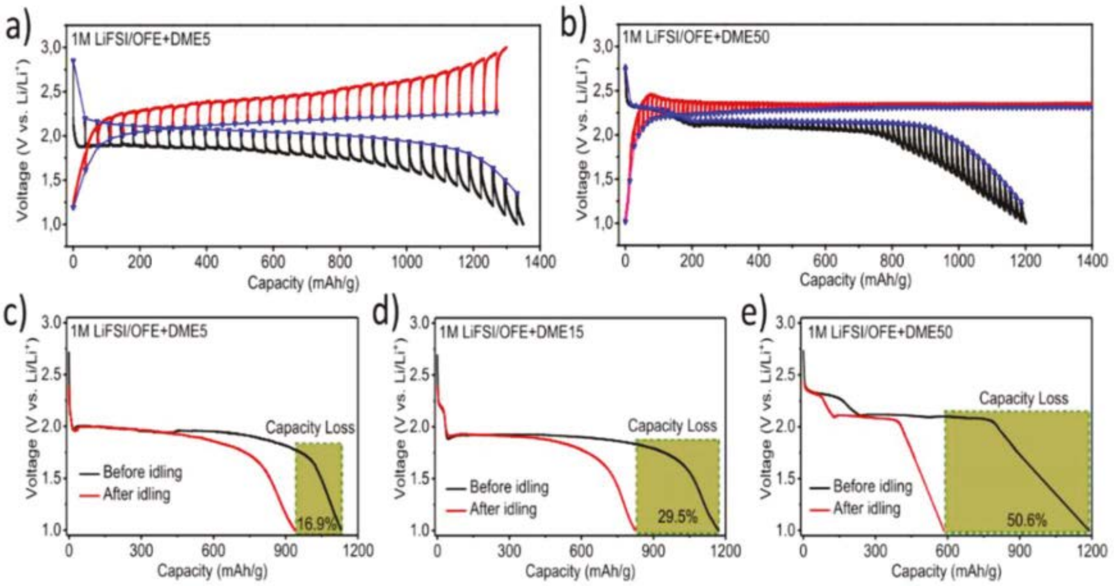

Figure 5. GITT curves in a) 1 M LiFSI/OFE + DME5 and b) 1 M LiFSI/OFE + DME50 electrolyte. Long-term self-discharge characteristics: discharge curves for Li–S cells before (black curve) and after (red curve) idling for 60 d in c) 1 M LiFSI/OFE + DME5, d) 1 M LiFSI/OFE + DME15, and e) 1 M LiFSI/OFE + DME50 electrolytes.

for DME50 (Figure 5e). The excellent capacity recovery in DME5 electrolyte is consistent with the significant suppression of shuttle reaction in DME5 via the maximum addition of OFE along with minimum low solubility of polysulfides, which can effectively improve the CE of sulfur cathode and give a promise of practical application of long-term high-performance Li–S batteries. These results can be attributed to the less and less polysulfide dissolution along with the increasing OFE content into the LiFSI/DME electrolytes, which are well consistent with the UV–vis results.

Cyclic voltammetry (CV) scans were first used to identify the redox reactions process of S@C composites (Figure S5, Supporting Information) in various electrolytes, as shown in **Figure 6**a. During the cathodic scan, the CV curves of the S@C in DME5 possess one main reduction peaks, which can be ascribed to the direct reduction of solid insoluble elemental sulfur to insoluble low-order polysulfide because of no free DME solvent to dissolve the high-order polysulfide in the LHCE of DME5. This unique redox behavior can also be confirmed by the charge–discharge curves in DME5 in Figure 6b, which possess only one plateau at its 2nd cycling. In the subsequent anodic scan, there is also only one oxidation peak at about 2.70 V, which can be attributed to the oxidation conversion of Li_2S_2/Li_2S into elemental sulfur in DME5 electrolyte. These phenomena in the DME5 electrolyte agrees with the obvious reports for the highly concentrated electrolyte.[19,22]

In contrast, for the CV curves of the S@C in DME15 electrolyte, two typical reduction peaks clearly appear, which is related to the reduction of solid sulfur to liquid high-order polysulfides and further reduction of higher order polysulfides to solid insoluble Li_2S_2/Li_2S, respectively. Accordingly, the 2nd discharge curve in DME15 reflects two plateaus attributed to the two step reduction process. Furthermore, owing to the high activity of abundant DME in DME50 electrolyte, three main reduction peaks at about 2.29, 2.02, and 1.78 V were observed in the CV curves for DME50, corresponding to the reduction of solid S to liquid high-order polysulfides, higher order polysulfides to lower order polysulfides, and deep reduction of polysulfide to Li_2S, respectively.[23] The corresponding discharge curve of DME50 in Figure 6b (bottom) also shows two obvious plateaus are appeared at around 2.31 and 2.09 V with a slop tail for formation of Li_2S, in accordance with the previously reported dilute electrolytes for Li–S batteries.[18b] Importantly, the upper voltage plateau in DME50 is much more longer (higher capacity) than that in DME15, indicating the higher dissolution of higher order polysulfides in DME50 with sufficient free DME solvent.

These different electrochemical behaviors in the OFE-based electrolytes are related to competitive solvation for Li^+ by solvents and FSI^- anions. Due to the different salt concentration and the structure of solvent and anions of electrolyte, the competition leads to various Li^+-solvation species from the SSIPs, CIPs, to AGGs with the increasing of concentration. In the LHCE, the solvation species is priority to generate the AGGs, hardly with any free solvent. Therefore, a quasi-solid-state reaction mechanism in LHCE will dominate the Li–S chemistry as compared with another reaction of solid–liquid–solid in dilute electrolyte.[24] As a result, the dissolution of high-order polysulfides in DME5 can be completely inhibited without upper CV peaks and corresponding discharge plateaus; while for the solid–liquid–solid mechanism in DME15 and DME50 electrolytes, there are evident upper-voltage peaks and plateaus corresponding to the polysulfides dissolution process. Moreover, when comparing the discharging/charging behaviors in various OFE-based electrolyte at 1st, 2nd, and 150th cycles in Figure 6b,c and Figure S6 in the Supporting Information, it can be obviously found that in the DME5 electrolyte, the discharge capacity is slightly higher than the charge capacity at 1st and 2nd cycles which should be attributed to the irreversible formation of SEI during the initial few discharge/charge cycles.

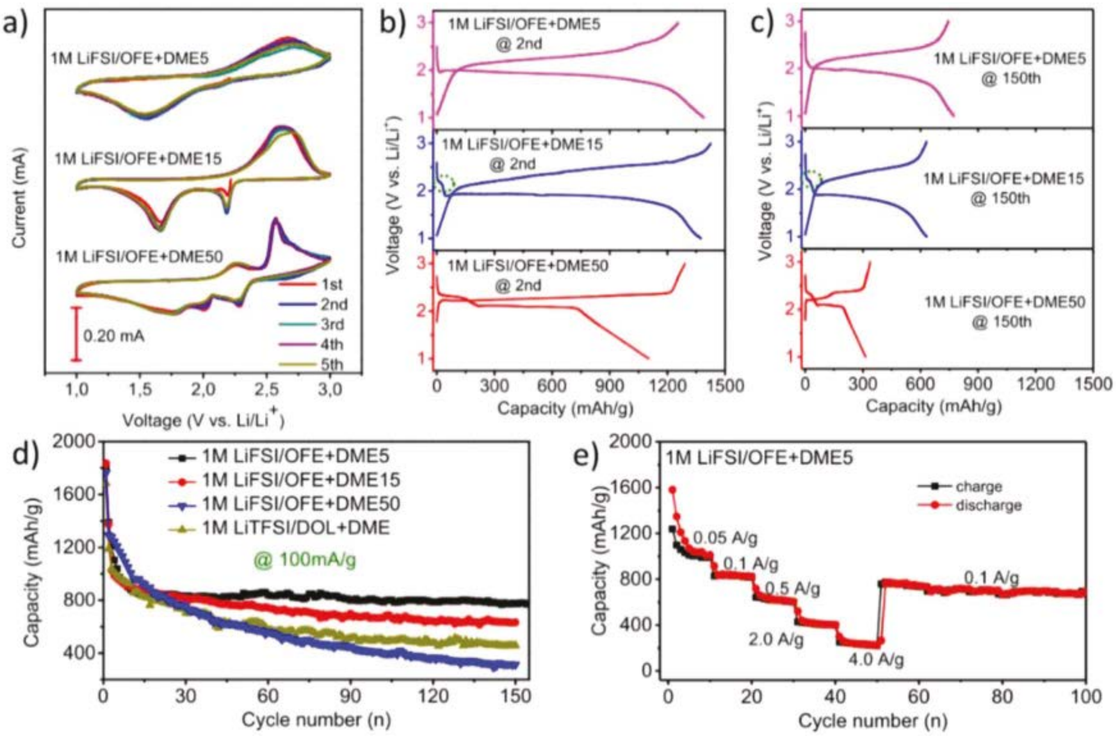

Figure 6. Electrochemical performance: a) Cyclic voltammogram in different electrolytes at 0.05 mV s^{-1}. Charge–discharge curves with current density of 100 mA g^{-1} at b) 2nd and c) 150th cycling. d) Comparison of specific discharge capacity at 100 mA g^{-1} in different electrolytes. e) The rate performance of Li–S batteries with 1 M LiFSI/OFE + DME5 electrolyte.

After that, the capacity difference decreased and ≈100% of CE is achieved after 10 cycles (Figure S7, Supporting Information). But for the electrolyte of DME15 and DME50, the discharge capacity is lower than the charge capacity no matter from the 1st, 2nd, to 150th with the CE of >100% (CE = charge capacity/discharge capacity). The obvious comparison indicates the existence of obvious shuttle effect in these dilute electrolytes of DME15 and DME50 but complete disappearance of shuttle effect in the LHCE of DME5. As a result, based on the CV redox peak signal and upper-voltage plateau in discharge curve, the polysulfide shuttle can be stepwise controlled only by gradually adjusting the OFE cosolvent content in these OFE-based electrolytes.

Figure 6d shows the cycling performance of S@C cathodes at a current density of 100 mA g^{-1} in various electrolytes. The DME5 electrolyte depicts the best cycling stability, maintaining a reversible discharge capacity of 775 mAh g^{-1} for 150th cycling with the initial CE of 83% and the average CE of 99.2%; while the DME15 possess 633 mAh g^{-1}, DME50 with 314 mAh g^{-1}, and DOL + DME with 458 mAh g^{-1} under the same conditions. For these dilute electrolytes of DME15, DME50, and DOL + DME, their corresponding CEs are all greater than 100% during all cycles, as indicated in the Figure S7 in the Supporting Information. More specifically, in the dilute electrolyte of DME50, there is a CE of 116% at the initial cycle and the average CE of >100%, which is attributed to the shuttle effect in the dilute electrolytes that transfer the high-order polysulfide through the separator to Li anode surface with irreversible consumption of the active material and electrolyte, leading to the rapid capacity fading and shuttle-reaction CE of more than 100%. Besides, as shown in Figure 6e, the Li–S battery with the DME5 electrolyte also shows excellent rate performance, with the discharge capacities of 1012, 823, 666, 402, and 223 mAh g^{-1} at current densities of 0.05, 0.1, 0.5, 2.0, and 4.0 A g^{-1}, respectively. When the current density switches back from 4.0 to 0.1 A g^{-1}, the discharge capacity maintains at 774 mAh g^{-1}, almost returning to its original capacity even after cycling at high current density, implying the superior reversibility, and excellent tolerance of high-rate capability in the DME5 electrolyte.

Importantly, owing to significant suppression of dissolution of polysulfide in DME5 electrolyte with the excellent high CE of 99.2% for S@/C cathode and 99.3% CE for Li anode, the amount of electrolyte using for the Li–S batteries was reduced to 4.56 g A^{-1} h^{-1}, which is much lower than that of most previous reported value for Li–S batteries, accompanied with much better commercial application.

Based on the above results and analysis, it can be concluded that the excellent electrochemical performance of the Li–S batteries in the LHCE of DME5 is ascribed to the following two reasons: i) the formation of robust SEI layer with rich LiF component on the surface of Li metal anode from reduction of OFE and FSI$^-$ which can effectively suppress Li dendrite growth and promote Li plating/stripping reversibility; ii) the shuttle reaction in Li–S chemistry is completely inhibited via introduction of the inert OFE cosolvent with low donor number for Li salt and minimum ability for dissolution polysulfides. The two advantages in the LHCE of DME5 promise a significant improvement of electrochemical performance for Li–S batteries.

3. Conclusion

In summary, a localized high-concentration OFE-based electrolyte was first developed by using the inert fluoroalkyl ether OFE as the cosolvent diluent in 1 M LiFSI/OFE + DME. We have successfully suppressed the Li dendrite growth and polysulfide shuttle reaction in Li–S batteries. As the most effective electrolyte for Li–S cells, the DME5 electrolytes shows its outstanding performance, which can simultaneously enable both the formation of dendrite-free Li cycling with a high CE up to 99.3% and completely suppression of shuttling effect of lithium polysulfide with stable cycling for the S cathode (99.2% of CE). When compared with the typical HCEs, this difficult burning LHCE of DME5 not only possesses the superior solvation structure and unique function for the formation of LiF-rich SEI layer but also maintains a lower cost, lower viscosity, better wettability, and lean electrolyte usage, making it more advantage for efficient and practical electrolyte systems for next generation Li–S batteries. The fundamental concept of LHCE can also be widely extended to many other battery electrolyte systems, such as the Li metal batteries, Na (K) metal batteries, and sulfur-based metal ion batteries. Therefore, it opens a new horizon for the further development and improvement of advanced electrolyte systems for next-generation energy storage technologies.

Supporting Information

Supporting Information is available from the Wiley Online Library or from the author.

Acknowledgements

The authors thank the support from US Department of Energy (DOE) under Award No. DEEE0008202 and DEEE0008200. The authors gratefully acknowledge the support of the Maryland NanoCenter and its Advanced Imaging and Microscopy (AIM) Lab.

Conflict of Interest

The authors declare no conflict of interest.

Keywords

inert fluorinated diluents, Li–S batteries, lithium dendrite, localized high-concentration electrolyte, polysulfide shuttle

Received: December 6, 2018
Revised: January 17, 2019

---

[1] A. Manthiram, Y. Fu, S.-H. Chung, C. Zu, Y.-S. Su, *Chem. Rev.* **2014**, *114*, 11751.

[2] a) J. Qian, W. A. Henderson, W. Xu, P. Bhattacharya, M. Engelhard, O. Borodin, J.-G. Zhang, *Nat. Commun.* **2015**, *6*, 6362; b) N. S. Choi, Z. Chen, S. A. Freunberger, X. Ji, Y. K. Sun, K. Amine, G. Yushin, L. F. Nazar, J. Cho, P. G. Bruce, *Angew. Chem., Int. Ed.* **2012**, *51*, 9994; c) L. Suo, Y.-S. Hu, H. Li, M. Armand, L. Chen, *Nat. Commun.* **2013**, *4*, 1481.

[3] a) L. Ji, M. Rao, H. Zheng, L. Zhang, Y. Li, W. Duan, J. Guo, E. J. Cairns, Y. Zhang, *J. Am. Chem. Soc.* **2011**, *133*, 18522; b) T. Lin, Y. Tang, Y. Wang, H. Bi, Z. Liu, F. Huang, X. Xie, M. Jiang, *Energy Environ. Sci.* **2013**, *6*, 1283.

[4] a) X. Ji, K. T. Lee, L. F. Nazar, *Nat. Mater.* **2009**, *8*, 500; b) S. Moon, Y. H. Jung, W. K. Jung, D. S. Jung, J. W. Choi, D. K. Kim, *Adv. Mater.* **2013**, *25*, 6547.

[5] L. Xiao, Y. Cao, J. Xiao, B. Schwenzer, M. H. Engelhard, L. V. Saraf, Z. Nie, G. J. Exarhos, J. Liu, *Adv. Mater.* **2012**, *24*, 1176.

[6] a) K. Yan, Z. Lu, H.-W. Lee, F. Xiong, P.-C. Hsu, Y. Li, J. Zhao, S. Chu, Y. Cui, *Nat. Energy* **2016**, *1*, 16010; b) G. Zheng, S. W. Lee, Z. Liang, H.-W. Lee, K. Yan, H. Yao, H. Wang, W. Li, S. Chu, Y. Cui, *Nat. Nanotechnol.* **2014**, *9*, 618; c) D. Lin, Y. Liu, Z. Liang, H.-W. Lee, J. Sun, H. Wang, K. Yan, J. Xie, Y. Cui, *Nat. Nanotechnol.* **2016**, *11*, 626.

[7] N. W. Li, Y. X. Yin, C. P. Yang, Y. G. Guo, *Adv. Mater.* **2016**, *28*, 1853.

[8] a) Y. Liping, M. Jun, Z. Jianjun, Z. Jingwen, D. Shanmu, L. Zhihong, C. Guanglei, C. Liquan, *Energy Storage Mater.* **2016**, *5*, 139; b) G. Xu, C. Pang, B. Chen, J. Ma, X. Wang, J. Chai, Q. Wang, W. An, X. Zhou, G. Cui, L. Chen, *Adv. Energy Mater.* **2018**, *8*, 1701398.

[9] S. Zhang, K. Ueno, K. Dokko, M. Watanabe, *Adv. Energy Mater.* **2015**, *5*, 1500117.

[10] a) J. Zheng, S. Chen, W. Zhao, J. Song, M. H. Engelhard, J.-G. Zhang, *ACS Energy Lett.* **2018**, *3*, 315; b) S. Chen, J. Zheng, D. Mei, K. S. Han, M. H. Engelhard, W. Zhao, W. Xu, J. Liu, J. G. Zhang, *Adv. Mater.* **2018**, *30*, 1706102.

[11] a) K. Dokko, N. Tachikawa, K. Yamauchi, M. Tsuchiya, A. Yamazaki, E. Takashima, J.-W. Park, K. Ueno, S. Seki, N. Serizawa, *J. Electrochem. Soc.* **2013**, *160*, A1304; b) T. Doi, Y. Shimizu, M. Hashinokuchi, M. Inaba, *J. Electrochem. Soc.* **2017**, *164*, A6412.

[12] R. Cao, W. Xu, D. Lv, J. Xiao, J. G. Zhang, *Adv. Energy Mater.* **2015**, *5*, 1402273.

[13] H. Moon, T. Mandai, R. Tatara, K. Ueno, A. Yamazaki, K. Yoshida, S. Seki, K. Dokko, M. Watanabe, *J. Phys. Chem. C* **2015**, *119*, 3957.

[14] a) Y. Yamada, A. Yamada, *J. Electrochem. Soc.* **2015**, *162*, A2406; b) O. Borodin, L. Suo, M. Gobet, X. Ren, F. Wang, A. Faraone, J. Peng, M. Olguin, M. Schroeder, M. S. Ding, *ACS Nano* **2017**, *11*, 10462.

[15] a) M. Shin, H.-L. Wu, B. Narayanan, K. A. See, R. S. Assary, L. Zhu, R. T. Haasch, S. Zhang, Z. Zhang, L. A. Curtiss, *ACS Appl. Mater. Interfaces* **2017**, *9*, 39357; b) J. Zheng, X. Fan, G. Ji, H. Wang, S. Hou, K. C. DeMella, S. R. Raghavan, J. Wang, K. Xu, C. Wang, *Nano Energy* **2018**, *50*, 431.

[16] a) J. Qian, W. A. Henderson, W. Xu, P. Bhattacharya, M. Engelhard, O. Borodin, J.-G. Zhang, *Nat. Commun.* **2015**, *6*, 6362; b) G. Bieker, M. Winter, P. Bieker, *Phys. Chem. Chem. Phys.* **2015**, *17*, 8670; c) M. S. Park, S. B. Ma, D. J. Lee, D. Im, S.-G. Doo, O. Yamamoto, *Sci. Rep.* **2014**, *4*, 3815.

[17] J. Zheng, J. A. Lochala, A. Kwok, Z. D. Deng, J. Xiao, *Adv. Sci.* **2017**, *4*, 1700032.

[18] a) S. S. Zhang, *Front. Energy Res.* **2013**, *1*, 10; b) S. S. Zhang, *J. Power Sources* **2013**, *231*, 153.

[19] M. Cuisinier, P.-E. Cabelguen, B. Adams, A. Garsuch, M. Balasubramanian, L. Nazar, *Energy Environ. Sci.* **2014**, *7*, 2697.

[20] J.-W. Park, K. Yamauchi, E. Takashima, N. Tachikawa, K. Ueno, K. Dokko, M. Watanabe, *J. Phys. Chem. C* **2013**, *117*, 4431.

[21] F. Jeschull, D. Brandell, K. Edström, M. J. Lacey, *Chem. Commun.* **2015**, *51*, 17100.

[22] M. Cuisinier, P.-E. Cabelguen, S. Evers, G. He, M. Kolbeck, A. Garsuch, T. Bolin, M. Balasubramanian, L. F. Nazar, *J. Phys. Chem. Lett.* **2013**, *4*, 3227.

[23] C. Barchasz, F. Molton, C. Duboc, J.-C. Leprêtre, S. b. Patoux, F. Alloin, *Anal. Chem.* **2012**, *84*, 3973.

[24] D.-W. Wang, Q. Zeng, G. Zhou, L. Yin, F. Li, H.-M. Cheng, I. R. Gentle, G. Q. M. Lu, *J. Mater. Chem. A* **2013**, *1*, 9382.

Sigma-Aldrich®
Lab & Production Materials

MilliporeSigma

supercharge your research & production

Advanced battery materials with extensive resources and services

Whether you're researching new battery materials, realizing prototypes, or already in production, we'll help you achieve it with fresh energy. Our comprehensive range of cutting-edge battery materials offers superior consistency, purity and quality for producing lithium-ion batteries with outstanding performance, durability and dependability. Discover how our unparalleled portfolio can boost your battery breakthroughs.

Your benefits

- **Broad portfolio** of cathode, anode and electrolyte battery materials, greener alternatives, foil materials, binders, electrodes, sheets and more
- **Extensive resources** from expert technical support to insightful literature on the latest battery designs
- **Custom services** including contract manufacturing, QC, documentation and special packaging
- **Bulk volumes** up to tons for large-scale production Reliable supply from 130 global distribution centers

Explore powerful battery materials
sigmaaldrich.com/battery

MilliporeSigma is the U.S. and Canada Life Science business of Merck KGaA, Darmstadt, Germany.

MS_AD9739EN Ver. 1.0 07/2022